Feasibility studies for the high precision X-ray spectroscopy of heavy Ξ^- hyperatoms at $\overline{\text{P}}$ANDA using the PANda GErmanium Array PANGEA

Dissertation
zur Erlangung des Grades
„Doktor
der Naturwissenschaften"
am Fachbereich Physik, Mathematik und Informatik
der Johannes Gutenberg-Universität
in Mainz

Marcell Steinen

JOHANNES GUTENBERG UNIVERSITÄT MAINZ

HIM HELMHOLTZ Helmholtz-Institut Mainz

geb. in Dernbach
Mainz, den 12. Dezember 2019

Erstgutachter: –
Zweitgutachter: –
Datum der mündlichen Prüfung: 20.05.2020

Zusammenfassung

Mit $\overline{\mathrm{P}}$ANDA entsteht ein Hadronenphysikexperiment an der neuen Beschleunigeranlage FAIR in Darmstadt, Deutschland. Dabei ermöglicht der gespeicherte Antiprotonenstrahl des HESR Speicherrings die Produktion hoher Raten von Hyperon-Antihyperon-Paaren mit ein- und mehrfacher Strangeness. Dies erlaubt mehrere Experimente im Strangeness-Sektor, wobei besonders die Wechselwirkung von (Anti-)Hyperonen und Kernmaterie untersucht werden kann, die ein wichtiger Baustein ist, um das „Hyperon-Puzzle“ im Zentrum von Neutronensternen zu lösen.

Dabei wird die hohe Modularität des $\overline{\mathrm{P}}$ANDA-Spektrometers benutzt, welche es erlaubt einzelne Detektorkomponenten für spezifische Experimente auszutauschen. Besonders das Hyperatom- sowie das Hyperkernexperiment machen davon Gebrauch. Diese Experimente benötigen zwingend einen hochauflösenden γ-Detektor: PANGEA. Das PANda GErmanium Array besteht aus insgesamt 60 hochreinen Germaniumkristallen in 20 Kryostaten. Die Optimierung der Anordnung dieser Detektoren sowie deren Integration innerhalb von $\overline{\mathrm{P}}$ANDA werden in dieser Arbeit diskutiert. Zusätzlich wird der Einfluss des hadronischen Untergrunds während der Experimente untersucht. Insbesondere schnelle Neutronen führen zu Strahlenschäden innerhalb der hochreinen Germaniumkristalle, was die hohe intrinsische Energieauflösung verringert. Dieser Einfluss wurde experimentell in zwei Bestrahlungstests am COSY Protonenbeschleuniger in Jülich, Deutschland, mit bis zu $5{,}6 \cdot 10^9\,\mathrm{Neutronen/cm^2}$ untersucht. Durch die digitale Analyse der Pulsformen konnte ein großer Anteil der Auflösungsverluste bei der Energiemessung korrigiert werden. Das thermische Ausheilen der Kristalle nach der Bestrahlung im Labor konnte die ursprüngliche Energieauflösung wiederherstellen.

Trotz alledem müssen die Einflüsse der Bestrahlung bei der Studie zur Machbarkeit des Hyperatomexperiments berücksichtigt werden. $\overline{\mathrm{P}}$ANDA wird das erste Experiment weltweit sein, das die Wechselwirkung von Ξ^--Hyperonen und vornehmlich Neutronen in der neutronendominierten Peripherie von Ξ^--^{208}Pb Hyperatomen untersuchen kann. Simulationen zeigen, dass mehrere experimentelle Observablen eine Bestimmung sowohl des Real- als auch des Imaginärteils des optischen Potentials von Ξ^--Hyperonen mit einer Genauigkeit von $\pm 1\,\mathrm{MeV}$ ermöglichen.

Abstract

$\overline{\text{P}}$ANDA is a new experiment in hadron physics at the upcoming FAIR facility in Darmstadt, Germany. The combination of $\overline{\text{P}}$ANDA and the antiproton beam, provided by the antiproton storage ring HESR, yields high production rates of strange hyperon-antihyperon pairs. This enables multiple experiments in strangeness nuclear physics which allow to study the interaction of hyperons and antihyperons within nuclear matter. This is essential to understand the composition of neutron star matter and solve the "hyperon puzzle".

The modularity of $\overline{\text{P}}$ANDA allows to design and integrate a dedicated setup for the high resolution X-ray and γ spectroscopy of heavy Ξ^- hyperatoms and double Λ hypernuclei. The germanium detector array PANGEA (PANda GErmanium Array) is mandatory for these experiments. Its optimization and integration into the $\overline{\text{P}}$ANDA target spectrometer is discussed in this thesis. During the experiments at $\overline{\text{P}}$ANDA, the HPGe (High Purity Germanium) crystals of PANGEA will suffer from inevitable hadronic background. Especially fast neutrons will damage the lattice structure of the crystal and deteriorate its resolution. This effect has been experimentally studied in irradiation tests at the COSY accelerator in Jülich, Germany, with up to $5.6 \cdot 10^9\,\mathrm{neutrons/cm^2}$. A large fraction of the performance loss of the detector could be corrected by analyzing the pulse shape of the detector response. The initial crystal performance could be restored by annealing of the crystal in the laboratory after the irradiation.

The effects of the irradiation had to be kept in mind when the feasibility of the hyperatom experiment was studied. $\overline{\text{P}}$ANDA is unique in its ability to study the Ξ^- nucleon interaction in the neutron-rich periphery of Ξ^--^{208}Pb hyperatoms. Full simulations of the experiment show that multiple experimental observables will allow to measure the real and imaginary part of the Ξ^- optical potential with a precision of $\pm 1\,\mathrm{MeV}$.

Contents

1 Motivation

One of the biggest challenges in the context of today's physics is the description of stellar objects in a common theoretical framework. Right now, there is no unified theory of all four fundamental forces. None of the present approaches succeeds in integrating gravity into a common concept with the strong, weak and electromagnetic force. Especially the observed motion of galaxies in the universe can not be explained. Visible matter alone is insufficient [1] and hence two possible scenarios are considered to solve this issue: either the presence of invisible dark matter explains the deviations or Einstein's General Relativity has to be adapted at these large scales.

Possible extensions of gravity (see e.g. [2, 3, 4]) can be tested within the strong gravitational fields of neutrons stars. These neutron stars can reach masses above 2 solar masses ($M_\odot$) [5, 6, 7] compressed to a radius in the range of $12\,\mathrm{km}$ which results in very dense objects which can exceed the density of atomic nuclei. None of the four fundamental forces can be neglected within these high densities [2, 8]. The size of such a neutron star is determined by the balance of the degeneracy pressure, caused by the Pauli-principle, expanding the system, and gravity shrinking it. Strong nuclear interactions are another ingredient of the equation of state of neutron stars (EOS). Only the repulsive support of these interactions prevents the collapse of neutron stars above 0.7 $M_\odot$ [9]. Electromagnetic interactions play only a minor role in the EOS. Nevertheless, neutron stars have the strongest magnetic fields in the universe due to their high rotation frequency. Weak interaction effects the EOS indirectly. It introduces new hadronic degrees-of-freedom in the high density core of the neutron star.

Under the assumption that gravity within this strong-field and high density follows the same laws as in the matter-free situation, mergers of binary neutron star systems [10] tightly constrain the tidal deformability and hence the EOS of neutron star matter [11, 12, 13, 14, 15]. In fact, already the first observations of merging neutron stars by the Advanced LIGO and Advanced Virgo gravitational-wave detectors in August 2017 (GW170817) [16, 17] allowed to constrain possible modifications of general relativity on astronomical scales [18, 19, 20]. The large amount of ejected matter ruled out a direct merging of GW170817 to a black hole. Nevertheless, recent observations of the Chandra observatory indicated a delayed formation of a black hole [21]. Based on this scenario, an upper limit for the mass of a neutron star could be estimated to $M_{\mathrm{max}} \approx 2.2\,M_\odot$ [22, 23, 24, 25].

In addition to these astrophysical observations, input parameters of the nuclear EOS can be studied in terrestrial experiments. Once these experiments establish a proper understanding of the nuclear EOS, a comparison to the EOS deduced from neutron star events might allow to isolate and understand the gravitational effects in the strong-field and matter-dominated regime. Nuclear reactions at high energies, the mapping of the chart of nuclear stability using radioactive beams and precision studies of nuclear few body reactions contribute to this challenge. Additionally, strangeness nuclear physics in all its facets can help to pin down the EOS.

Nevertheless, after decades of research the EOS of neutron stars still remains an open question. The composition of neutron star matter is still not fully understood. A recent overview of this can be found e.g. in [26]. Today many possible compositions are under investigation (see figure 1.1) and none of them can be ruled out a priori.

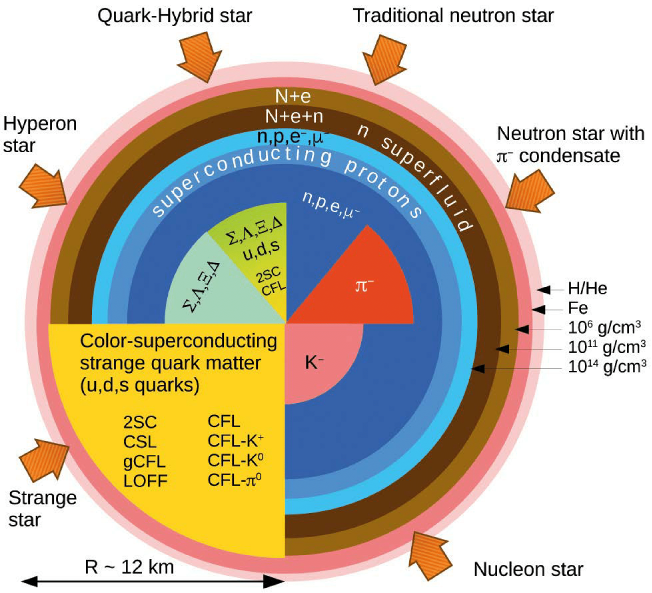

Figure 1.1: Possible compositions of cold neutron stars [27, 28] (figure from [27]).

The transformation of neutrons into hyperons[a] within neutron star matter has already been suggested in 1959 [29] - 8 years before the first observation of a pulsar [30]. Within a non-interacting Fermi-gas model the hyperon transformation threshold is situated at 5 times the normal nuclear density ρ_0 (see left part of figure 1.2). In such a non-interacting gas Σ^- would be the first appearing hyperon [31]. When nuclear interactions are taken into account, there is a wide consensus in most present theoretical descriptions of neutron stars that the transformation threshold for hyperons is reduced to 2-3 ρ_0. At the same time, the additional strangeness degrees of freedom decreases the degeneracy pressure of the neutron star matter. This softens conventional EOS of neutron stars to a level that is too low to explain e.g. the measured mass of $2.01 \pm 0.04\,M_\odot$ of PSR J0348+0432 [6]. This is the so called “hyperon puzzle”.

A possible solution for this issue is the addition of repulsive two- and three-body hyperon interactions to the EOS [32]. The experimental uncertainty of these interactions is large. Because of that, even the sequence of the appearance of hyperons within neutrons stars can not be unambiguously predicted. This sequence depends on the chemical potentials of the hyperons which scales with their mass and their hadronic interaction strength. As an example for this, a nucleonic (top) and a hyperonic EOS (bottom) are shown in the right part of figure 1.2. Both models are consistent with the measured neutron star masses above $2\,M_\odot$. The plots show the density dependence of the composition of neutron star matter in the corresponding EOS. The colored bands of the various hadrons in the hyperonic EOS are based on the experimental

---

[a] Hadrons containing at least one strange quark, e.g. $\Lambda = uds$, $\Sigma^- = dds$, $\Xi^- = dss$

uncertainties of their nuclear interactions. The width of these bands show the large uncertainty of these interactions. Within these uncertainties Λ or Σ^- hyperons could appear first - and in the case of a very attractive Ξ^- and a repulsive Σ^-, Ξ^- hyperons might even appear at lower densities than Σ^-.

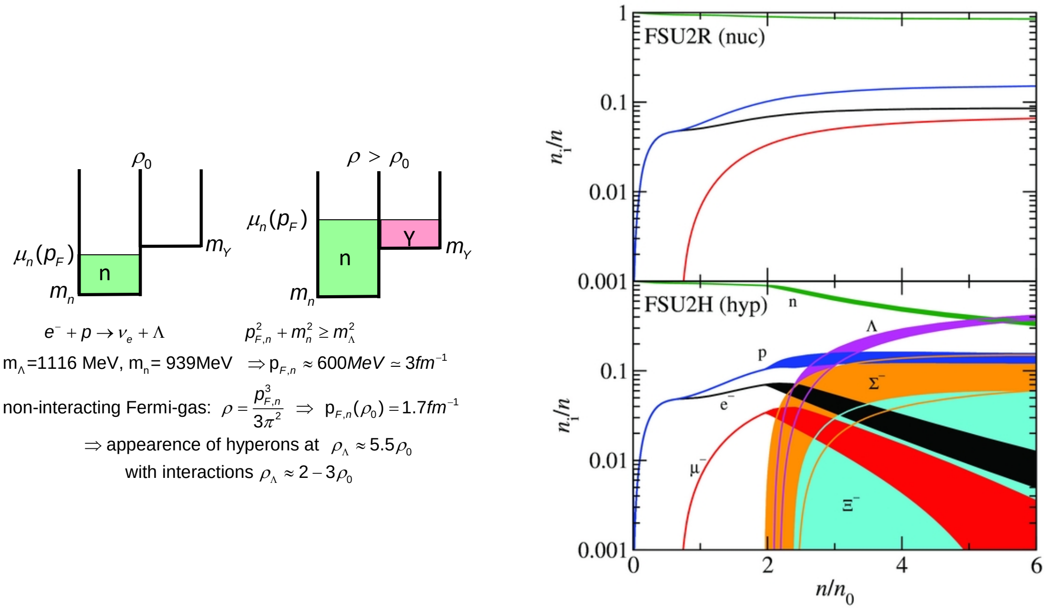

Figure 1.2: Simplified potential well model of neutron stars (left). In the high density core region of neutron stars, the Fermi energy rises to extremely high levels. Because of that, it is energetically favored to convert neutrons to hyperons [29]. The calculations at the bottom show the density threshold for the appearance of Λ hyperons which highly depends on the strength of the interactions (figure taken from [33]). These interactions define the sequence of the appearance of hyperons within neutron stars as shown on the right. Both plots show the density-dependent composition of neutron star matter for either a nucleonic (FSU2R) or hyperonic EOS (FSU2H). The uncertainties of the hadronic interactions influence the composition in the hyperonic model. Within the present experimental uncertainties, the sequence of the appearance of hyperons is ambiguous (figure from [34]).

This ambiguity indicates that additional experimental input is required for these models. Since direct experimental studies at the high densities inside neutron stars are not possible, multiple terrestrial experimental approaches are ongoing to measure the hyperon-nucleon interaction at various densities and neutron-to-proton-ratios (N/Z) (compare fig. 1.3):

- Direct scattering experiments with hyperons are difficult due to their short life time. The closest to this are femtoscopic studies performed at STAR [35, 36, 37, 38] and ALICE [39, 40]. Recently the interaction of Ξ^- with free protons was studied at ALICE [41].
- Ξ^- hypernuclei allow to probe the Ξ^- nucleus potential at nuclear density and N/Z = 1. These hypernuclei can either be studied in emulsion detectors (KEK-PS E373 [42], J-PARC E07 [43]) or in missing mass spectroscopy using (K^-,K^+) reactions. This was performed in the past at KEK E224 [44] and BNL E885 [45] and will be continued by J-PARC E05 [46] and E70 [47] in the future with higher statistics and resolution.

- The strong atomic binding of Ξ^- hyperatoms also allows to access the Ξ^--nucleus potential. Due to the high mass of the Ξ^-, its radial density distribution overlaps the nucleus and the arising strong interaction influences the X-ray spectrum of these hyperatoms. This interaction occurs in the nuclear periphery, where the nuclear density is lower than in the core region but the composition is shifted towards an excess of neutrons. Various kinds of hyperatoms across the periodic table will be studied experimentally at J-PARC E07 [43], J-PARC E03 [48] and at $\overline{\text{P}}$ANDA. Due to its split up target design, the high resolution spectroscopy of cascading X-rays of heavy Ξ^--^{208}Pb hyperatoms is a unique feature of $\overline{\text{P}}$ANDA.

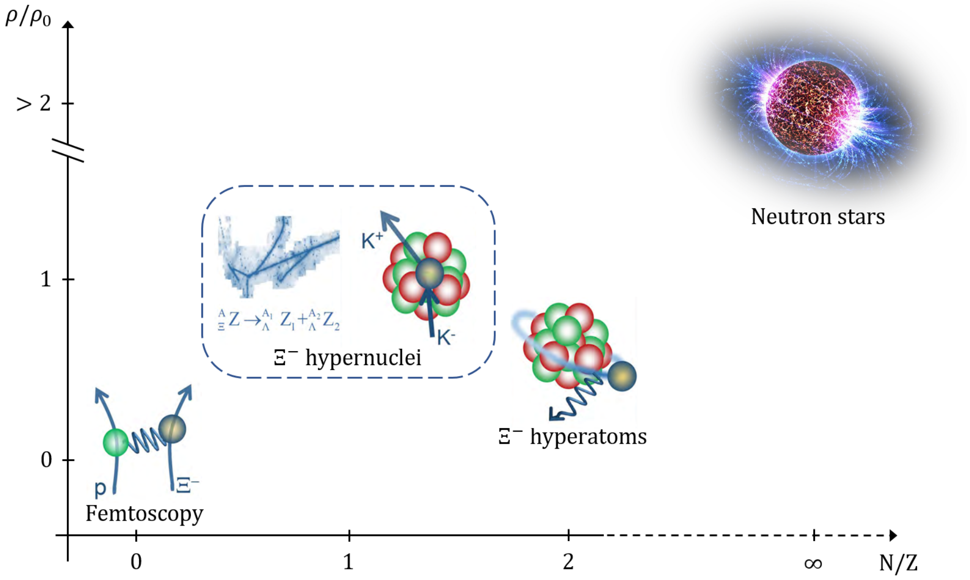

Figure 1.3: The direct measurement of the Ξ^- potential within neutron stars is impossible. Terrestrial experiments can be performed at lower density and N/Z. Theses range from femtoscopic studies of finite state interactions to Ξ^- hypernuclei and Ξ^- hyperatoms. The results of these experiments can confine the EOS for neutron stars.

A brief overview of the $\overline{\text{P}}$ANDA experiment will be given in chapter 2. In the same chapter, the experiments of the strangeness nuclear physics program of $\overline{\text{P}}$ANDA and the required modifications of the experimental setup will be introduced in more detail.

After that, chapter 3 briefly presents the physics of exotic atoms, while focusing on hadronic atoms. This includes a brief introduction of both hyperatom experiments at J-PARC E03 and E07.

As high precision X-ray and γ spectroscopy is mandatory for these studies, chapter 4 is dedicated to the conception and optimization of the PANda GErmanium Array PANGEA with its novel cooling system. This includes the mechanical and electronical integration into the $\overline{\text{P}}$ANDA target spectrometer.

The performance of a germanium detector in a high hadronic background as expected for $\overline{\text{P}}$ANDA is challenging. Especially neutrons will deteriorate the high intrinsic resolution of the High Purity Germanium (HPGe) crystals over time. It is therefore essential to estimate the amount of neutrons that the crystals will have to withstand. Monte Carlo simulations as well as experimental irradiation tests at the COSY accelerator in Jülich, Germany, were performed for this purpose. The data of these tests at COSY could be used to estimate the resolution loss and develop an algorithm that is able to partially negate the effects of the radiation damage. All this is shown in chapter 5.

The final chapter 6 studies the feasibility of the hyperatom experiments at $\overline{\text{P}}$ANDA. It will be shown that Ξ^--^{208}Pb hyperatoms offer promising possibilities to measure the strength of the optical potential of Ξ^- within neutron-rich matter. The optimization of the experiment in a full simulation is shown. Finally, this pseudodata is used to optimize the signal-to-noise ratio of the experiment and calculate expectations for the achievable uncertainties of the experimental observables and translate these to estimations of the real and imaginary part of the potential.

1.1 Personal contributions in the context of my thesis

This section will briefly summarize my personal contributions in the context of my thesis.

- While I was only slightly involved in the hardware development of PANGEA, the integration in $\overline{\text{P}}$ANDA was done by myself. This includes the optimization of the geometry in simulations. The mechanical integration was based on my ideas and performed under my supervision by engineers from Ferchau Engineering. The design of the integration on the electronical side was done by me following the regulations given by the $\overline{\text{P}}$ANDA collaboration.
- The irradiation tests at COSY have been planned and performed by me. Since the experiments required a continuous supervision of the detectors, coworkers helped me by taking shifts. I analyzed the data of both test. Only a small part, the optimization of the pulse shaping parameters, has been performed in the context of the Bachelor's thesis of T. R. [49] which I supervised. The annealing of the irradiated detectors was performed at GSI.
- The full feasibility studies of the $\overline{\text{P}}$ANDA hyperatom experiment were performed by me. This includes the optimization of the setup as well as the search for effective cuts and their study in simulations within the PandaRoot framework. I expanded this framework by the required geometries as well as analysis code. Besides PandaRoot, which is a collaborative developed software, I used for the feasibility studies a software by E. F. based on [50] which was able calculate the experimental observables for various target materials.

Partial results of this thesis have already been published previously in [51, 52, 53, 54] and have been presented at the STRANEX Workshop [55] and THEIA-STRONG2020 workshop [56].

2 The $\overline{\mathrm{P}}$ANDA experiment at FAIR

The $\overline{\mathrm{P}}$ANDA hyperatom and hypernuclear experiments are important pillars of the strangeness nuclear physics program of the $\overline{\mathrm{P}}$ANDA experiment. $\overline{\mathrm{P}}$ANDA will be situated at the future Facility for Antiproton and Ion Research (FAIR). These experiments and the facility itself are briefly introduced in the following sections.

2.1 FAIR and the HESR

FAIR is currently under construction at the GSI Helmholtzzentrum für Schwerionenforschung in Darmstadt, Germany. FAIR extends the existing experimental facilities with new accelerators and experiments (see figure 2.1). These accelerators provide high energy proton or heavy ion beams. Moreover, secondary beams of antiprotons or radioactive particles can be produced and stored in dedicated storage rings.

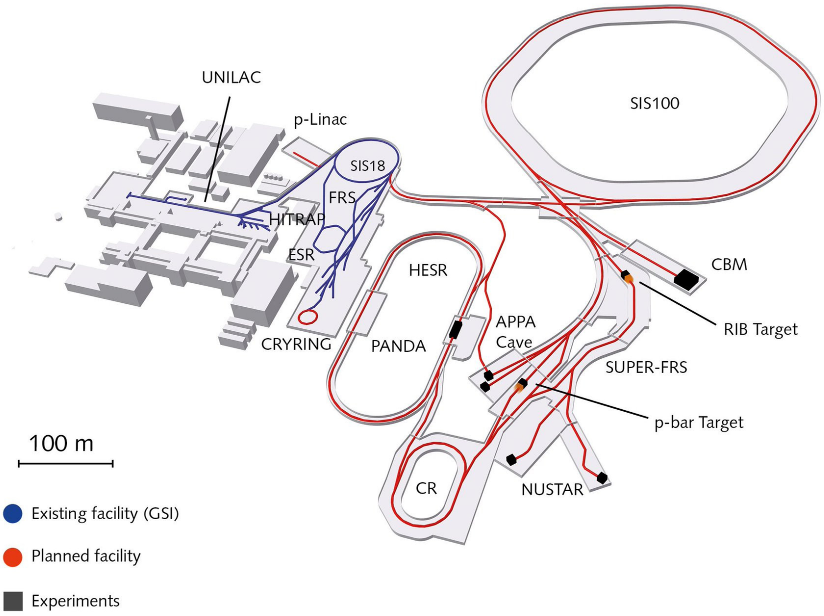

Figure 2.1: Overview of the new FAIR facility. The new accelerators are drawn in red, the existing ones in blue. The new facility provides high energy proton and heavy ion beams, as well as secondary antiproton and radioactive beams, for the experiments (figure taken from [57]).

The experiments of the modularized start version of FAIR [58] are structured in four main experimental collaborations:

- **NUSTAR** examining exotic nuclei by using radioactive beams [59]
- **APPA** studying topics in biology, atomic physics and plasma physics [60]
- **CBM** investigating QCD at high baryon densities [61]
- **$\overline{\text{P}}$ANDA** exploring hadron physics in many facets [62].

$\overline{\text{P}}$ANDA will use the annihilation of an antiproton and a proton or within a nuclear target as primary reaction for its various experimental topics. The High Energy Storage Ring (HESR) will provide this antiproton beam. Within the framework of the modularized start version of FAIR, the HESR is designed to store up to 10^{10} antiprotons in a momentum range of 1.5 to $15\,\text{GeV}/c$. The beam is cooled by stochastic cooling which cools the beam to a relative momentum spread below $5 \cdot 10^{-5}$ [63]. The HESR is sketched in figure 2.2.

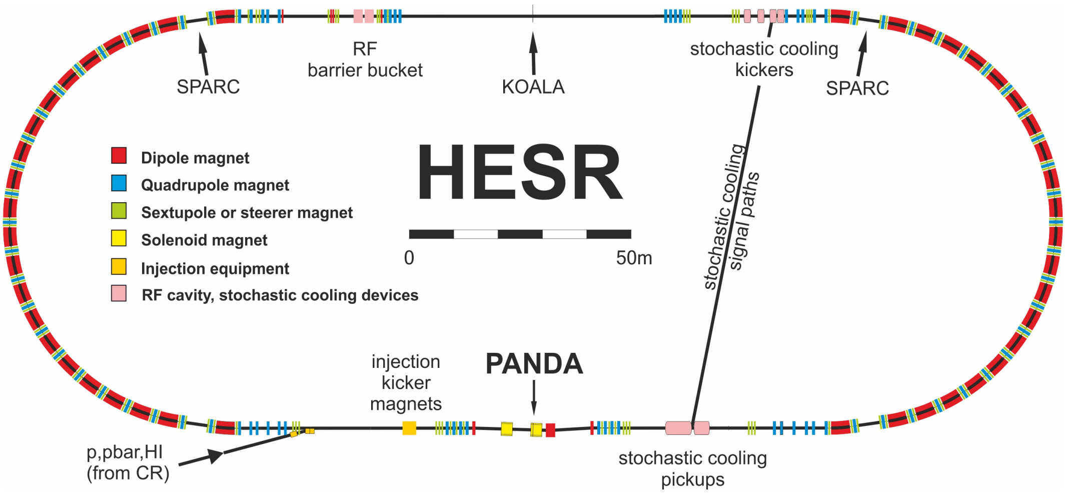

Figure 2.2: Sketch of the High Energy Storage Ring. $\overline{\text{P}}$ANDA will be situated in the experimental area at the bottom. In its start version, the HESR is designed to store up to 10^{10} antiprotons in a momentum range of 1.5 to $15\,\text{GeV}/c$. The stochastic cooling of the beam reduces its relative momentum spread to less than $5 \cdot 10^{-5}$ (figure from [64]).

The high momentum range of the antiproton beam allows to produce a broad range of hadrons. Light, strange and charm-rich hadrons can be produced within the available center-of-mass energy in the range of 2 to $5.5\,\text{GeV}$ as well as possible more exotic systems. In contrast to other primary production mechanisms, the primary annihilation reaction imposes no limit to spin and angular momentum states of the produced particles. Additionally, the annihilation process allows the production of pairs of hadrons and antihadrons with low background and high resolution when beam momenta close to their production threshold are chosen. This results in a high purity event tagging mechanism for open and hidden strangeness and charm.

2.2 The physics program of $\overline{\text{P}}$ANDA

As introduced in the last section, the HESR allows $\overline{\text{P}}$ANDA to study bound states and dynamics of QCD in a wide energy range. A very detailed description of this can be found in [62] and because of that, only a short summary of the main experimental pillars will be given here:

1. The annihilation of antiprotons allows to achieve quantum numbers that are not reachable for e^+e^- colliders where the virtual photon limits the quantum numbers of the products. This offers the possibility to produce large amounts of strange and charm bound systems in highly excited states and to study their decays. This enables the search for exotic quark and gluon combinations.
2. The high momentum antiproton beam allows to extend the study of in-medium modifications to the strange and charm sectors when nuclear targets are used. Modifications of the mass and the life time are expected due to interactions with the nuclear matter and can be measured at high precision.
3. The time-like form factor of the proton is accessible by the primary annihilation process of antiprotons. This adds the previously experimentally unreachable $Q^2 < 0$ range to the knowledge of space-like measurements as summarized in [65].
4. Experiments with strangeness are the fourth main pillar of $\overline{\text{P}}$ANDA. They are scheduled for all experimental phases of $\overline{\text{P}}$ANDA and are enabled by the large production cross sections of hyperon-antihyperon pairs (see figure 2.5). During phase one (compare figure 2.4) spectroscopy and polarization studies of free hyperons will be performed [63]. An experiment to study the $\bar{\Lambda}$ potential within nuclear matter is planned in the same phase (section 2.4.1 for more detail). In the later phases of $\overline{\text{P}}$ANDA, a dedicated detector setup will be available for high precision γ spectroscopy of excited $\Lambda\Lambda$ hypernuclei [66] (see also section 2.4.2 and 2.4.3). A similar setup will allow the X-ray spectroscopy of heavy Ξ^- hyperatoms to study the strength of the Ξ^- potential within neutron-rich matter. The feasibility of this experiment is discussed in detail in chapter 6.

2.3 The $\overline{\text{P}}$ANDA detector setup

As a fixed target experiment, the primary reaction products of $\overline{\text{P}}$ANDA are boosted forward in the laboratory system. Therefore, $\overline{\text{P}}$ANDA consists of two main parts, the barrel shaped target spectrometer and the forward spectrometer (see figure 2.3). This combination achieves a solid angle coverage close to 4 π. Both spectrometers are composed of multiple layers of detectors with increasing distance to the target. In its default setup $\overline{\text{P}}$ANDA uses frozen gases as target. These are created via either a cluster-jet or pellet target. The clusters or pellets are moving perpendicular to the beam, hitting them at the primary interaction point at the center of the target spectrometer [67].

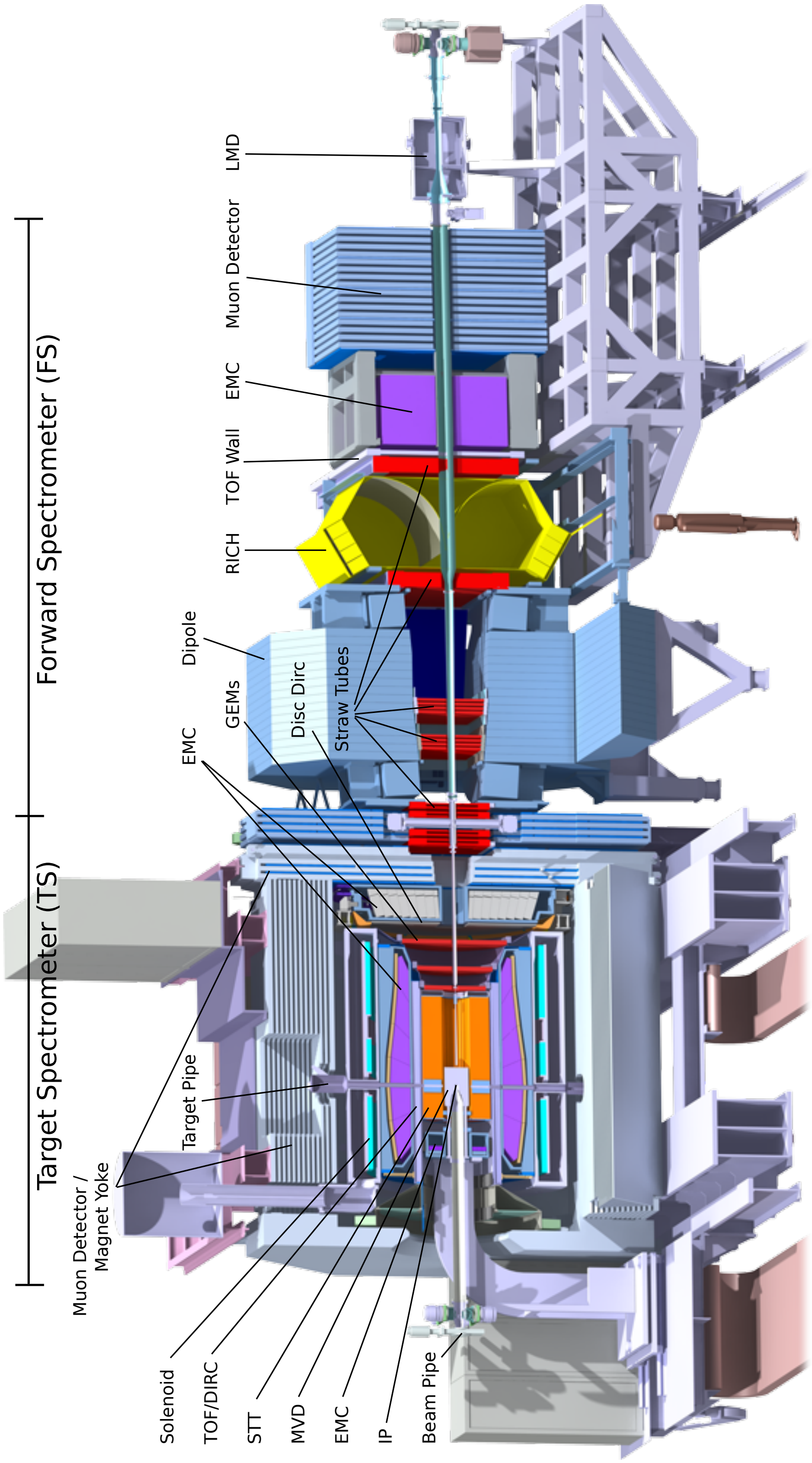

Figure 2.3: The $\overline{\text{P}}$ANDA detector in its standard configuration (figure from [68]).

The innermost layer of detectors, close to the interaction point, are used to track short living primary particles and the identification of secondary reactions by tracking their decay products. These detectors are designed for high rates and high spatial resolution which allows to reconstruct the particle tracks as well as the position of secondary vertices. This tracking system consists of the silicon detector based Micro Vertex Detector [69], the Central Tracker composed of gas-filled tubes [a] [70] and the GEM[b] detector [62] inside the target spectrometer. These tracking systems are completed by the forward tracker [62] at small polar angles in the forward spectrometer.

The strong magnetic field required for momentum measurements of charged particles is provided by a superconducting solenoidal magnet in the target spectrometer and a dipole magnet in the forward region [71].

The next detector layer following the tracking detectors is used for particle identification. Cherenkov and time of flight detectors are included in both spectrometers to fulfill this purpose in a large momentum range and a variety of particles [62].

Following the particle identification, calorimeters are added to measure the energy of charged and neutral particles. In the target spectrometer, this job is done by the Electromagnetic Calorimeter (EMC) [72]. This calorimeter is split into three parts named after their position within the target spectrometer: the forward endcap, the barrel EMC and the backward endcap. The Forward Spectrometer Calorimeter (FSC) covers the same task in the forward spectrometer [73].

The furthest layer of detectors are muon detectors. In the target spectrometer they are embedded into the magnetic coils [74]. Following the same order, the muon detectors are placed behind the FSC in the forward region. The luminosity detector (LMD) is added further downstream behind the muon detectors. This detector uses low angle Coulomb scattering to measure the luminosity [68].

This described setup is the default configuration of $\overline{\text{P}}$ANDA. The hyperatom and hypernuclear experiments will require modifications of this. Details of these modifications are presented in section 2.4.3.

At the time of writing, $\overline{\text{P}}$ANDA is under construction (see figure 2.4). Finished components will be tested and used in other experiments during phase 0. Phase 1 of $\overline{\text{P}}$ANDA will start with the first antiproton beam in the HESR and is scheduled for the beginning of 2026. The experiments of this phase are designed for a reduced setup of $\overline{\text{P}}$ANDA that will be available at this time [63]. The full setup is expected for phase 2 and 3. The latter will offer an increased luminosity.

---

[a] Straw Tube Tracker (STT)

[b] Gas Electron Multiplier

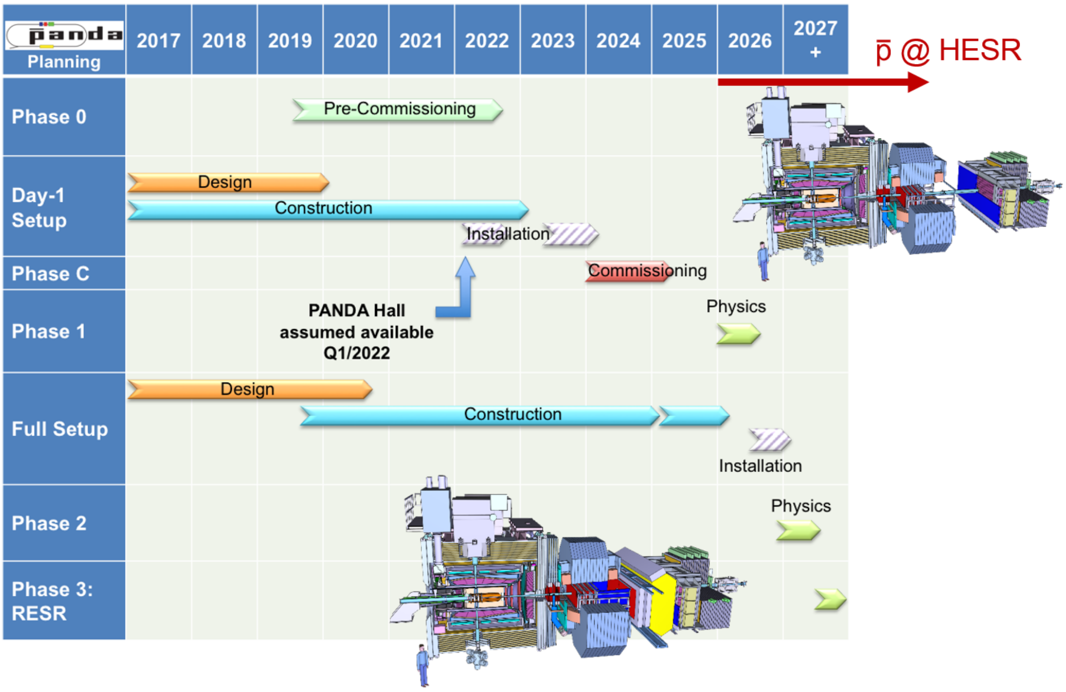

Figure 2.4: $\overline{\text{P}}$ANDA is scheduled in multiple phases. In the pre-commissioning phase 0 individual detector components will be tested and used in other experiments. Meanwhile the design and construction for phase 1 is ongoing. In this phase dedicated experiments will be performed with a reduced setup [63]. Phase 1 is scheduled to start when antiprotons are available in the HESR at the beginning of 2026. The full setup of $\overline{\text{P}}$ANDA will be available in phase 2. The increased luminosity, due to an improved accelerator setup of FAIR, will allow the performance of the most demanding experiments in phase 3 (figure from [64]).

2.4 The strangeness nuclear physics program of $\overline{\text{P}}$ANDA

The antiproton annihilation reaction of $\overline{\text{P}}$ANDA has large cross sections for the production of hyperon-antihyperon pairs as shown in figure 2.5. Considering an interaction rate of 2 MHz a yield of more than 1000 $\Lambda\bar{\Lambda}$ pairs will be produced per second at beam energies close to the production threshold. This rate decreases only by roughly one order of magnitude for the double strange $\Xi^-\bar{\Xi}$ pairs.

Because of these high rates, various experiments of the strangeness program of $\overline{\text{P}}$ANDA can be performed in its full operational time. These are designed to study the (anti-)hyperon interaction within nuclear matter in various ways. The reduced setup and luminosity in phase 1 of $\overline{\text{P}}$ANDA will prevent most charm related physics at that time [63]. Strangeness physics however is more robust against this lack of luminosity due to much higher production cross sections and consequently counting rates. An experiment to study hyperon-antihyperon pairs in medium by measuring their angular momentum asymmetries is thus planned for phase 1 (see section 2.4.1). While this experiment can be performed with the reduced default $\overline{\text{P}}$ANDA setup available in this phase, the studies of hyperatoms and hypernuclei require a dedicated setup. Both experiments

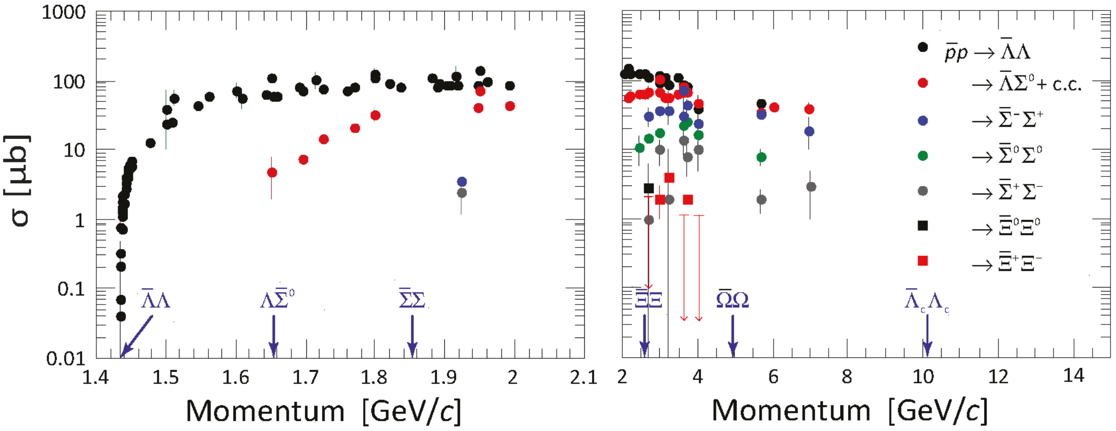

Figure 2.5: The primary antiproton annihilation reaction of $\overline{\text{P}}$ANDA has large cross sections for the production of hyperon-antihyperon pairs. Only the high production rates of these strange pairs enable the various experiments of the $\overline{\text{P}}$ANDA strangeness program (figure from [62]).

offer insight into the interaction of hyperons in nuclear matter and complement each other. While the hyperatom experiment studies the interaction in the neutron-rich periphery of heavy nuclei, the double Λ hypernucleus experiment probes the bulk of the nucleus where the amount of protons and neutrons is equal. These experiments are designated for phase 2 of $\overline{\text{P}}$ANDA when the characteristics of the experimental setup will be better understood. These three experiments are briefly introduced in the following sections.

2.4.1 Antihyperons in nuclear matter

Experimental information concerning the interaction of individual baryons or antibaryons in nuclei only exist for neutrons, protons and some strange baryons. The situation for antibaryons is rather scarce. So far, only the nuclear potential of the antiproton could be narrowed down experimentally [75]. Its (Schrödinger equivalent) potential at normal nuclear density was found to be in the range of $V_{\bar{p}} \simeq 150\,\text{MeV}$. This is a factor 4 weaker than the expectation from G-parity transformations [76]. As suggested by Gaitanos *et al.* [77], this discrepancy can be caused by the missing energy dependence of the proton-nucleus optical potential in conventional relativistic mean-field models. This energy and momentum dependence could be reclaimed by adding non-linear derivative equations to the Lagrangian density of relativistic hydrodynamics [77, 78, 79] thus imitating many-body forces [80].

Currently, there are no experimentally measured optical potentials for any other antibaryons because of their short life time and rapid annihilation in nuclear matter. $\overline{\text{P}}$ANDA is going to tackle this issue by studying the optical potential of single and double strange antibaryons. As suggested in [81], pairs of hyperon and antihyperon will be produced in a primary p̄-nucleus reaction close to threshold favoring the exclusive pair production and thus a symmetric two-body kinematic. This symmetry is broken by intranuclear interactions of the (anti)hyperon (see figure 2.6) and their momentum asymmetry can be used to measure the strength of their respective potentials. The transversal and longitudinal momentum asymmetries (α_T and α_L) are calculated by dividing the difference of the respective momentum of hyperon ($p_{T/L}(Y)$) and antihyperon ($p_{T/L}(\overline{Y})$) by

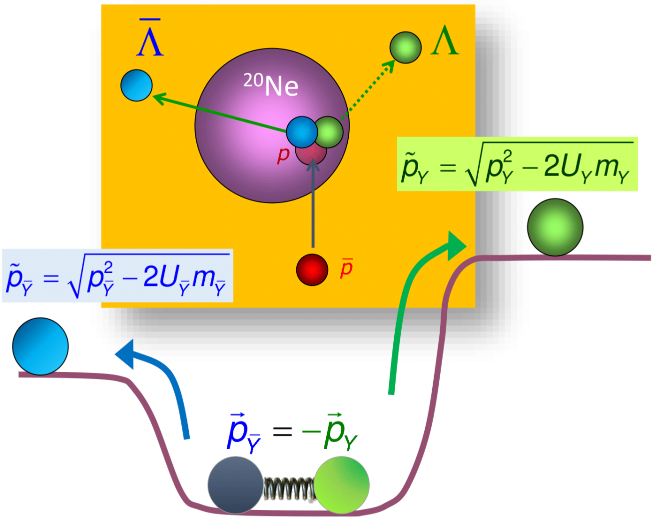

Figure 2.6: Scheme of the antihyperon-hyperon-pair production. The respective nuclear potentials break the momentum symmetry of the two-body production process and the arising asymmetry in the momenta can be used to observe the relative strength of the respective optical potential (figure from [54]).

their sum:

$$\alpha_T = \frac{p_T(Y) - p_T(\overline{Y})}{p_T(Y) + p_T(\overline{Y})}, \qquad \alpha_L = \frac{p_L(Y) - p_L(\overline{Y})}{p_L(Y) + p_L(\overline{Y})}. \tag{2.1}$$

Transport calculations of this process, using the Giessen Boltzmann-Uehling-Uhlenbeck model (GiBUU) [82], were shown in [83]. Based on the knowledge of $V_{\bar{p}}$ a scaling factor $\xi V_{\bar{\Xi}^-}$ was applied to the pure G-parity potential of antihyperons. Figure 2.7 shows the results of these simulations for $\bar{\text{p}} + {}^{20}\text{Ne} \rightarrow \Lambda\bar{\Lambda}$. The plot shows α_T as a function of α_L which has a remarkable dependence on the strength of the antihyperon potential. The statistics shown for $\Lambda\bar{\Lambda}$ can be achieved by $\overline{\text{P}}$ANDA within less than one hour of beam time which shows its feasibility for the Day-1 phase of $\overline{\text{P}}$ANDA. These estimations include the reduced luminosity of the experiments in this time. The same measurement for $\Xi\bar{\Xi}$-pairs will be possible with $\overline{\text{P}}$ANDA in a reasonable time of a few days of measurement [52].

2.4.2 Bound strange systems at $\overline{\text{P}}$ANDA

In contrast to the experiment presented in the previous section, the hyperatom and hypernuclear experiment will study bound atomic or nuclear systems with double strangeness. These experiments require a dedicated setup of the $\overline{\text{P}}$ANDA detector to produce these systems and perform high precision X-ray or γ spectroscopy. In the case of hyperatoms, the strength of the nuclear interaction of the Ξ^- within the neutron-rich periphery of a heavy nucleus can be extracted from the measured transition energy, the line width and the relative yield of the last observable X-ray of the atomic cascade. Further transitions are strongly suppressed by the strong nuclear absorption. A detailed explanation of this physics and the experiment is delayed to chapter 3 and 6.

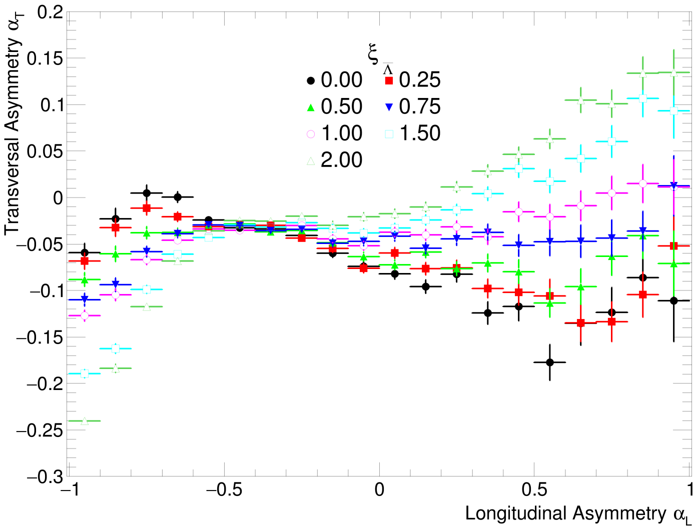

Figure 2.7: Asymmetries of $\Lambda\bar{\Lambda}$ pairs. The picture shows the result of GiBUU simulations of $\bar{\text{p}} + {}^{20}\text{Ne} \rightarrow \Lambda\bar{\Lambda}$ at a kinetic energy of 850 MeV. A significant sensitivity on the scaling of the $\bar{\Lambda}$ potential via $\xi V_{\bar{\Xi}^-}$ is visible. The presented statistics can be gathered at $\overline{\text{P}}$ANDA within less than one hour of data taking (figure taken from [54]).

In contrast to that, $\Lambda\Lambda$ hypernuclei are able to probe the center of the nucleus. Both Λ are produced in the $\Xi^- p \rightarrow \Lambda\Lambda + 28\,\text{MeV}$ reaction after the Ξ^- has been stopped within the absorber nucleus. Due to this excess energy the produced hypernucleus is in a highly excited state. Spectroscopy can be performed during the deexcitation process and at the ground state (see figure 2.8). The highest of these excited states decay by particle emission and can be studied in heavy ion reactions for example at CBM (see e.g. [84]). Additionally, a rich spectrum of particle stable excited states [85] is available in $\Lambda\Lambda$ hypernuclei which deexcite electromagnetically. The γ spectrum of a ${}^{\text{A}}_{\Lambda\Lambda}\text{Z}$ hypernucleus is highly related to the ${}^{\text{A}-2}\text{Z}$ core nucleus and differences can be traced back to structural changes due to the interaction of the Λ particles within the nucleus (see e.g. [86]). $\overline{\text{P}}$ANDA will be the first experiment that is able to investigate these structural changes in double Λ hypernuclei by using high precision γ spectroscopy.

Measuring the ground state mass will not be possible at $\overline{\text{P}}$ANDA because this requires the precise knowledge of the complete kinematics and the identification of all educts and products of the double Λ hypernucleus. Even today these experimental requirements can only be fulfilled by nuclear emulsions as used by the J-PARC E07 experiment [43]. E07 took data in 2017 and the analysis is ongoing [87]. At $\overline{\text{P}}$ANDA, however, the double mesonic decay of the ground state hypernucleus will be used to tag the $\Lambda\Lambda$ hypernucleus event. Therefore, $\overline{\text{P}}$ANDA is limited to light $\Lambda\Lambda$ hypernuclei because this decay mode is suppressed by the Pauli-exclusion principle for heavy $\Lambda\Lambda$ hypernuclei.

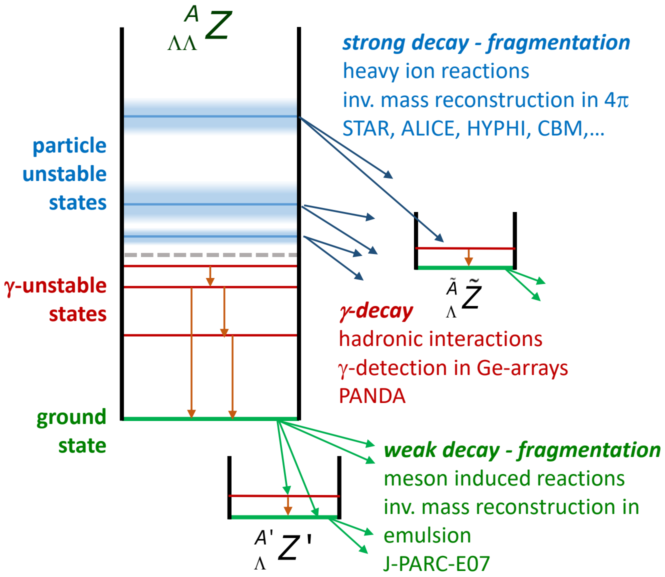

Figure 2.8: Spectroscopic experiments of $\Lambda\Lambda$ hypernuclei can focus on particle unstable or γ unstable states. While the first will be performed in heavy ion collision experiments, P̄ANDA will perform high resolution γ spectroscopy of the γ transitions. In addition to that, nuclear emulsion experiments like J-PARC E07 are able to measure the ground state mass of $\Lambda\Lambda$ hypernuclei (figure from [52]).

As an example for the mentioned structural changes due to the two Λ, figure 2.9 shows calculations of the neutron and Λ density distribution of ^{8}Be and the corresponding ${}^{10}_{\Lambda\Lambda}$Be where both Λ populate the s state [88]. A sizable shrinkage of the ^{8}Be core is predicted, motivated by the measurements of the single Λ hypernucleus ${}^{7}_{\Lambda}$Li [86]. For the s state of ${}^{10}_{\Lambda\Lambda}$Be a shrinkage of the distance between both "α clusters" by $0.2\,\mathrm{fm}$ is predicted [88]. This and other structural changes can be observed in high resolution γ spectroscopy [89].

2.4.3 Production and spectroscopy of hyperatoms and hypernuclei at P̄ANDA using the dedicated setup

The production of hyperatoms and hypernuclei at P̄ANDA requires a two-step process - first producing double strangeness in the form of a Ξ^- and second creating the bound strange system. Therefore, a dedicated target and detector setup is required. Figure 2.10 is a sketch of this production process. The three colored boxes are used to distinguish the three elements of the setup - the primary target, the secondary target and PANGEA.

The primary target, marked by the red background, is used to produce the double strange Ξ^-. Here, the antiproton beam with a momentum slightly below $3\,\mathrm{GeV}/c$ [c] annihilates within this internal target to produce $\Xi^-\bar{\Xi}^+$ ($\Xi^-\bar{\Xi}^0$) pairs in interactions with protons (neutrons) of the primary target nucleus. Since only slow Ξ^- can be stopped before their decay (compare figure 6.1), rescattering

---

[c] $\Xi^-\bar{\Xi}^+$ production threshold of $\sqrt{(s)} = 2.642\,\mathrm{GeV}$ is hit for $p_{\mathrm{beam}} = 2.620\,\mathrm{GeV}/c$

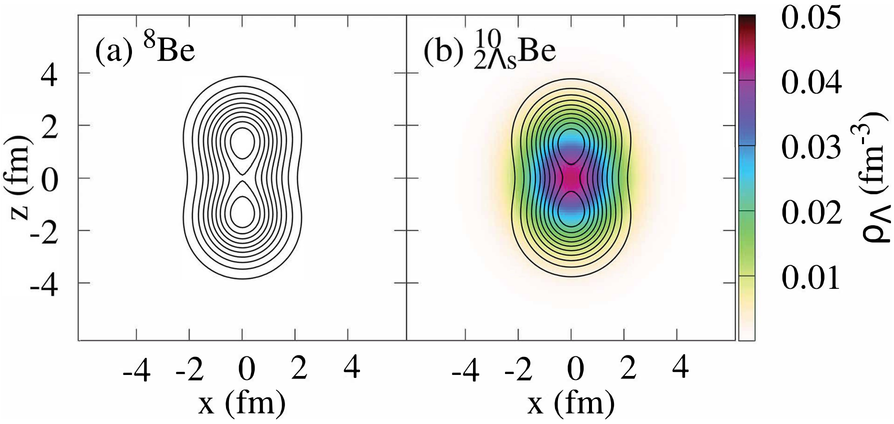

Figure 2.9: Neutron (contour lines) and Λ (colors) density distribution of ^{8}Be (left) and $^{10}_{\Lambda\Lambda}$Be in an the ground state of both Λ (right). The neutron densities start at $0.1/\mathrm{fm}^3$ in the periphery with an increment of $0.1/\mathrm{fm}^3$ when advancing to the center. The addition of the hyperons influences the nucleon distributions and shrinks the size of the core nucleus which can be observed in γ spectroscopy. For the given example a shrinkage of the distance between both "α clusters" by $0.2\,\mathrm{fm}$ is predicted (figure from [88]).

within the primary target nucleus is essential to reduce their momentum and consequently increases the overall stopping probability. Because of that, a nuclear primary target is mandatory for these experiments (see section 2.4.3.1). The coincidently produced antihyperon can be used for event tagging by detecting its decay products within the $\overline{\text{P}}$ANDA spectrometer.

The secondary target is visualized by the violet box. Its main purpose is the stopping of the Ξ^- and the creation of the hyperatomic or hypernuclear bound system. Only in the case of the hypernuclear experiment, the secondary target has the additional task of tagging the event by tracking both characteristic decay π^- of the double mesonic decay of the $\Lambda\Lambda$ hypernucleus. The Pauli-exclusion principle suppresses this decay for heavy targets which limits the absorber material to light elements, in contrast to the hyperatom experiment where the event tagging is only based on the strangeness detection within $\overline{\text{P}}$ANDA and the event topology within PANGEA (see section 6.3.3). Because of that, dedicated modules for each experiment are required which will be presented in section 2.4.3.2. Last but not least, the green background visualizes the high-precision X-ray and γ spectroscopy. PANGEA is developed and optimized to fulfill this task for both experiments. PANGEA is featured in detail in chapter 4.

Performing the required modifications of the $\overline{\text{P}}$ANDA target spectrometer will take approximately three months (detailed overview in table 4.3) and requires to remove the standard target, the MVD and the Backward endcap EMC before the combined target system as well as PANGEA can be included. A shift of the primary interaction point by $55\,\mathrm{cm}$ upstream increases the available space for the target system and the solid angle coverage of PANGEA. Details on the dedicated components will be given in the following subsections.

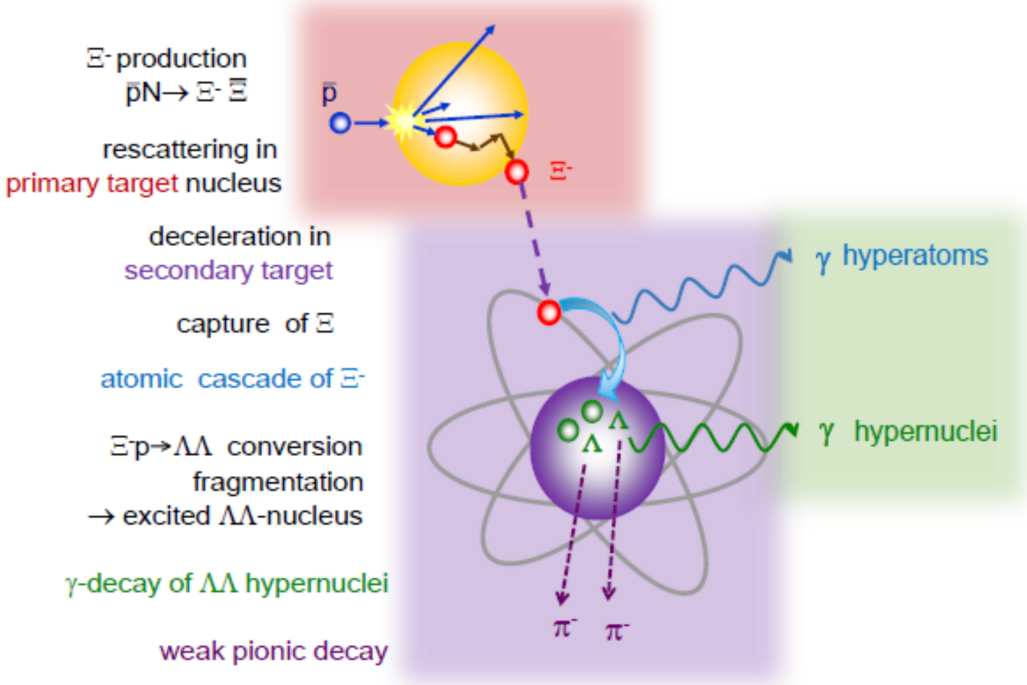

Figure 2.10: The production of hyperatoms and double Λ hypernuclei at $\overline{\text{P}}$ANDA is a two-step process. Inside a primary target (red box) a Ξ^- is produced from the primary antiproton beam. This Ξ^- is stopped and absorbed in a secondary, active target system (violet box). The capture into an atomic orbit forms a hyperatom that decays by emitting characteristic X-ray radiation. When the Ξ^- enters the nucleus a it can convert to Λ and produce a highly excited compound nucleus. After the fragmentation, a particle stable double Λ hypernucleus can be created, that decays to its ground state electromagnetically. The sequential mesonic decay of this hypernucleus creates two π^- with characteristic momenta that must be tracked by the detector layers of the secondary target. The green box symbolizes the high resolution photon detector required for the spectroscopy of X-rays and γ.

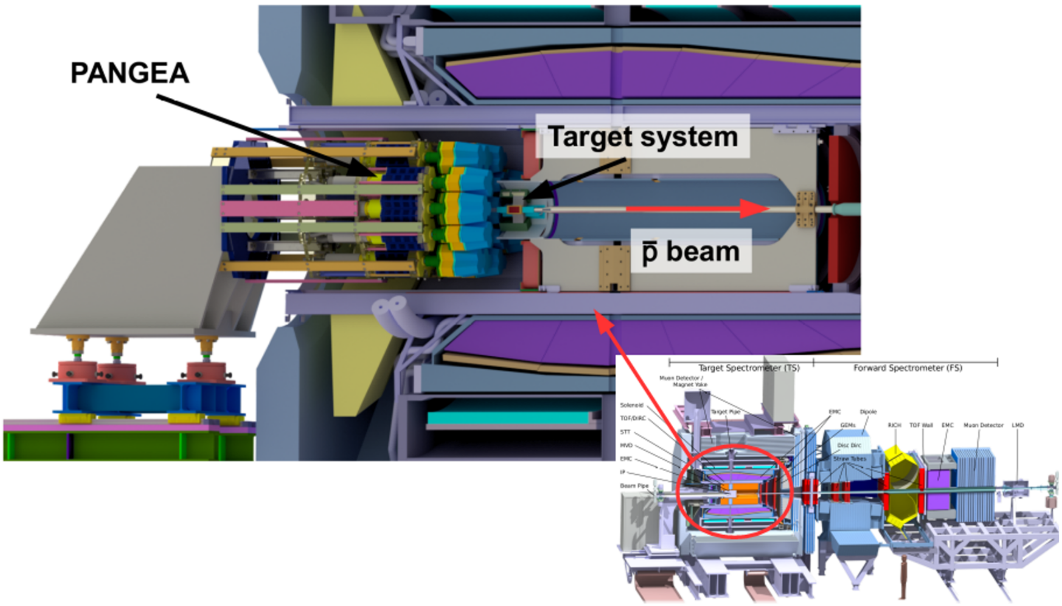

Figure 2.11: CAD drawing of the dedicated setup of the $\overline{\text{P}}$ANDA hyperatom and hypernucleus experiment. The primary interaction point of the two-staged target system is shifted by $55\,\text{cm}$ upstream to increase the solid angle coverage of the germanium detector array PANGEA (figure previously published in [53]).

2.4.3.1 Primary target

The production of large amounts of low energy Ξ^- at $\overline{\text{P}}$ANDA requires an internal nuclear target inside the stored antiproton beam pipe. Carbon offers the best balance between maximizing the creation of slow Ξ^- and minimizing the disturbance of the antiproton beam [66]. Nevertheless, the proposed average interaction rate of $2 \cdot 10^6/\text{s}$ can only be realized when a very thin filament with a radius of a few μm is used. Higher interaction rates would consume the beam too quickly while causing high dead times in the detectors. [90] was successful in extracting individual carbon filaments from fiber bunches and gluing these to a thin frame (compare right part of figure 2.12). In addition, its thermal reliability when heated up by the beam was successfully shown by simulating the appropriate power load with an electric current.

The fragility of the target could make it susceptible for possible mechanical and radiation damage during the experiment and hence a stock of replacement targets must be present in the target system. This task can be fulfilled by a target stage that can precisely move the targets in two dimensions, perpendicular to the beam as well as along this axis (left part of figure 2.12).

This mobility allows to achieve a constant interaction rate within the measurement period of an experimental cycle (see figure 2.13 (top)) by steering the target. Despite the small size of the filament, it has to be positioned with some offset from the beam center to meet the designated average interaction rate of $2\,\text{MHz}$. This offset depends on the beam and target geometry and is in the range of a few mm (see figure 2.13 (bottom)). Only a small readjustment of the target position

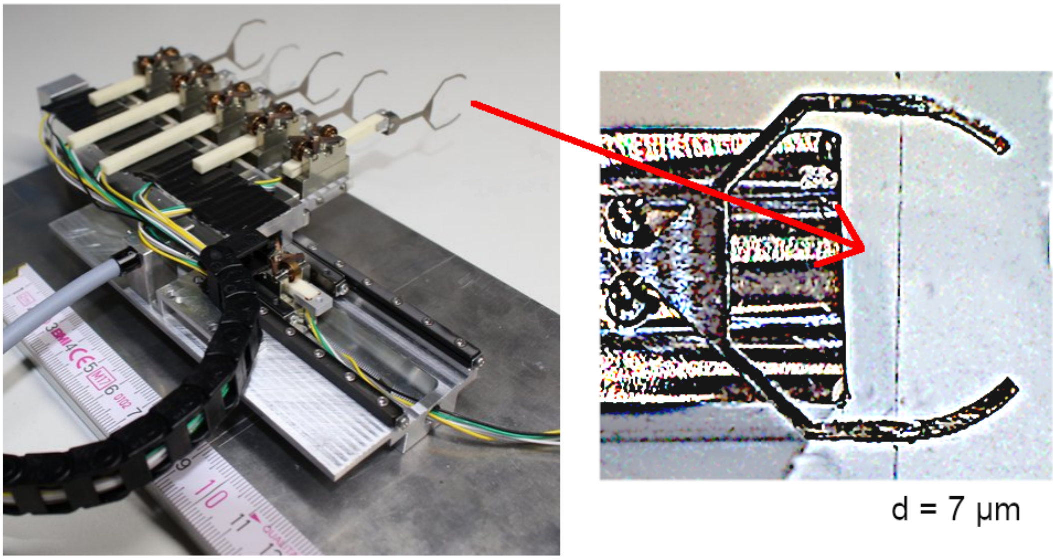

Figure 2.12: The real size prototype of the primary target system includes all actuators required to move 5 filament targets perpendicular and along the beam axis. The probe head of the positioning system (see figure 2.14) is situated behind the movable carriage and is connected to its electronics by the gray coated optical fiber (pictures by courtesy of [91]). A zoom on one of these target frames is shown on the right. The thin carbon filament with a measured diameter of 7 μm is glued to it (picture modified from [90]).

for a measurement time of 2000 s is required to compensate the reduction of antiprotons in the storage ring due to interactions. A large fraction of the experimental cycle is required for the refilling of the HESR. During this time the primary target is in its parking position. Because of that, a realistic duty factor for a full experimental cycle is in the range of 0.5 [66].

The choice of actuators for this precise movement is limited, especially when the operation within the high magnetic field of the solenoidal magnet, the strong particle background close to the interaction point and the ultra high vacuum inside the HESR beam pipe must be assured. In addition, the small life time of the Ξ^- (details see section 6.2) requires a target system as compact as possible. Its minimum dimensions are limited by the HESR. A minimum beam pipe radius of 1 cm is required to assure proper beam control. Therefore, the primary target system has to fit into a 2 cm high beam pipe and an attached vacuum chamber. Because of these requirements only piezo actuators can be used. Five of these motors are placed on a movable carriage, each dedicated to the perpendicular movement of an individual filament.

A sixth piezo actuator moves the complete system along the beam axis to interchange between the targets (compare figure 2.12 (left)). While the overlap of target position in the beam - and hence the luminosity - can be controlled with the luminosity detector of $\overline{\text{P}}$ANDA, the development of a dedicated position control for the movement along the beam axis was necessary. This system must be radiation tolerant and highly reliable in its precise positioning because a badly positioned target might crash into the vacuum chamber of the integrated absorber (compare figure 2.15) and break which could end the whole experiment. Because of that, a light based system was

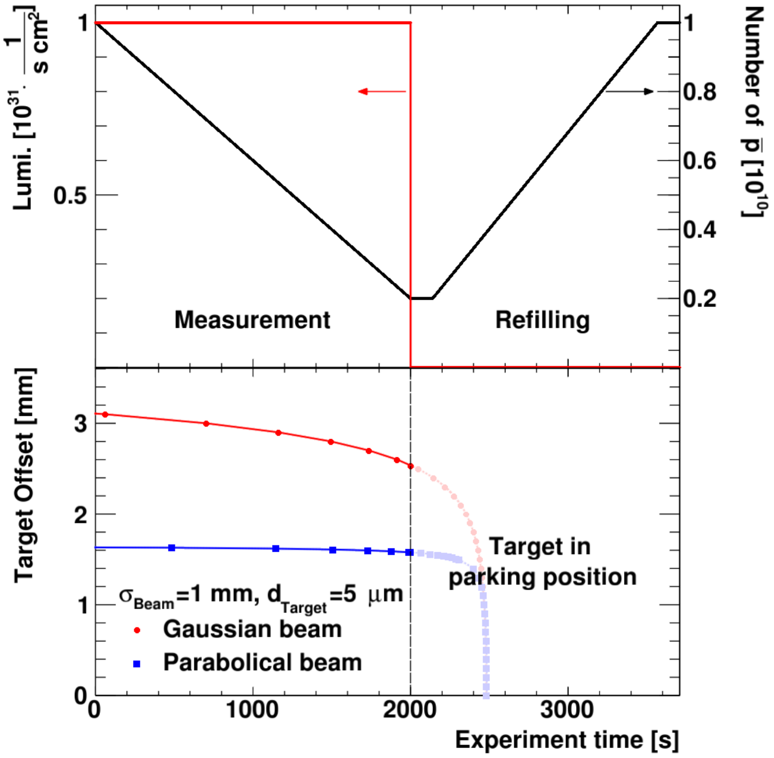

Figure 2.13: The movable primary target allows to achieve a constant luminosity despite the decreasing number of beam particles. The top diagram shows a full experimental cycle consisting of the measurement and refilling periods. To achieve this constant luminosity, very thin targets are required and even those need to be positioned with some offset from the beam center (bottom). During the measurement this target is then slowly steered towards the center of the beam to compensate the reduction of circulating antiprotons. This movement strongly depends on the shape and size of the beam and will use the $\overline{\text{P}}$ANDA luminosity detector as feedback. The length of the measurement time has been optimized in [66] to 2000 s. During the refilling the target must be brought to its parking position (figures taken from [66]).

designed and successfully tested in [92]. This system is based on a combined infrared emitter and receiver, connected via long optical fibers to a probe head inside the vacuum chamber. Trapezoidal structures on a custom-built aluminum logic plate allow to estimate the position very precisely by measuring the fraction of reflected light (compare figure 2.14). The fibers allow to place all active electronics of the system behind protective shielding which assures its performance during the experiments. A similar system, using a split up emitter and receiver as a light barrier, interlocks the exchange of targets when any target is outside of its parking position. This prevents damaging the targets by collision with the vacuum chamber [93].

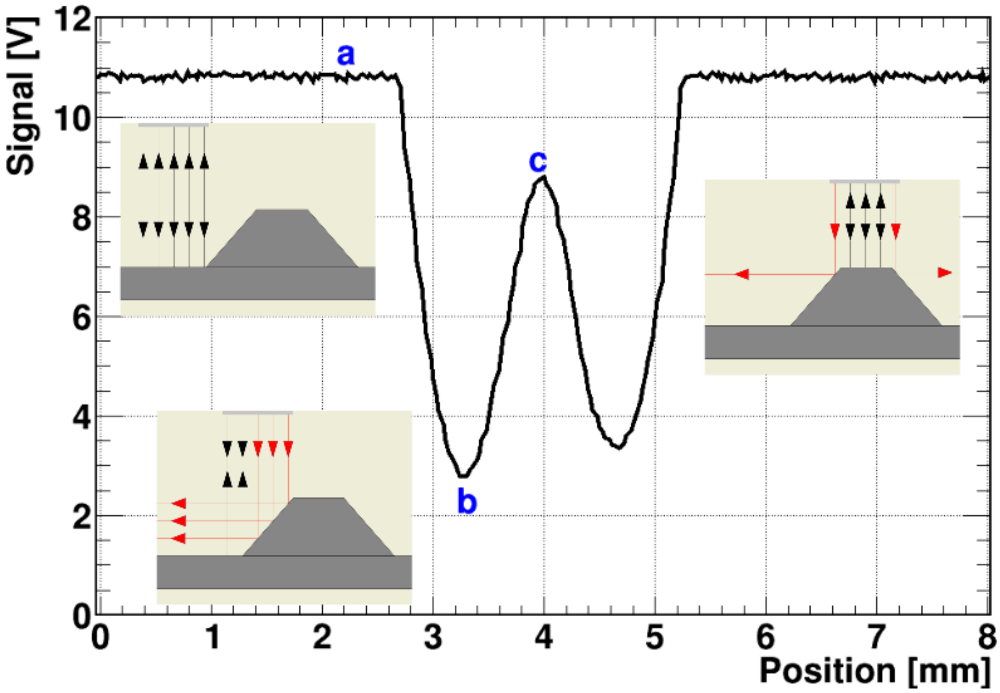

Figure 2.14: The position of the primary target along the beam axis can be precisely measured by detecting the fraction of reflected light. The figure shows how the system is able to distinguish the different reflections of a trapezoid structure depending on its position relative to the center of the structure. At point (a) the structure is not hit yet and all light is reflected, resulting in a high signal in the ADC. Once the light sensor arrives at the slope of the trapezoidal, more and more light is diffusely scattered, lowering the measured voltage (point b). The signal rises again once the plateau is reached and maximizes at the center (c). After this position, the previous process repeats in reversed order. The local maximum at the center (c) can be precisely reached by the system (figure based on [92]).

2.4.3.2 Secondary target

In contrast to the primary target, the secondary target differs for the hyperatomic and the hypernuclear experiment. The first one only consists of a single absorber and its optimization is described in detail in chapter 6. Compared to this, the secondary target of the hypernuclear experiment is more complex [d]. It has the additional task of detecting the hypernuclear decay products. This is achieved by alternating layers of absorbers and silicon strip detectors. Three blocks of these sandwich structures fill the available space around the vacuum chamber of the primary target.

Each of the blocks consists of five alternating tracking and absorber layers followed by two additional tracking layers. The innermost of these layers is an absorber integrated into the beam pipe which reduces the material budget. Boron has been selected as absorber material for the first experimental runs. Its low mass number allows the creation of light double Λ hypernuclei with high probability [94]. Boron offers enough stopping power to stop and absorb slow Ξ^- (compare

---

[d] A very detailed summary of the secondary target of the hypernuclear experiment can be found in [66].

figure 6.1) while having a small absorption cross section for photons due to its low atomic number. From the mechanical point of view, solid boron slices are available for the sandwiched layers in between two tracking layers. The innermost layer will be made of boroncarbide B_4C which can withstand the pressure gradient and its vacuum capabilities have been successfully tested in [66].

The tracking layers consist of $300\,\mu\text{m}$ thin double-sided silicon strip detectors with a size of $35\,\text{mm} \cdot 60\,\text{mm}$. These detectors allow a precise tracking of the decay pions. These silicon detectors are identical to the strip part of the MVD. Because of that, the read-out and supply electronics can be based on the developments of the MVD group [95]. By using thin capton ribbon cables the front-end electronics can be fanned out and the material budget in front of PANGEA reduced.

Figure 2.15 shows a CAD drawing of the full target system. The secondary target has been optically separated from the primary target and the vacuum system for a better overview. The primary target on the left is situated within its target chamber and shows the layout described and shown in section 2.4.3.1. The cutout in the vacuum chamber provides the required space for the secondary target. Both versions of this component are shown in the right half of the figure.

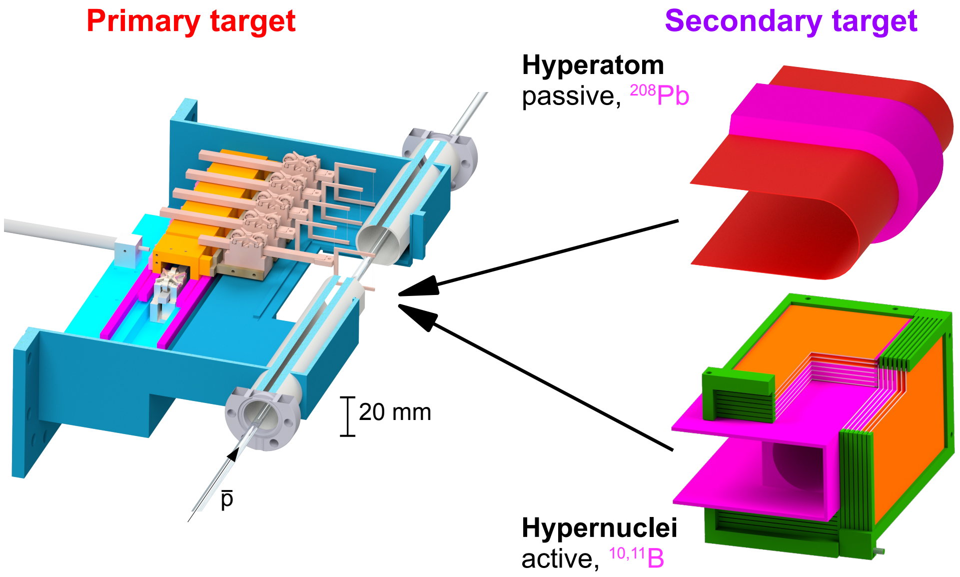

Figure 2.15: This CAD drawing shows the complete target system of the hyperatom and hypernuclear experiment. The primary target does not differ for these experiments and is drawn on the left. An optical cut allows to have a look inside the target chamber and see the two-dimensional movement system as well as the internal filament target (compare section 2.4.3.1). The secondary target is optically separated from the vacuum chamber for better visibility and shifted to the right. The figure shows both options of secondary targets: the passive hyperatomic one and the active one of the hypernuclear experiment. The absorber of both secondary targets is drawn in magenta. The alternating layers of silicon trackers (orange) and absorbers are visible in the hypernuclear target (figure previously published in [53]).

2.4.3.3 PANda GErmanium Array

The last dedicated component of this setup is the high resolution γ detector PANGEA. PANGEA is required to measure the electromagnetic transitions of the excited states of either hyperatoms or hypernuclei. The $\overline{\text{P}}$ANDA EMC can not fulfill this role in the required energy range below $1\,\mathrm{MeV}$ or $10\,\mathrm{MeV}$, respectively. PANGEA consists of 60 High Purity Germanium crystals (HPGe) arranged in 20 electro-mechanically cooled triple detectors. Details of PANGEA are provided in chapter 4.

3 Exotic atoms

This chapter will briefly summarize the experimental situation of the study of exotic atomic systems. These are formed by the binding of muons or negatively charged hadrons to conventional nuclei. Their interaction is dominated by the Coulomb force. Strong nuclear forces must be considered for small distances between the hadron and the nucleus which usually corresponds to small principal quantum numbers of the system. The theoretical description of these systems is briefly introduced to show the relevant observables for $\overline{\text{P}}$ANDA. A simple form for the nuclear potential which follows the nuclear density distributions is used for this. This model is sufficient to study the feasibility and sensitivity of the experiment later on in chapter 6. After this excursus to the theoretical description, the present experimental situation for the various species of exotic atoms is shown. The focus is on baryonic atoms.

3.1 Basic considerations of exotic atoms

The formation of an exotic atom requires the capture of a heavy negatively charged particle by this atom. The spectroscopy study of this exotic atom is then only possible for captured particle that live long enough for the atomic cascade. This limits the selection of particles to those that do not decay strongly. The resulting system has a higher reduced mass $m_{\mathrm{red}} = \frac{m_Y \cdot m_{\mathrm{nuc}}}{m_Y + m_{\mathrm{nuc}}}$ than the conventional atom, which shrinks the radial density distribution of the bound particle. The expectation value of this distribution $\langle r_{(n,l)} \rangle$ for the atomic state with the principal quantum number n and the azimuthal quantum number l can be estimated by

$$\langle r_{(n,l)} \rangle = r_B \cdot [3n^2 - l(l+1)]/2 \tag{3.1}$$

with the Bohr radius r_B:

$$r_B = \frac{\hbar c}{m_{\mathrm{red}} c^2 \alpha Z}, \tag{3.2}$$

where α is the fine structure constant. For heavy Ξ^- hyperatoms with a rest mass of $1321.71 \pm 0.07\,\mathrm{MeV}/c^2$, the reduced mass is approximately 2570 times larger than for the corresponding conventional atom. Consequently the Bohr radius shrinks by this factor. At such a small radius the Ξ^- is not shielded by the electron shell and is attracted by the full Coulomb force of the nucleus. Because of that, the energy of the atomic Ξ^- states can be described in leading order of α by

$$E_n = \frac{m_{\mathrm{red}} c^2 \alpha^2 Z^2}{2n^2} + O(\alpha^3). \tag{3.3}$$

Following the assumption that the Ξ^- replaces an electron with the principal quantum number n_e which has the same excitation energy, the initial principal quantum number of the Ξ^- n_i can be estimated by

$$n_i = n_e \sqrt{\frac{m_{\mathrm{red},\Xi^-}}{m_{\mathrm{red,e}}}}. \tag{3.4}$$

This assumption is based on the detailed study of full atomic cascades of muonic atoms in the past (e.g. ref. [96, 97, 98, 99]). In the studies of muonic ^{203}Th Backe *et al.* found the best agreement of their data for an initial $n_i = 20$ [97]. Using this as a basis for the estimation of initial states of Ξ^- hyperatoms yields $n_i \approx 70$ when scaled via equation 3.4. At these high states Auger transitions dominate the deexcitation process of the Ξ^-. At $n \approx 50$ the transition energy becomes too high to match the energy of any shell electron and kick it out of the atomic shell. Consequently, radiative electric dipole (E1) X-ray transitions take over the dominant role. At small n states the Ξ^- begins to overlap and interact strongly with the nucleus. This nuclear interaction and finally the nuclear absorption limits the detectable transitions of the cascade down to the final state $n = n_0$ [a]. The overview of these atomic transitions is sketched in figure 3.1.

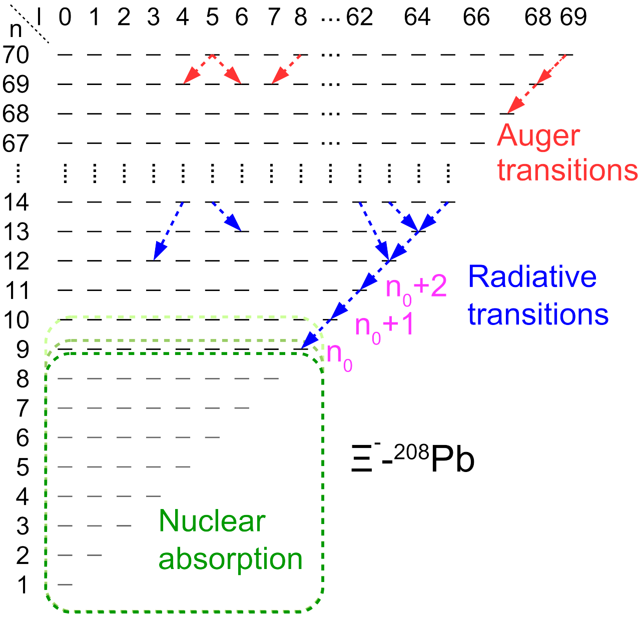

Figure 3.1: Overview of the atomic transitions in Ξ^--^{208}Pb hyperatoms. Due to its high mass, the radial density distribution of the Ξ^- is approximately 2570 smaller than for electrons. At these small radii, the Ξ^- is affected by the unshielded (Coulomb) potential of the nucleus and the binding energy is increased by the same factor. The Ξ^- enters the atomic binding at principal quantum numbers in the range of $n_i \approx 70$ by replacing the strongest bound electron and starts to cascade down by emitting Auger electrons. At $n \approx 50$ the transition energy becomes too high for the production of Auger electrons and radiative electric dipole (E1) transitions start to dominate. For small n the wave function of the Ξ^- overlaps the nuclear potential. The resulting nuclear interactions will be studied in the $\overline{\text{P}}$ANDA hyperatom experiment (figure adapted from [100]).

The nuclear absorption of the Ξ^- takes place in the periphery of the nucleus. This is visualized in figure 3.2 where the overlap of the radial density distribution of the Ξ^- at the $(n = 9, l = 8)$ state $|\Psi_{(9,8)}|^2$ and the nuclear potential $U(r)$ for the example of a Ξ^--^{208}Pb hyperatom is drawn (red). This overlap indicates the strength and the position of this interaction in the periphery of

---

[a] For Ξ^--^{208}Pb $n_0 = 9$

the nucleus. Especially for heavy nuclei, this region is dominated by an excess of neutrons. The plot at the bottom displays this by showing the nuclear density distributions for protons ρ_p and neutrons ρ_n as well as their ratio that strongly shifts towards a larger share of neutrons in the regions of interest for the strong Ξ^--nucleus interaction.

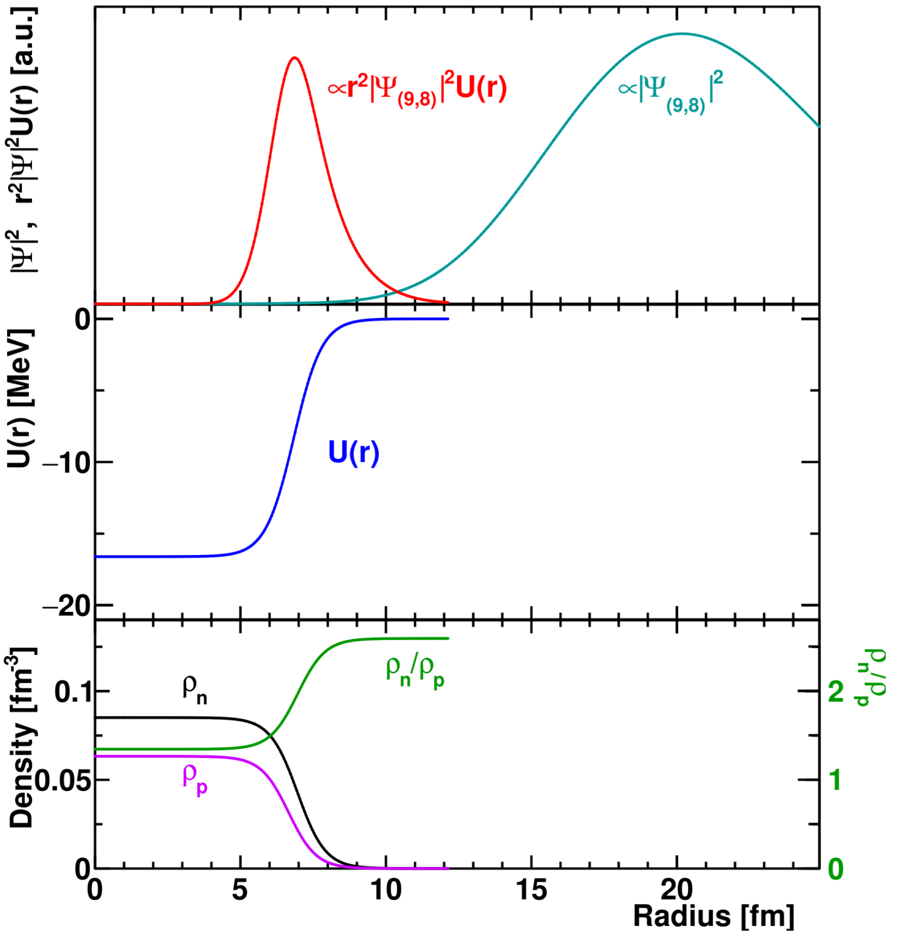

Figure 3.2: The strong interaction of the Ξ^- and the nucleus can be characterized by the overlap of the nuclear potential $U(r)$ and the radial density distribution of the Ξ^-, $|\Psi_{(\mathrm{n,l})}|^2$. In this example the $|\Psi_{(9,8)}|^2$ state for a Ξ^--^{208}Pb hyperatom is show. The overlap (red) is situated in the periphery of the nucleus which is dominated by neutrons as shown by the nuclear density distributions for protons ρ_p and neutrons ρ_n as well as their ratio at the bottom of the figure. The plots are generated via the calculations shown in section 3.2. These use a software kindly provided by E. F. which is based on the model shown in [101] (figure previously published in [53]).

Experimentally, the strong interaction of the Ξ^- and the nucleus can be observed in multiple ways. First of all, it shifts the energy level to larger or smaller binding energies depending on whether the interaction is repulsive or attractive. This small deviation from pure QED calculations can be measured with high precision. Since the energy shift of the final state is much higher than the one of the initial state, the measured shift of the transition energy essentially equals the shift of the final state.

In addition to that, the nuclear absorptive interaction reduces the life time of the atomic states which results in a Lorentzian broadening of levels in direct proximity to the nucleus. This can be observed in the natural line width $\Gamma^{\mathrm{abs}}_{n_0}$ of the final X-ray transition. Compared to the precise measurement of the energy shift, the direct determination of $\Gamma^{\mathrm{abs}}_{n_0}$ can be hampered by the limited detector resolution. Alternatively, the absorptive width $\Gamma^{\mathrm{abs}}_{n_0+1}$ can be estimated indirectly by measuring the relative yield of the $(n_0+1) \to (n_0)$ transition γ_2 (compare e.g. ref [102, 103]). It will be shown later in chapter 6 that the relatively thin secondary target used at $\overline{\mathrm{P}}$ANDA allows to study coincident cascades of transition X-rays. As illustrated in figure 3.3 the relative yield of γ_2 can be estimated by the division of the absolute counting rates of the consecutive coincidences Y_{n_0}/Y_{n_0+1}.

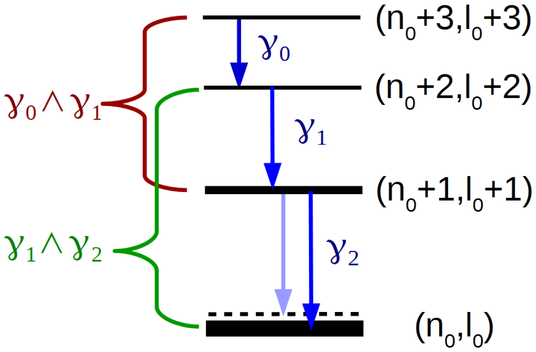

Figure 3.3: Schematic visualization of transitions and observables in Ξ^- hyperatoms. The transition γ_2 ($(n_0+1) \to (n_0)$) is the last one that can be observed before the nuclear absorption becomes too strong. For ^{208}Pb, the lowest level is (n_0, l_0)=(9,8). The energy of γ_2 is affected by the strong energy shift of the low lying Ξ^- states, which are widened by the nuclear absorption width $\Gamma^{\mathrm{abs}}_{n_0}$. While the direct detection of $\Gamma^{\mathrm{abs}}_{n_0}$ of the final state might be hampered by the detector resolution, $\Gamma^{\mathrm{abs}}_{n_0+1}$ can be estimated from the relative yield of γ_2. This yield can be calculated by the fraction of coincident transitions $(\gamma_1 \wedge \gamma_2)$ and $(\gamma_0 \wedge \gamma_1)$.

Y_{n_0+1} is a measure for the population of the n_0+1 level and is given by the number of measured coincidences of $\gamma_0 \wedge \gamma_1$. It relates to the sum of the radiative and the absorptive width of the n_0+1 level ($\Gamma^{\mathrm{rad}}_{n_0+1} + \Gamma^{\mathrm{abs}}_{n_0+1}$). In contrast to that, Y_{n_0} is the number of measured coincidences $\gamma_1 \wedge \gamma_2$ and defines the number of measured transitions γ_2 that are affected by the nucleus. This yield is only proportional to the radiative width $\Gamma^{\mathrm{rad}}_{n_0+1}$ which can be precisely calculated in QED. When detector systematics are considered, $\Gamma^{\mathrm{abs}}_{n_0+1}$ can be extracted from the relation

$$\frac{Y_{n_0}}{Y_{n_0+1}} = \frac{\Gamma^{\mathrm{rad}}_{n_0+1}}{\Gamma^{\mathrm{rad}}_{n_0+1} + \Gamma^{\mathrm{abs}}_{n_0+1}}. \tag{3.5}$$

3.2 Theoretical description of hyperatoms

In general, the spectroscopy of exotic atoms can provide information on the orbiting particle (e.g. its mass and magnetic moment [104]) or the atomic nucleus as well as the interaction of these. In case of sufficient knowledge of the interaction from other experiments, exotic atoms probe the nucleon distribution of the nucleus. On the other hand, in the case of well known nuclear distributions, the observables allow to extract information of the effective nuclear potential. For both cases one has to keep in mind, that the orbiting particle spends most of its life time in the far periphery of the nucleus and consequently probes the interaction in this region. Either way, a theoretical description of the exotic system is required for predictions of the observables.

These relativistic atomic systems can be described by the Dirac equation. Nevertheless, a simplified model using the Klein-Gordon equation and a simple nuclear potential (compare equation 3.9) is sufficient to study the sensitivity of the hyperatom experiment and was kindly provided by E. F.. The use of the Klein-Gordon equation was justified by Friedman *et al.* [105] with experimentally not resolvable fine-structure effects. The results of the Klein-Gordon equation can be identified as the weighted average of the fine-structure levels. The dispersion relation to describe the interaction of the Ξ^- inside nuclear matter of density ρ is

$$E^2 - \mathbf{p}^2 - m^2 - \Pi(E, \mathbf{p}, \rho) = 0, \;\; \Pi = 2EV_{\text{opt}} \tag{3.6}$$

where $\Pi(E, \mathbf{p}, \rho)$ is the hadron self-energy and V_{opt} the optical potential of the hadron in the medium [106]. The other parameters are the rest mass m, the three-momentum $\mathbf{p}$ and the energy E. For finite nuclei close to threshold, like Ξ^--atoms, equation 3.6 forms in natural units ($\hbar = c = 1$) the Klein-Gordon equation:

$$[\nabla^2 - 2\mu(B + V_{\text{opt}} + V_c) + (V_c + B)^2]\Psi = 0 \tag{3.7}$$

with the reduced mass μ of the atomic system, the complex binding energy B and the finite-size Coulomb potential of the nucleus V_c, including vacuum-polarization terms [105]. If the system is reduced to a point-sized charged nucleus and vacuum polarization is neglected, the binding energy can be calculated analytically [107]:

$$B(n, l) = \frac{\mu}{2n^2}(\alpha Z)^2 \left[1 + \frac{(\alpha Z)^2}{n^2}\left(\frac{n}{l + 1/2} - \frac{3}{4}\right)\right], \tag{3.8}$$

considering terms up to second order in $(\alpha Z)^2$. α is the fine structure constant. n and l are the radial and angular quantum number of the atomic system. Adding the size of the nucleus as well as vacuum polarization complicates the system so that only numerical solutions are available.

The same limitations apply to the strong part of the atomic interaction. The simplest way to describe the nuclear potential is the $t\rho$ potential. For an s-wave it has the form [101]

$$2\mu V_{\text{opt}}(r) = -4\pi \left(1 + \frac{\mu}{M}\right) b_0 \left(\rho_{\text{n}}(r) + \rho_{\text{p}}(r)\right). \tag{3.9}$$

In this equation, M is the mass of the nucleon. The complex parameter b_0 is related to the hadron-nucleon scattering length. A default value of

$$b_0 = 0.25 + i\,0.04 \tag{3.10}$$

is proposed by Batty *et al.* [101] and used for the calculations shown in chapter 6. This corresponds to a potential depth of $20.5\,\mathrm{MeV}$ for the real part and $3\,\mathrm{MeV}$ for the imaginary part. The real part of the potential mainly determines the energy shift caused by the strong interaction of Ξ^- and nucleus. On the other hand the absorptive width of the state scales mostly with the imaginary part of the potential. ρ_p and ρ_n are the normalized proton and neutron densities. The proton density can be derived from experimental nuclear charge densities and can be described in this model by a two or three parameter Fermi distribution

$$\rho_\mathrm{p}(r) = \rho_{0,p}\frac{1 + wr^2/c^2}{1 + \exp((r-c)/a)} \tag{3.11}$$

with the parameters c, a and w. c describes the half-density of the distribution and a is a measure of the diffuseness. w helps to reproduce a possible dip of the distribution at small radii. For the two parameter distribution, the last parameter w is fixed to 0 [108].

The neutron distribution is experimentally harder to access and therefore less known. Friedman *et al.* [105] suggest to describe the neutron distribution via a semi-phenomenological model that is based on the distribution of the protons. The difference of the rms radii of the distributions of neutrons and protons, the so called neutron skin Δr_np, is connected to the asymmetry in the amount of both nucleons N and Z via

$$\Delta r_\mathrm{np} = r_\mathrm{rms,n} - r_\mathrm{rms,p} = \gamma\frac{N-Z}{N+Z} + \delta. \tag{3.12}$$

Both parameters γ and δ in equation 3.12 are determined from fits to experimental data which yield $\gamma = 1.25$ and $\delta = -0.35$ [105]. Since the diffuseness parameter of the neutron distribution a_n is also unknown, Friedman proposes to use the same diffuseness as for the measured proton distribution $a_n = a_p$. This allows to extract the half-density of the neutron distribution c_n via

$$r^2_\mathrm{rms} = \frac{3}{5}c^2 + \frac{7}{5}a^2\pi^2 \tag{3.13}$$

which is required as input for equation 3.12. The precision of this is sufficient to predict the experimental observables and study the sensitivity of the experiment.

Systematic calculations for various elements are necessary to find an appropriate experimental target. A software [b] to calculate these has been provided be E. F.. It is based on old fortran code by Hüfner [98] for muonic atoms and was adapted to include strong interactions by Batty *et al.* [101]. This program has been successfully used for the description of various other exotic atoms [105]. Examples of these calculations are shown in figure 3.4 where the predictions of the observables for Ξ^--^{40}Ca and Ξ^--^{208}Pb hyperatoms are presented. The figure shows the yield of the X-ray transitions (blue dots, right axis), the absorptive width (green triangles, left axis) as well as the energy shift (red squares, left axis) as a function of the principal quantum number n of the state. The numbers given below the quantum numbers (n, l) are the transition energies of the corresponding X-rays.

The detailed study of the $\overline{\mathrm{P}}$ANDA hyperatom experiment will be presented in chapter 6.

---

[b] annapbarsSPY1107.f, attached on CD

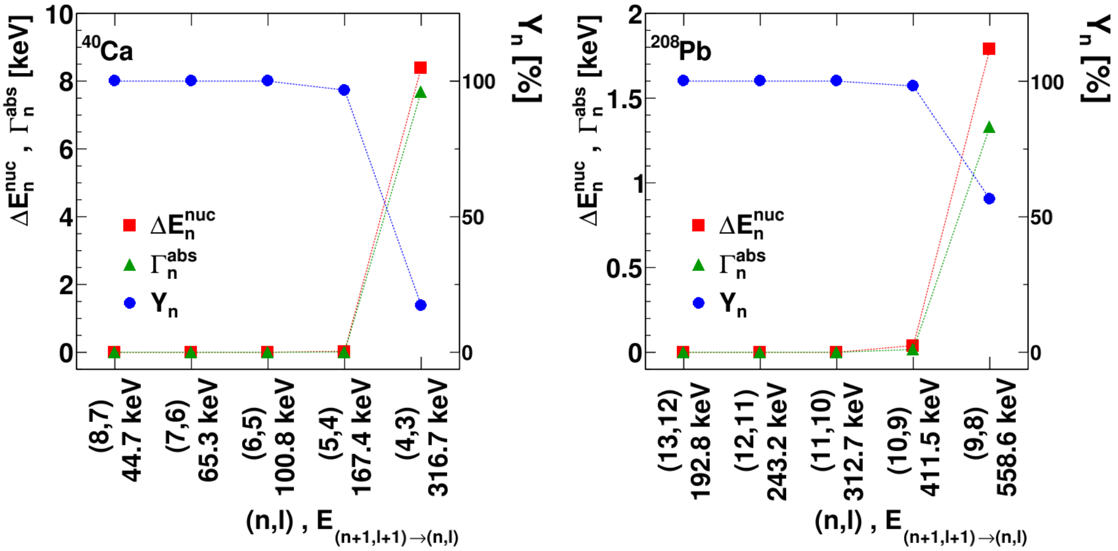

Figure 3.4: Overview of the energy shifts $\Delta E_n^{\mathrm{nuc}}$ and the absorption line widths Γ_n^{abs} for Ξ^--^{40}Ca (left) and Ξ^--^{208}Pb (right) hyperatoms. The influence of the strong interaction is visible for the lowest two states for both hyperatoms. For the calcium hyperatom the quantum numbers are much lower than for lead due to its lower atomic number. Both $\Delta E_n^{\mathrm{nuc}}$ and Γ_n^{abs} show strong effects at the final states of both hyperatoms.

3.3 Experimental situation of exotic atoms

Exotic atoms have been studied for many decades. The lightest type of these are muonic atoms. One of the most prominent recent observations is the precise laser spectroscopy of the hyperfine structure of muonic hydrogen at PSI by Pohl *et al.* in 2010 [109] and muonic deuterium in 2017 [110]. They observed a significantly smaller proton radius compared to the previous common average of results gained from electron scattering experiments and the spectroscopy of regular hydrogen (see e.g. [111]) and initiated the so called “proton radius puzzle” (see e.g. [112]). Recent measurements of the proton radius for electronic hydrogen [113] and low momentum electron scattering [114] are in line with the results of the muonic atoms. This indicates that the discrepancy to the previous measurements could be caused by systematic effects in these measurements [115].

While the interaction of muonic atoms is fully electro-weak, strong interaction arises when switching from leptonic to hadronic atoms. The lightest of these is the pionic atom where a π^- is bound to a nucleus. Precise measurements of pionic hydrogen and deuterium were performed at PSI [116]. For heavier pionic atoms deeply bound states of pionic ^{3}He were studied in the recoil-free (d,^{3}He) reaction [117] which populates these states from the inside of the nucleus, avoiding the cut-off that limits the population via X-ray cascades due to nuclear absorption. This technique allowed to study these states in Pb and and multiple isotopes of Sn [118] which opened the door to investigate the influence of the neutron density distribution in different isotopes.

X-ray spectra of kaonic atoms have been measured for a broad band of elements from hydrogen to uranium at multiple facilities around the world [105]. In addition, significant progress has been made for precision measurements on kaonic hydrogen. Experiments at KEK [119] showed a repulsive shift of the 1s level contrary to prior experiments which was confirmed by more recent results from DAΦNE [120, 121]. At J-PARC, the E57 collaboration will perform the first measurement of kaonic deuterium. This will allow to extract the antikaon-nucleon isospin dependent scattering lengths [122]. First successful observations of transitions to the 2p level of kaonic ^{3}He and ^{4}He have been accomplished by SIDDHARTA at DAΦNE [123, 124, 125]. These observations allow to determine the isotope shift with an accuracy of ± 2 eV. The E62 collaboration at J-PARC aims at a further improvement of this accuracy by one order of magnitude to ± 0.2 eV by making use of a novel high-resolution cryogenic detector [126]. The data taking for this new measurement was completed in 2018 and the detailed analysis is ongoing.

3.3.1 Antiprotonic atoms

First strong-interaction shifts and level widths in antiprotonic atoms were reported by Backenstoss *et al.* [102] and Barnes *et al.* [127] in 1972. These studies observed optical antiproton-nucleus potentials [128, 129] which are compatible with s-wave $\overline{p}$-nucleon scattering lengths deduced from scattering data [130].

Multiple decades after these observations, experiments with antiprotonic atoms got a big boost by the PS209 experiment at CERN [131, 132, 133, 134, 135]. Up to now, a total of 44 level shifts and 62 widths could be determined for 34 isotopes (see figure 3.5). In addition, the ratios of peripheral neutron to proton densities could be studied by the use of radiochemical methods which allow to distinguish between the annihilation on a neutron or proton [137, 138]. These experiments provided information on the thickness of the neutron skin for 24 nuclei as shown in

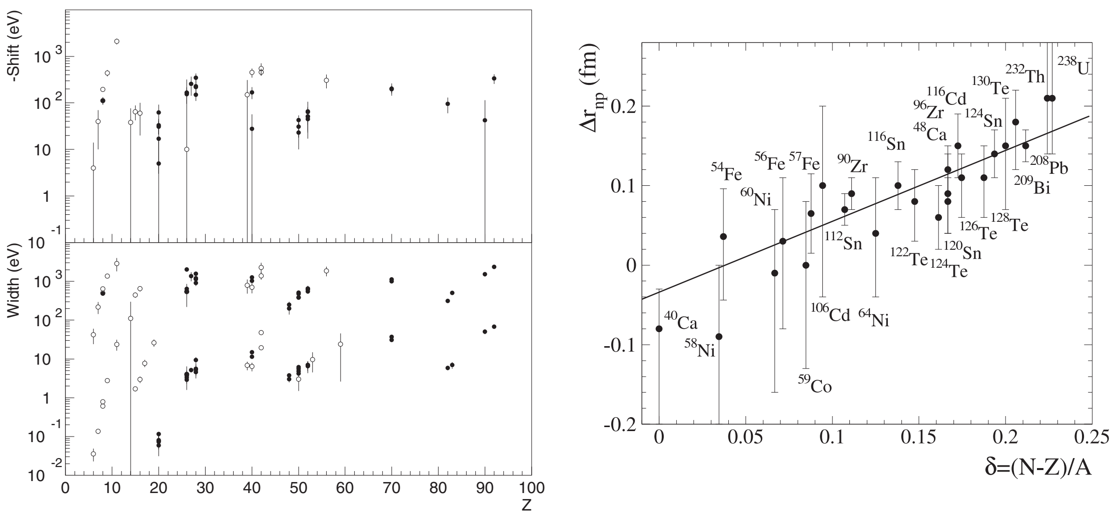

Figure 3.5: Left: Combination of all measured antiprotonic strong interaction level widths and energy shifts plotted as a function of the atomic number Z (figure from [133]). Right: Thickness of neutron skins deduced from antiprotonic atoms as a function of the isospin asymmetry δ =(N-Z)/A (figure from [134], updated in [136]).

the right of figure 3.5 [134, 136]. The full dataset of antiprotonic atoms was used to determine the antiproton-nucleus potential. This was done by fitting a phenomenological model with two complex strength parameters [139] and achieved a fair consistency of the data for stopped $\bar{\mathrm{p}}$ and the $\overline{\mathrm{N}}$N scattering data for all atomic numbers.

The FLAIR facility at FAIR - if realized - will further improve the experimental data. In its full version the new facility offers the ability to cool the antiproton beam down to kinetic energies of $20\,\mathrm{keV}$ which is more than 100 times lower than at the antiproton decelerator at CERN [140] which was used for previous experiments. This highly increases the stopping rates of antiprotons in a variety of target nuclei. The high rates and quality of the antiproton beam at FLAIR would enable a precise study of neutron-rich nuclei and would allow to investigate structural effects like halos or skins, where detailed knowledge is missing. These studies can be extended to neutron-rich unstable atoms when combined with the fragment separator SuperFRS [141].

3.3.2 Σ^- atoms

The present experimental information on hyperatoms is limited to Σ^- atoms. Experiments at CERN [103, 142], RAL [143] and BNL [144] provided 23 data points for various core atoms: 7 measurements of the energy shift, 5 direct measurements of the strong absorption width and 11 measurements of the relative yield [50]. These points are summarized in figure 3.6. Unfortunately, only 10 of these data points have a relative accuracy below $50\,\%$ [145, 146].

The positive energy shift suggests an increased binding of the Σ^- hyperon in the nuclear periphery. Fits with the simple $t\rho$ potential, presented in section 3.2, by Batty and co-workers [143, 148] suggest an attractive real part of the potential $\mathrm{Re}(V_{\mathrm{opt},\Sigma^-}) \approx -26\,\mathrm{MeV}$ and a shallow imaginary part $\mathrm{Im}(V_{\mathrm{opt},\Sigma^-}) \approx -14\,\mathrm{MeV}$. Especially the data taken for heavy W and Pb targets at BNL [144] showed that modifications of the simple $t\rho$ potential were required. The introduction of a phenomenological density dependence into the Σ^- nucleus potential lead to significant improvements [148, 149].

In contrast to this peripheral attractive potential, (π^-, K^+) scattering data [150, 151, 152] indicated a repulsive interaction at the inside of the nucleus. This repulsive core potential has been confirmed by fitting relativistic mean-field potentials. [153, 154] suggested a repulsive real potential in the nuclear interior and a shallow attractive part in the nuclear periphery. These potentials were obtained by fitting phenomenological optical model potentials [105, 146] to the combined available data of Σ^- hyperatom and (π^-,K$^+$) scattering. The diagrams on the right side of figure 3.6 show multiple nuclear potentials as a function of the radial distance between the Σ^- and the ^{208}Pb nucleus. The figure is split into the real part (top) and the imaginary part of the Σ^--^{208}Pb potential (bottom). The arrows at $r = 1.1(A-1)^{1/3} = 6.52\,\mathrm{fm}$ mark the nuclear radius of the hyperatomic system [147]. The variety in these models illustrate that the available data still allows a wide range of repulsive potentials within the nucleus. None of these calculations have a sufficient attractive pocket in the potential to create nuclear bound states. The only exception for this is the lightest Σ^- hypernuclear system, $_{\Sigma}{}^{4}$He [155, 156], where the isovector contribution is large enough to provide strong binding [157]. Additional binding can be provided by Coulomb interaction which is not included in any of these models. This additional binding might be sufficient for strongly bound states in the far periphery [158]. These states may have a reasonable small width of $\Gamma \approx 1\,\mathrm{MeV}$ and could therefore be observable in near-recoil-less inclusive (K^-, π^+) reactions.

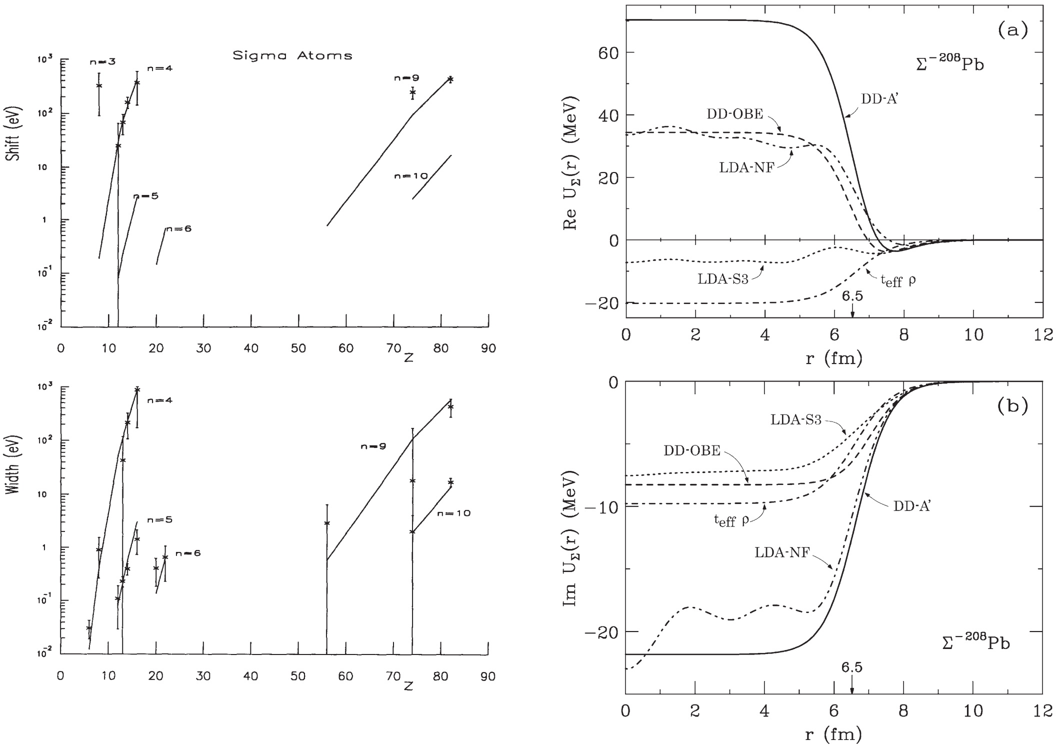

Figure 3.6: Left: Summary of the 23 data points available for Σ^- hyperatoms. The measured energy shifts (widths) are shown at the top (bottom) (figure from [50]). Right: Real (top) and imaginary (bottom) parts of the Σ^--^{208}Pb potential as a function of the radial distance between the Σ^- and the center of the nucleus. Various models for the potential are shown. The arrows at r = 1.1(A-1)$^{1/3}$ = 6.52 fm mark the nuclear radius of the Σ^-–^{208}Pb atomic system. The attractive Coulomb potential is not included in the potentials (figure from [147]).

3.4 Status of Ξ^- nuclear systems

Presently, the information of the Ξ^--nucleon interaction is very limited. The ALICE experiment at LHC observed an attractive interaction of Ξ^- and proton in femtoscopic studies of p-Pb collisions at $\sqrt{s} = 5.02\,\text{TeV}$ [41]. This strong attractive potential is compatible with recent lattice calculations by the HAL-QCD collaboration [159, 160]. Within nuclear matter, the only experimental information of the strength of the Ξ^- potential yields from a single $^{14}_{\Xi^-}$N hypernuclear event decaying into twin Λ hypernuclei within emulsions. The analysis of this event named "KISO", found at the KEK-PS E373 experiment, results in a binding energy of $B_{\Xi^-} = 4.38 \pm 0.25\,\text{MeV}$ [42]. The data of both experiments is shown in figure 3.7.

Further information of the strength of this potential at nuclear densities will arise from Ξ^- hyperatom experiments. Besides $\overline{\text{P}}$ANDA at FAIR, there are two more experiments at J-PARC [161]. The hybrid emulsion experiment E07 [43] employed the (K^-, K^+) double strangeness exchange reaction to create tagged Ξ^- hyperons and absorb them within nuclear emulsion plates. The main task of these emulsions was the identification of $\Lambda\Lambda$ hypernuclei decays where light elements like hydrogen and carbon are required for the tracking of these. Besides these elements,

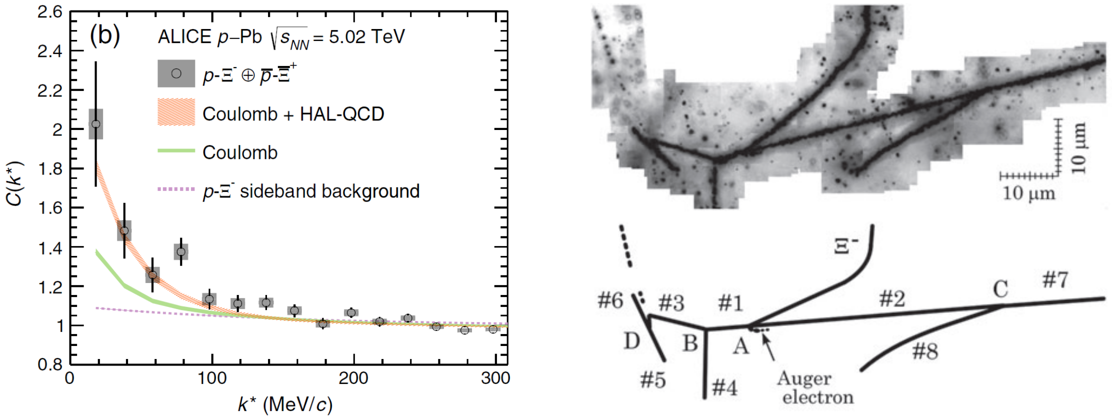

Figure 3.7: The correlation functions C(k*) measured by ALICE [41] are in-line with an attractive strong Ξ^--proton potential (left). The right picture shows the "KISO" event [42] observed at KEK-PS E373. The formation of a ${}^{14}_{\Xi^-}$N and its decay into twin Λ hypernuclei was identified at vertex A. Vertex B and C correspond to the decay of the hypernuclei ${}^{10}_{\Lambda}$Be and ${}^{5}_{\Lambda}$He, respectively (figures from [41] and [42]).

such emulsion plates consist of large amounts of ^{79,81}Br and ^{109}Ag which can absorb the Ξ^- and form the corresponding Ξ^- hyperatoms. This target system was surrounded by the Hyperball-X germanium detector array [162], designated to search for X-ray transitions. The experimental setup is sketched in figure 3.8.

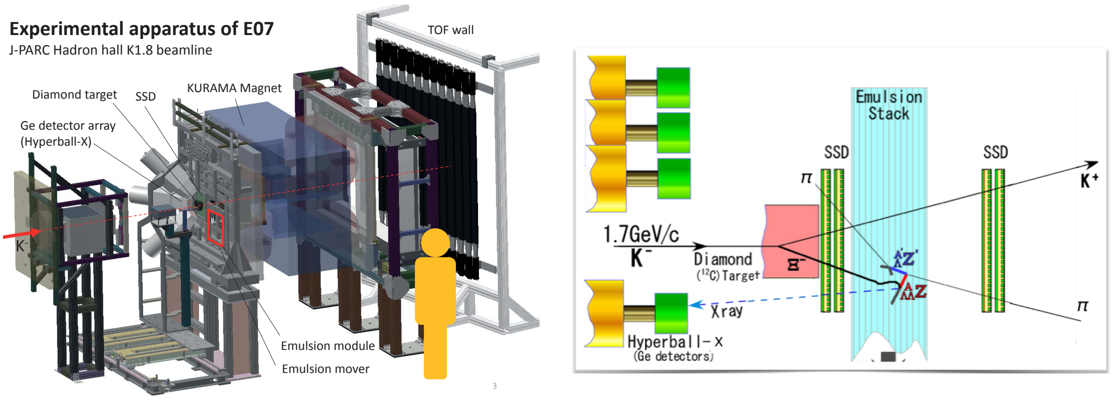

Figure 3.8: Schematic drawing (left) and detection scheme (right) of the hybrid emulsion experiment J-PARC E07. Besides $\Lambda\Lambda$ hypernuclei, Ξ^- hyperatoms could be produced within the nuclear emulsions and their atomic X-ray transitions detected in the surrounding Hyperball-X germanium detector array (figures from [43].

Based on simulations E07 expects to find approximately 13 (8,7)→(7,6) transitions for Ag hyperatoms and 8 (7,6)→(6,5) transitions for Br [163]. The energy shift expected for those hyperatoms is in the range of 0.3 to 5 keV with a width of 0.2 to 1.8 keV depending on the model used [164]. Data taking of the experiment was finished in 2017 and the digitalization of the emulsion data was completed in February 2018. The detailed analysis is in progress. Figure 3.9 shows a preliminary X-ray spectrum of approximately 15 % of the full data. The spectrum is cut on events where the stopping of a Ξ^- hyperon has been identified within the nuclear emulsion plates [87]. The estimated X-ray energies are around 316 keV and 370 keV for Ξ^--Br and Ξ^--Ag hyperatoms, respectively. Despite a low background, the spectrum shows that the analysis of the full data is required to establish a clear signal.

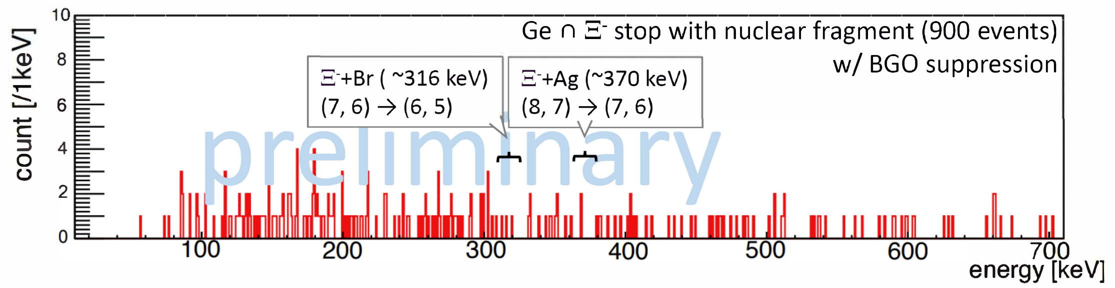

Figure 3.9: X-ray spectrum produced in events where a stopped Ξ^- hyperon was identified in the nuclear emulsion plates of the J-PARC E07 experiment. This data corresponds to 15 % of the data taken and does not allow to establish a clear signal for one of the hyperatoms. The full analysis is ongoing. (Figure from [87])

On the other hand, the E03 experiment is optimized for the detection of hyperatomic X-rays. It will be performed at the same beam line of J-PARC as the previously described experiment E07 and will share the same secondary K^- beam. Contrary to E07, E03 will use a thick iron target to create and stop the Ξ^- inside. Because of that, the event identification lacks the emulsion information and will have to rely on the detection of the outgoing K^+ in a combination of tracking detectors and the KURAMA spectrometer. Hyperball-X will be used again for X-ray spectroscopy of the produced Ξ^--^{56}Fe hyperatoms. The estimated yield for the (6,5)→(5,4) transition, affected by the nucleus, is 220 for phase-1 of the experiment in 2020 with low background [c](see figure 3.10) [165].

In contrast to both experiments at J-PARC, the hyperatom experiment at $\overline{\text{P}}$ANDA is less limited in its choice of the target material. As it will be shown in chapter 6, Ξ^--^{208}Pb hyperatoms, created in a Pb absorber, offer very promising results. These heavy hyperatoms will probe the Ξ^- neutron interaction in the neutron skin of the ^{208}Pb nucleus. As shown in figure 3.5 the neutron skin of ^{208}Pb is well established which reduces the systematic uncertainty introduced by the nuclear potential. The unique split up target design allows to use thin Ξ^- absorbers resulting in low X-ray absorption and the possibility to study coincident cascades of X-ray transitions. The $\overline{\text{P}}$ANDA hyperatom experiment will be discussed in full detail and compared to the experiments at J-PARC in chapter 6.

---

[c] 15 days, 50 kW beam power

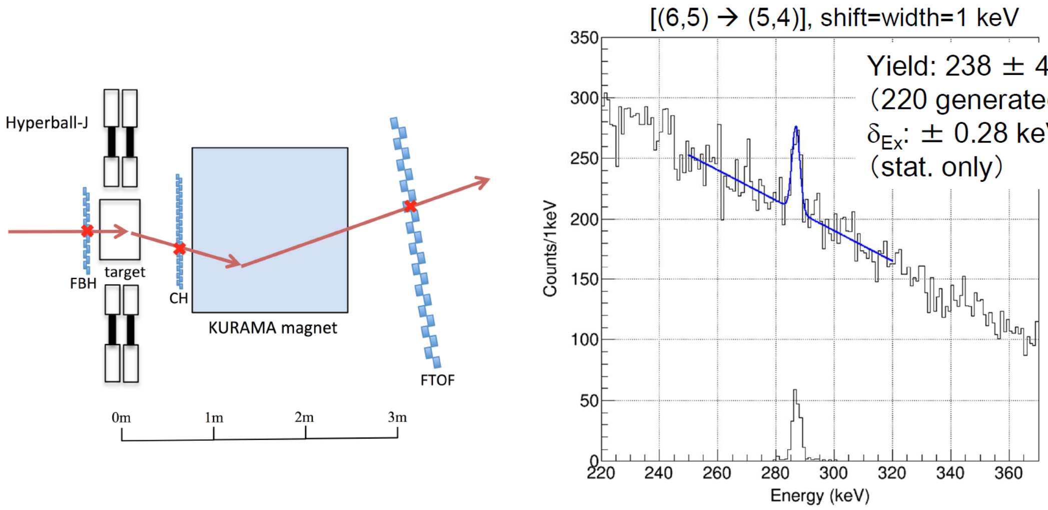

Figure 3.10: In contrast to the J-PARC E07 experiment, E03 will use a thick iron target to create and stop Ξ^-. The event tagging via the outgoing K^+ will have to rely on tracking detectors as well as the KURAMA spectrometer (left) (figure from [166]). The right plot shows a simulation of the expected spectrum for phase-1. The low background allows to identify a proper signal peak (figure from [165]).

3.5 Beyond S=-2: The Ω^- hyperon in nuclear systems

The study of Ξ^- atoms could also serve as an initial step towards the search for Ω^- hyperatoms. First studies of these triple strange hyperons can be similar to Ξ^- hyperatoms and observe their strong energy shift and absorptive width [101, 105].

Furthermore, these Ω^- hyperatoms could help to explore the fundamental question whether baryons are deformed. Like all composed particles, baryons are expected to be deformed objects and hence posses a finite intrinsic quadrupole moment Q_0. However for spin J=0 and J=1/2 hadrons, the spectroscopic quadrupole moment Q vanishes independent of the size of Q_0. Spin J=3/2 particles on the other hand allow to extract Q_0 from the spectroscopic moment according to (see e.g. [167])

$$Q = \frac{J(2J-1)}{(J+1)(2J+3)} Q_0. \tag{3.14}$$

Its spin 3/2 and comparably long life time makes the Ω^- the only candidate for direct experimental information of Q_0 for an individual baryon. Because of that, this measurement is an important complement to the world wide activities trying to nail down the shape of the proton or the transition quadrupole moment of baryons. Unlike for nucleons, pion exchange is irrelevant for Ω^- and the influence of heavier mesons is strongly suppressed. Therefore, meson cloud corrections are expected to be small [168]. Since contributions of light quarks are small, the quadrupole moment of Ω^- will also be a sensitive benchmark for lattice QCD simulations. As summarized in [51], all recent lattice calculations predict an intrinsic quadrupole moment Q_0 in the order of $0.01\,e\,\mathrm{fm}^2$. This positive Q_0 signals an oblate distribution of the three s-quarks in the Ω^- hyperon and measuring Q_0 can put unique constraints on the composite models of baryons.

First calculations of the quadrupole splitting in Ω^--^{208}Pb hyperatoms have been performed by Sternheimer and Goldhaber in 1973 [169]. Their calculations, however, were based on a quadrupole moment 100 times higher than today's prediction. Later, calculations were performed by Giannini [170], Karl and Novikov [171] and Krivoruchenko and Fässler [172]. Depending on the size of the quadrupole moment, the spin splitting of the X-ray (n=11,l=10)→(n=10,l=9) transitions can reach tens of keV (compare figure 3.11). The energy of this transition is in the range of $520\,\mathrm{keV}$. The proximity to the electron annihilation line at $511\,\mathrm{keV}$ allows to use it for stability monitoring and precise calibration.

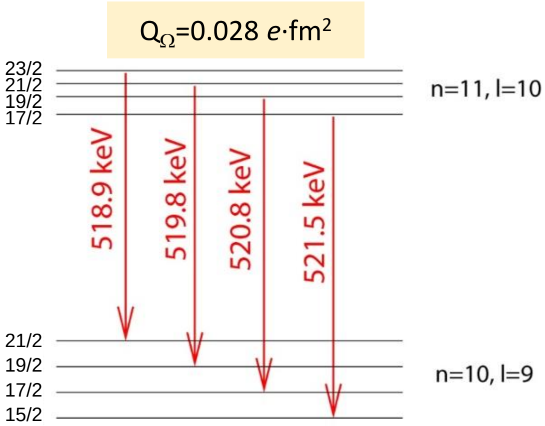

Figure 3.11: Expected X-ray energies of the (n=11, l=10 → n=10, l=9) fine structure transition in the Ω^--^{208}Pb hyperatom assuming a quadrupole moment of Q_Ω = 0.028 e·fm^2. The line splitting could be observable when sufficient statistics is available (figure based on [170]).

Concerning the question if the creation of Ω^- atoms is possible at all, it was shown by Alvarez [173] that three emulsion events observed in 1954 [174, 175] can be interpreted as Ω^- decays. This observation in cosmics was 10 years before the discovery of the Ω^- at Brookhaven in 1964 [176]. Two of these events can be attributed to the decay of atomically bound Ω^-. While one of these is bound to a light emulsion nucleus, the second event shows the atomic binding of a Ω^- to a ^{14}N nucleus. In all three events the Ω^- was most probably produced by the $\Xi^0 + n \rightarrow \Omega^- + K^+$ reaction inside a heavy nucleus.

Unfortunately, the production cross section of $\Omega^-\bar{\Omega}^+$ pairs in p̄p annihilation is experimentally completely unknown. Predictions are scarce [177] and may have large uncertainties. Therefore, quantitative predictions for Ω^- hyperatoms are not possible at this time. Nevertheless, the study of $|S| = 3$ hyperatoms might be possible at the end of the scheduled time scale of P̄ANDA. The production will require a high luminosity or even an antiproton-proton collider. This possible HESR-$\overline{\text{HESR}}$ setup would greatly reduce the average Ω^- momentum which would increase the stopping probability and could compensate the lower production cross section (compare figures 2.5, 6.1 and 6.3).

3.6 Summary of the chapter

As shown in this chapter, the study of exotic atoms has been an important experimental tool in the past and present. Muonic atoms allowed to study the radius of the proton and opened up the “proton radius puzzle”. Hadronic, mesonic and baryonic, atoms offer a unique way to study the hadron, the nucleus as well as their interactions. For baryonic atoms, most data is available for antiprotonic atoms and this dataset will greatly increase if the FLAIR facility at FAIR will be constructed. The X-ray spectroscopy of Σ^- atoms in a wide range of the periodic table revealed the complex shape of the radial nuclear potential. None of its theoretical descriptions predicts strongly bound systems with the only exception of ${}^{4}_{\Sigma^-}$He.
No data is available for hyperatom with higher strangeness yet, but the experiments at J-PARC and $\overline{\text{P}}$ANDA will change this situation for $|S| = 2$.

4 PANGEA - the PANda GErmanium Array

As previously mentioned in chapter 1, the high precision γ (X-ray) spectroscopy of hypernuclei and hyperatoms requires a dedicated detector. PANGEA is designed to fulfill this task in $\overline{\text{P}}$ANDA. The detector is composed of an array of High Purity Germanium (HPGe) detectors. This chapter shows the development of the detector. First the requirements on the detector and its limitations imposed by the $\overline{\text{P}}$ANDA spectrometer are shown in section 4.1. The following section 4.2 presents an individual detector module housing three HPGe crystals. The development of these modules is a shared task with the DEGAS group [178] of the NUSTAR collaboration and is mostly performed at GSI.
PANGEA is composed of several of these triple detectors. The optimization of this composition and the integration of the full PANGEA detector into $\overline{\text{P}}$ANDA is then summarized in detail in the two last sections of this chapter, 4.3 and 4.4.

4.1 Requirements

PANGEA needs to have maximum sensitivity in detecting electro-magnetic transitions in an energy range up to $10\,\mathrm{MeV}$. This requires a high energy resolution and detection efficiency In addition, the solid angle coverage must be optimized to maximize the sensitivity of the full detector. At the same time, the granularity of the detector has to be high enough to process the particle flux created by the high primary interaction rate of up to $4 \cdot 10^6/\mathrm{s}$. This can be achieved by using individual crystals arranged in cluster detectors and placing them close to the interaction point. Nevertheless, dedicated read-out electronics are required to process these high interaction rates.
The high energy resolution is intrinsic for HPGe detectors in the required energy range. A sharper signal peak allows tighter cuts and thus reduces the background of the experiments. The reduces the amount of background that needs to be reduced by event filtering (compare section 6.3). Still, the hadronic background has to be taken into account in the design of PANGEA. Especially fast neutrons are critical for HPGe crystals. The radiation damage caused by them (compare chapter 5) deteriorates the structure of their atomic lattice, hampering their high energy resolution. This background is mainly caused by primary particles or their daughter particles and is boosted forward due to the fixed-target setup. In contrast to that, the decaying hyperatoms and hypernuclei are at rest and because of that, the transition photons of both experiments will be irradiated isotropically in the full solid angle. Therefore, high polar angles relative to the beam axis (backward angles) are favored to improve the signal-to-noise ratio. Thus, the best position for the germanium array is the one occupied by the backward endcap EMC in the standard $\overline{\text{P}}$ANDA setup which consequently has to be removed for the insertion and operation of PANGEA. Nevertheless, the space for the detectors is still very limited. Because of that, shifting the primary interaction point upstream is mandatory for the operation of PANGEA in both experiments. A shift of $55\,\mathrm{cm}$ allows to integrate the target system as well as PANGEA and increases its solid angle coverage. Without this shift, the straw tube tracker (STT) would block most of the solid angle and limit the

minimum distance to the interaction point. In this position the outer dimensions of PANGEA are restricted to a radius of 40.3 to $43.8\,\mathrm{cm}$ by the cable frame of the STT (see figure 4.1). On the inside, the beam pipe for both strangeness experiments will have a radius of $4.5\,\mathrm{cm}$ mimicking the standard beam pipe of the HESR outside of the experimental area.

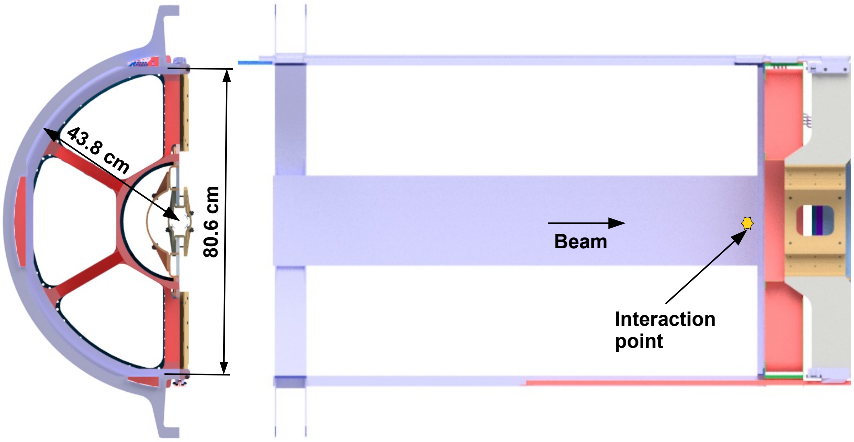

Figure 4.1: The cable support frame of the straw tube tracker limits the outer diameters of the PANGEA detector. A maximum radius of $43.8\,\mathrm{cm}$ is available. Safety margins of $1\,\mathrm{cm}$ must be met on the inside and outside of the detector. In the right view of the frame the shifted interaction point at z = $-55\,\mathrm{cm}$ is shown. This shift moves the interaction point to the end of the STT (red structure) and increases the available the solid angle of PANGEA.

In contrast to the standard $\overline{\text{P}}$ANDA setup, all the support lines and cables of the (active) target system will be routed on the outside of the germanium array [a], reducing the material budget in front of the detectors. A safety distance of $1\,\mathrm{cm}$ on the inside and outside further reduces the available space.

This limited space is a major challenge for germanium detectors since they usually depend on being cooled with liquid nitrogen and therefore require a bulky dewar. For PANGEA a new electro-mechanical cooling system is intended (see section 4.2.1).

In addition to these spatial limitations, the high particle background and strong magnetic fields require dedicated electronics. While the application of germanium detectors within strong magnetic field was successfully tested in [179], the development of new radiation hard and fast read-out and control electronics is still in progress. Details on this is given in section 4.2.2.2. Table 4.1 summarizes the most important requirements of the detector array.

---

[a] In standard $\overline{\text{P}}$ANDA these lines and cables are attached to the beam pipe.

Energy range	Noise threshold	Energy resolution (at $1.3\,\mathrm{MeV}$)	Time resolution (at $1.3\,\mathrm{MeV}$)	Overload recovery time	Max. event rate
0.1 to $10\,\mathrm{MeV}$	$15\,\mathrm{keV}$	$2.3\,\mathrm{keV}$	$10\,\mathrm{ns}$	$100\,\mathrm{ns/MeV}$	$2\,\mathrm{MHz}$

Table 4.1: Requirements of the PANGEA detector. Most of them are shared with the DEGAS detector [178]. The difference in the required energy range is taken care of by an adjustable preamplifier.

4.2 PANGEA Triple Detector

As all other big germanium detectors, the PANGEA detector will be composed of an array of individual cluster detectors each featuring its individual cryostat. Each of these will house three encapsulated HPGe crystals of the tapered EUROBALL type [180]. This allows a much more flexible arrangement of the individual clusters compared to its parental germanium array RISING [181], where 7 crystals were combined in a single cryostat. In addition, the improvements of the cryostat allow to get rid of the bulky liquid nitrogen (LN_2) dewars.

The development is shared with the DEGAS germanium detector [178] of NUSTAR which reduces the financial needs and manpower required for R&D and construction and will be briefly presented in the following.

4.2.1 Development of the cryostat

The spatial limitations inside the $\overline{\text{P}}$ANDA target spectrometer do not allow a classical LN_2 cooling for the PANGEA detector to reach the typical operational temperature of 77 to $110\,\mathrm{K}$. The dewars required for this kind of coolers would not fit into the available space. Instead, electro-mechanical cooling devices allow to reduce the footprint of the detector modules. Additionally, these coolers do not need any kind of automated LN_2 refilling system or special safety features in contrast to traditional cooling options.

When using electro-mechanical coolers the size of the cryostat is dominated by the size of the triangularly arranged encapsulated germanium crystals (see figure 4.2), which is necessary for the tight arrangement of the triple clusters.

The capsule, made of $0.7\,\mathrm{mm}$ thin aluminum, mimics the shape of the crystal on the inside. The basic shape of the crystal is a $78\,\mathrm{mm}$ long cylinder with a diameter of $70\,\mathrm{mm}$. The crystal is then conically cut and forms a hexagon with an edge length of $34\,\mathrm{mm}$ at its front. The same parameters for the capsule are $100\,\mathrm{mm}$, $75\,\mathrm{mm}$ and $35.3\,\mathrm{mm}$, including the supply and interfacing area in the lid of the capsule [182] (see figure 4.3).

Due to the temperature gradient of more than $200\,\mathrm{K}$ between the inside and outside of the cryostat, it is critical to minimize the thermal transfer. The three important processes of this transfer are radiative heating, the thermal conductivity of remaining thermal bridges and residual molecular heating. The latter directly depends on the quality of the vacuum inside the cryostat (see section 4.2.2).

The flow rate of radiative heating q is given by

$$q = \epsilon\,\sigma\,A_i\,F_{ij}\,(T_i^4 - T_j^4) \tag{4.1}$$

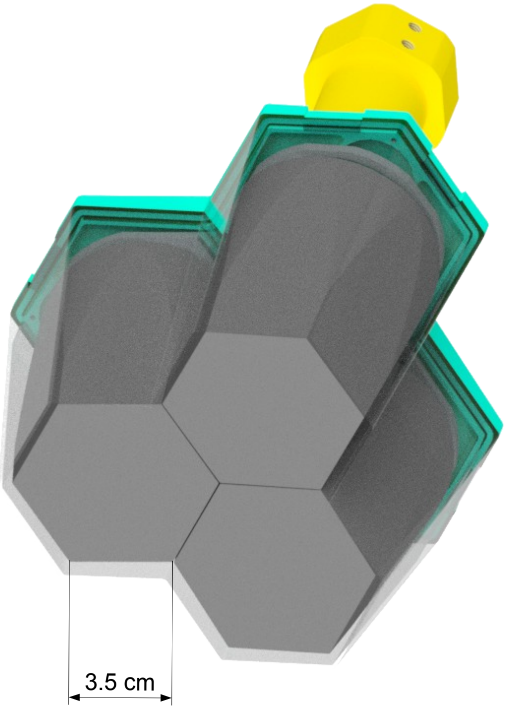

Figure 4.2: The three encapsulated crystals of an individual cryostat are arranged in a triangle. For better visibility, the detector end cap is transparent in this picture and only the detector head is shown.

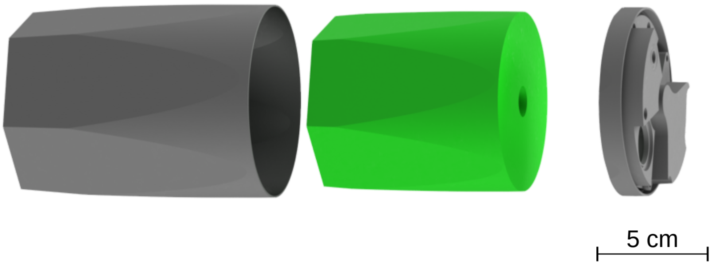

Figure 4.3: Exploded view of a EUROBALL HPGe encapsulated crystal. The thin aluminum capsule (gray) protects the sensitive crystal (green). The supply and readout feedthroughs are included in the lid on the right.

with ϵ, the emissivity of the surface, $\sigma = 5.6704 \cdot 10^{-8}\,\mathrm{W/m^2/K^4}$, the Stefan-Boltzmann constant, A_i, the area of surface i, the form factor of surface i and j F_{ij} and the absolute temperatures of surface i and j, T_i and T_j. The only parameter among these that can be technically improved is the surface emissivity ϵ. ϵ has to be minimized by a high quality processing of the end cap of the detector made of aluminum. The emissivity of aluminum ranges from 0.05 to 0.14 depending on the processing and its temperature [183]. Because of that, electro polishing is required for the inside of the end cap. This processing can achieve an emissivity of 0.08 [184] which is sufficient for the operation of the detector. Experimental data in [183] shows a good agreement with $\epsilon = 0.1$ or slightly lower values for a commercially available encapsulated HPGe detector by ORTEC. Figure 4.4 shows the large influence of this radiative heating in calculations of the cool-down time. The influence of the variation of ϵ is especially visible at small temperatures.

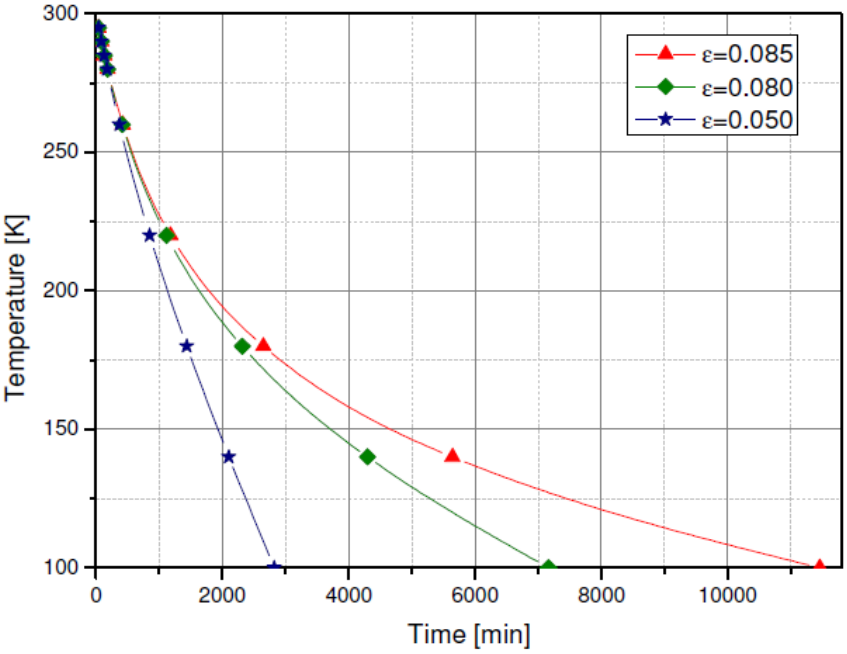

Figure 4.4: Comparison of the cool-down time of a triple detector with varying emissivity ϵ. Especially at low temperatures, this variation strongly effects the radiative heating and hence the cool-down time (figure taken from [183]).

The emissivity of the outer surface of an encapsulated crystal is supposed to vary between 0.1 to 0.2. Further processing of this aluminum surface is not possible to prevent damage to the crystal on the inside. Therefore, conservative values for the emissivity of $\epsilon_{\text{cryostat}} = 0.1$ and $\epsilon_{\text{crystal}} = 0.2$ are chosen in thermal studies of the triple detector. Figure 4.5 shows the temperature distribution in simulations using these emissivities. The temperature of the copper cold finger inside the cryostat is $70\,\text{K}$ while the ambient is at room temperature ($295.15\,\text{K}$). The temperature gradient within the crystals is approximately $3\,\text{K}$.

Heat transfer by direct contact always has to be taken into account and hence reduced to a minimum. The main portion arises from the thermal bridges caused by the fixing of the cold finger inside the cryostat. Figure 4.6 shows the results of thermal simulations of one of these optimized distance holders of the cold finger. Its shape is optimized to minimize the conductive heating. This high thermal resistance is achieved by its labyrinthine shape that virtually creates a long distance between both temperature regimes while keeping the conduction cross section small. The heat loss of the part shown could be reduced to $0.077\,\text{W}$ which is less than a quarter

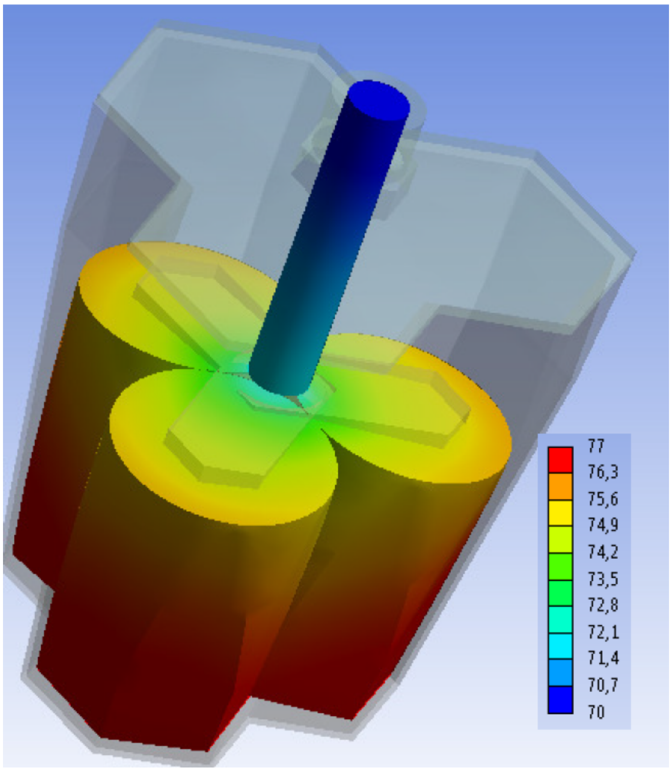

Figure 4.5: Temperature distribution of the encapsulated crystals connected to the cold finger with a temperature of 70 K. The ambient temperature is 295.15 K and the emissivity of the processed inner cryostat surface is 0.1. The aluminum encapsulation of the HPGe crystals have an emissivity of 0.2. The temperature gradient within the crystals is approximately 3 K (figure from [183]).

of the comparable part in the seven-fold cluster detectors of EUROSphere/RISING. Furthermore, the cold finger itself has to be optimized in order to decrease its thermal resistance. A lot of effort was put into this and especially the thermal transmission at boundary surfaces could be improved for instance by ultrasonic bonding [185].

Combining all enhancements made to the cryostat reduces the necessary cooling power of a triple detector to less than 5 W, which is a large improvement compared to older detectors (see figure 4.15 later in this chapter).

Two different electro-mechanical coolers are available that can potentially be used for the detector:

- The first one is the ORTEC X-Cooler III [186]. Its cooling power is not specified in detail by ORTEC. This device is separated into a cold head which needs to be attached directly to the cold finger and a compressor based cooling aggregate that can be placed on the outside of the $\overline{\text{P}}$ANDA target spectrometer. Both parts are connected by insulated flexible tubes.
- The second option is a cooler manufactured by Sunpower. This company offers two viable coolers, the CryoTel CT (11 W) and CryoTel GT (16 W) [187]. Both coolers are very compact. The size of a full cooling unit is similar to the size of the cold head of an X-Cooler. This allows a compact structure of the complete cluster. In this configuration the cooler is

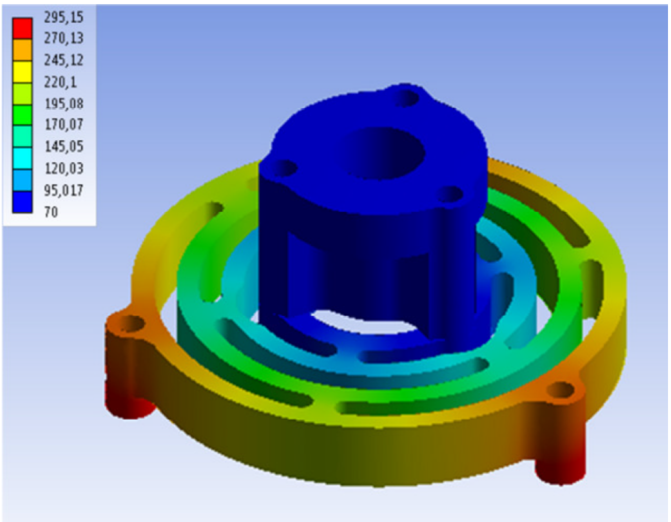

Figure 4.6: Thermal simulations of the fixing labyrinth of the cold finger show that the heat transfer of this important part has been reduced by more than a factor of 4 compared to previous detectors (0.077 W) (figure taken from [178]).

situated inside the magnetic field of the target spectrometer which can reach up to 2 T. Tests of these devices inside a magnetic field of 4 T showed no influence on their performance and hence do not limit their usage in $\overline{\text{P}}$ANDA [188]. Supplying these CryoTel coolers with water jackets allows to use a common water line to carry the heat out of the target spectrometer. In addition to that, these coolers only need a single supply voltage of 48 V DC and are equipped with an external control unit, that will be placed outside of the target spectrometer and thus the magnetic field and radiation area. The direct attachment of the mechanical compressor of the cooler however might lead to microphonic noise. To reduce this, an active noise cancellation system and a decoupled mounting of the cooler to the detector is available by the manufacturer.

The results of the thermal simulations were validated by the construction of two single crystal prototypes equipped with X-Cooler II coolers, the precursor of the X-Cooler III [190]. These detectors have been used at GSI since 2011 and were used for the irradiation test described in chapter 5.3.

4.2.2 Mechanical design of a triple cluster

Each triple cluster detector is divided into two main parts: The detector head, housing the crystals and the cold stage of the preamplifier, and the electronics and support stage with the attached cooler. For the interconnection of these main parts, there are two possible options under investigation which can house veto detectors for Compton and background suppression. Details of all aspects are given in the following sections.

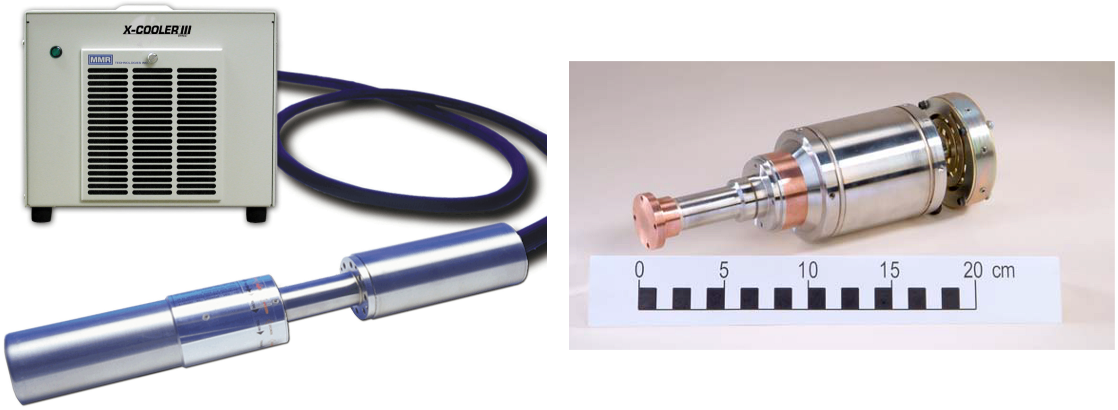

Figure 4.7: Two viable electro-mechanical coolers for the PANGEA cluster detectors are available. The ORTEC X-Cooler III is split up into a cold and the compressor unit. Both are connected by a insulated flexible tube (left). The Sunpower CryoTel CT (right) is more compact and fits into the space of the cold head of a X-Cooler II/III. In contrast to the X-Cooler II/III the cooling power of the CryoTel CT cooler is specified with $11\,\mathrm{W}$ and still offers the possibility to upgrade to the more powerful GT version with $16\,\mathrm{W}$ cooling power if necessary. In the picture the cooler is shown with attached air cooling fins. For PANGEA the water cooled version of would be used (figures from [186] and [189]).

4.2.2.1 Detector head

The detector head houses the three triangularly arranged EUROBALL crystals. Due to their tapered shape, the three crystals are tilted and their conical side faces are aligned in parallel to each other so that a compact structure is achieved (see figure 4.2). The three capsules are attached to the aluminum cold frame that is connected to the cold finger. In order to reduce the thermal noise, the first stage of the preamplifier is also situated inside the cryostat and cooled down to cryogenic temperatures. A vacuum better than $1 \cdot 10^{-6}\,\mathrm{mbar}$ has to be maintained to ensure the insulation inside the detector head. Therefore a residual gas absorber is included in the detector head. This further increases the vacuum quality after the initial pumping.

The shape of the detector head is defined by the shape of the crystals. It is made of aluminum to minimize its radiation length. The cryostat has a wall thickness of $1.5\,\mathrm{mm}$ and is manufactured via CNC. The inside of the aluminum cap is finished by electro-polishing to achieve the necessary emissivity (see section 4.2.1). The distance of the outer surfaces of the capsules and this polished inner surface of the detector cap is $3\,\mathrm{mm}$.

4.2.2.2 Electronics and cooling stage

The cluster detector is designed to integrate as much of its support and read out electronics as technically possible. This reduces the amount of required (ground) connections and thus the possibility for ground loops that can deteriorate the energy resolution. Therefore, the second main part of each individual detector is the electronics stage with the attached cooling device. This stage is attached to the central, vacuum insulated, cold finger in a tri-hexagonal layout, mirroring the outline of the detector head.

The electronics stage itself can be divided into two main decks (see figure 4.8). The deck closer to the detector head is reserved for the generation of high voltage needed to run the germanium crystals and for the preamplifiers (see section 4.2.2.2). Both will be combined into a single unit for each crystal. Hence, each of the three hexagonal sections of this deck will be occupied. The sections in the second stage each fulfill a different job. The first of them can hold the data acquisition (section 4.2.2.2). While the second one houses the electronics used for the detector control (see section 4.2.2.2), the last one is designed for supply electronics, voltage dividers and regulators. Because of that, only a single supply voltage of 48 V DC has to be applied to the detector from the outside. The Sunpower coolers also run at this voltage so that a common supply is possible and the amount of ground connections can be minimized.

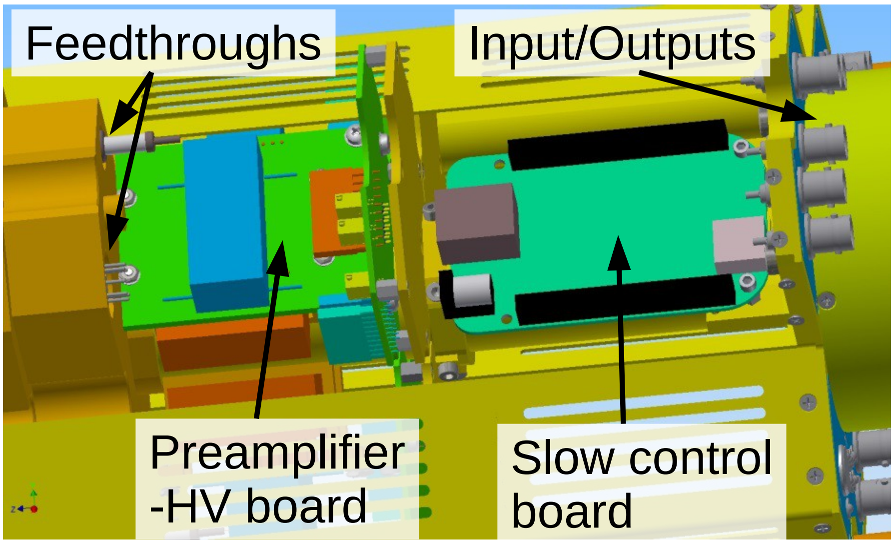

Figure 4.8: CAD drawing of both electronics decks of the cluster detector. The one closer to the crystals, the left one in the picture, houses the three preamplifier and high voltage boards. The second deck is designed to hold the slow control, data acquisition and supply voltage generation.

Preamplifier and high voltage generation

Since the preamplifier is the first part of the front-end electronics, its purpose is to collect and process the energy deposit inside the germanium crystal. PANGEA has two specific requirements to the preamplifier. On the one hand, the high interaction rates require a possibility to reset the preamplifier quickly. This reduces the otherwise long dead time due to the slowly decaying signals. On the other hand, the energy range that PANGEA has to cover depends on the experiments and varies from 0.1 to 1 MeV up to 0.1 to 10 MeV. Because of that, the amplification and thus the energy range needs to be adjustable.

Specifications can be found in table 4.2. The preamplifier board must be specifically designed to fit into the limited space and run in the environmental conditions inside the $\overline{\text{P}}$ANDA target spectrometer. This means that it has to run inside the strong magnetic field and in a high irradiation environment. The circuit board is build as a combination of a main board and a piggyback board (figure 4.9). The main components of the preamplifier are included on the main board. The rather bulky HV components are placed on the piggyback. This reduces the spatial requirements and creates a form factor small enough to fit into the designated space inside the detector. In addition, the maintainability increases due to an easy replacement of individual components.

Property	AGATA	PANGEA
Conversion gain	$100\,\mathrm{mV/MeV}$	Variable 50 to $500\,\mathrm{mV/MeV}$
Noise	$800\,\mathrm{eV}$ ($0\,\mathrm{pF}$)	same
Rise time	$13\,\mathrm{ns}$	same
Decay time	$50\,\mu\mathrm{s}$	same
Integral non-linearity	$< 0.025\,\%$	same
Output polarity	Differential, $Z = 100\,\Omega$	same
Fast reset speed	$\approx 10\,\mathrm{MeV}/\mu\mathrm{s}$	same
Power supply	$\pm 6.5\,\mathrm{V}$, $\pm 12.5\,\mathrm{V}$	$\pm 6\,\mathrm{V}$, $\pm 12\,\mathrm{V}$, $\pm 24\,\mathrm{V}$
Power consumption	$< 980\,\mathrm{mW}$	$< 500\,\mathrm{mW}$
Dimensions	$62 \times 45 \times 7\,\mathrm{mm}^3 = 19\,530\,\mathrm{mm}^3$	$< 5000\,\mathrm{mm}^3$

Table 4.2: Comparison of important detector parameters of AGATA and PANGEA (based on [178] with small updates).

The main component of the HV piggyback board is the BP060674n12 high voltage generation module from iseg Spezialelektronik which can be operated within the magnetic field [188]. This module provides up to $-6\,\mathrm{kV}$ with low ripple and noise of less than $10\,\mathrm{mV}$ and small space requirements [191]. The high voltage applied to the crystal can be controlled by the application of an analog voltage in the range of 0 to 5 V to the $\mathrm{V}_{\mathrm{set}}$ pin of the module. This can be done remotely. Iseg proposes two options for this: either using a voltage divider or a digital-analog-converter. Both options have been compared in [192] and performed equally well. The remote control will be done via the $\mathrm{I}^2\mathrm{C}$ interface. In addition, $\mathrm{I}^2\mathrm{C}$ controlled analog-digital-converters to monitor the high voltage (V_{Mon} pin) and the detector current (I_{Mon}) are included in the piggyback board. The other big module on this board is the HV filter which further reduces the noise of the high voltage. The piggyback board is plugged into the mainboard.

The mainboard houses all the components of the warm stage of the preamplifier. The first stage is the charge collection which is based on the 0706LPA integrator chip from ORTEC. This so called hybrid is delivered on a PCB which is then plugged into the mainboard. To achieve the high intrinsic precision of the germanium detector, a fairly long charge collection time is necessary. This results in a slow detector signal with a typical exponential decay time of $50\,\mu\mathrm{s}$. At the expected signal rates of $\overline{\mathrm{P}}$ANDA, piling-up of these slow germanium signals is a critical issue (compare section 6.3.4). For that reason a fast-reset after the first preamplifier stage has been implemented and included into the pole-zero-cancellation circuit [193]. This quickly discharges the charge collection capacitor after the signal exceeds a user-defined threshold. The third and last stage is the differential output stage. A second amplifier based on the ADA4895-2 low noise rail-to-rail operational amplifier, manufactured by Analog Devices, is integrated here. The amplification is remotely adjustable in order to obtain the optimal resolution for the specific experiment. This can be realized e.g. by using a digitally controllable rheostat (e.g. AD5272 from Analog Devices) in the feedback loop of the amplifier. This rheostat is controlled via the $\mathrm{I}^2\mathrm{C}$ bus. The full preamplification chain is sketched in figure 4.10.

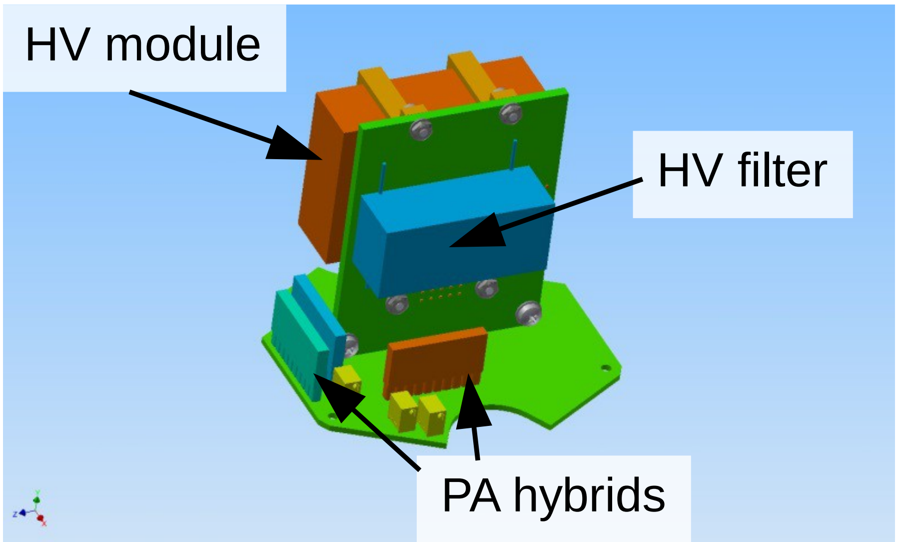

Figure 4.9: CAD drawing of the combined preamplifier and HV board. The HV board is built as a piggyback board to simplify the maintenance. The preamplifier is based on ORTEC HPA0706LPA hybrid integrated circuits. The high voltage is generated by an iseg BP060674n12 module (figure by courtesy of I. K.).

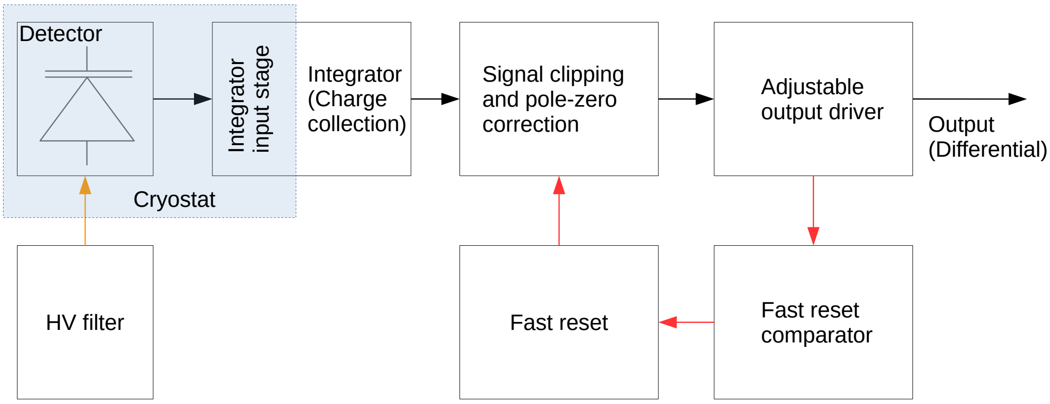

Figure 4.10: Sketch of the PANGEA preamplifier. The main parts of it are the charge collection stage, the pole-zero-cancellation with included fast reset, and the second, adjustable, amplification stage that includes the output driver. The output of the preamplifier is differential [188].

Data Acquisition

After passing the preamplifier, the signal of the germanium crystal needs to be digitized for further processing. A sampling rate in the order of 100 MHz is required for the pulse shape analysis. This analysis allows to extract energy and timing information from signals online for triggering and event building, while allowing further offline studies with higher precision (compare section 5.3.2). Multiple options for this are still under investigation.

The straight forward option is to use the FlashADCs that are in development for the $\overline{\text{P}}$ANDA EMC [194]. These offer a sampling rate of up to $125\,\mathrm{MHz}$ with a resolution of 14 bit. Since these modules are designed for much higher granularity a single module with 64 channels can cover the full PANGEA detector. The integrated FPGAs can be used for online signal processing. The full access to the programming and configuration of these modules allows to implement all required features like online event building or event filtering via energy thresholds or simple event topology (see section 6.3.1) within this module. These FlashADCs are designed for compatibility to the common $\overline{\text{P}}$ANDA DAQ that uses SODANET [195] for timestamping and synchronization of all components. This FlashADC module would be placed outside of the $\overline{\text{P}}$ANDA target spectrometer in the available racks on the auxiliary platform at the back of the target spectrometer. Because of that, the differential detector signal needs to be routed to these digitizers.

In contrast to that and following the path of fully integrated detectors, the other possible option consists of digitizers inside the detector. The FPGA based nanoDPP [196] module produced by LabZY offers the possibility to perform the signal digitization and processing in a very compact size. A single module requires only $50\,\mathrm{mm} \cdot 30\,\mathrm{mm} \cdot 8\,\mathrm{mm}$ and has a low power consumption of less than $800\,\mathrm{mW}$ per module. Since each module covers one channel, three of these would be required for each triple detector. The output of these boards is completely digital and thus reduces the sensitivity to pick-up noise. Nevertheless, further studies will be required to investigate the performance of these modules under the radiation and magnetic field conditions expected at $\overline{\text{P}}$ANDA and therefore this integrated option is seen more as a possible long-term upgrade. In addition the integration to the common $\overline{\text{P}}$ANDA DAQ requires additional R&D.

Detector control system

The $\overline{\text{P}}$ANDA detector control system (DCS) uses the Experimental Physics and Industrial Control System (EPICS) [197]. EPICS is based on a mesh of input output controllers (IOC) connected via Ethernet using the Channel Access protocol (CA). In PANGEA each cluster detector will include its individual IOC whose main task is to control the high voltage of all three crystals and the corresponding preamplifiers as well as the control and monitoring of various detector temperatures and supply voltages. A scheme of this is shown in figure 4.11. For the sake of clarity, the figure is simplified in a way that only a single preamplifier board as well as only a single supply voltage chain is included. The full table of signals can be found in table A.1 in the appendix.

Hardware wise the slow control of the first prototype will be based on the cheap single board computer BeagleBone Black with a form factor of $86.4\,\mathrm{mm} \cdot 54.6\,\mathrm{mm}$ [198]. This ARM-based board offers sufficient connection options to monitor and set all signals. First progress on this was made in [192]. This board will also be used to set the digitally adjustable resistors and voltages of the preamplifier board (see section 4.2.2.2).

A radiation tolerant solution is required for the final detector. This can be based on the common FAIR development of a radiation hard DCS board (figure 4.12) [199]. This board called FTLMC [b] is based on the ARM Cortex-R5F processor family which offers a redundant architecture to correct single event errors caused by irradiation of the chip. This processor is able to run an EPICS IOC on a RTEMS real time operation system. The board will share its form factor with the BeagleBone Black and thus allows an easy replacement in the progressing development. In

---

[b] Fault Tolerant Local Monitor and Control board

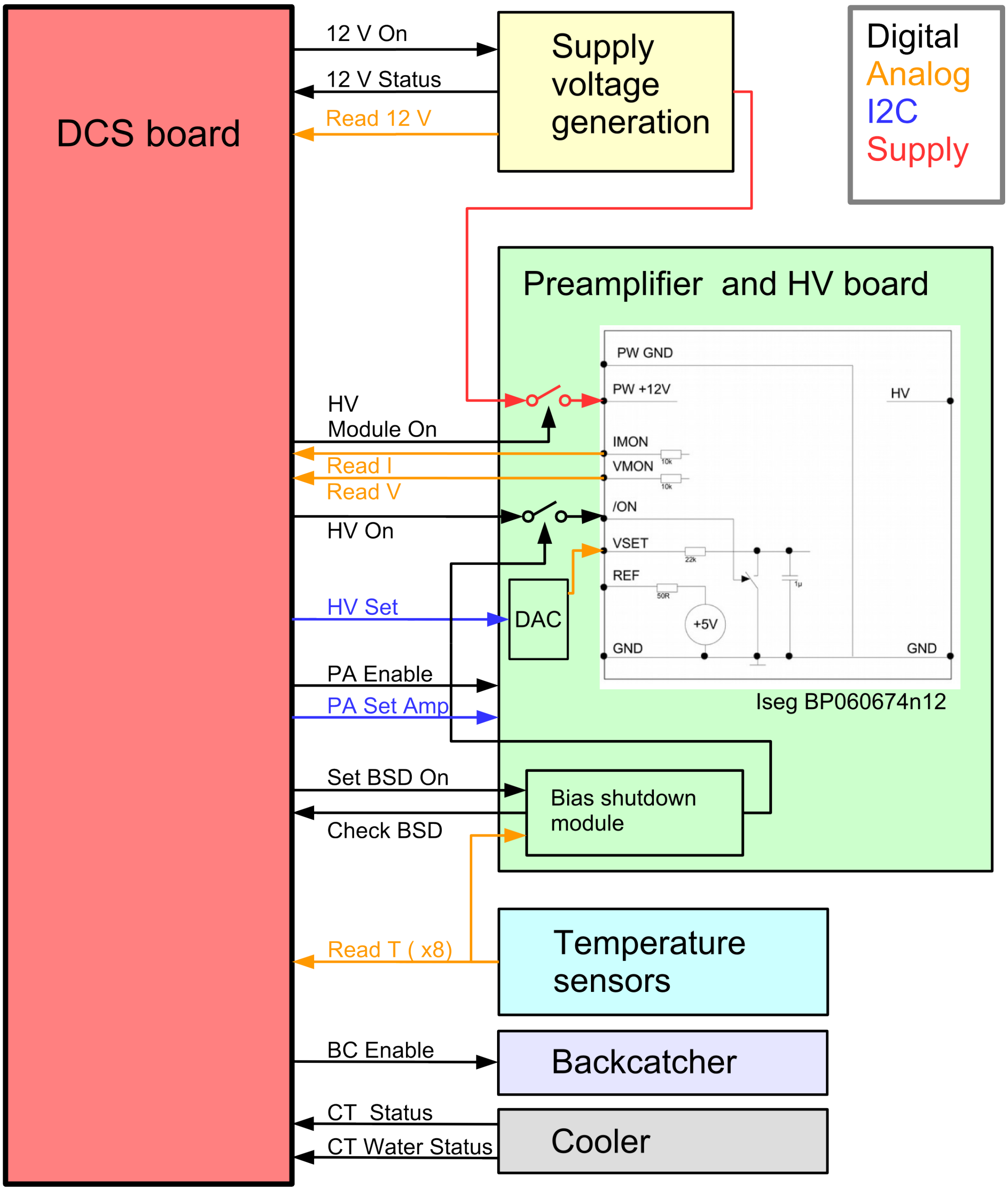

Figure 4.11: Sketch of the slow control of a triple detector. The DCS board running the EPICS IOC is used to control and monitor the whole detector. Most of the signals are connected to the three preamplifier boards. Only one of the preamplifiers is shown for better clarity. The same is done for the supply generation. Only the 12 V line is sketched. The temperature sensors are monitored by the slow control. Besides this, a hardwired direct connection to the bias shutdown module prevents damage of the detector in the case of too high operational temperatures. These might be caused by a failure of the cooler whose status is also monitored. Finally the DCS board controls the usage and status of the veto detectors (backcatchers). A list of all signals can be found in table A.1 in the appendix.

addition, a dedicated version of the FTLMC will include no parts that are sensitive to the magnetic field to allow a proper performance inside the $\overline{\text{P}}$ANDA target spectrometer. This requires either magnetically shielded Ethernet sockets or optical links for the communication to the counting room.

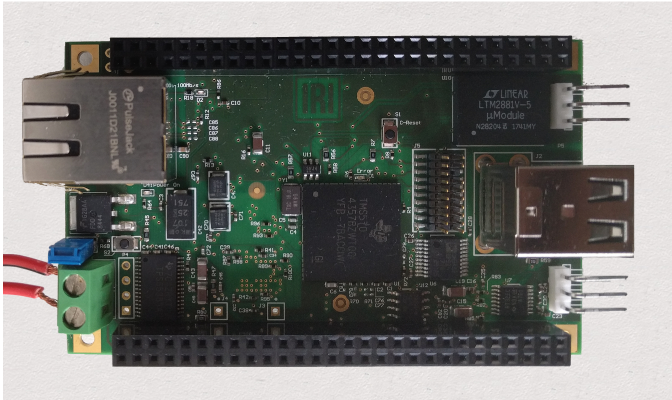

Figure 4.12: A radiation hard detector control board FTLMC is in development [199]. This is a common project of FAIR. With $87\,\mathrm{mm} \cdot 53\,\mathrm{mm}$ it has the same form factor as the BeagleBone Black that is used during the development. The redundant architecture of the processor allows to use the FTLMC within the radiation background of $\overline{\text{P}}$ANDA. The RTEMS real time operation system on the FTLMC allows to run EPICS as required for $\overline{\text{P}}$ANDA (picture by courtesy of [200]).

4.2.2.3 Connection of crystal vessel and electronics stage

To connect the two previously described main parts of the detector, two options are envisioned. The first one is a stiff, straight detector geometry which will also be used for DEGAS (figure 4.13). This design allows to include so called backcatchers, based on BGO crystals, behind each germanium crystal, as well as their electronics. These crystals can be used as veto detectors to reduce background produced by Compton scattering or high energetic particles. The BGO crystals can be operated at room temperature and hence can be placed on the outside of the cryostat. Inside the cryostat, the cold finger includes a small flexible section made of copper wires to decouple the electro-mechanical cooler and the germanium crystals. This reduces microphonic noise in the detector signal that could be introduced by vibrations of the mechanical cooler.

The second option differs in the use of a flexible neck between the crystal vessel and the electronics part. The backcatchers need to be removed in this case. This neck offers a higher flexibility in arranging the crystals of the complete array. Further, the front of each crystal can be pointed towards the interaction point. Figure 4.14 shows this flexible option. A flexible cold finger is fixed by a spiraling thermally low-conducting frame inside a vacuum bellow. For the assembly of the full array both ends of the flexible neck have to be fixed which increases the complexity of the holding frame. Nevertheless, this flexible neck prevents the requirement of dedicated cryostat designs for each detector position which are ruled out as third option.

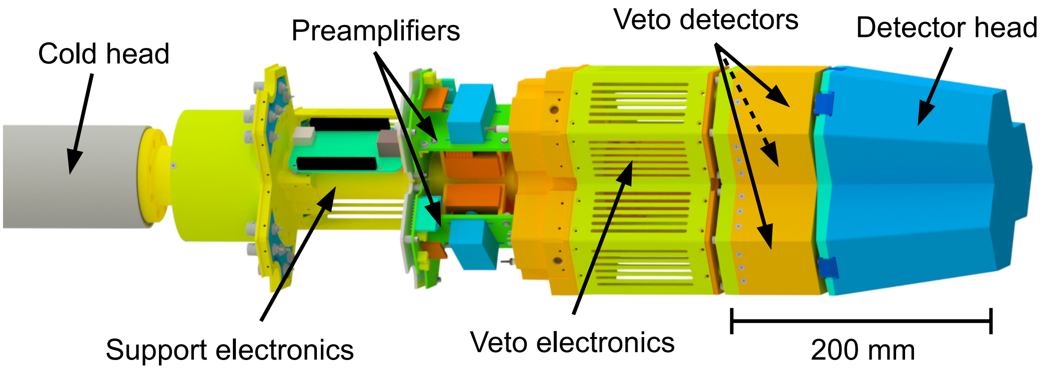

Figure 4.13: CAD Drawing of a single PANGEA triple detector. This design will be used for the DEGAS experiment. In this design, the detector head and the electronics stage are connected by a straight section. This section houses veto detectors (backcatchers) and their electronics. Since the veto detectors run at room temperature they do not need to be integrated into the cryostat. In this picture the covers of the electronic decks are left out to allow a look on the inside. The electronics are partially included (picture by courtesy of I. K.).

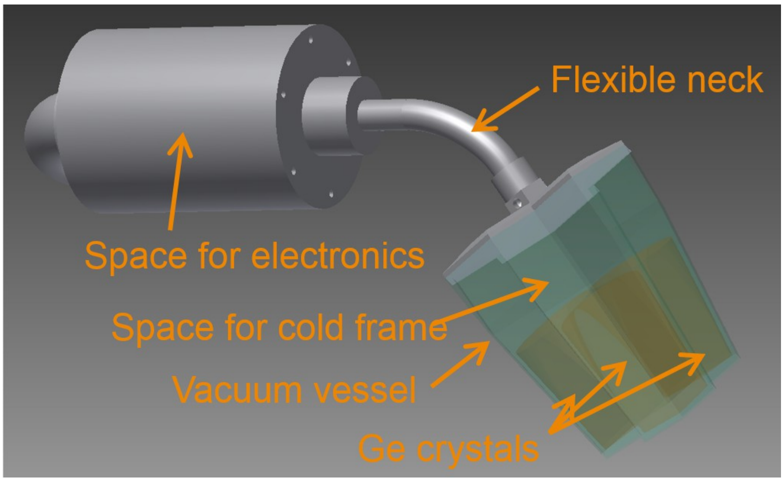

Figure 4.14: As an alternative to the DEGAS design, a flexible neck, based on a bellow and a flexible cold finger on the inside of the cryostat, can be used to connect the detector head and the electronics stage. This design would increase the flexibility of the detector integration but would require additional R&D if this deviation from the DEGAS design would be necessary.

Both options are compared in section 4.3.2 concerning possible detector arrangements and their detection efficiency. Since the stiff one will be used for DEGAS no additional R&D would be needed for this option and it should be favored if no large performance boost can be achieved by the flexible neck.

Currently, the assembly and testing of the first full scale triple prototype with a stiff neck is in progress at GSI. This detector is cooled by an X-Cooler II. Thermal load measurements of the assembled prototype showed a lack of cooling power for this cooler (figure 4.15) which can be solved by using the Sunpower CryoTel CT cooler. The same figure shows the reduced thermal power consumption of PANGEA (DEGAS) compared to older multi-crystal detectors.

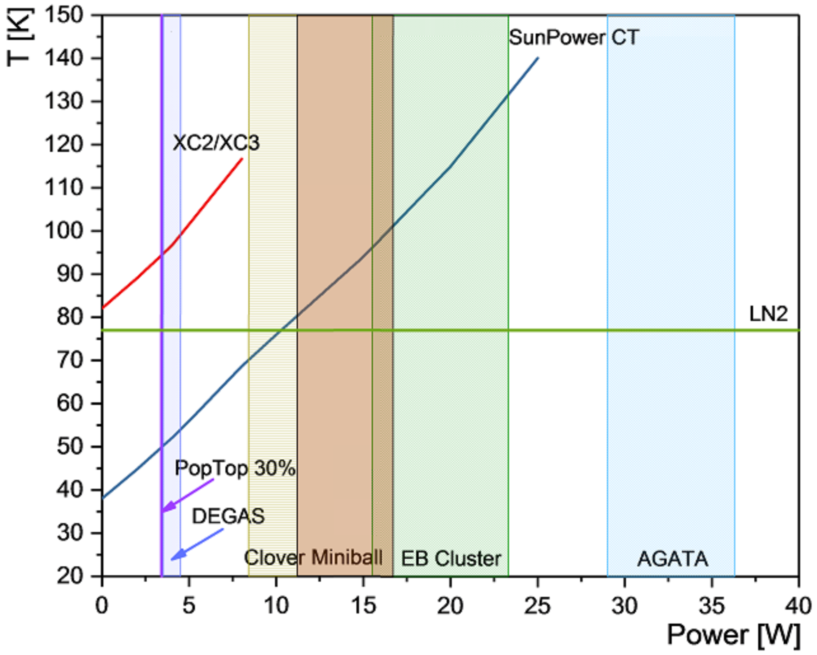

Figure 4.15: The operational temperature reachable with electro-mechanical coolers strongly depends on the cooling power that a detector requires. This cooling power requirement could be highly reduced for PANGEA (DEGAS) compared to older multi-crystal detectors. This power requirements of the respective detectors are visualized by the colored bands. The triple clusters of PANGEA are nearly on a par with an Ortec PopTop detector which houses only a small HPGe crystal. As the data shows, the Ortec X-Cooler II is too weak too reach acceptable equilibrium temperatures. The Sunpower CryoTel CT cooler is more effective. It is able to reach much lower operational temperatures in the required power range which can even be below the temperatures of LN2 cooling [188]).

Nevertheless, the measured energy resolution of the detector is very promising under these conditions. It was specified with 2.8 keV [188] using a prototype of the actively resetting preamplifier (see figure 4.16 (top right)). This resolution was influenced by the high operational temperatures which prevented a full biasing of the crystal. Pictures of this prototype assembly are also shown in figure 4.16.

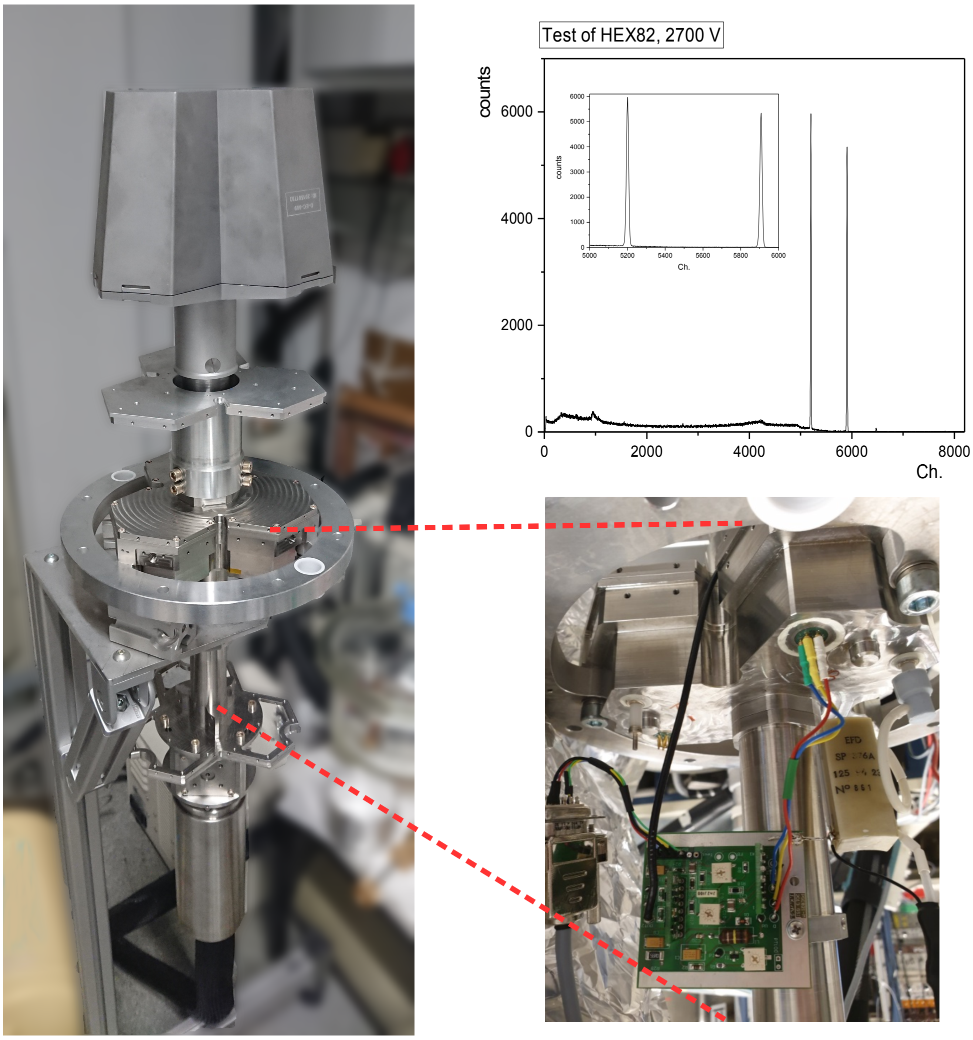

Figure 4.16: Impressions of the assembly of the full scale prototype of the first triple crystal detector of PANGEA. The picture on the left shows the exterior view on the detector. On the right, the spectrum of the first measurement of a ^{60}Co source with this prototype is presented. An energy resolution of 2.8 keV could be reached (shaping time 3 µs). This resolution was influenced by the high operational temperature of this prototype which prevented a complete biasing of the crystal. This measurement was performed using a provisional setup with a prototype of the final preamplifier as shown on the bottom right (pictures by courtesy of [188]).

The timeline of the developments for the hyperatom setup is shown in figure 4.17. Besides the target system, this includes the development of the individual cluster detectors of PANGEA as well as the construction of the full detector array. Since the experience with the X-Cooler II is much higher, first detectors will be using this cooler or even liquid nitrogen cooling. After the R&D on the Sunpower coolers is finished, the existing detectors will be modified to be usable with these more powerful coolers. First experiments with a small number of detectors are scheduled for 2021 at the fragment separator (FRS) at GSI. The experiments with DEGAS will start in 2022. This will not interfere with $\overline{\text{P}}$ANDA since only a single detector is planned for the commissioning starting in 2024 and the full setup will not be required before 2027/2028 when the hyperatom and hypernuclear experiments are scheduled for phase 2 of $\overline{\text{P}}$ANDA.

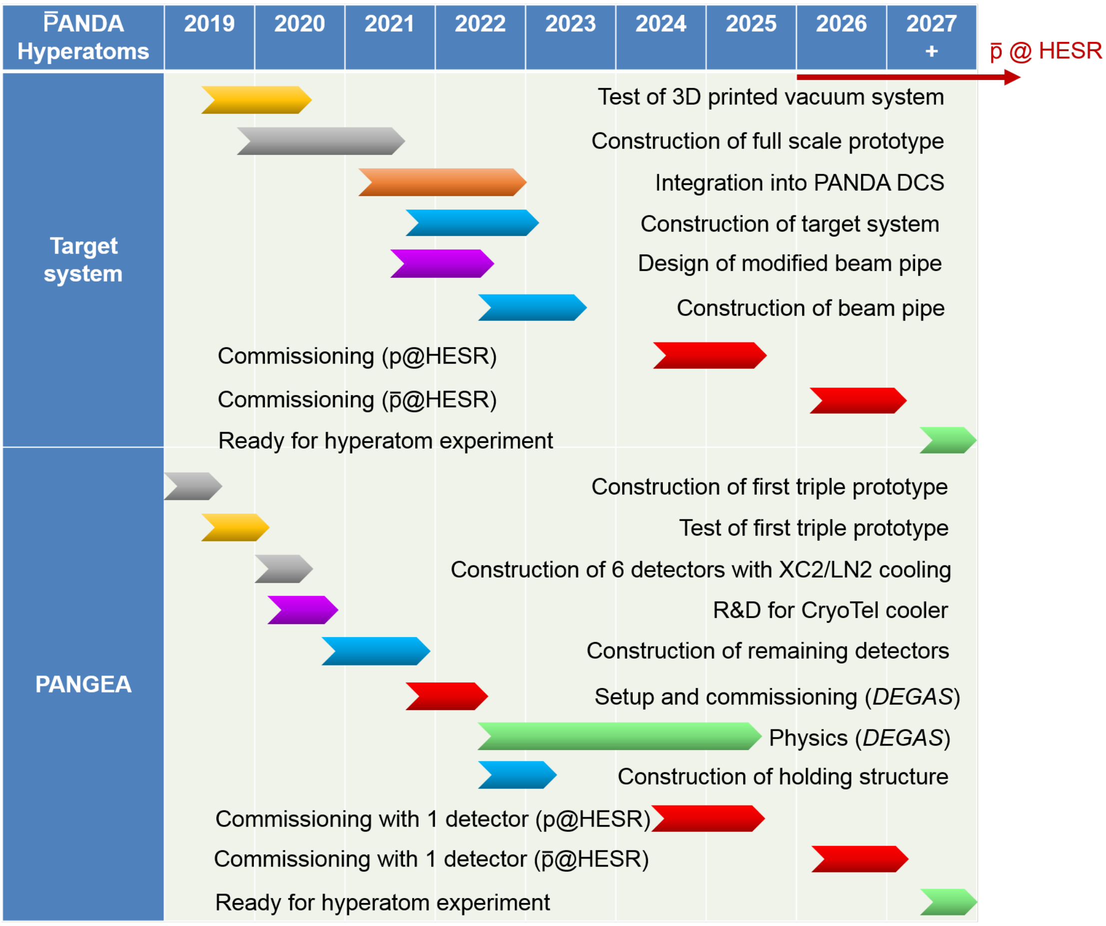

Figure 4.17: Detailed timeline for the production and commissioning of PANGEA and the target system required for the hyperatom experiment. The germanium detectors used for PANGEA are shared with DEGAS and hence need to be ready early. The hyperatom experiment is scheduled for 2027/2028. The commissioning of the hyperatom setup with the target system and a single cluster detector will be performed with protons and finalized with antiprotons once they are available in the HESR.

4.3 Optimization of the layout of PANGEA

As explained in the previous sections, PANGEA has to operate in a very limited space and is looking for rarely occurring events. Therefore, it is essential to optimize the detector arrangement which means maximizing the full-energy-peak efficiency of photons in the range of $100\,\mathrm{keV}$ to $10\,\mathrm{MeV}$. At the same time the neutron background, deteriorating the crystals, must be taken into account. The following subsections cover this simulation-based optimization process.

4.3.1 Development of the geometry

Two tools were primarily used for the development of the geometry: Autodesk Inventor as CAD tool and PandaRoot[c] [201].

CAD was used to design possible detector arrangements. The 3D models of an individual cluster were used as a starting point. These have been designed by I. K. from GSI, Darmstadt. Autodesk Inventor allowed to arrange multiple of these clusters inside the available space (see section 4.1).

PandaRoot is the simulation framework developed and used by the $\overline{\mathrm{P}}$ANDA collaboration for all detector and physics studies concerning the $\overline{\mathrm{P}}$ANDA experiment. It is based on the ROOT framework from CERN [202] and offers the possibility to use various transport models for simulations by the implementation of the virtual Monte Carlo interface [203]. The studies in this thesis were using the Geant4 transport model [204]. The detector geometries in PandaRoot are based on the ROOT geometry classes [205]. Details on this are given in section 4.3.1.3.

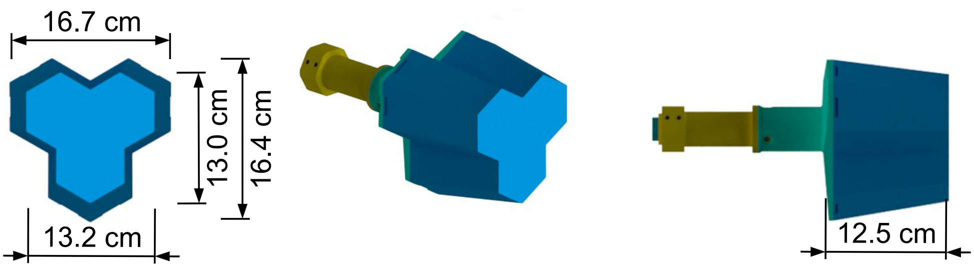

Figure 4.18: Three perspectives of the detector head. It is designed to allow a dense package of detectors, therefore reflecting the shape of the inner components, mainly the triangular arranged crystals. The dimensions given are the limiting constraint for the arrangement of the detectors.

4.3.1.1 Design of the detector head

As previously explained in section 4.2.1, the footprint of a cluster detector is determined by the size of the detector head. Therefore, its dimensions are the main constraints that have to be taken into account when combining individual detectors to a full array. Here one has to distinguish between two different approaches. The first one uses the tapered design of the detector head and arranges them spherically around the central interaction point. In this case, the front side of the detector head points towards the interaction point. The second approach ignores the tilting towards the interaction point. All detectors are facing the same direction parallel to the beam axis.

---

[c] SVN version 28266 used as base for modifications and additions. Code attached on CD

While this detector setup can be achieved with the straight detector design, the tilted one requires the flexible neck. Depending on the detector orientation either the dimensions at the front (tilted) or at the back (straight) determine the space requirements. In addition, the length of the detector head must be considered in the tilted setup. Figure 4.18 shows the design of the detector head and its main dimensions which are fixed by the size of the encapsulated crystals.

4.3.1.2 Geometries of the full detector array

As explained in section 4.1 the space for the individual detectors is highly limited by the surrounding STT detector and its supply frame on the outside as well as the beam pipe on the inside. This leads to a possible polar angle range of approximately $90°$ to $160°$, relative to the shifted interaction point at z = $-55\,\mathrm{cm}$. While this excludes some arrangement options, like a full box-like geometry, there are still multiple options thinkable to combine multiple clusters.

The first option is a fully spherical geometry. In this geometry the front faces of all detector heads are pointing towards the primary interaction point and their distance to it is constant for every position. This also means that the solid angle of each crystal is constant. The negative side of this geometry is, that only a relatively small radius of the sphere is possible which limits the solid angle in which the cluster can be positioned and for this reason the number of detectors. In addition, the tilting of the detectors increases their radial space requirement which at the same time increases the required tilting angle of the intermediate flexible connection bellows. Finally the background of neutrons is boosted forward and therefore their rates depend on the polar angle of the detector (see figure 5.6). This leads to a strong non-uniformity of the neutron irradiation of the detectors. Crystals at lower polar angles will suffer from higher neutron fluxes and consequently radiation damage. Based on this knowledge, the positioning should be adjusted to achieve a more constant irradiation profile. Nevertheless, this kind of geometry was studied beforehand in [206].

A more promising approach was to increase the radius of the sphere and then shift the full array in downstream direction. This led to an angular dependence of the distance from detector to the interaction point. The distance increased for smaller polar angles Θ and could be easily calculated by using the law of cosine. Looking at the sketch in figure 4.19 the law of cosine could be written as

$$R^2 = r(\Theta)^2 + O^2 - 2\,r(\Theta)\,O\,\cos\Theta$$

with the radius of the sphere R and the Offset O. This could be solved for $r(\Theta)$ and yields

$$r(\Theta) = O\,\cos\Theta + \sqrt{R^2 - O^2\sin^2\Theta}. \tag{4.2}$$

For backward angles, this led to a minimal distance of $r(180°) = R - O$ and a maximal distance of $r(90°) = \sqrt{R^2 - O^2}$. For the arrangement of the cluster detectors a radius of $R = 40\,\mathrm{cm}$ and an offset of $O = 20\,\mathrm{cm}$ was chosen. These values allowed to position the clusters in a way that the tilting was small and the neutron rates on the crystals more equalized (see section 5.2). r could be calculated by the magnitude of the detector coordinates (x,y,z) with respect to the shifted interaction point by

$$r(\Theta) = \sqrt{R^2 - 2\sqrt{R^2 - h^2}\,O - O^2} \tag{4.3}$$

with the polar radius $h = \sqrt{x^2 + y^2}$. The z coordinate was calculated by

$$z(h) = \sqrt{R^2 - h^2} - O\,. \tag{4.4}$$

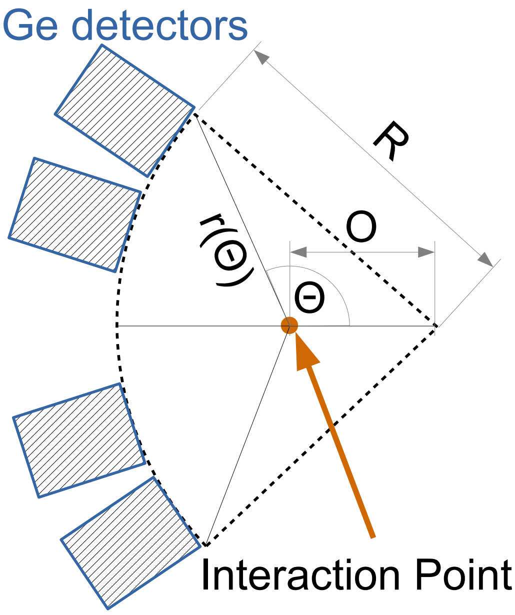

Figure 4.19: In order to even out the neutron dose of each crystal, the clusters are positioned on a sphere with a radius of $R = 40\,\mathrm{cm}$ and the center of the sphere is shifted by $O = 20\,\mathrm{cm}$ downstream with respect to the shifted primary interaction point.

By using this approach it was possible to include 18 clusters into the available space which results in a total of 54 crystals. They were placed in a hexagonal symmetry around the beam pipe which meant that there were only three different detector positions that could be rotated in steps of 60° around the beam axis. This decreased the complexity of the whole system. The minimal distance between two clusters was approximately $6\,\mathrm{mm}$ which was required for the assembly of the array. Detectors in this geometry need the flexible neck and therefore a fixation of the detector head as well as the electronics stage. Positions and tilting angles of this geometry are gathered in table A.2 in the appendix.

The second approach of the cluster placement completely ignored the tilting of the clusters. This means that the detector axis is parallel to the beam axis and incoming photons from the target have to pass the side faces of the cryostat. This should not influence the efficiency since the front and side faces do not differ in their material budget. The advantage of this kind of detector placement is that no flexibility in the intermediate connection is required and therefore the original design planned for DEGAS is applicable.

The easiest way to create such a geometry was to start with a flat, wall-like, detector arrangement. This allows to place the clusters in a very compact and structured way. Only two different orientations of the detector were needed for such a close-packed arrangement. The second one was just a rotation by 180° around the cold finger axis as visible in the frontal view in the right of figure 4.22. Due to the straight orientation the footprint of a cluster increased because the bigger length and width at the back of the detector head had to be taken into account. Nevertheless, the absence of tilting saved a lot of space and thus 20 detectors could be placed inside the available space. The gap between two detectors was at least $4\,\mathrm{mm}$. This allowed to include a holding

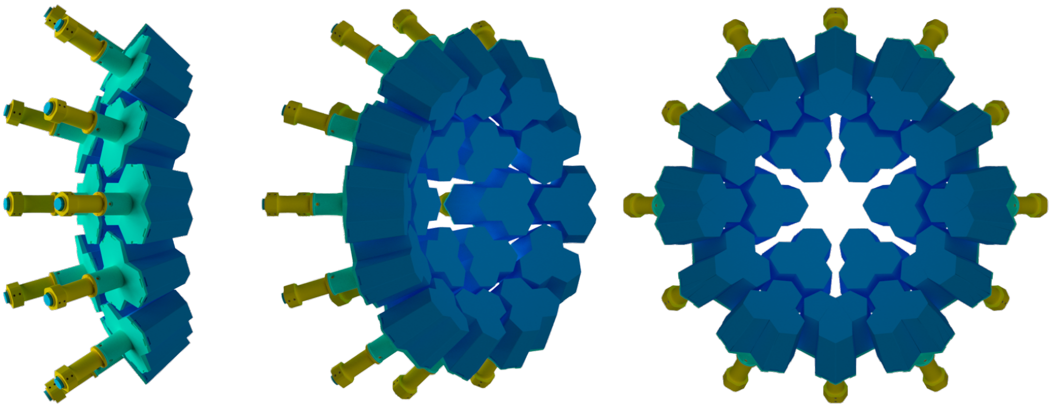

Figure 4.20: Three perspectives of the spherical detector layout. 18 clusters can be placed on the sphere with a radius of $R = 40\,\mathrm{cm}$ radius. The clusters are placed in hexagonal symmetry with three detector positions repeating every $60°$.

structure as it will be shown in section 4.4.1. The presence of the beam pipe was taken into account by leaving out the central cluster which was already considered in the amount of placeable detectors. In addition to that, small global vertical shifts of the upper (lower) 8 detectors by $5\,\mathrm{mm}$ up (down) were required to offer sufficient space for the beam pipe including the safety margin.

This flat arrangement could be modified to a sphere-like structure of the clusters by moving individual detectors along the beam axis (z axis). The idea was to place the central point of the front side of the detector head on the same coordinate that would correspond to the spherical geometry. This is sketched in figure 4.21 and the detector coordinates and the associated rotation angles can be found in table A.3. Figure 4.22 shows this geometry built in Autodesk Inventor. The horizontal symmetry of the arrangement was increased by a small horizontal shift of the full array. Due to this shift two detectors at horizontally mirrored positions share the same distance to the beam axis. This increased symmetry reduces the amount of z positions of the detectors.

The sphere-like geometry required seven different z positions which might complicate the mechanical integration into $\overline{\mathrm{P}}$ANDA. Therefore, two simplified geometries were designed. The first one only used two different z positions by combining the detectors into two rings. Both rings are marked in figure 4.23. The z coordinate of these rings was calculated by the average of the distance to the beam axis h of all detectors within the ring as input of equation 4.4. This resulted in a z coordinate of $-5.81\,\mathrm{cm}$ for the outer ring and $-16.10\,\mathrm{cm}$ for the inner one, both relative to the shifted primary interaction point. The x and y coordinates remained unchanged compared to the previous geometry (compare table A.4 in the appendix).

The second simplified geometry used columns instead of rings. The triple detectors could be organized in five columns. Due to their mirror geometry, three different z positions were required which were again calculated from the average of their distance from the beam axis h and are visualized in the right side of figure 4.23. The z coordinates of these columns are $z = -4.03\,\mathrm{cm}$, $z = -12.53\,\mathrm{cm}$ and $z = -14.64\,\mathrm{cm}$ from the outer to the central column. A full list of the coordinate for this detector configuration is given in table A.5.

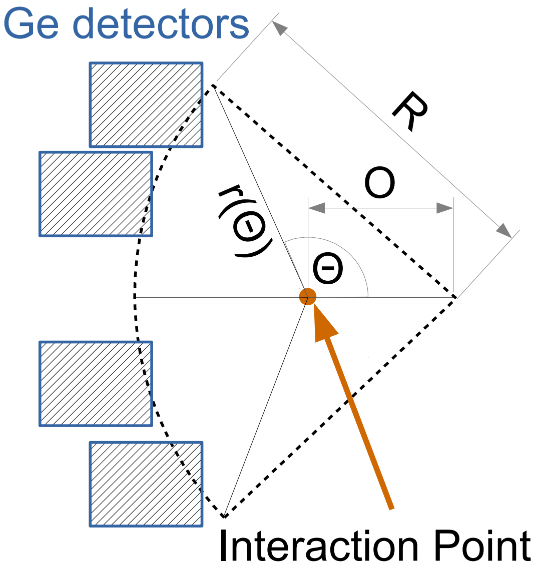

Figure 4.21: In the sphere-like version of the straight geometry, the front side of a cluster is pointing downstream. The spherical positioning of the detectors is mimicked by shifting the clusters forward until the center of the frontal face reaches the same coordinate as in the corresponding tilted geometry. This optimizes the solid angle coverage of the array.

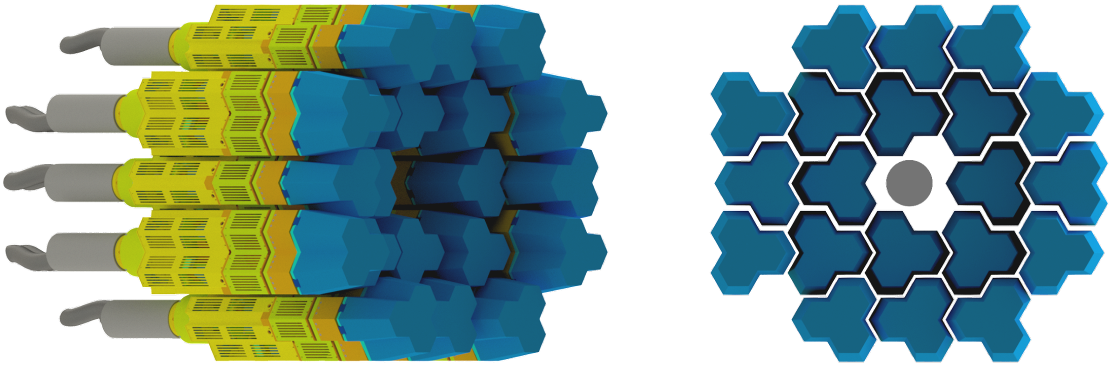

Figure 4.22: Isometric and frontal view of the sphere-like arrangement of the detectors. 20 clusters can be put into the available space by designing a closely packed wall as shown in the right view. The beam pipe is situated in the center of this arrangement. A sketch of it with a diameter of 9 cm is added to the frontal view and shows the available safety margins. The clusters are then arranged spherically as visualized in figure 4.21 mimicking the spherical arrangements presented in figure 4.20.

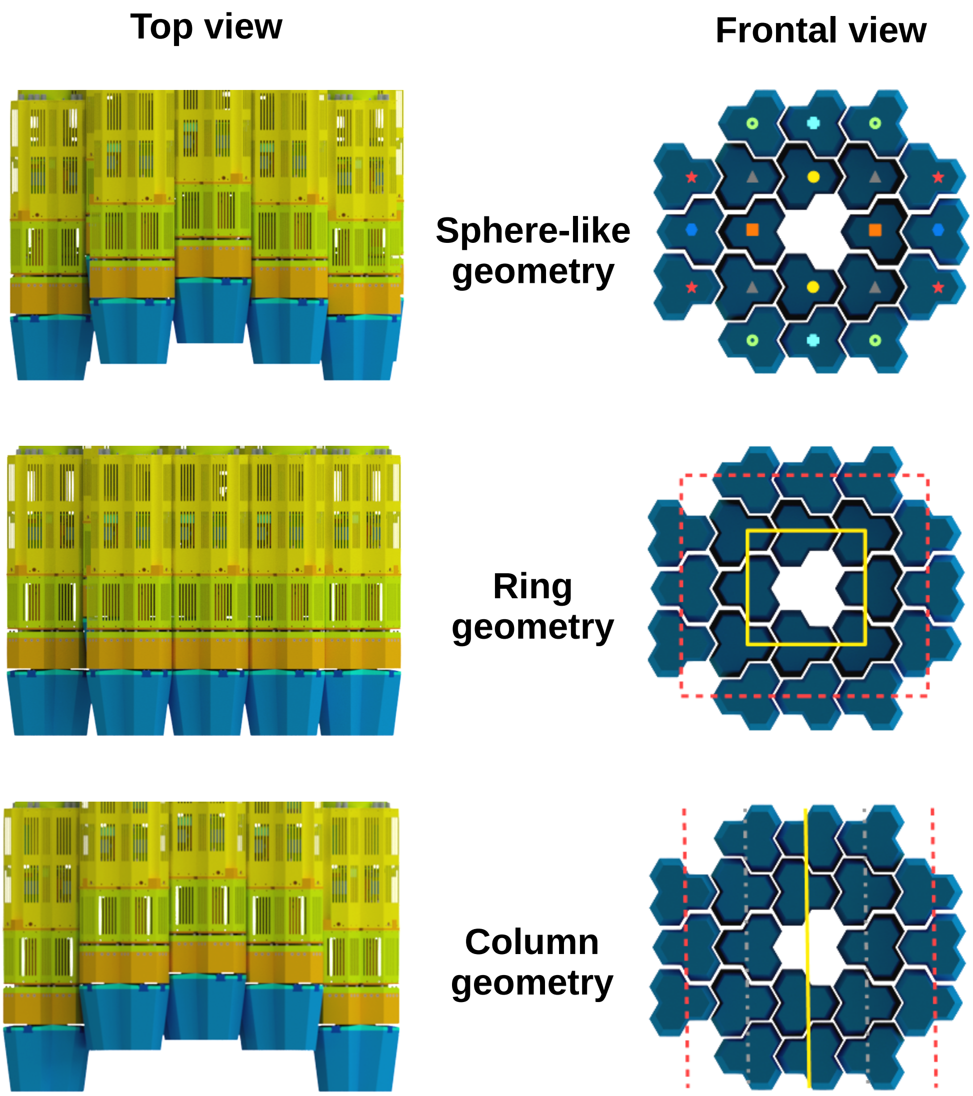

Figure 4.23: The three arrangements of the PANGEA detector with straight detector geometry are shown in this picture. Starting from the top, the sphere-like, ring and column geometry are shown. The left side of each is the top view were the z position of the topmost detector is visible. On the right, the frontal views of each geometry are presented. They give further insight in the detector positioning. The z coordinate of a detector is visualized by the colored markers where same color means same z-position within this geometry. In the ring and column geometry the two rings or the 5 columns, respectively, are visualized.

4.3.1.3 Implementation of the detector array in PandaRoot

The next step required to study the experimental efficiencies was to translate these geometries to a format suitable for PandaRoot. The $\overline{\text{P}}$ANDA MVD group developed a converter [207] for this purpose, but due to the complexity of the crystal and cryostat design tests of this tool for automated conversion were not successful. Because of that, the geometry had to be recreated manually. The tools for this are the geometry classes provided by ROOT (TGeo*). They allow to create and combine various geometrical shapes to create the desired volumes.

Compared to previous work in [206] the implementation of this geometry creation process has been completely revised. The hard-coded ROOT script was changed to an object-oriented structure. This setup is more flexible and easily adaptable to modifications of the detectors and new arrangements. Subclasses for each individual part of the detector have been implemented. The complete cluster detector resides in its own object-class which includes simple interfaces to create and place a detector in a ROOT macro. This interface only requires the coordinates of the center of the front face and the three Euler angles relative to the beam axis (z axis)for its orientation and tilting.

At present, only the detector head, housing the encapsulated germanium crystals, has been implemented. Other parts of the cluster detector were less important for this study and were left out due to their complexity and possible changes during further development. Details on the construction and composition of a cluster detector are given in appendix A.1. Figure 4.24 shows exemplary the implemented versions of the spherical geometry as well as the column geometry an example of a straight geometry.

In addition to the geometry of PANGEA a simplified version of the target system had to be added to the simulation. This assures proper absorption of particles in the material in front of the germanium detectors. Figure 4.25 shows an example of a complete geometry as it was used in the various simulations described in the following.

4.3.2 Efficiency simulation studies of various possible PANGEA geometries

The performance of the various presented geometries with respect to the full-energy-peak efficiency had to be compared in simulations. The PndBoxGenerator of PandaRoot allowed to simulate specific particles with a defined energy in a given angular range. GEANT4 was used in these simulations as transport model to simulate the physical processes.

The efficiencies for the hyperatom and the hypernuclear experiment had to be studied individually because both experiments differ in their secondary target (compare figure 2.15) and their energy range:

- In these studies the absorbers of the secondary targets acted as starting points for the simulated photons. These vertices were generated in stopping simulations of primary Ξ^- (see section 6.2). Figure 4.26 shows these vertices for the case of the hypernuclear experiment in a view along and perpendicular to the beam axis. The starting points for the hyperatom experiment can be found in figure 6.10. More details on this can be found in chapter 6.

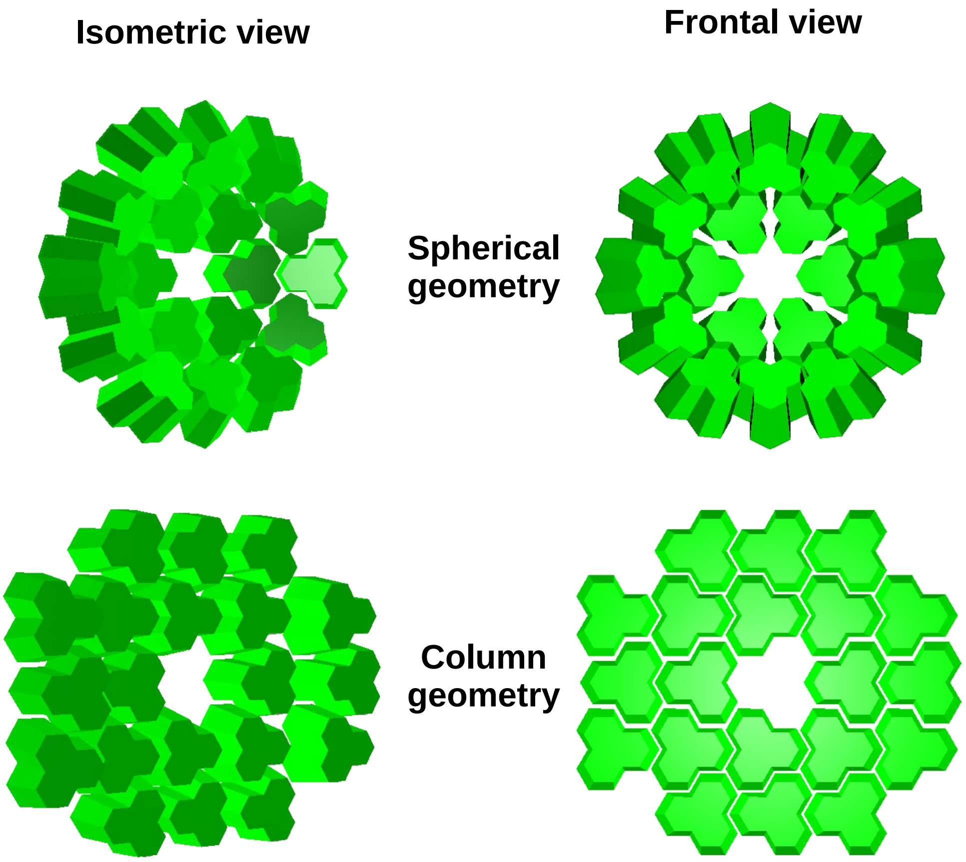

Figure 4.24: Two possible geometries of the PANGEA detector in its ROOT geometry based version used for simulations. The spherical one with tilted detectors is shown at the top of the figure and the straight one using columns for detector placement at the bottom. An isometric (left) and a frontal view (right) of both geometries is presented.

- As previously mentioned, the energy range of both experiments differ which had to be considered in the simulations. For the X-ray spectroscopy of hyperatoms an energy range of 0.1 to $1\,\mathrm{MeV}$ was sufficient. The γ emitted by excited hypernuclei however required to study a larger energy range of up to $10\,\mathrm{MeV}$.

While these photons in the experiments will be emitted isotropically in 4π, the polar angle of all crystals of PANGEA exceeds $90°$. Therefore, it was reasonable to limit the polar angle of created photons to the range of $90°$ to $180°$. This virtually doubled the amount of statistics generated or could also be understood as a halving of the required computing time compared to a distribution in 4π. For each configuration of detector geometry and photon energy 10^7 events were simulated. 38 energies from 0.05 to $10\,\mathrm{MeV}$ were used to scan the predicted energy range.

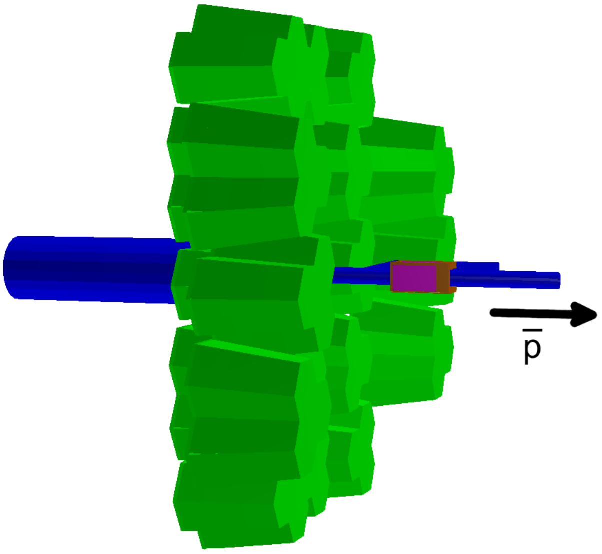

Figure 4.25: Example of the full geometry used for simulations. A mockup of the target system as well as a simplified beam pipe design was added in order to simulate a realistic absorption of particles.

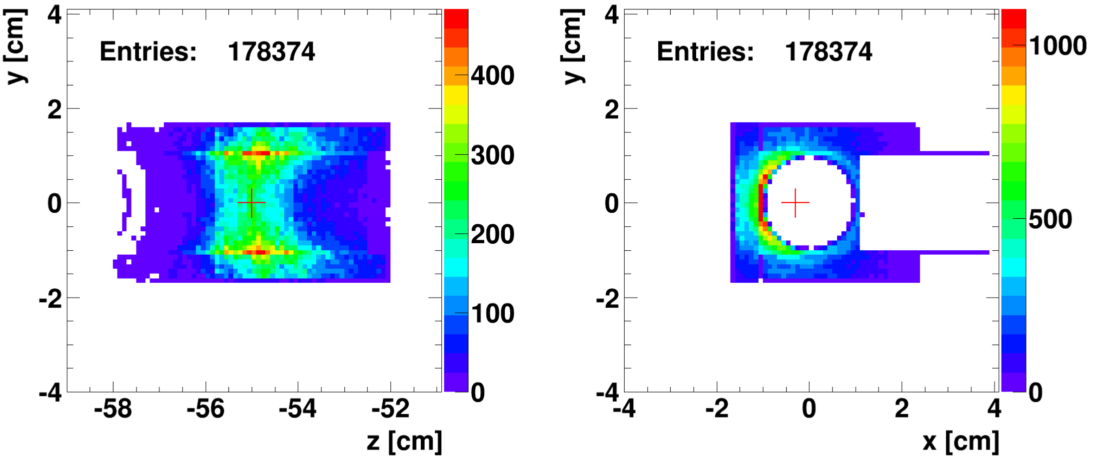

Figure 4.26: Starting vertices of the generated photons for the studies of the full-energy-peak efficiency. These vertices reside inside the absorber of the secondary target. The binning is too coarse to resolve the layer structure of the secondary target of the hypernuclear experiment. The left picture shows the view perpendicular to the beam axis. The right one is along this axis. Approximately $5 \cdot 10^7$ Ξ^- were used as input for this simulation.

In the event-wise analysis of these simulations the energy deposit in each germanium crystal was saved. At first, all hits in an individual crystal were added up and then smeared using a Gaussian distribution to simulate the energy resolution of the detector. The width of this smearing was energy dependent and follows the equation

$$\sigma_{\text{gauss}}(E) = \sqrt{1.408\,72 \cdot 10^{-7}\,\text{MeV}^2 + E \cdot 4.161\,93 \cdot 10^{-7}\,\text{MeV}}, \tag{4.5}$$

which is based on experimental data of measurements of ^{152}Eu (see figure A.2).
Especially for high photon energies, Compton scattering and pair production increase the number of crystals involved in the complete detection of the primary photon and its daughter particles. Therefore, adding up multiple crystals was favorable. Several option were implemented and studied:

- **full add-back** sums up the energy measured in all crystals.
- **next neighbor add-back** adds up the energy of the primary crystal and all next neighbors.
- **cluster add-back** adds up only the three crystals of a triple cluster detector.
- **no add-back** treats every crystal individually.

The efficiency drops from the first to the last option. The robustness against particle background rises at the same time. In $\overline{\text{P}}$ANDA this has to be taken into account because of the particle background (see section 6.3). As starting point, the cluster add-back algorithm seemed naturally and was used as a basis for comparisons. Figure 4.27 shows an exemplary spectrum of generated $1.332\,\text{MeV}$ γ on its left side. Besides the full-energy-peak at $1.332\,\text{MeV}$, the Compton edge as well as the single and double escape peaks can be identified. A zoom on the same full-energy-peak is shown on the right side to visualize the Gaussian smeared signal, mimicking a real detector response.

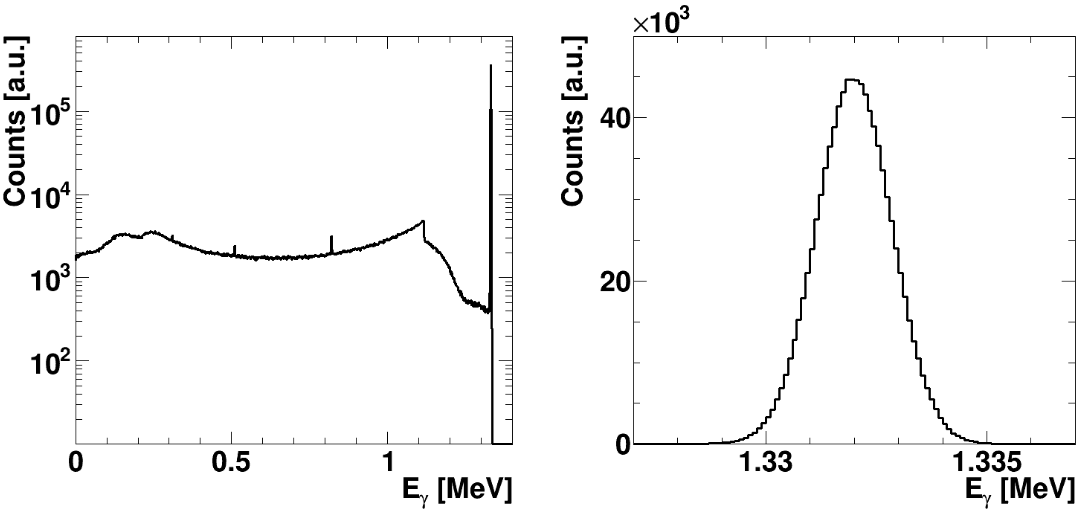

Figure 4.27: Exemplary γ spectrum for the efficiency studies. The full spectrum of γ with an energy of $1.332\,\text{MeV}$ is shown on the left. In the logarithmic plot, the Compton edge as well as the single and double escape peak are visible besides the full energy peak. The right plot is a zoom on this peak. Its energy is smeared by a Gaussian distribution in the simulation to mimic the resolution of the detector.

This full-energy-peak was fitted by using a normalized Gaussian distribution plus a simple linear function as background

$$f(x) = \frac{A}{\sqrt{2\,\pi}\,\sigma} \cdot e^{-\frac{1}{2}\left(\frac{x-x_0}{\sigma}\right)^2} + a \cdot x + b \tag{4.6}$$

where A, x_0, σ, a and b were the fit parameters. For the automation of this fitting routine a robust fit was needed. This required a robust way to get proper starting values for the fit parameters of the Gaussian and background. This could be achieved by fitting an isolated normalized Gaussian first and use its parameters as input for the real fit using equation 4.6.
When corrected by the bin width, the amplitude A gives the number of counts in the peak. Scaling this by the total number of simulated events and a factor of two to compensate for the reduced angular range of the simulated photons directly yields the full-energy-peak efficiency f

$$f = \frac{A}{n_{\text{sim}} \cdot 2} \tag{4.7}$$

In the systematic studies with the hypernuclear target, the peak of this efficiency was situated around $100\,\text{keV}$, independent of the geometry of PANGEA or the add-back method used. The drop at lower energies can be explained by higher absorption. For higher energies the interaction probability inevitably decreases which lowers the detection efficiency. Additionally, the probability for Compton scattering and pair production increases. Both create secondary particles that might leave the crystal and thus do not contribute to the full-energy-peak. This effect could be reduced when more crystals were added up in the simulation as shown in figure 4.28. The figure shows a comparison of all four add-back methods for the column detector geometry. As expected the full add-back showed the highest efficiency followed by the next neighbor algorithm and the cluster add-back. Without any add-back the efficiency severely dropped especially for higher energies. Taking into account the background expected during the experiment (see section 6.3) it is highly doubtful to get proper results with the full add-back method because of high rates of

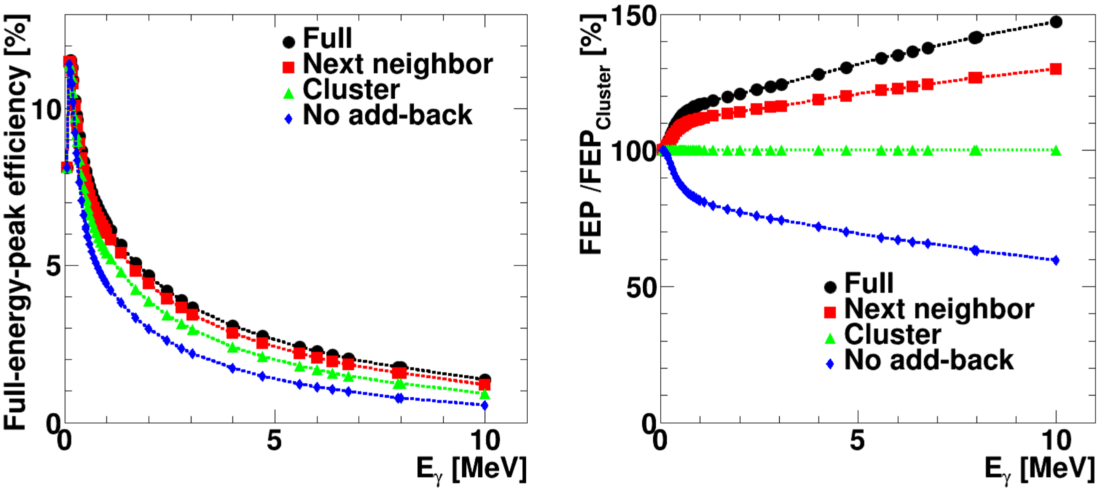

Figure 4.28: Comparison of the four add-back methods for the column geometry. Independent of the add-back algorithm, the efficiency peaks around $100\,\text{keV}$ with up to $11.5\,\%$, dropping down to a minimum of $0.5\,\%$ for $10\,\text{MeV}$ and no add-back. For better direct comparison of the add-back methods, the right plot is normalized to the results of the cluster add-back. For low energies the differences between the methods are small but increase with the γ energy due to a higher number of secondary particles created by the primary photon which can be detected in surrounding crystals when used to add back.

accidental coincidental events. The cluster add-back seems more promising since the number of crystals used in an event is much lower with a maximum of 3 crystals compared to the total 60 crystals, while only dropping in efficiency by a few percent (see right part of figure 4.28). The efficiency of the next neighbor add-back and the single crystal one were in line with the number of crystals involved in the algorithm.

Since the background is not expected to be negligible in the experiment, the cluster add-back algorithm has been chosen for the comparison of the performance of the four previously presented geometries. Figure 4.29 shows the results of Monte Carlo simulations for each geometry and both experiments. Each individual data point is based on the result of 10^7 photons of the specific energy. The error bars are smaller than the size of the markers in the plots.

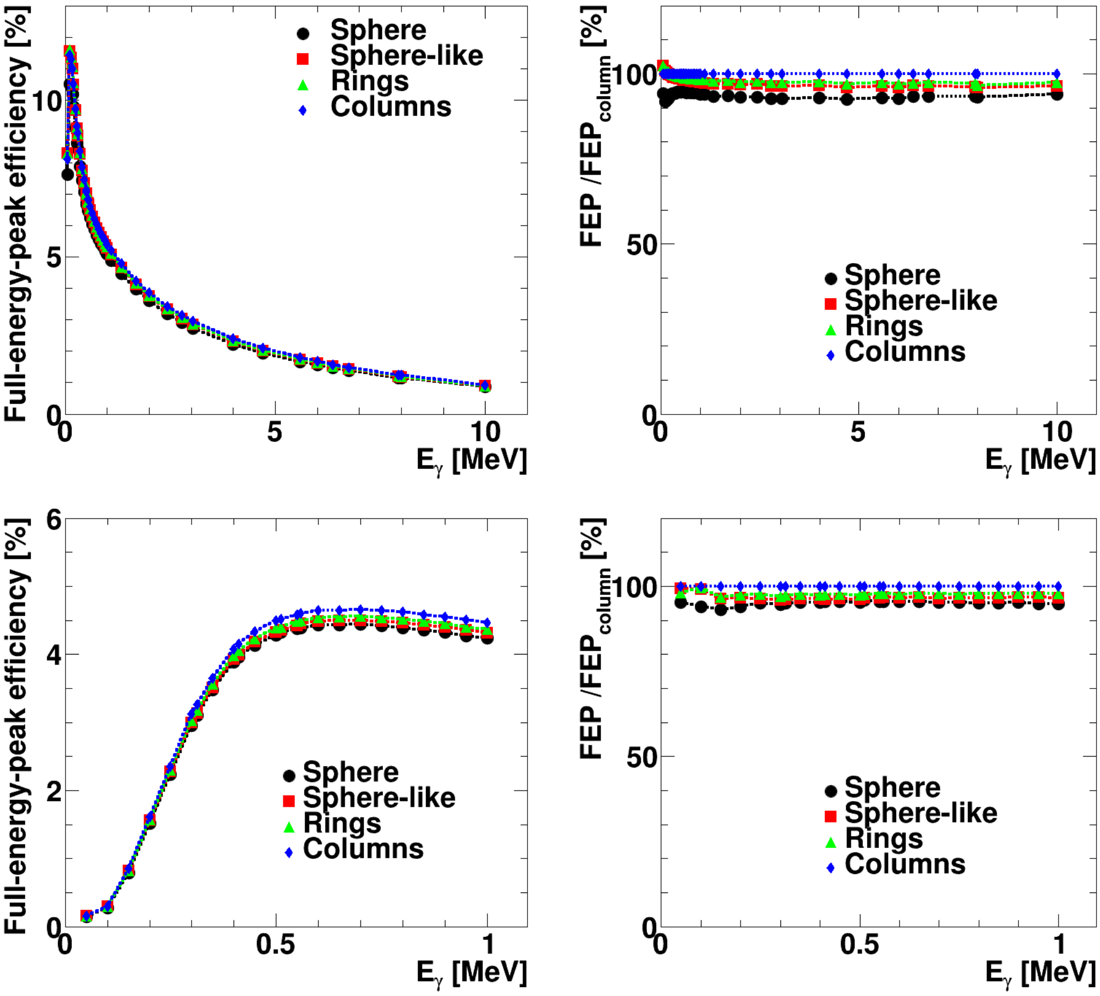

Figure 4.29: Comparison of the results of the full-energy-peak efficiency studies for all geometries using cluster add-back. The results of both experiments favor the column geometry. Compared to the hypernuclear experiment in the top pictures, the maximum of the full-energy-peak efficiency of the hyperatomic one at the bottom is less than half. This is caused by the heavy lead absorber of the hyperatom experiment and its increased γ absorption compared to boron.

The data shows that the spherical geometry has the worst efficiency of all the four geometries and therefore the tilting of the crystals is irrelevant or at least can be more than compensated by the increased amount of detectors. This shows that the dedicated design of the cryostat with the flexible neck will not be required to improve the performance. The three other geometries, all based on the DEGAS design, offer a similar performance within a few percent of each other. The column based geometry offers the best performance for energies above 250 keV. Especially photons above a few MeV will be more efficiently detected with this geometry. Below 250 keV the sphere-like and ring geometry outperform the column geometry only by a small margin. Therefore, the column geometry performs best overall.

When comparing both experimental setups to each other the hyperatomic one shows a reduced efficiency compared to the hypernuclear setup for every data point. The reason for this is that the lead absorber used for the hyperatomic experiments absorbs a bigger fraction of photons compared to the boron absorbers of the hypernuclear one. This is expected due to the higher photon absorption cross section of lead and shows that a proper optimization of the shape of the lead absorber is mandatory for this experiment (see chapter 6).

All possible combinations of add-back methods and detector geometries can be found in appendix A.4 (figures A.3 and A.4).

4.4 Integration into $\overline{\text{P}}$ANDA

For the integration of the PANGEA detector into $\overline{\text{P}}$ANDA two main topics will be addressed in the following. On the one hand, the mechanical integration will be discussed. This includes a time estimate for the procedure of the conversion from the standard $\overline{\text{P}}$ANDA setup to the hypernuclear/hyperatomic one. On the other hand, the integration of the electronics is shown. This is split into the data acquisition and the detector control.

4.4.1 Mechanical integration

Since PANGEA will replace the backward endcap of the EMC, the mechanical integration of PANGEA is similar to this detector. This means that a structure is required that supports the detector from the outside of the $\overline{\text{P}}$ANDA target spectrometer. The placement of this structure on a platform, movable on precision rails, allows to drive the detector array in and out of the target spectrometer when $\overline{\text{P}}$ANDA is in its maintenance position. This is achieved by a system of elongated rails in the so called service area which is designed to allow full access to all inner systems of the $\overline{\text{P}}$ANDA target spectrometer. Figure 4.30 shows a CAD drawing of this. It includes both positions of $\overline{\text{P}}$ANDA. The in-beam position is shown at the top and the maintenance one at the bottom. The service area in the bottom left shows the rail system. The backward endcap EMC as well as the central tracker are shown in their maintenance positions. In this position the modifications required for the hyperatomic and hypernuclear setup will be performed.

4.4.1.1 Support structure of PANGEA

When designing a support structure for PANGEA it is wise to take a closer look at the backward endcap EMC first (top of figure 4.31). A conical support with a length of 1.16 m connects the active detector part of the endcap to its base support outside of the $\overline{\text{P}}$ANDA target spectrometer. The cone must be strong enough to carry a weight of 700 to 800 kg which mostly consists of the

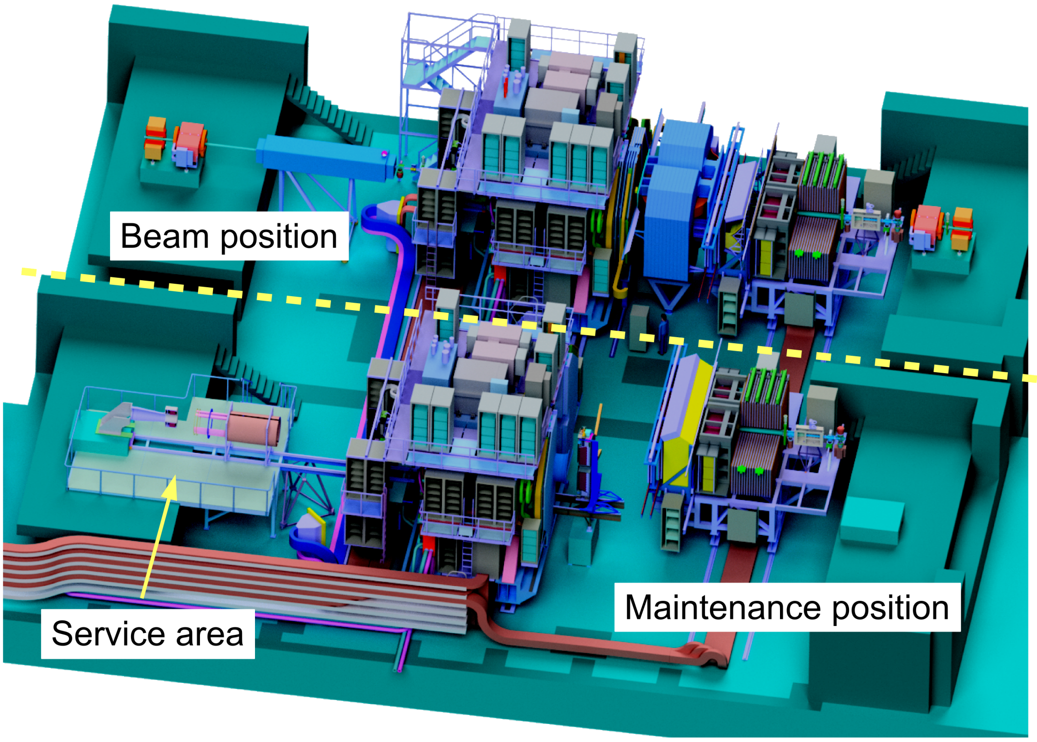

Figure 4.30: Inside the $\overline{\text{P}}$ANDA hall the detector can be placed in two positions. For experiments it is situated in its beam position inside the HESR ring. For longer maintenance or modifications of the detector setup $\overline{\text{P}}$ANDA will be moved into its maintenance position outside of the accelerator area. Here a rail system on the back of the target spectrometer allows to bring the backward endcap EMC as well as the central tracker to their service area. In this area the modifications required for the hyperatomic/hypernuclear setup will be performed [208].

PWO crystals. Because of that, stainless steel is chosen as material for most of the holding frame with some glass fiber elements as insulators to prevent current loops induced by the antiproton beam. Counterweights will be placed outside of the target spectrometer on the base support. The full system is moved via precision rails. Level adjusters are included to compensate for the tilting due to the weight of the detectors.

PANGEA will use a similar concept (see figure 4.31). Especially on the outside of the target spectrometer the holding structure is very similar. The rail system will remain unchanged and a copy of the level adjusters will be used. The base support only needs slight modifications to compensate for the differences between the EMC endcap and PANGEA. The main difference is that the endcap consists of a single big cryostat and PANGEA is composed of 20 closely packed, individual detectors at multiple positions along the beam axis as shown in section 4.3. In addition the length of such a germanium detector requires a modified design of the support inside the target spectrometer. This design consists of a skeleton frame made of aluminum. It is composed

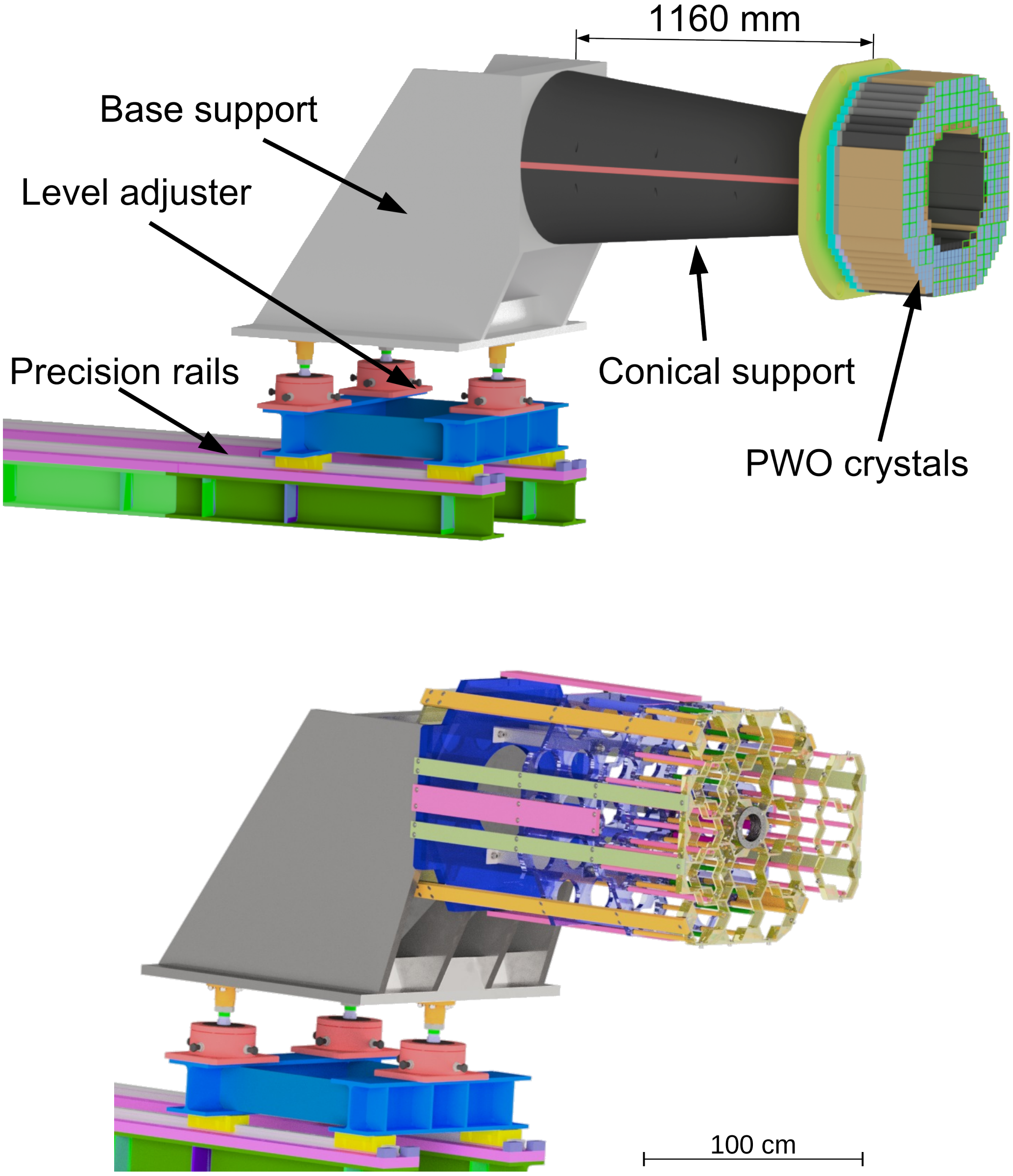

Figure 4.31: The holding structures of the backward EMC (top, picture by courtesy of [209]) and PANGEA (bottom) are designed similarly. Both rely on a base support on the outside of the target spectrometer to hold the detector on its inside. While a conical support connects the base and the detector for the EMC, the length of PANGEA requires a modified design. This consists of an aluminum skeleton frame made of three plates perpendicular to the beam axis and a total of 28 interconnections. The visibility of this frame is increased in the picture by coloring the parts and making them partially transparent. The foremost yellow module frames hold the triple detectors.

of three aluminum plates perpendicular to the beam axis with a thickness of 20 mm and a total of 28 interconnections along the beam axis. These aluminum plates include holes for cabling and cooling lines of the detectors as well as a big central cutout for the beam pipe. Insulation against current loops is included by polyethylene parts. Because of that, the plates are halved vertically.

Mechanical load simulations for this frame have been performed using Autodesk Inventor. These simulations use finite element methods to calculate e.g. the stability of a structure or its displacement caused by gravity or other external forces. The expected weight of 20 detectors is in the range of 400 to 500 kg. The detectors themselves had to be excluded from these simulations because the computing power to include even a simplified version was lacking. Because of that, a load is applied to the frame at the center of mass position of each detector. This simplification is sufficient to study the stability and bending of the frame. Each detector is simulated by a load of 100 kg which exceeds the reality by at least a factor of four and offers a good safety margin. Figure 4.32 shows the results of these simulations. Careful consideration is required for the maximum displacement of 6.3 mm. This local maximum is caused by the lack of detectors whose main frames stiffen the honeycomb structure of the frame. Because of that, a maximum global shift in the range of 4 mm seems more realistic as an estimate for the full system under these exaggerated load conditions. This bending is uncritical. It can be compensated by the level adjusters and is within the designated safety margin of 10 mm around the detector array.

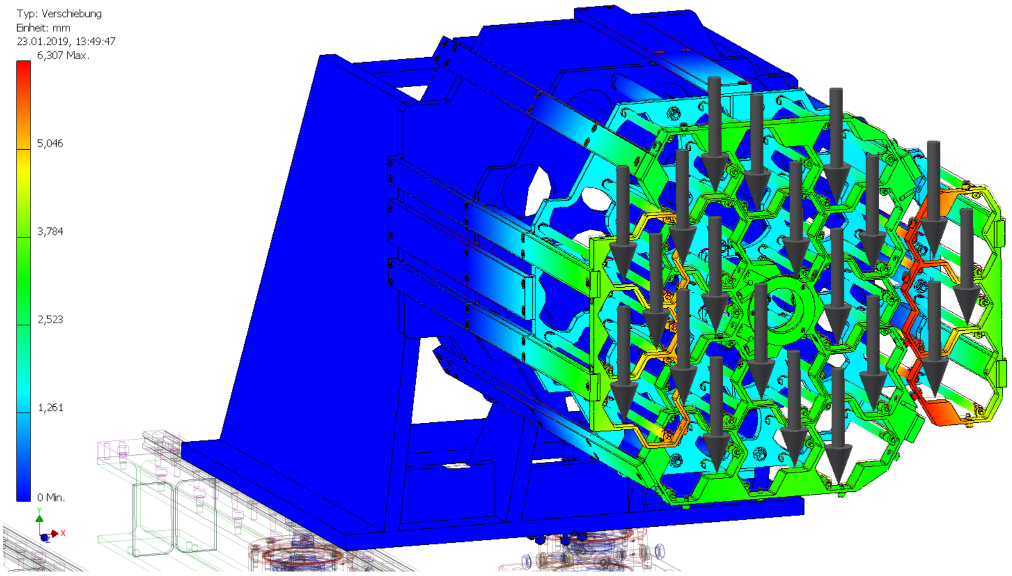

Figure 4.32: Results of finite-element simulations of the holding structure of PANGEA. Computational limitations prevent the direct addition of the 20 cluster detectors. Because of that, a force of 1000 N is applied at the center of mass position of each detector, marked by the arrows. The total force applied is roughly four times the expected weight of PANGEA and thus offers a lot of safety margin compared to reality. The visible maximum displacement of 6.3 mm is distorted by the lack of the detectors. Their central frames stiffen the thin honeycombs and therefore a maximum displacement of 4 mm is more realistic. This displacement can be compensated by the level adjusters and is within the safety margin considered in the design of the detector.

In addition to that it is necessary to study the effect of a fast shutdown of the solenoidal magnet in case of an emergency. The time constant of this shutdown procedure is $18\,\mathrm{s}$. Simulations of this have been performed at GSI by J. L. using the OPERA software[d] for finite element calculations of electronic problems. A slightly simplified version of the detector setup has been used for this. With a magnetic field of $2\,\mathrm{T}$, which is four times higher than planned for the hypernuclear and hyperatom experiment, and an electrical conductibility of $1.7\,\mathrm{MSv/m}$, corresponding to aluminum alloy, the axial force reaches a maximum of $200\,\mathrm{N}$ after $1\,\mathrm{s}$ before slowly dropping down [208]. This force is in a similar magnitude as the dynamic force caused by smaller earthquakes that should be considered. To handle these a static equivalent load of $1.2\,\mathrm{m/s^2}$ [208] can be used which leads to a force of $600\,\mathrm{N}$ considering a weight of the detector of $500\,\mathrm{kg}$. Both of these loads are much smaller than the $5000\,\mathrm{N}$ caused by gravity and are expected to be covered by the safety margins.

The detectors are attached to the frame via screwable rods. Three of these rods with a diameter of $16\,\mathrm{mm}$ are attached to the detector base and the corresponding holes in the frame. For the column geometry rods with a length of $264.2\,\mathrm{mm}$, $285.5\,\mathrm{mm}$ and $371.5\,\mathrm{mm}$ are required to account for the three different positions of the triple clusters. This length includes the threads on both sides of the bar. Figure 4.33 shows an example of this attachment method. In the figure the orange and pink rods are used to hold the clusters in place. They connect the detector base made of stainless steel to the first plate of the holding frame.

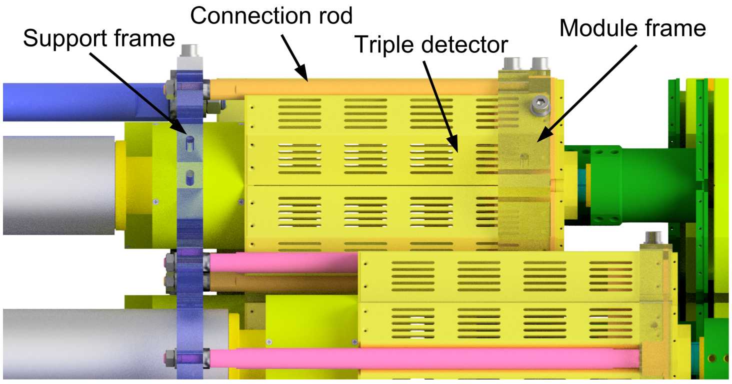

Figure 4.33: Example of the connection of a cluster detector to the frame. This zoomed view shows how the rods are used to attach the detector modules to the first plate of the support frame, shown in transparent blue. The z-position of the detector can be adjusted by rods of different lengths for other positions or configurations.

The clusters themselves are structured in five modules. The base is a central module of six detectors around the beam pipe. Further, four modules consisting of three or four detectors can be attached around the base. Each module consists of an aluminum frame supporting all detectors of the module. This frame is strong enough to lift the full module with a crane. This simplifies the process of setting up the detector array as well as its maintenance because each detector can be

---

[d] `https://operafea.com`

accessed easily. Since the bottom module cannot be accessed by the crane, a lifting tool that can be attached to the rail system needs to be designed in the future. This will fulfill the same task as the crane for the upper and side modules. An exploded view of this modularized setup is shown in figure 4.34.

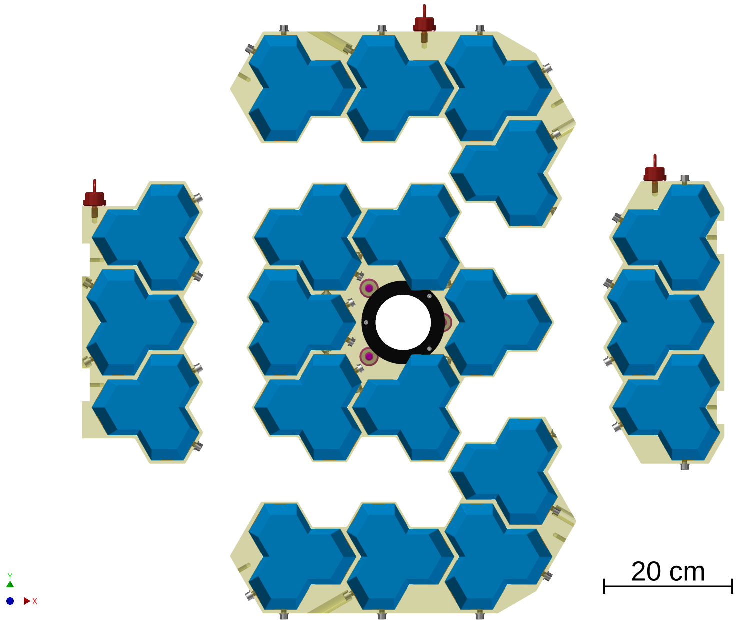

Figure 4.34: Frontal view of the PANGEA detector. An exploded view is shown to visualize the five modules. The outer modules can be added and removed with a crane. The lifting brackets for this are included in this picture but can be removed when not needed. This flexibility increases the maintainability of the detector array by allowing fast access to all individual detectors.

The complete setup of PANGEA is shown in figure 4.35. It includes all the details explained previously.

4.4.1.2 Conversion procedure from standard $\overline{\mathrm{P}}$ANDA to the hypernuclear setup

After the support structure of PANGEA has been established, the next step is to study the conversion procedure to transform $\overline{\mathrm{P}}$ANDA into its hyperatomic/hypernuclear setup. As shown in figure 4.31 $\overline{\mathrm{P}}$ANDA needs to be moved to its maintenance position for the conversion. The predictions for the time required by this process is in the order of one week since a large number of cables and support lines need to be unplugged. In addition, the radiation protection shielding must be opened for the movement. No high activation of long living radioactive materials within the $\overline{\mathrm{P}}$ANDA cave is expected so that no additional delay has to be considered.

The next step, after the target spectrometer has been brought to the parking position, is to drive out the backward EMC and the inner detectors. Both of these feature a dedicated railing system that allows to remove them quickly from the target spectrometer for maintenance. The expectations for this are in the range of a few hours to one day. After this, the backward endcap must be unplugged and dismounted. The required time for this and the proper storage of the detector is in the range of one to two weeks, based on predictions of the EMC group [209].

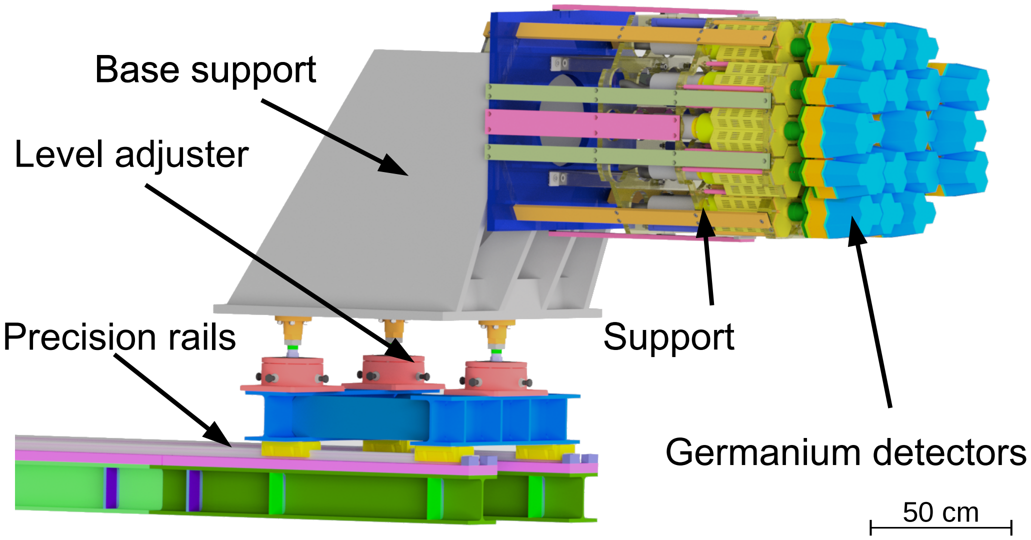

Figure 4.35: Complete PANGEA detector with its support structure. The main features of this structure are inherited from the backward endcap EMC and adapted to the specific needs of PANGEA.

For the central detectors the situation slightly differs. The main difference is that the STT will be used in the hyperatom/hypernuclear setup and because of that not the full system can be dismounted and stored. The STT, the MVD as well as the beam pipe are all attached to a central frame. The STT is constructed in two halves that are attached to this frame. The MVD is situated on the inside surrounding the beam pipe. Figure 4.36 shows an exploded view of this system and shows how the halves of the STT can be dismounted. After that, the remaining system held by the central frame can be carried away and stored. Obviously this requires a new central frame for the hyperatomic/hypernuclear setup but this new frame allows to prepare the target system as well as the new beam pipe off-site and decreases the time required for the modifications. Because of that, the prediction for the detachment of the STT and the removal of the remaining central system is in the range of two to three weeks. Only one week is predicted for the mounting of the hypernuclear central frame and reattaching the STT because the number of connections is much lower compared to the MVD.

After that, PANGEA can be mounted. The modularity of the system, described in the previous section, simplifies this process and thus one week is estimated for it. Another week is scheduled for the reintegration of the modified central system as well as PANGEA into the $\overline{\text{P}}$ANDA target spectrometer. Calibration procedures can also start at this time.

With the modifications of $\overline{\text{P}}$ANDA completed, it can be returned to its beam position. This will need another week until all cabling is restored. For the final pumping and cooling of the magnet two weeks are planned which can also be used for final calibrations of the detector before the experiment begins.

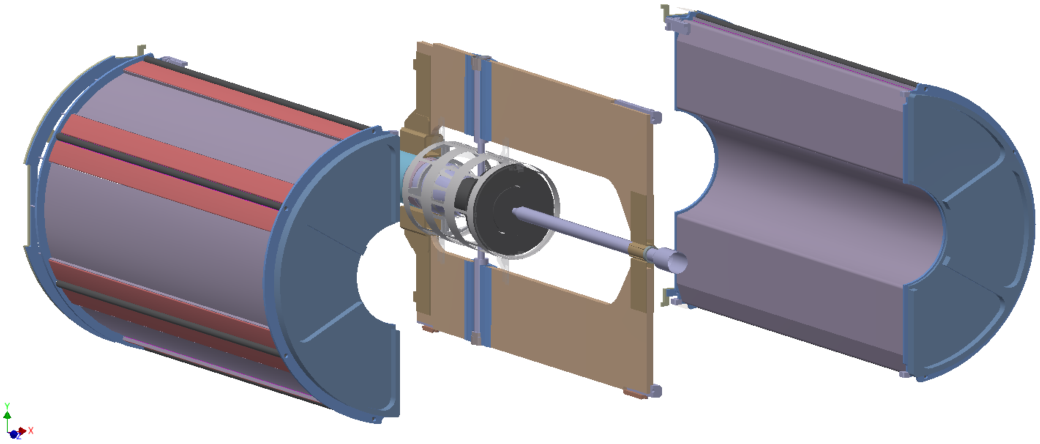

Figure 4.36: Exploded drawing of the central trackers. The two halves of the STT are shifted to the side to open up the view on the central frame that supports the MVD and the beam pipe. The central module must be exchanged for the hypernuclear setup. After that both sides of the STT are reattached.

In total the prediction of the required time is 10 to 12 weeks which fits into the duration of a maintenance break of $\overline{\text{P}}$ANDA which is three months. The parallel work on multiple components could even increase the time buffer if enough man power is available. The individual steps of the modification and the time requirements are summarized in table 4.3.

Process	Time requirement
Move $\overline{\text{P}}$ANDA to maintenance position	1 week
Remove EMC endcap	1-2 weeks
Detach STT and remove MVD and beam pipe (central frame)	2-3 weeks
Install target system and beam pipe (central frame), reattach STT	1 week
Build up PANGEA	1 week
Move and calibrate hyperatomic/hypernuclear setup into target spectrometer	1 week
Move $\overline{\text{P}}$ANDA to beam position	1 week
Cool down magnet, pumping, final calibration and commissioning	2 weeks
Total	10-12 weeks

Table 4.3: Summary of the installation procedure of the hyperatomic/hypernuclear setup. The time predictions are based on estimations of the specific detector subgroups [208, 209, 210].

4.4.2 Electronical integration

4.4.2.1 Data acquisition

The electronics of PANGEA have to fulfill the specifications given by $\overline{\text{P}}$ANDA. For the data acquisition this means that there is no hardware trigger and that it has to be compatible with the time synchronization protocol SODANET (Synchronization Of DAq NETwork) [195]. Both criteria are fulfilled by default when the digitizer system developed for the EMC is used [194]. This system is development for the much larger number of channels in the EMC and because of that a single digitizer with 64 channels would be sufficient for the full PANGEA detector. The FPGA in this digitizer can be configured freely which allows to perform an online energy measurement. This can be used to add-up multiple crystals online (compare section 4.3.2) and use this information for software triggering. When a trigger occurs digitized pulse shapes can be stored for more detailed offline signal processing and analysis.

As in the EMC, a data concentrator [194] is fed by the output of the digitizer before the data is sent to the compute node where the data of PANGEA is combined with the rest of $\overline{\text{P}}$ANDA. All these connections are established via optical fibers. Figure 4.37 sketches this data acquisition chain.

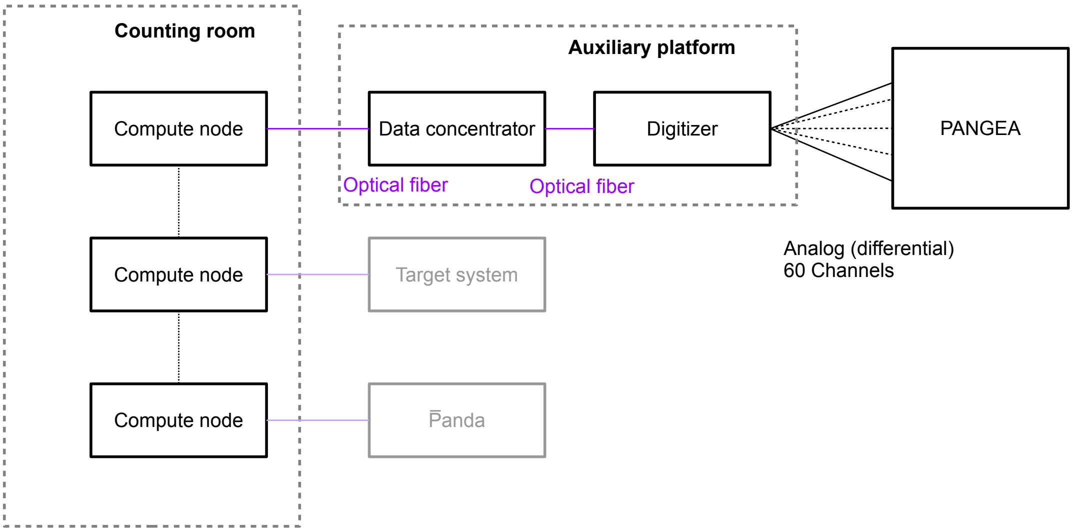

Figure 4.37: Sketch of the data acquisition chain of PANGEA. The digitizer and data compressor are those of the $\overline{\text{P}}$ANDA calorimeter and are situated in racks on the auxiliary platform behind the $\overline{\text{P}}$ANDA target spectrometer. Event building is performed inside the compute node where signals of all detectors are joined.

While the compute nodes will be situated within the counting room, the digitizer and data compressor will be placed on the auxiliary platform (see figure 4.38) directly behind the $\overline{\text{P}}$ANDA target spectrometer. Sufficient rack space is reserved and the removal of the backward EMC allows to use even this previously occupied space. With more than 500 channels the endcap has much more channels than PANGEA and thus requires more rack space.

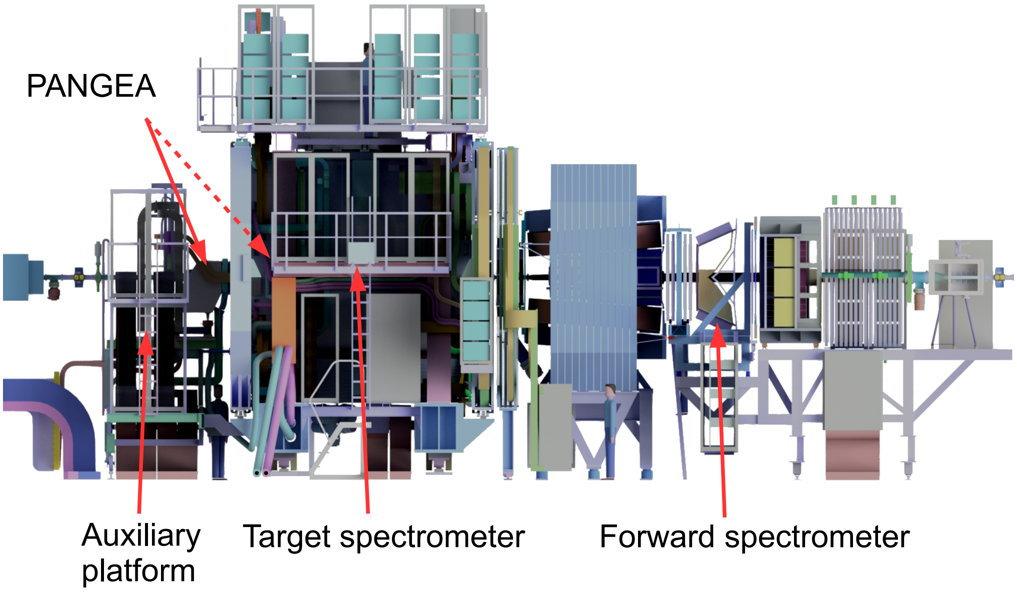

Figure 4.38: The read out modules for PANGEA will be situated inside the racks on the auxiliary platform behind the target spectrometer. Sufficient space is reserved and even more might be available when the backward EMC is not in use.

4.4.2.2 Slow control

For the detector control system (DCS) $\overline{\text{P}}$ANDA uses the EPICS framework. This allows to create a distributed system that is connected via Ethernet and uses the channel access protocol for communication. The $\overline{\text{P}}$ANDA DCS is structured in three layers as shown in figure 4.39. The supervisory layer is the layer that directly interfaces with the human user. Below this layer the system is split into subnetworks for each module. A dedicated gateway for each module connects each subnetwork to the supervisory layer. This structure reduces the global load of the network and allows an autonomously operation of the individual subsystems. The gateway acts as a central hub in the control layer that connects multiple IOCs which are used to gather data from sensors or control hardware components. These sensors and devices form the field layer.

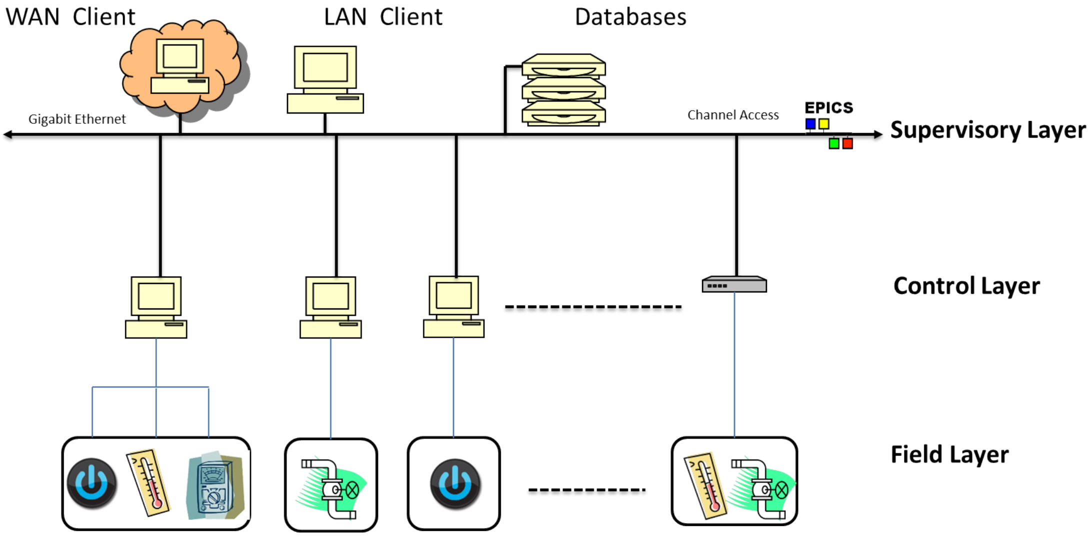

Figure 4.39: The $\overline{\text{P}}$ANDA slow control system can be separated in three layers: the supervisory layer, the control layer and the field layer. The supervisory layer directly interfaces with the human user. The field layer, however, are the various hardware devices that communicate with any kind of electronic interface. The aggregation of these and their translation to Channel Access process variables is performed in a meshed system of Input Output Controllers (IOC) within the control layer. In addition to that, this layer accommodates gateways that connect the IOCs to the supervisory layer. This structure reduces the global load of the network (figure from [211]).

In the case of PANGEA this structure can be easily achieved. Each of the 20 triple detectors includes one of the radiation hard control boards running an EPICS IOC (see section 4.2.2.2) which form the control layer. Each of these systems can be run on its own and includes automatic security measures to protect the detector in the case of a critical temperature rise or other issues. A central hub is connected to each detector via Ethernet or optical fibers and monitors and controls these. This hub, consisting of a computer with multiple Ethernet ports, acts as a gateway to the supervisory layer. This is sketched in figure 4.40.

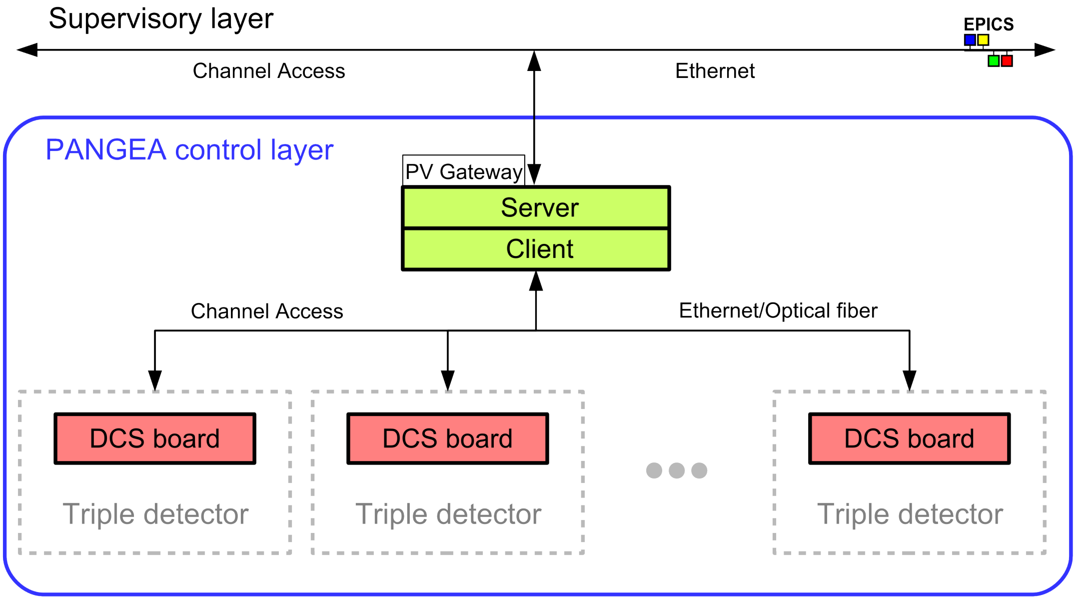

Figure 4.40: Sketch of the PANGEA control layer. The DCS boards (compare section 4.2.2.2) inside each of the 20 triple detectors are running an EPICS IOC and can be connected to a central hub. This computer serves as channel access gateway to the supervisory layer.

4.5 Summary

PANGEA is the high resolution γ detector required for the hyperatomic and hypernuclear experiment of $\overline{\text{P}}$ANDA. It shares the fully integrated and electro-mechanically cooled detectors with the DEGAS detector of the NUSTAR collaboration. A total of 60 HPGe crystals can be used within the $\overline{\text{P}}$ANDA target spectrometer, organized in 20 triple detectors. Their arrangement in a column structure is able to reach a combined full-energy-peak efficiency of $4.8\,\%$ at $1.332\,\text{MeV}$ for the hypernuclear setup when the measured energy of the three crystals within the same triple detector is summed up (cluster add-back). The lead absorber of the hyperatom experiment reduces this efficiency slightly due to stronger absorption within the target.
Due to the modular design of $\overline{\text{P}}$ANDA, the time required for the conversion of the standard $\overline{\text{P}}$ANDA setup to the hyperatom/hypernucleus experiment fits into a scheduled maintenance break of three month. This is achieved by the design of a modular holding frame for PANGEA that is as close as possible to the one of the backward endcap EMC. The integrated design of PANGEA eases its integration into the DAQ and DCS systems of $\overline{\text{P}}$ANDA.

5 Influence of the neutron background in $\overline{\text{P}}$ANDA on PANGEA

As explained in the previous chapters, the high rate of antiproton-carbon reactions in $\overline{\text{P}}$ANDA will produce large amounts of hadronic background. This background deteriorates the signal-to-noise ratio. In addition to that, it will decrease the performance of the High Purity Germanium (HPGe) crystals of PANGEA. Especially fast neutrons must be considered for this as it will be presented in section 5.1. Because of that, the predictions of the neutron load for the crystals during experiments at $\overline{\text{P}}$ANDA are crucial (section 5.2). Since these numbers can not be neglected, irradiation tests of germanium detectors were performed at the COSY facility in Jülich. Details of these tests are presented in section 5.3. The data of these tests was analyzed by a digital pulse shape analysis which allowed a partial recovery of the effects caused by the irradiation.

5.1 Influence of neutrons on HPGe detectors

Any semiconductor used as particle detector requires a crystal lattice with high purity. Any defect can lead to trapping of charge carriers causing incomplete charge collection. Especially the high energy resolution of HPGe detectors suffers from this effect when used extensively in high radiative background environments. Their large size compared to silicon detectors further increases the effect of bulk radiation damage. Since the creation of electron-hole pairs is fully reversible, leaving no damage, only the non-ionizing energy transfer to atoms in the lattice has to be considered. Particularly heavy particles can transfer enough energy to individual atoms to damage the lattice structure. Charged particles are mostly absorbed in the surroundings of the crystal so that fast neutrons are the biggest threat to germanium crystals. Their scattering transfers sufficient kinetic energy to displace individual atoms and leave a vacancy in the lattice. This so called Frenkel (or point) defect creates a trapping site inside the crystal. Further damage can be caused on the track of the primary knock-on atom when sufficient energy has been transferred to it. The interaction with secondary atoms forms big clusters of crystalline damage as visualized in the left part of figure 5.1. Cleland *et al.* [212] estimated that such a trapping site produced by a $1\,\mathrm{MeV}$ neutron can have a net ionization of $Q = -100\,e$. These trapping sites produce deep-lying energy levels close to the Fermi level of the energy gap (compare right part of figure 5.1). These intermediate levels reduce the band gap $E_b(T)$ and increase the leakage currents of the crystal which can be described by

$$I_b \propto T^{\frac{3}{2}} \exp^{-\frac{E_b(T)}{2kT}} . \tag{5.1}$$

In addition to this noise introduced by increased leakage currents, these trapping sites result in a loss of detected charge carriers. Due to the high negative charge of these sites, holes are far more susceptible to trapping than electrons. The capture cross section for holes inside these trapping sites is four orders of magnitude higher compared to the intrinsic absorption cross section of

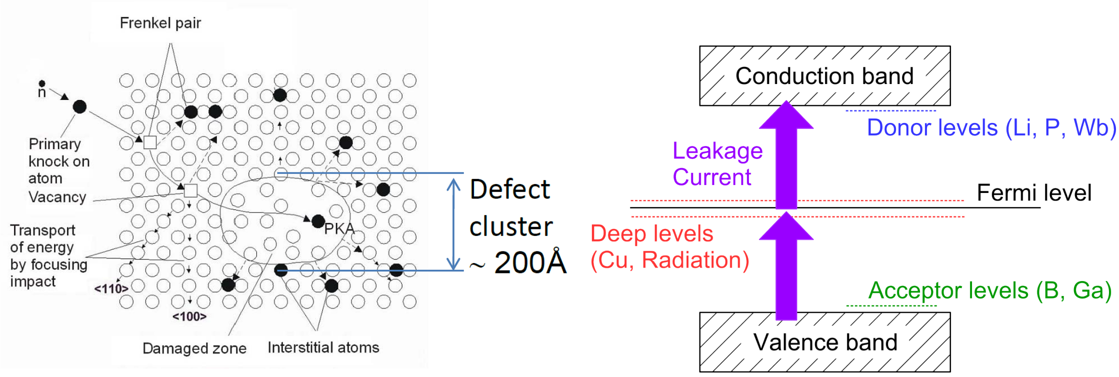

Figure 5.1: The scattering of neutrons inside the atomic lattice of germanium can produce big cluster defects due to secondary scattering of the primary knock-on germanium atom. With a typical size of 200 Å these sites form deep-lying energy levels close to the Fermi level. These deep levels reduce the band gap which increases the leakage current I_b (left figure based on [213]).

high-purity germanium [214]. Because of that, the holding time of trapped holes can exceed the charge collection times of data acquisition systems and consequently the trapped charge is lost in the energy measurement. Electrons are much less affected by these sites [215]. Because of this difference in the charge carrier sensitivity, large differences in the strength of radiation damage can be found for p and n type coaxial germanium detectors with typical diameters of 5 to $8\,\mathrm{cm}$. In a p-type detector the negative high voltage is applied to the central core contact. Because of that, holes are travelling to the center, electrons to the positive outer contact. This configuration, and consequently the direction of the charge carriers, is reversed in a n-type germanium detector (see figure 5.2). The coaxial geometry favors interaction points at large radii and hence the charge carriers travelling to the central contact statistically pass a longer distance within the crystal. Considering the higher trapping chance for holes shows that p-type detectors are more susceptible to radiation damage. In studies of n- and p-type detectors of comparable size and purity, the n-type detector was able to withstand a 28 times higher neutron dose before showing the same peak broadening as the p-type detector [216]. Because of that, only n-type germanium detectors are usable in high radiation environments like $\overline{\text{P}}$ANDA.

In addition to the type of the detector, the measurements of Hull *et al.* [217] revealed a temperature dependence of the performance of irradiated detectors. Especially above $100\,\mathrm{K}$ a degradation was observed that is in line with the temperature dependence of the leakage currents I_b and has been confirmed by H.G. Thomas *et al.* [218]. Figure 5.3 shows the results of their measurements. Compared to the unirradiated detector on the left, the resolution of the same crystal after an irradiation of $2 \cdot 10^9\,\mathrm{n/cm^2}$ (right) is worse in the whole temperature range. When heating up the detector, the higher leakage currents increase the noise above an operation temperature of $95\,\mathrm{K}$. Compared to the unirradiated detector, this performance loss occurs approximately $25\,\mathrm{K}$ earlier. Additionally, the heat up cycle of the detector leads to irreversible degradation of the resolution. This is explained by the clusterization and crystallization of defects enabled by the increased mobility of these at higher temperatures. Additional heat up cycles showed no further degradation.

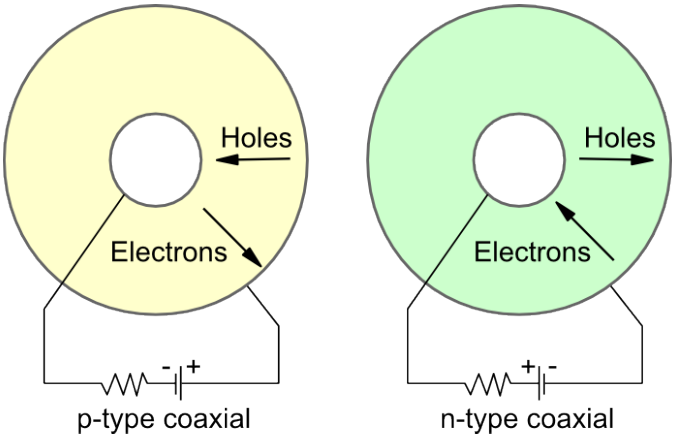

Figure 5.2: In a p-type coaxial germanium detector, the negative high voltage is applied to the core contact. The outer contact is grounded and because of that the produced holes are travelling to the center in contrast to electrons that are drawn to the outer contact. The high voltage application is reversed for n-type germanium detectors and consequently the directions of the charge carriers is inverted.

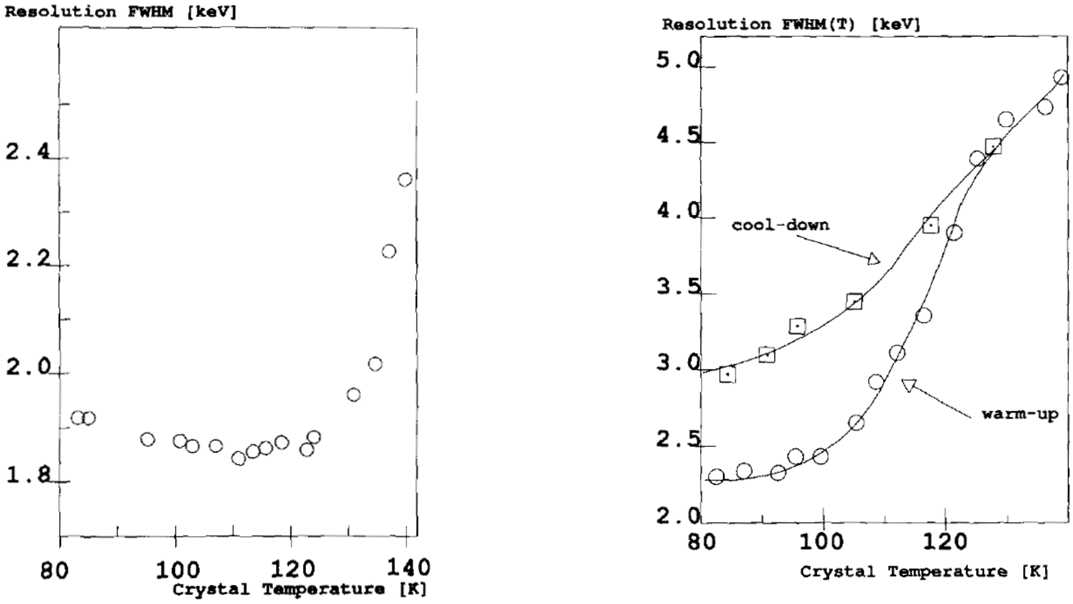

Figure 5.3: Temperature dependence of the resolution before (left) and after the irradiation with $2 \cdot 10^9\,\mathrm{n/cm^2}$. The irradiation reduces the detector performance even at low operation temperatures. When heating up the crystal, the loss of resolution kicks in quicker for the irradiated detector. Additionally this heating cycle permanently worsens the resolution even at low temperatures due to crystallization of defects at higher temperatures. Annealing procedures can be used to cure these effects (figure from [218]).

In conventional cooled germanium detectors the boiling point of liquid nitrogen at $77\,\mathrm{K}$ limits the operational temperature of the HPGe crystal. A further reduction is possible by the use of mechanical coolers. Hyperball-X [162] is able to reach a crystal temperature of $67\,\mathrm{K}$. When using these coolers, the fluctuations in the environmental temperature affect the crystal temperature which results in small shifts of the energy spectrum which are corrected in [162] solely by the knowledge of the room and crystal temperature. At $\overline{\text{P}}$ANDA the environment will be kept at a stable temperature so that this can be neglected. Nevertheless, temperature monitoring and frequent calibration measurements are required for possible corrections in long term measurements. During the experiments at J-PARC, Hyperball-X will be irradiated by approximately $3 \cdot 10^8\,\mathrm{n/cm^2}$ [162] which is uncritical in contrast to the expectations in the range of $1 \cdot 10^{10}\,\mathrm{n/cm^2}$ for $\overline{\text{P}}$ANDA (compare section 5.2).

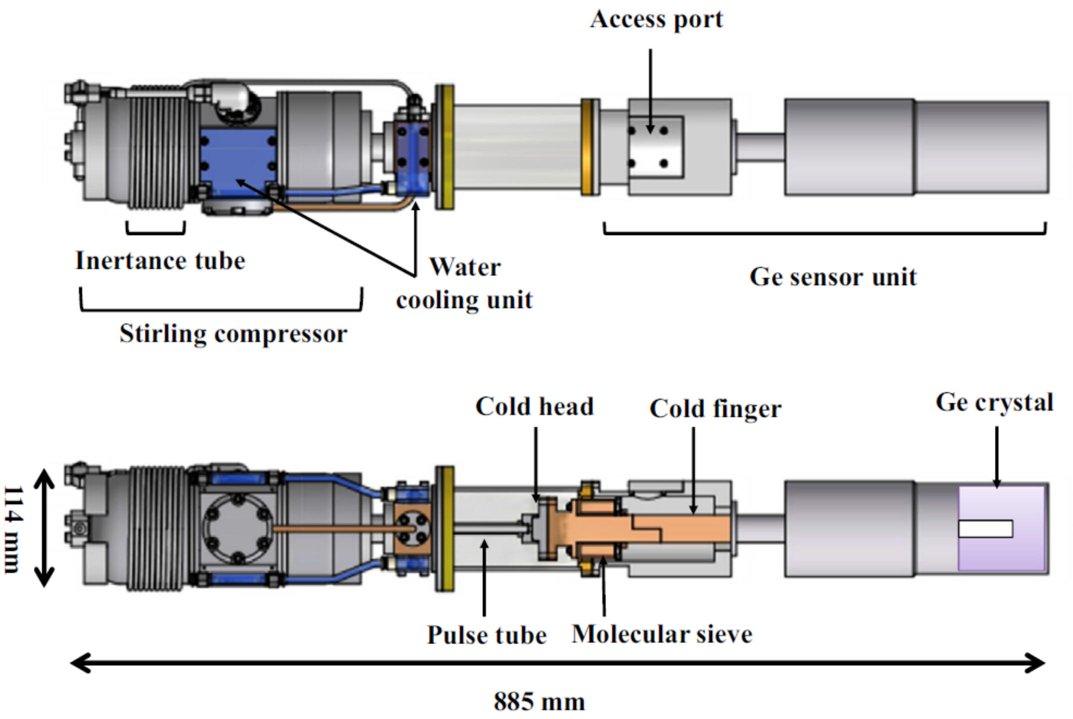

Figure 5.4: CAD drawing of an individual detector of Hyperball-X. The basic design is similar to the detectors of PANGEA, but each detector houses only a single crystal (figure from [162]).

After such an irradiation the crystal needs to be annealed. Fourches *et al.* [219] showed that heating up the crystal to temperatures above $100\,^{\circ}\mathrm{C}$ suffices to restore the crystal lattice. This annealing procedure requires multiple hours to relax the structure of the lattice and must be performed under vacuum conditions. This procedure has been successfully repeated for EUROBALL crystals at GSI for many years and during this time the temperature profile has been optimized. Figure 5.5 shows such a profile for a typical annealing procedure. The biggest fractions of the duration are used to slowly heat up and cool down the crystals. This prevents thermal stress while giving the crystal lattice sufficient time to reconfigure itself.

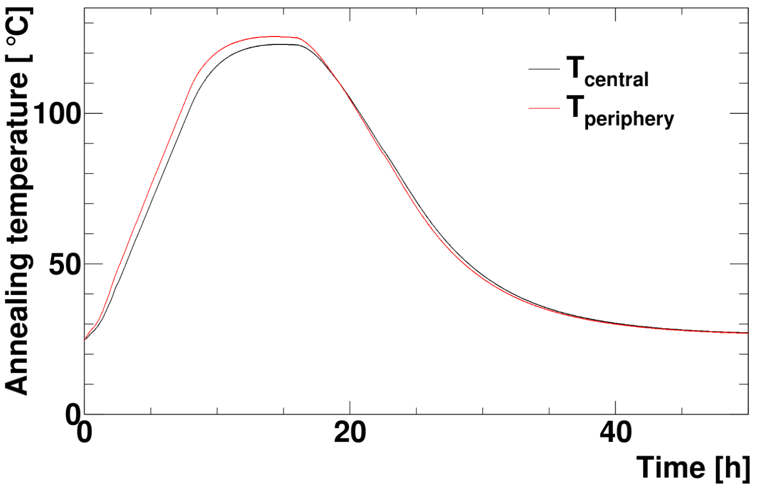

Figure 5.5: In a typical annealing procedure of a EUROBALL crystal, as performed at GSI [188], the vacuum oven is heated up to $125\,°\mathrm{C}$. This allows the crystal lattice to relax and recover from distortions. A slow heat up and cool down procedure prevents thermal stress. Multiple crystals can be annealed in the oven at the same time. The temperatures were monitored by two temperature sensors peripherally to the crystals (black) and in their center (red). The small difference is negligible and caused by the finite thermal conductivity of the material of the oven and the crystals that dominate the heat transfer within the vacuum vessel.

5.2 Estimations of the neutron background in $\overline{\text{P}}$ANDA

The neutron load of the HPGe crystals within $\overline{\text{P}}$ANDA experiments can be estimated in simulations. PandaRoot was used for this just as for the efficiency studies in the previous chapter. In contrast to these studies where the PndBoxGenerator was used to generate individual photons, full events have been used as input now. These events were generated from the reactions of the antiproton beam and carbon nuclei. The momentum of the beam was set slightly above the Ξ^--$\bar{\Xi}^+$ production threshold of $2643.4\,\mathrm{MeV}$ which corresponds to a beam momentum of $p_{beam} = 2622.6\,\mathrm{MeV}/c$. Again the Giessen Boltzmann-Uehling-Uhlenbeck transport framework (GiBUU) [a] [82] was used to simulate this primary reaction. A total of 100 million events corresponding to $50\,\mathrm{s}$ of $\overline{\text{P}}$ANDA beam time at the designated average interaction rate of $2\,\mathrm{MHz}$ were simulated for these studies. The same pseudodata will be used for the studies of the particle background of the hyperatomic experiment which will be shown in section 6.3.

The angular distribution of these primary neutrons is shown in figure 5.6. The figure shows the distribution in $\cos(\Theta)$ which should be flat for an isotropic distribution in Θ. The peaking towards $\cos(\Theta) = 1$ shows that the distribution of primary neutrons is boosted downstream towards small polar angles as it can be expected for fixed-target experiments. This strengthens the positioning of PANGEA at large polar angles to reduce the particle background.

---

[a] GiBUU release 1.5

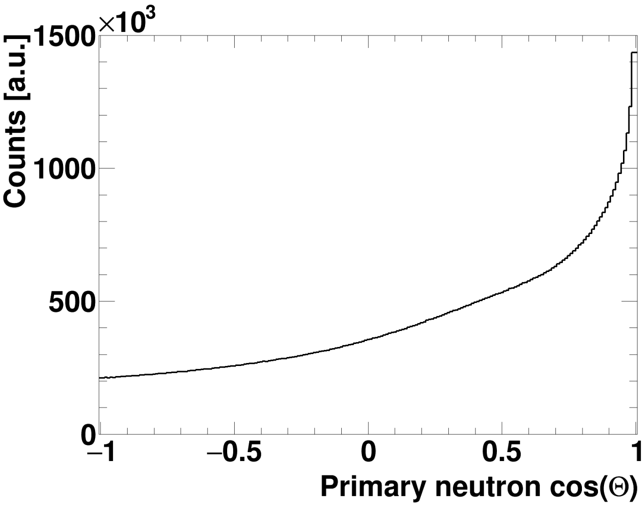

Figure 5.6: As expected for a fixed-target experiment, the angular distribution of neutrons produced in simulations of the primary interaction at $\overline{\text{P}}$ANDA is boosted towards $\cos(\Theta) = 1$ which is equivalent to forward angles.

In addition to that, the HPGe crystals will suffer from neutrons produced in secondary reactions in surrounding material. Because of that, the components of $\overline{\text{P}}$ANDA in the proximity of PANGEA - the barrel DIRC, the STT as well as the magnet - are included in the simulations besides the dedicated target system and PANGEA in its column layout (compare section 4.3.1.2). The simulations within PandaRoot used the GEANT4 transport model and were performed for the hyperatom setup of the secondary target with the optimized lead absorber. Details on the shape of the target are presented in chapter 6 where its optimization is presented.

In the literature, the irradiation of HPGe crystals is described by the number of neutrons that hit the crystal from an external source. Secondary neutrons produced within the crystal are not counted. These external sources are not limited to primary reaction. In fact, the origin of a neutron can even be a nuclear reaction inside one of the other 59 crystals. If these neutrons escape their originating crystal and hit another one they must be considered. In contrast to that, neutrons that do not leave their production crystal are not considered in the algorithm.

Even without counting those internal neutrons, most of the neutrons hitting the germanium crystals are produced in secondary reactions. This is visualized in figure 5.7 in two different ways. The left plot shows the mother particle of the corresponding neutron. It is identified by its code based on the Monte Carlo numbering scheme of the particle data group (PDG code) [220] and sums up to $5.81 \cdot 10^7$ neutrons for all crystals in the completed simulation. The mother of primary neutrons in this figure is attributed as the beam antiproton with a PDG code of -2212. Obviously these primary neutrons do not dominate the spectrum. More than double the amount originates from other neutrons (2112) causing nuclear reactions and thus producing secondary neutrons. The nuclear reactions induced by charged pions (-211, 211) also produce a large amount of neutrons. The last noteworthy origin of neutrons are proton induced reactions (2212). The fraction of neutrons with more exotic mother particles is negligible. On the right side the origin of the neutron is broken down to a more spatial way. Only the small fraction of $16.4\,\%$ of hits originate from neutrons created in the primary reaction while the much larger share ($83.6\,\%$) is created in secondary reactions. This confirms the numbers in the left plot. A quarter of the total neutrons is produced within the volume of the target system. The target is close to the interaction point which explains its large fraction. Besides the primary and secondary target this share includes neutrons originating from the beam pipe. However, the dominating component is the secondary target with its lead absorber and silicon detectors[b] as it can be seen in figure 5.8 where the secondary target is represented by the red bins at $z = -55\,\mathrm{cm}$ and close to $y = 0\,\mathrm{cm}$. An even slightly higher part of the neutrons are produced within the germanium crystals. The close proximity of the crystals to each other and consequently the high solid angle explains this large amount of neutron background originating here. It is important to note that only the hits of neutrons outside of their originating crystal have been taken into account, as explained previously. In addition to the crystals, other parts of PANGEA have to be considered. In the geometry these mainly consist of the cryostats of the cluster detectors, the encapsulation of the crystals and the BGO veto detectors in the back of the crystals. With $14.2\,\%$ the influence of these is not negligible. Finally, neutrons produced within the remaining components of $\overline{\text{P}}$ANDA must be considered. With $18.2\,\%$ of all neutrons the large fraction mirrors the large volume of these components. The distribution of neutron origins is shown in figure 5.8 in a projection to the yz plane.

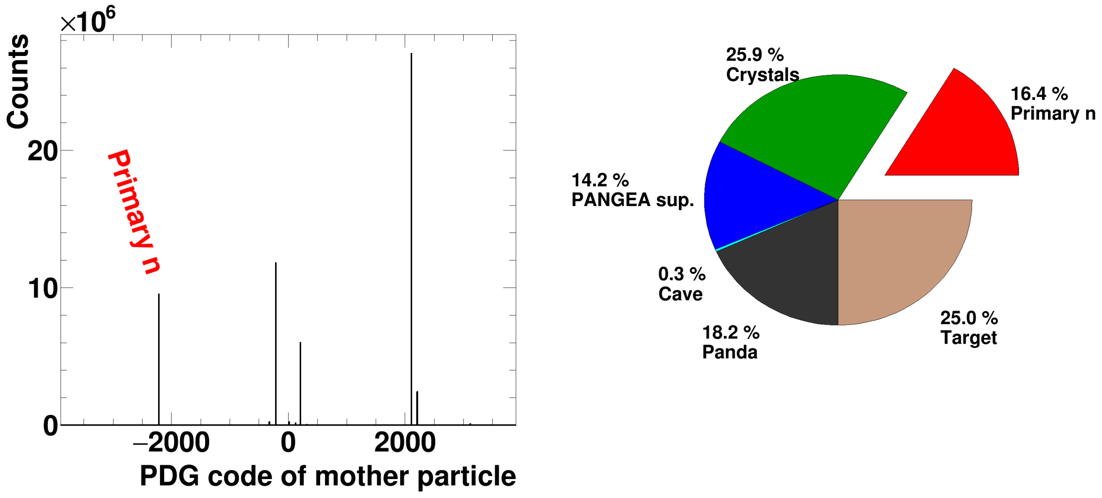

Figure 5.7: Most of the neutrons hitting the germanium crystals are produced in secondary reactions. The left plot shows the mother particle of these neutrons. This is dominated by other neutrons (2112) that produce daughter neutrons in nuclear reactions. Neutrons from primary reactions are represented by antiprotons as mother particle (-2212). Their contribution is less than half of the neutrons produced by neutron induced reactions. Charged pions (-211, 211) have a comparable contribution as the primary neutrons. The last noteworthy mother particles are protons (2212). The fraction of neutrons with more exotic mother particles is negligible. In addition to that, the pie chart on the right shows the origin components of the neutrons. As already seen in the left diagram, the fraction of neutrons from primary reactions is rather small ($16.4\,\%$). The main source of secondary neutrons are the target system and surrounding germanium crystals.

---

[b] As it will be shown in chapter 6 the silicon detectors are not required in the hyperatom experiment and will be left out in the final setup. This was identified after these studies which could not be repeated. The omission of this detector is expected to slightly reduce the neutron load.

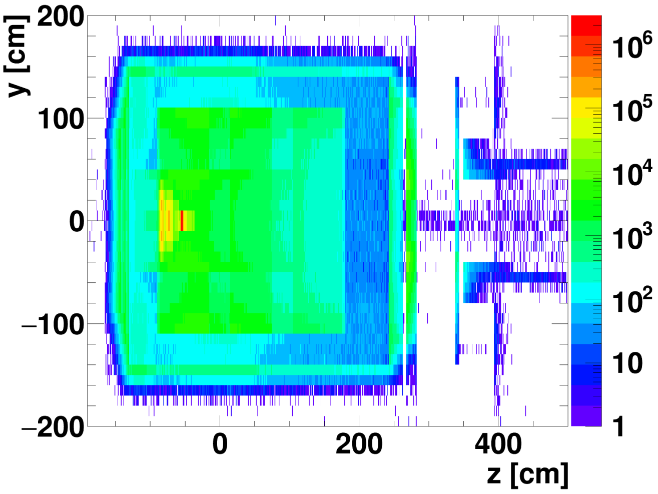

Figure 5.8: Position of the neutron origin in a projection to the yz plane. The plot only includes secondary neutrons. Neutrons produced in the primary reaction and those produced within germanium crystals are left out. The secondary target at $z = -55\,\mathrm{cm}$ and around $y = 0\,\mathrm{cm}$ shows a high concentration of neutron starting points. At smaller z of -100 to $-70\,\mathrm{cm}$ and $y = -40$ to $40\,\mathrm{cm}$ the cryostats of PANGEA are visible. The green and blue areas belong to the surrounding P̄ANDA components.

Looking at this information of the origin of the neutrons, it is obvious that the material in the proximity of the primary interaction point should be reduced as much as possible. Doing so will reduce the total amount of secondary particles which results in less nuclear reactions in the surrounding components of the experiment. Besides this scaling effect, the amount of neutrons originating from the crystals or their support can not be reduced and the space in between is too small to add sufficient amounts of shielding which could at the same time reduce their γ detection efficiency. The neutron background originating from the remaining P̄ANDA components would also decrease due to the same scaling effect when the material budget near the target is reduced.

In the next step the neutron flux for each individual crystals must be studied. The previously presented neutron counts are separated for each of the 60 crystals. Figure 5.9 shows this on the left side. The range of neutron hits N_{n_sim} still varies by more than a factor of 2 for the crystals from $0.62 \cdot 10^6$ to $1.37 \cdot 10^6$ in the pseudodata of $50\,\mathrm{s}$. This averages to $0.97 \cdot 10^6$ per crystal in this $50\,\mathrm{s}$. The right plot of this figure splits up the hits based on the origin of the neutron. Here two kinds of distributions are visible. The hit distribution of the neutron originating from P̄ANDA and the cave are rather flat. They show a slight increase for the crystal numbers below 10 and above 51. These crystals correspond to the outer column of triple detectors on each side (compare bottom of figure 5.9) which means that they are in close proximity to the surrounding P̄ANDA components. Central cluster detectors are less likely to be hit due to their higher distance to this origin and shielding due to the outer crystals. In contrast to that the other distributions show the same trend as the summed plot on the right. The neutron count is peaking for individual crystals which can be identified as the inner ring of crystals. This is visualized at the bottom of figure 5.9. In this figure the crystal number is assigned to its position in the full array. The crystals with the highest neutron load are marked in red. A limit of $1.2 \cdot 10^6$ hits is chosen for this which corresponds to $24\,\mathrm{kHz}$. These crystals form the innermost ring around the beam pipe which have the smallest distance to the primary interaction point. On the other end of the scale are the crystals marked in green. The threshold for these is less than $0.73 \cdot 10^6$ hits which equals to $14.6\,\text{kHz}$. These crystals are situated on the outside of the array with the highest distance to the beam pipe.

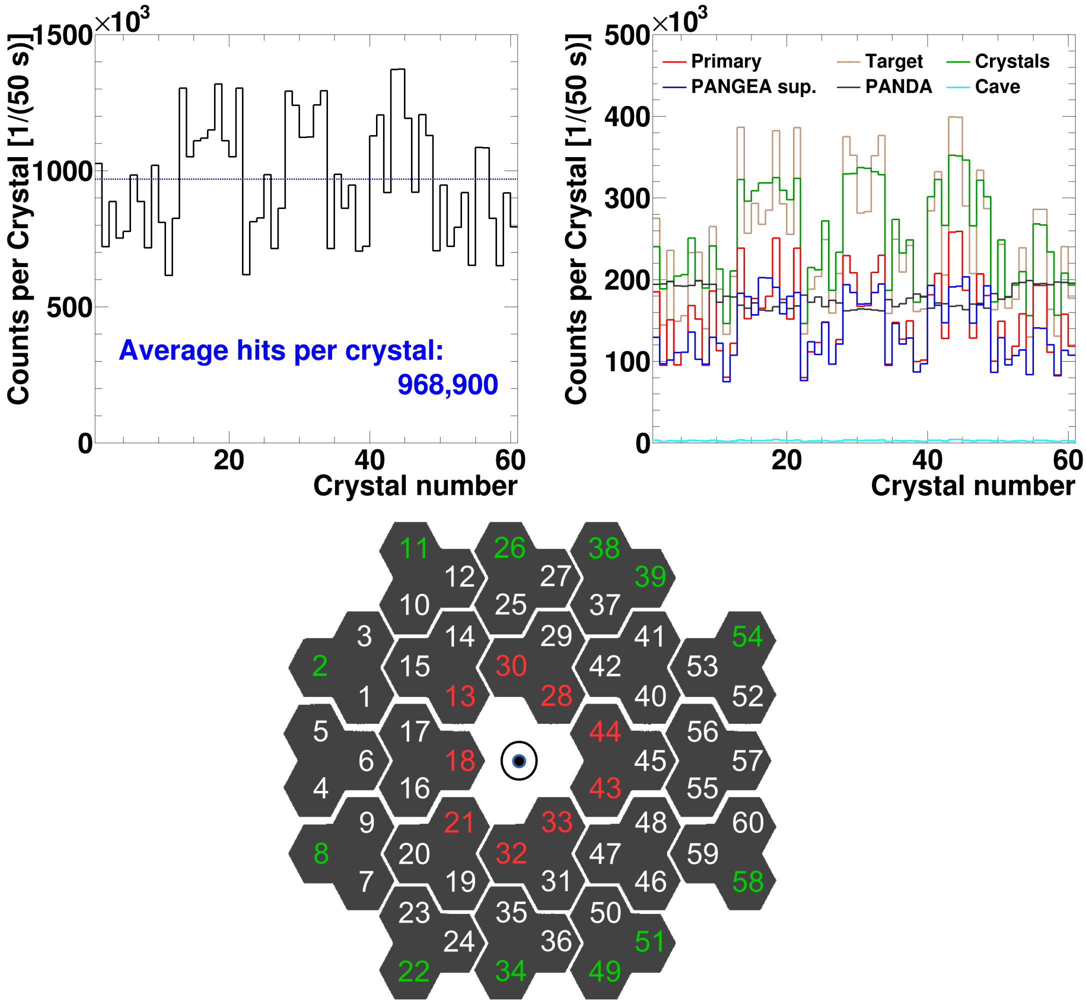

Figure 5.9: Distribution of the neutron hits of the individual crystals. In the top left the number of hits for the individual crystals is shown. These hits range from $0.62 \cdot 10^6$ to $1.37 \cdot 10^6$ within the simulated pseudodata that corresponds to $50\,\text{s}$ of beam time at $\overline{\text{P}}$ANDA. The average number of hits per crystal is $0.9 \cdot 10^6$. In the left, these hits are broken down to their origins shown previously. Neutrons originating from the surrounding $\overline{\text{P}}$ANDA detector and the cave are equally distributed with slight increase for crystal numbers below 10 and above 51. All other origins follow the same distribution as the total distribution. The assignment of the crystal numbers to their position in the full detector is shown at the bottom of the figure. In this frontal view of the array the beam is running towards the reader. The crystal with the highest and lowest loads are marked in this overview in red and green, respectively.

With these rates it is possible to estimate the amount of neutrons that a germanium crystal has to withstand within a full experimental period of $180\,\mathrm{days}$. This can be done by scaling the simulation results of $50\,\mathrm{s}$ to the expected beam time of the experiment. In addition to that, the total number of neutrons must be divided by the area of the frontal face of one germanium crystal ($A_{\text{crystal}} = 30.11\,\mathrm{cm}^2$) in order to get results that can be compared to literature,

$$N_{\text{n,Panda}} = \frac{N_{\text{n,sim}}}{A_{\text{crystal}}} \cdot \frac{3600 \cdot 24 \cdot 180}{50} \,. \tag{5.2}$$

The estimates for $N_{\text{n,Panda}}$ range from $0.64 \cdot 10^{10}$ to $1.42 \cdot 10^{10}\,\mathrm{n/cm^2}$ depending on the position of the crystal. In average a total neutron load of $1.00 \cdot 10^{10}\,\mathrm{n/cm^2}$ is predicted which is an amount that has to be reckoned with concerning radiation damage (compare section 5.1).

	$n_{\text{n,sim}}$ $\left[\frac{n}{cm^2}\right]$	R_n [kHz]	$N_{\text{n,PANDA}}$ $\left[\frac{n}{cm^2}\right]$
Maximum	$1.37 \cdot 10^6$	27.5	$1.42 \cdot 10^{10}$
Minimum	$0.62 \cdot 10^6$	12.3	$0.64 \cdot 10^{10}$
Average	$0.97 \cdot 10^6$	19.4	$1.00 \cdot 10^{10}$

Table 5.1: Summary of the neutron loads of the germanium crystal within a $\overline{\mathrm{P}}$ANDA experimental period of $180\,\mathrm{days}$. The estimations based on the results of the simulations range from $0.64 \cdot 10^{10}$ to $1.42 \cdot 10^{10}\,\mathrm{n/cm^2}$ depending on the position of the crystal. In average a total neutron load of $1.00 \cdot 10^{10}\,\mathrm{n/cm^2}$ is predicted.

The distribution of the kinetic energy of these neutrons in the simulation is presented in figure 5.20 in the next section. They will be compared to the simulations of the irradiation test at COSY and used to scale these tests to the experimental conditions at $\overline{\mathrm{P}}$ANDA.

5.3 Irradiation tests of EUROBALL crystals at COSY

With this high load of neutrons it is important to study the influence of these on the EUROBALL crystals designated for the experiments at $\overline{\mathrm{P}}$ANDA. This requires the production of similar amounts of neutrons within a reasonable time that follow a comparable distribution of kinetic energies. Because of that, the COSY facility (COoler SYnchrotron) [221] at Forschungzentrum Jülich, Germany, was chosen for these tests. The crystals have been irradiated in two beam times in June and July 2014. They lasted for 6 and 7 days, respectively.

5.3.1 Experimental setup at COSY

The core of the COSY facility is its synchrotron storage ring which accelerates and stores protons with up to $3.3\,\mathrm{GeV}/c$. It offers internal as well as extracted proton beams to experiments. The JESSICA area was available for the irradiation tests (see figure 5.10). The extracted proton beam with a momentum of $2.78\,\mathrm{GeV}/c$ is comparable to the beam momentum planned for the hypernuclear and hyperatom experiment. JESSICA (Juelich Experimental Spallation Target, Set-up In COSY Area) is part of the development of the European Spallation Source (ESS) and consists of a massive mercury target surrounded by lead absorbers inside a cylindrical steel tank with a diameter of $1.3\,\mathrm{m}$ [222]. The main task of this tank in the ESS testing campaign has been the production of neutrons inside the nearly $1\,\mathrm{m}$ long mercury target. JESSICA is mandatory in this beam area. It is part of the beam dump and can not be removed for any experiment. Because of that, it has to be considered in the simulations.

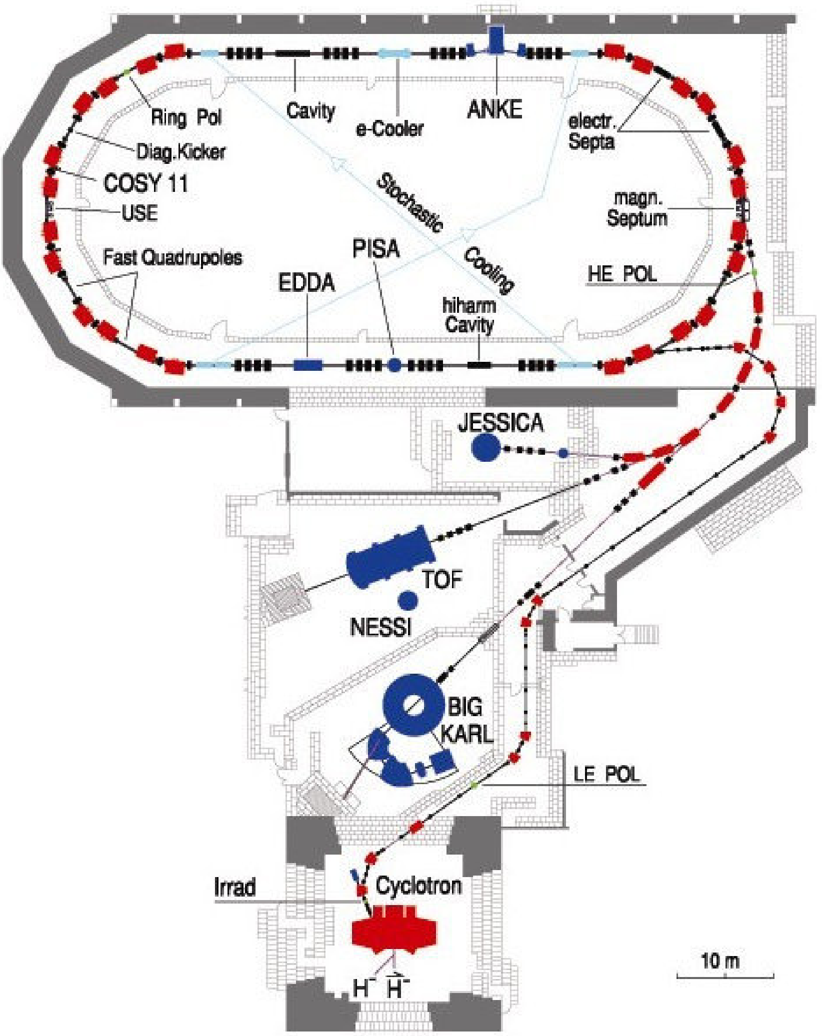

Figure 5.10: Floor plan of the COSY accelerator facility. For the irradiation of the germanium detector the beam was extracted to the JESSICA area (figure from [223]).

As a measure to reduce the influence of JESSICA the distance of the experimental setup of the irradiation test needed to be maximized. Because of that, the production target was positioned close to the outlet pipe of the proton beam. Inside the JESSICA area the beam is conducted in air. Because of that, a large cubic block of graphite could be used as target for the production of neutrons. With an edge length of $5\,\mathrm{cm}$ the interaction probability of the protons is in the range of $10\,\%$. This block is placed at a distance of $3.14\,\mathrm{m}$ in front of the JESSICA tank. In addition to these components, the $\overline{\text{P}}$ANDA luminosity detector group [68] used the beam time parasitically. Test samples were added downstream into the beam. Glue samples on microscope slides were put at a distance of $1\,\mathrm{m}$ behind the graphite target to test their capabilities after the irradiation. In addition to that, electronic components were added for the same purpose directly behind the glue samples.

While the previously described components were situated inside the proton beam, the HPGe detector was irradiated indirectly. It was placed in a horizontal position with its front facing the graphite target. The distance to the target center was $15\,\mathrm{cm}$ and the angle to the beam axis $120°$ (see sketch at the top of figure 5.11). Both parameters are comparable to the detector placements in $\overline{\text{P}}$ANDA (compare section 4.3.1.2). In both irradiation tests the detector was cooled electro-mechanically via an ORTEC X-Cooler II, but different detectors had to be used in each test. This was caused by a mechanical issue inside the cryostat of the first detector that could not be replaced in the short time between both beam times. Because of that, this most recent prototype of PANGEA/DEGAS at the time of the test had to be replaced by its precursor in the second test. The main difference of both detectors was the improved cryostat of the newer detector. Unfortunately, the lower operational temperature was partially negated by the mechanical issues in the first test which led to higher thermal bridging. This will be discussed in more detail in section 5.3.1.1.

Both detectors housed a single EUROBALL crystal (first test: HEX 158, second test: HEX 146). A ^{60}Co source in the close proximity to the detectors was used to study the effect on the measured spectrum over the course of the irradiation. Due to the lack of an actively resetting preamplifier (compare section 4.2.2.2 and 6.3.4) the data taking had to be limited to the refilling periods of COSY when no beam was present in the JESSICA area.

In addition to the germanium detector, neutron detectors were added to the setup. In both beam times a passive Bonner sphere type detector with a diameter of $12\,\mathrm{inch}$ ($\approx 30.5\,\mathrm{cm}$) was used. Since the direct information about the amount of neutrons irradiating the germanium crystal is not available, this detector could be used to validate the simulation results. A second neutron detector was available in the first beam time. This MAB NM500, an active neutron detector, offered the ability to measure the dose online. The positioning of both neutron detectors is shown in figure 5.11. The sketch in the top of the figure shows the position of the three detectors relative to the graphite target. The NM500 is placed on a small frame on top of the germanium detector to achieve the same polar angle of $120°$. The Bonner sphere was placed further backwards. On the bottom of the figure a photograph of the same situation is shown. The photograph was taken during the first beam time.

As already mentioned, it had to be assured that the data of the germanium detectors was taken when the beam was offline. Otherwise, the interaction rate was too high to be handled by the non-resetting preamplifier (compare section 6.3.4). Because of that, the triggering of the data acquisition was done via a coincidence of the signal of the germanium detector and the negated beam extraction status of COSY. The signal of the germanium detector had to be split up for this. In the triggering branch it had to be processed in a timing filter amplifier (ORTEC TFA 474) and then discriminated in a constant fraction discriminator (ORTEC CF8000). The other half of the germanium signal as well as the trigger signal was led to a FlashADC [c] to digitize its pulse shape. A readout system based on MBS [224] was used to store the pulse shapes. Hardware-wise this system consisted of the VME modules ENV1, VULOM4 and TRIVA7. The system was controlled

---

[c] CAEN V1724, $14\,\mathrm{bit}$, $100\,\mathrm{MSa/s}$

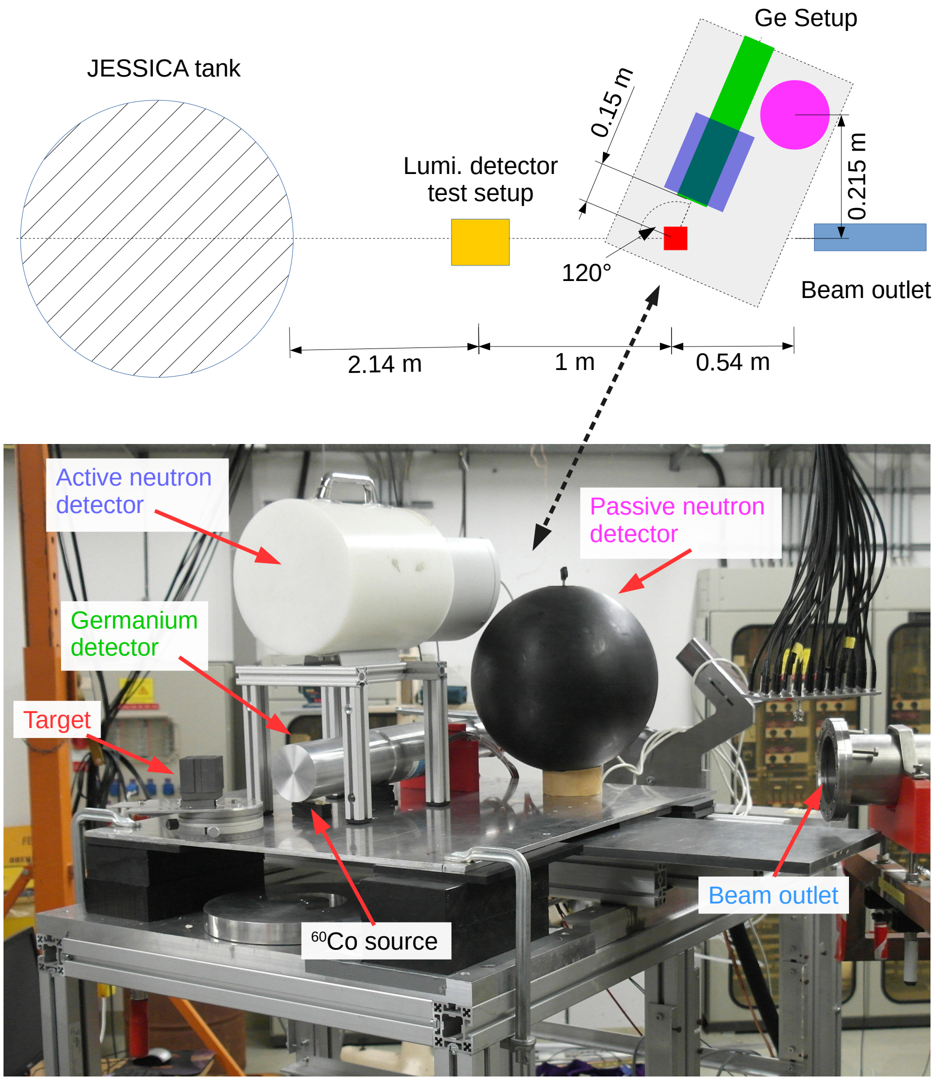

Figure 5.11: Sketch and photograph of the setup used for the irradiation test. Both show the setup brought to the JESSICA area at the COSY facility. Besides the germanium detector two neutron detectors were added for monitoring the irradiation. A ^{60}Co source was added beneath the germanium detector to study the effect of the irradiation on the measured spectrum. The neutrons were produced in the graphite target situated directly in the $2.78\,\mathrm{GeV}/c$ proton beam. The sketch at the top of the figure also includes the test setup for the luminosity detector and the JESSICA tank that were considered in the analysis of the data.

via a RIO4 VME CPU that was connected via Ethernet to a desktop computer. This PC was used for controlling the system as well as storing the data. A sketch of the data acquisition system is shown in figure 5.12. The online as well as offline analysis of the pulse shapes was performed in the ROOT based GO4 [225] designed for direct communication to the MBS system.

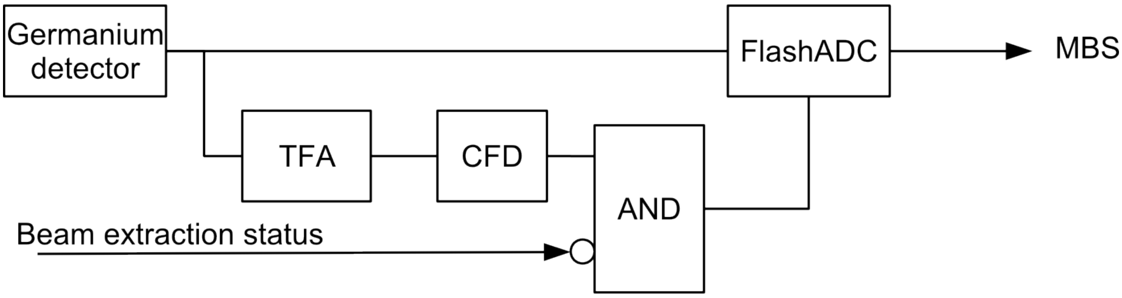

Figure 5.12: The lack of an actively resetting preamplifier limited the data taking to the refilling phases of COSY when no beam was present. Because of that, a coincidence of the negated beam extraction status and the signal of the germanium detector was used to trigger the FlashADC. The signal of the germanium detector had to be split up in order to achieve this. The addition of a timing filter amplifier as well as a constant fraction discriminator was required to process the detector signal to trigger the FlashADC.

5.3.1.1 Influence of the mechanical issues during the first beam time

As previously explained the detector in the first beam time had mechanical issues. The fixing labyrinth was damaged, probably during the transport to COSY. This part was designed to stabilize the cold finger and hold it in place (see left part of figure 5.13). Since it connects the cold and warm surfaces of the cryostat, it must be designed for the lowest possible thermal conductance which makes it fragile. The damaged 3D-printed part can be seen in the right of figure 5.13. Three cracks are visible, marked by circles. Especially the bottom left region of the labyrinth was completely detached due to the cracks on both sides. Because of that, the structure could not stabilize the cold finger and crystal as designed (compare figure 5.13). This reduced the isolation capabilities of the cryostat especially for the horizontally placed detector. In this orientation, the crystal partially touched the inside of the cryostat due to gravity and led to thermal bridges. All checks of the detector before its installation in the irradiation setup were performed in a vertical orientation where the damaged part is irrelevant and hence the issue was not observed before this point.

Without any action the thermal contact of the capsule and the cryostat was too high when the detector was orientated horizontally. This severely reduced its isolation capabilities and led to the formation of condensation on the cryostat while the temperature of the crystal increased at the same time. As a quick fix - in order to continue the irradiation test - the detector cup was slightly pressed upwards which eliminated the direct contact of the capsule. This could recover most of the isolation and reduce the operational temperatures. Nevertheless, the temperature of the crystal could not be fully recovered. As shown in the left plot of figure 5.14 the temperature was oscillating around $-169\,^{\circ}\mathrm{C}$ ($104\,\mathrm{K}$). The origin of the oscillation can be identified by the change of the room temperature in the day/night cycle in June which hints on a remaining flaw

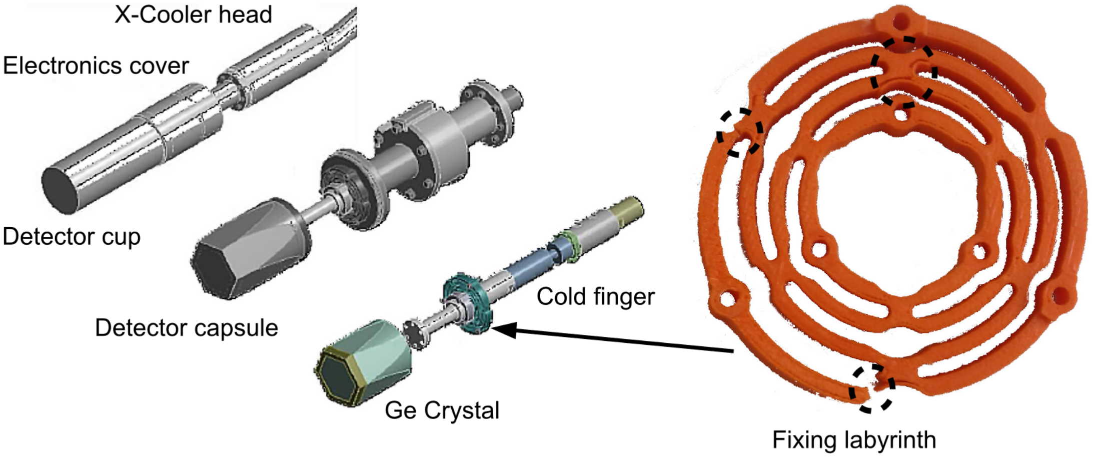

Figure 5.13: On the left three different layers of the prototype detector used for the first irradiation test are shown. In each of these drawings, another layer of the cryostat is stripped. Because of that, the fixing labyrinth, connecting the cold finger and the cryostat, is only visible in the innermost layer. The thermal resistance of this part must be maximized to optimize the thermal insulation of the system. The part used in the prototype was a 3D-printed part which seemed to be too fragile. The part cracked most probably during transportation. Due to the three cracks, marked by the circles in the picture on the right , the cold finger and the attached crystal could not be held properly in place which decreased the thermal capabilities of the cryostat.

of the cryostat due to the damage and the limited cooling power typical for electro-mechanical coolers [162]. The third day shown in the plot was rainy and because of that not as warm as the other days, observable in the lower amplitude of the oscillation. The right plot shows the temperature of the same detector measured in the laboratory before going to Jülich. The average temperature of the undamaged detector was about $-179\,°\mathrm{C}$ ($94\,\mathrm{K}$) which is $10\,\mathrm{K}$ below the operational temperature of the detector during the irradiation. Nevertheless, it was decided to continue the irradiation even with this performance loss.

After the beam time, when the setup was dismounted, the thermal capabilities of the detector were tested again. The dismounting allowed to bring the detector into a vertical position. As shown in figure 5.15 the temperature began to drop in this position. This emphasizes the described smaller influence of the fixing labyrinth in the vertical orientation.

This damage could not be repaired before the next beam time, less than a month later. Because of that, the precursor in the development of PANGEA had to be used. Since the cryostat of this detector lacks optimization compared to the other detector the operational temperature was even higher. During the beam time an operational temperature of about $-149\,°\mathrm{C}$ ($124\,\mathrm{K}$) was measured. This measurement is shown in figure A.8 in the appendix.

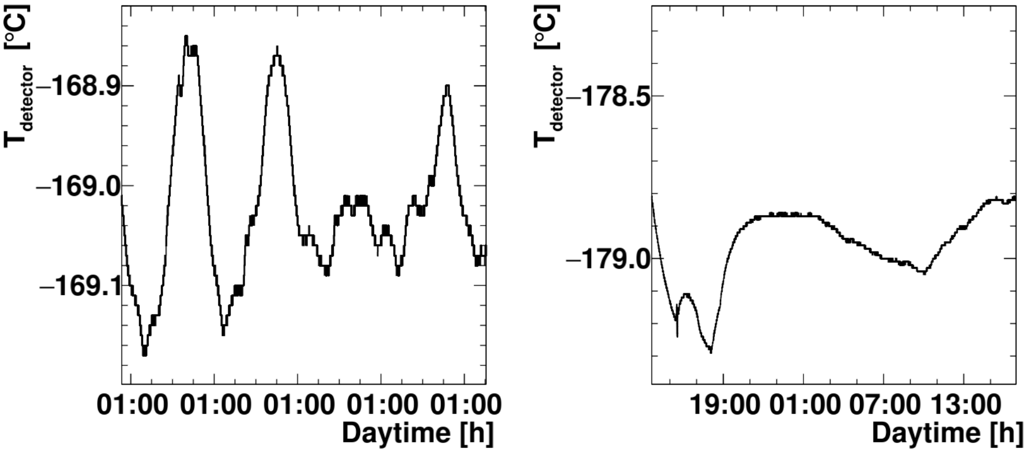

Figure 5.14: The damaged fixing labyrinth in the first beam time, starting June 11, 2014, deteriorated the performance of the cryostat resulting in increased detector temperatures. As shown on the left the average temperature has been −169 °C (104 K), oscillating due to changes of the room temperature in the day/night cycle. On the right a temperature measurement prior to going to Jülich is shown. Here the average temperature is 10 K lower which shows the remaining flaw of the detector during the irradiation.

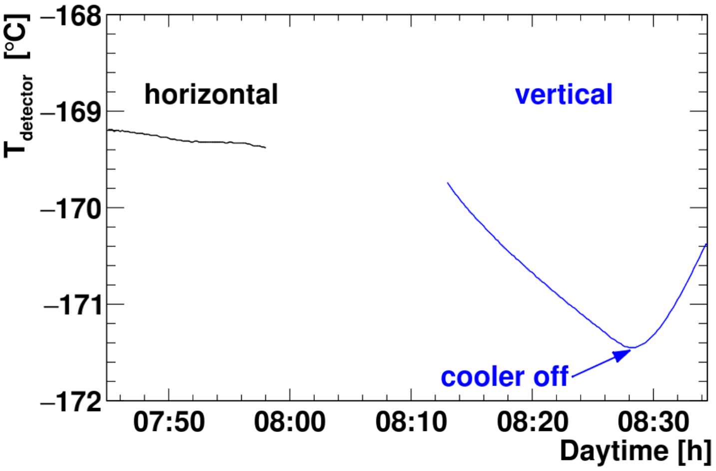

Figure 5.15: After the irradiation the germanium detector could be placed vertically. In this orientation the fixing labyrinth is less important and the operational temperature decreased rapidly until the cooler was switched off.

Besides the difference in the cryostat, the HPGe crystals used in both irradiation tests differed. Both were EUROBALL n-type crystals. In the first test the crystal HEX 158 was used. This crystal is specified with a bias voltage of 3000 V and an initial resolution of 2.25 keV (FWHM[d]) for the 1.332 MeV ^{60}Co based on measurements in the germanium detector laboratory of GSI [188]. The FWTM/FWHM[e] ratio in this measurement was 1.924 which is close to the expectations for a pure Gaussian signal of 1.823.

---

[d] Full Width at Half Maximum

[e] FWTM: Full Width at Tenth Maximum

In the second test HEX 146 was irradiated which is specified with $4000\,\mathrm{V}$, a resolution of $\mathrm{FWHM}_{\mathrm{Co}} = 1.96\,\mathrm{keV}$ and the FWTM/FWHM ration of 1.864.

At COSY the bias voltage was supplied via a CAEN A1832N inside a CAEN SY2527 high voltage crate which allowed remote control via Ethernet. When the thermal problems of the detector during the first beam time were noticed the high voltage was reduced. Since its cause was quickly identified and could be provisionally fixed, the detector was able to be kept in operation. The bias voltage was reduced to $2000\,\mathrm{V}$. This happened less than $3\,\mathrm{h}$ after the start of the irradiation test. Since no further problems were observed for about $30\,\mathrm{h}$, the high voltage was raised to $2500\,\mathrm{V}$ again. Later that day (June 12, 2014) a $3\,\mathrm{h}$ maintenance of COSY was used to check the stability of the detector when running at its specified bias voltage of $3000\,\mathrm{V}$. Since this test was successful this high voltage was reapplied for the remainder of the beam time. More details on the course of the test can be found in the log file attached in appendix A.5.1.

The high voltage could be applied to the detector for the whole week of beam time, besides one incident after three days where the complete supply and DAQ systems crashed due to a blown fuse which unfortunately resulted in an unresolvable increase of the noise level (see section 5.3.3). The log of this beam time is attached in appendix A.5.2.

5.3.1.2 Estimations of the total amount of protons

As shown in the log files in appendix A.5.1 and A.5.2, respectively, the beam parameters had to be changed and optimized during both beam times by the COSY operators. While the beam momentum of $2.78\,\mathrm{GeV}/c$ was unchanged, the amount of extracted protons as well as the extraction time were modified. This was necessary to maximize the irradiation without being shut down by the automatized radiation protection measurements. Their neutron detectors were programmed to shut down the whole beam extraction system after the detection of a specific amount of neutrons per hour and prevented to restart it for the rest of this hour. Because of that, it was a stepwise approach until the optimal settings were found. Figure 5.16 shows the dose rate measurement of the active neutron detector (MAB NM500). This data could be used to calculate the neutron flux. Especially the stepwise changing of the beam intensity is visible and could be assigned to the information of the beam intensity given by the COSY staff (see log files in the appendix (table A.7)). Furthermore, pauses in the operation of the accelerator can be identified.

With this information it was possible to calculate the total amount of protons during the irradiation by summing up the proton flux multiplied with the corresponding time interval of this flux. As shown in detail in table A.7 this sums up to $6 \cdot 10^{13}$ protons for the complete first beam time.

In the second beam time, the proton flux tolerated by the radiation protection systems was lower than in the first beam time. The active neutron detector, used for monitoring the status of the beam, was not available for this beam time. Because of that, the irradiation periods are based on the beam status information given by the operators of COSY (compare log file A.9). Repeating the calculations analog to the first beam time yields a total number of protons of $3 \cdot 10^{13}$ which is half of the first beam time (see table A.10). In addition to this method, the dose measurements of the passive neutron detector can be used to compare the total doses of both beam times. As shown in table A.8 the total dose measured in the first beam time was $187.4\,\mathrm{mSv}$. For the second beam time the same detector measured a total dose of $135.2\,\mathrm{mSv}$ [188] which is $72\,\%$ of the first dose. Since none of both methods can be ruled out, the average of both is used as relative scaling factor $61 \pm 11\,\%$. The difference to the individual methods is considered as systematic error. In addition to the amount of protons the size of the beam is important to estimate the strength of the

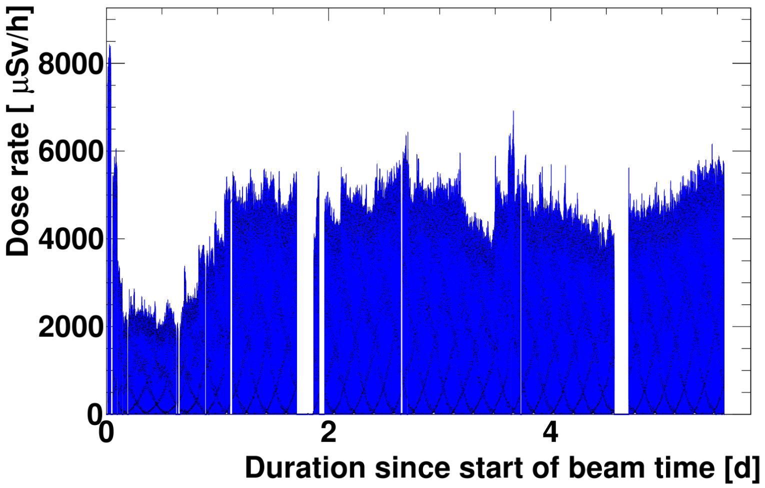

Figure 5.16: The dose rate measurement of the active neutron detector could be used to identify pauses in the operation of the accelerator as well as variations in the rate of extracted protons. The asynchronous beam extraction cycles and neutron detector measurements resulted in the graphical substructures that can be seen in the plot as well as the strong fluctuation in the maxima. Nevertheless, a total amount of $6 \cdot 10^{13}$ protons during the first beam time was calculated using this data.

irradiation. For this, the multi-wire chambers close to the beam outlet of the proton beam could be used. They measured a σ of $13.6\,\mathrm{mm}$ for the horizontal as well as the vertical direction of the Gaussian shaped beam. The measurements of the multi-wire chamber are shown in figure A.5 in the appendix.

5.3.1.3 Simulation of the irradiation test

Since the energy distribution of neutrons in $\overline{\text{P}}$ANDA and the irradiation test might differ, it was not possible to simply rely on the total luminosity to compare each other. Further, the experimental environment must not be ignored as already shown in the simulation of the neutron background within $\overline{\text{P}}$ANDA in section 5.2. Because of that, simulations of the setup at COSY were performed. These used the same simulation framework and configurations as the simulations of $\overline{\text{P}}$ANDA, only the detector geometry differed. At first, the immediate surroundings of the germanium detector were modelled. Besides both neutron detectors this included the aluminum support close to the germanium detector as well as the graphite target block. Furthermore, the main source of background was expected to originate from material in direct contact with the primary beam. Thus, the test setup of the luminosity detector as well as the big JESSICA tank was added to the simulation. The simplified design of JESSICA was based on the description given in [222]. Finally, the concrete shielding of the beam area was added. Figure 5.17 shows this geometry, while the left picture shows the whole setup used in the simulation, the right side is a zoom on the area close to the germanium detector.

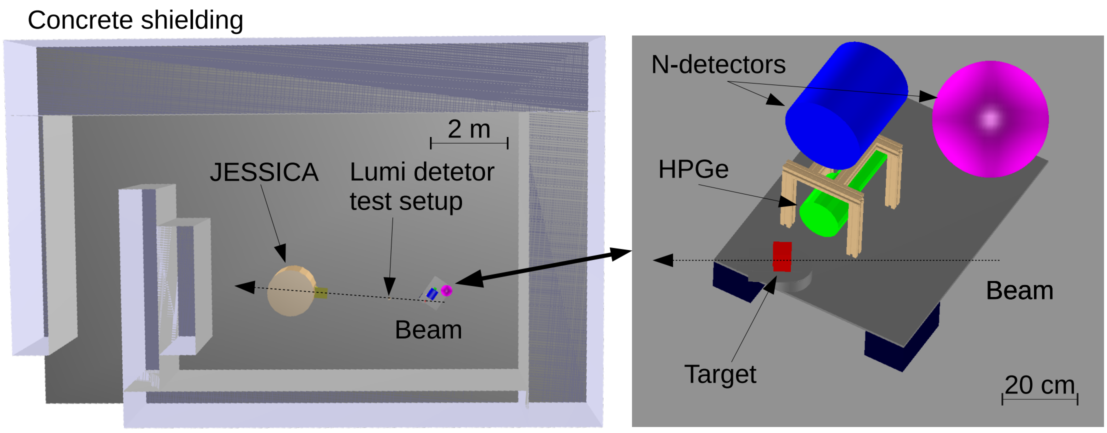

Figure 5.17: Design of the setup modelled for the simulation of the irradiation tests. The left side shows the whole beam area. Here the components directly in the beam as well as the surrounding concrete were added. The ceiling of this concrete shielding is removed for this picture to allow the glimpse on the components. On the right a zoom on the surroundings of the germanium detector is shown. The color code of the components is the same as in the sketch in figure 5.11.

Using this geometry $1 \cdot 10^8$ protons were simulated with a momentum of $2.78\,\mathrm{GeV}/c$. The size of the proton beam of COSY was simulated by a combination of a two-dimensional Gaussian smearing of $10\,\mathrm{mm}$ and an additional random beam divergence in the range of $0°$ to $0.2°$. The starting vertex of the beam is positioned $50\,\mathrm{cm}$ in front of the target.

For the analysis of these simulations most of the code used for the simulation of $\overline{\mathrm{P}}$ANDA could be reused. Only modifications due to the changed geometry were required. The basic algorithm was identical and focused on the counting of neutrons hitting the germanium crystal as well as the neutron detectors.

First of all the origins of neutrons hitting the germanium were studied. As shown in figure 5.18 their main origin was not the graphite target. As expected, roughly $90\,\%$ of the protons passed this target without interaction. While a small fraction of these interacted in the components of the test setup of the luminosity detector, most of them were stopped within the JESSICA tank, the beam dump. The dense and heavy material produced a lot of neutrons and a fraction of these was able to hit the germanium detector. In total, this amount was larger than the neutrons produced within the graphite target or the direct proximity of the germanium detector. This can be seen in the projection of the neutron origin to the z-axis (right side of figure 5.18). Additionally, the numbers are summarized in table 5.2. These show that more than double the amount of neutrons originate from JESSICA than from the dedicated target.

Since the direction of the neutrons entering the germanium crystal is irrelevant, all these neutrons could be combined and only their kinetic energy is important for their influence on the performance of the detector (see section 5.3.1.4).

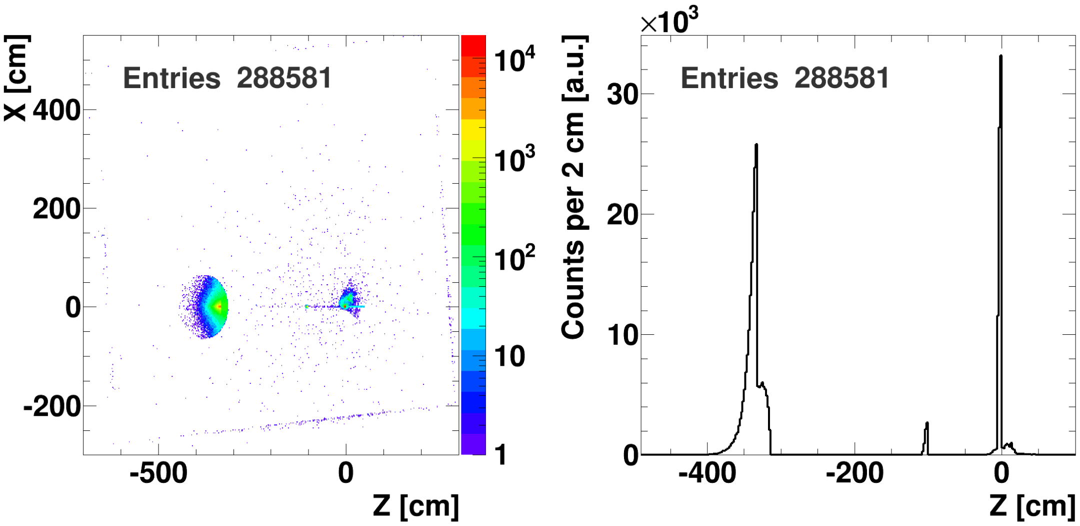

Figure 5.18: Overview of the production vertices of neutrons that hit the germanium crystal in the simulations. Since the graphite target was designed for an interaction rate with the proton beam of $10\,\%$ most of the protons were dumped inside the JESSICA tank. This high interaction rate produced a large number of neutrons that hit the crystal even at its comparably small solid angle and very backward angle. This is shown on the left in a projection to the horizontal plane of the simulation where the two main clusters are the graphite target and the setup close to the germanium crystal, around (0,0), and the JESSICA tank around (-350,0). On the right a further projection to the beam axis z is shown. Both previously explained regions are prominently represented. The small bump at $z = -100\,\text{cm}$ is the luminosity detector test setup, but its influence is small.

Component	Neutrons
Target and Proximity	80401
Luminosity detector test setup	6141
JESSICA tank (beam dump)	199950
Other	3089
Total	288581

Table 5.2: Amount of neutrons from various origins. Despite the high distance to the JESSICA tank, the highest portion of neutrons hitting the germanium detector originated from this beam dump.

Validation of the simulations via neutron detector

While the hits in the germanium detector were used to estimate the irradiation of the crystal, the passive neutron detector could be used to verify the quality of these simulations. The comparison of the measured dose and the simulations required to correct the pseudodata with the energy-dependent efficiency of the Bonner sphere for the detection of neutrons and convert this in a second step to a total dose. This process is shown in figure 5.19. In the first plot the black

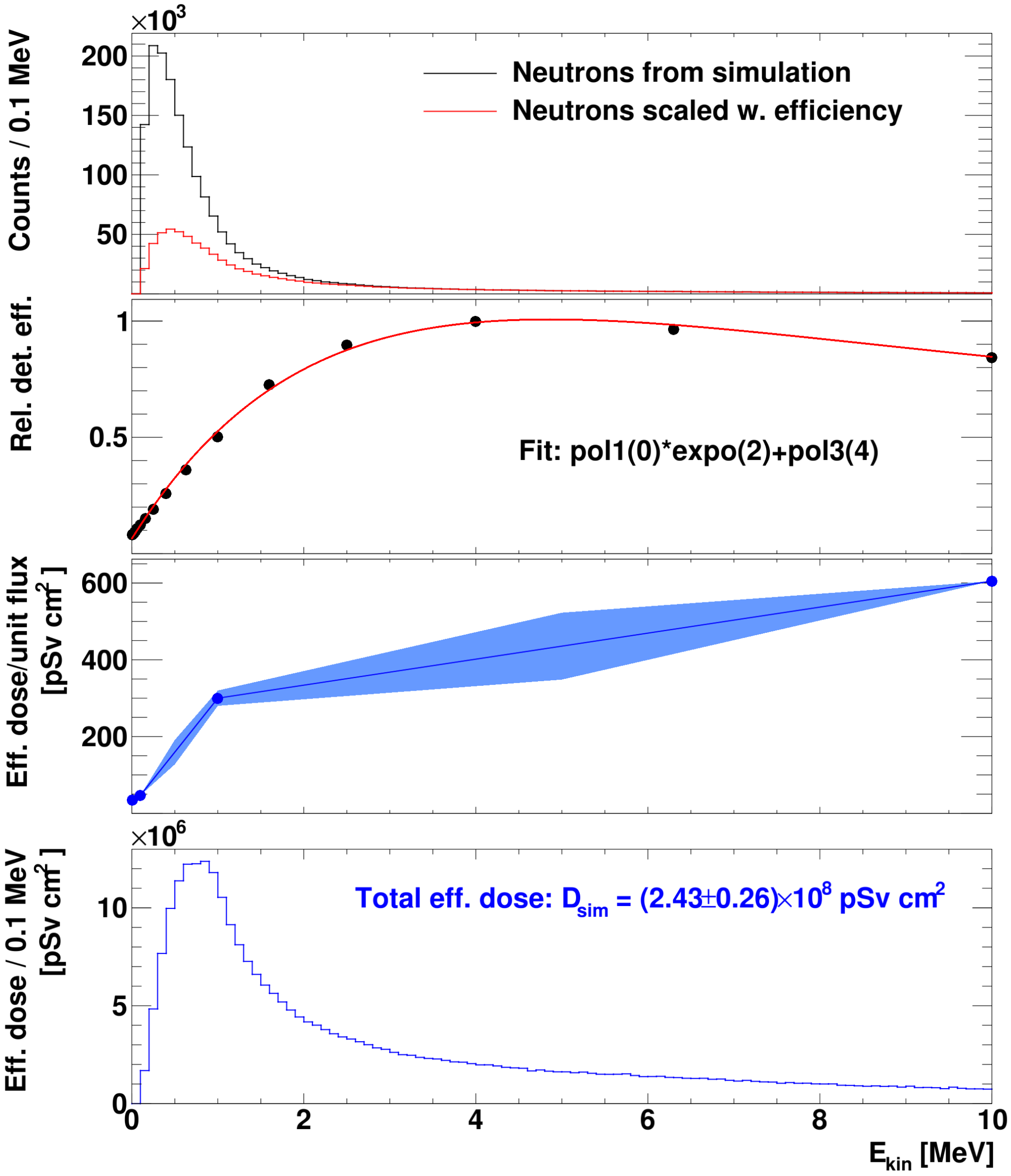

Figure 5.19: The comparison of the simulation and measurements of the passive neutron detector required the conversion of the kinetic energy distribution of the pseudodata to the total measured dose. At first, the neutrons from simulation (top, black) must be scaled with the efficiency of the detector [226] (second plot), resulting in the red distribution in the first plot. Further, the conversion to the measured dose is required which is based on [227], shown in the third plot. Since fitting with the low number of data points was hardly possible, interpolation of the data was used. The systematic uncertainties caused by this interpolation were estimated by adding two more data points at $0.5\,\mathrm{MeV}$ and $5\,\mathrm{MeV}$ and varying these by $\pm 20\,\%$ of their value from interpolation. Using this conversion yields the distribution at the bottom which was integrated to gain the total dose per unit flux of $D_{\mathrm{sim}} = 2.43 \pm 0.26 \cdot 10^{8}\,\mathrm{pSv\,cm^{2}}$.

histogram shows the distribution of the kinetic energy of the neutron hits in the Bonner sphere in the pseudodata. The red distribution in the same plot is the same pseudodata after the efficiency correction. The correction function [226] is shown in the second plot. These data points were fitted by a combination of an exponential and polynomial function which was then used for the efficiency correction. After this correction, it was required to convert the kinetic energy into the effective dose. Measurements of this can be found in [227] but the number of data points in the required range of 0.1 to $10\,\mathrm{MeV}$ is small. Because of that, a proper fit to these data points was hardly possible and the data was interpolated instead. This conversion function is shown in the third plot of figure 5.19. Since this low density of data points was the main source of inaccuracy in the conversion process, two additional data points were added manually to estimate this systematic uncertainty. The points were placed at a kinetic energy of $0.5\,\mathrm{MeV}$ and $5\,\mathrm{MeV}$ to fill gaps in the available data where the largest influence on the pseudodata was expected. Their value was varied by $\pm 20\,\%$ around their estimate from interpolation to gain an upper and lower estimate for the uncertainty of this method. Applying this conversion to the efficiency corrected pseudodata resulted the estimate of the energy dependent effective dose (bottom plot in figure 5.19). The integral of this distribution yielded the estimate of the total effective dose per unit flux measured by the Bonner sphere of $D_{\text{sim}} = 2.43 \pm 0.26 \cdot 10^8\,\mathrm{pSv\,cm^2}$ with the systematic error caused by the conversion process.

This dose was based on the events of $N_{\text{p,sim}} = 1 \cdot 10^7$ simulated primary protons and had to be rescaled to the full number of protons of the beam time $N_{\text{p,tot}} = 6 \cdot 10^{13}$. Further, the scaling with the area of the front face of the Bonner sphere A_{bs} is required to gain the total effective dose of the irradiation test D_{tot}

$$D_{\text{tot}} = \frac{D_{\text{sim}}}{A_{\text{bs}}} \cdot \frac{N_{\text{p,tot}}}{N_{\text{p,sim}}}. \tag{5.3}$$

Having a diameter of $32\,\mathrm{cm}$ the area is $A_{\text{bs}} = 804.25\,\mathrm{cm}^2$ which leads to a total effective dose of $D_{\text{tot}} = 181 \pm 19\,\mathrm{mSv}$. Comparing this to the measured value of $187.4\,\mathrm{mSv}$ shows an excellent agreement within the uncertainties and because of that the simulations seems viable to estimate the strength of the irradiation of the germanium crystal without an additional correction.

5.3.1.4 Estimations of the irradiation of the germanium crystal

Since the results of the simulations for the beam time are in line with the measurements of the neutron detector, the same scaling via the amount of beam particles could be performed for the germanium detector:

$$N_{\text{n,tot}} = \frac{N_{\text{n,sim}}}{A_{\text{Ge}}} \cdot \frac{N_{\text{p,tot}}}{N_{\text{p,sim}}}, \tag{5.4}$$

with the areal neutron density during the complete irradiation $N_{\text{n,tot}}$ and within the simulation $N_{\text{n,sim}} = 288\,581$. The frontal area of the germanium crystal is $A_{\text{Ge}} = 30.11\,\mathrm{cm}^2$. These numbers result in $N_{\text{n,tot}} = 5.6 \cdot 10^9/\mathrm{cm}^2$ which is $57\,\%$ of the average neutron load previously calculated for a crystal within 180 days of $\overline{\text{P}}$ANDA beam time. Translated to $\overline{\text{P}}$ANDA days this amount equals to 103 days.

The previous estimation still ignored the difference in the distribution of the kinetic energy of neutrons in $\overline{\text{P}}$ANDA and the irradiation test. Both of these are shown in figure 5.20. Here the simulated distributions are normalized for easier comparison and a slightly higher average of the kinetic energy in the neutron distribution of $\overline{\text{P}}$ANDA is visible.

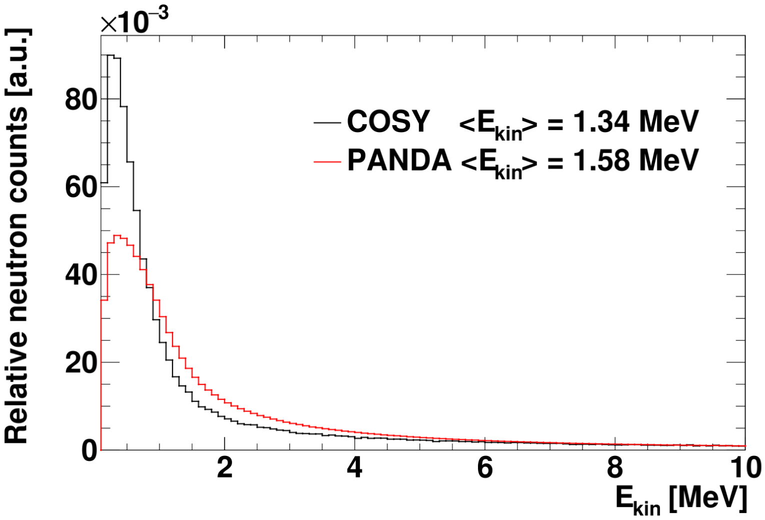

Figure 5.20: Comparison of the distributions of the kinetic energy of neutrons in the simulations of $\overline{\text{P}}$ANDA and COSY. Both were normalized for a better comparison. While both pseudodata have their maximum at similar energies of $0.4\,\text{MeV}$, the average kinetic energy of neutrons in $\overline{\text{P}}$ANDA is slightly higher due to a more pronounced high energy tailing.

This difference could be factor in when the total non-ionizing energy loss (NIEL) was used to compare both scenarios It reflects the damage caused to the lattice structure of a solid depending on the kinetic energy of the impinging particle. Unfortunately, measurements of this effect for germanium are rare and especially for neutrons unavailable. Because of that, a workaround was required which was based on measurements of the NIEL for other particles and target materials. In addition, the displacement damage cross section D was used which is proportional to the NIEL.

The process of this conversion is shown in figure 5.21 and will be explained in the following. The top left diagram shows measurements of the NIEL for protons. These are available for silicon as well as germanium [228] spanning a wide range of kinetic energies. The similar mass of protons and neutrons allows a direct translation of the kinetic energy in the relevant range for the irradiation test as well as $\overline{\text{P}}$ANDA (0.1 to $10\,\text{MeV}$). Since measurements of the displacement damage of neutrons in silicon were available [229] the idea was to apply the same scaling factor to this data as it could be extracted from the proton data. This scaling is energy dependent as shown in the top right plot of figure 5.21. A function, composed of exponential and polynomial parts, was used to fit and interpolate the data points.

In the bottom left the neutron data for silicon is shown. This data is normalized to the displacement damage for neutrons at a kinetic energy of $95\,\text{MeV}$ and rises with increasing kinetic energy of the neutron. In addition to that, resonances in the displacement damage for specific energies can be observed. Since these are supposed to be material dependent, they were ignored in the fit. Multiplying the fitted function with the scaling function gained from the proton data yielded the estimation for germanium (red function in the plot).

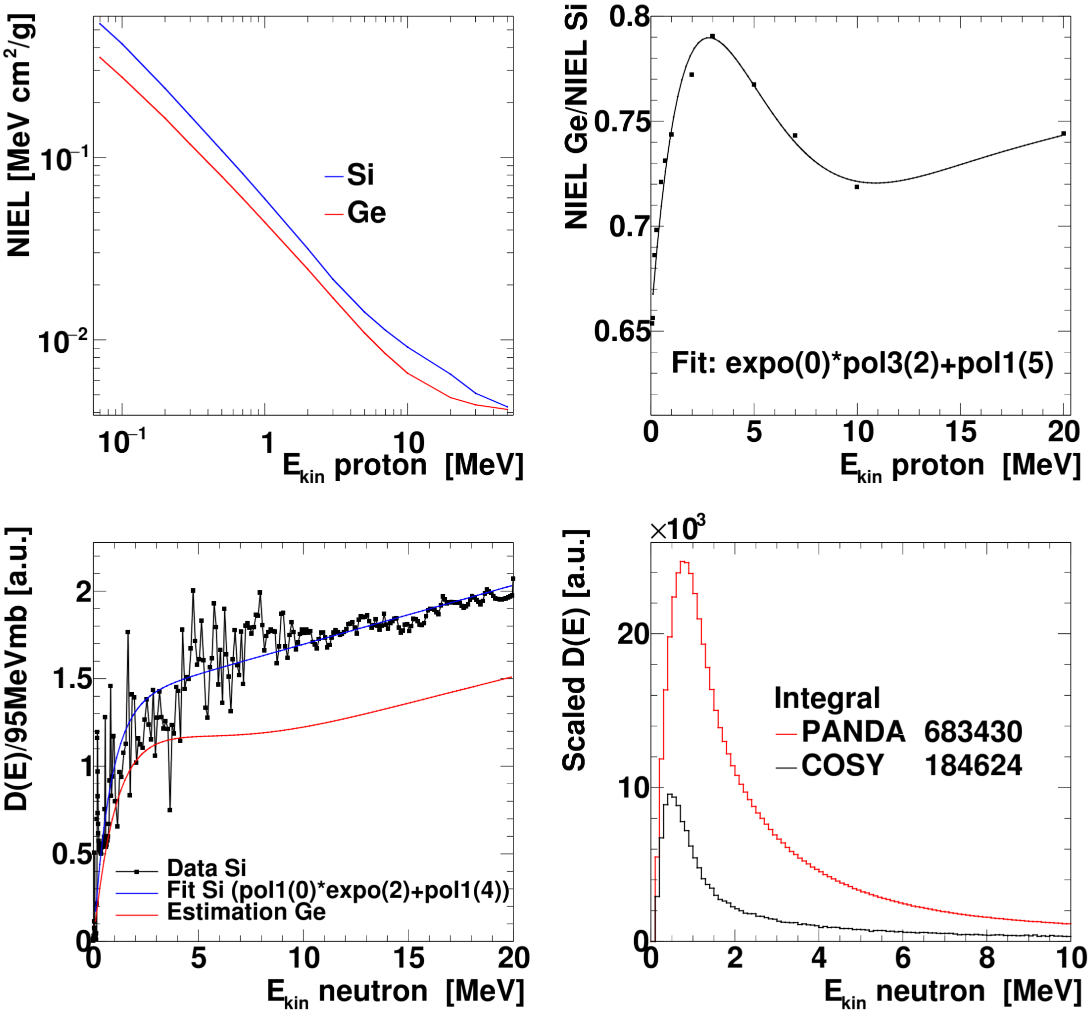

Figure 5.21: For a proper comparison of the irradiation tests and the conditions at $\overline{\mathrm{P}}$ANDA a scaling via the total non-ionizing energy loss NIEL is possible. Since no data was available for germanium, an estimation based on proton data for germanium and silicon [228] (top left) was used. The same scaling as extracted from these proton data (top right) was applied to the data of the displacement damage of neutrons in silicon [229] (bottom left). A fit of this data allowed to smoothen the data and reduce element-specific effects. The estimation for germanium (red) is shown in the bottom left plot which is the product of the fit to the silicon data (blue) and the scaling factor. This estimation folded into the neutron energy distributions of the simulations of $\overline{\mathrm{P}}$ANDA and the test setup at COSY are shown in the bottom right. Scaling the integrated displacement damage shows that the irradiation tests were able to cover 93.8 days and 56 ± 9 days of $\overline{\mathrm{P}}$ANDA conditions.

Folding this estimation with the neutron distributions of a single crystal from both simulations (figure 5.20) resulted in the bottom right plot. The integral of these distributions yielded $683\,430$ for $\overline{\text{P}}$ANDA and $184\,624$ for COSY as a comparable measure for the strength of the displacement damage. Finally, these numbers needed to be scaled to the full beam time in the same way as shown for $\overline{\text{P}}$ANDA in equation 5.2 and COSY in equation 5.4, respectively. This gave a total displacement damage of $2.13 \cdot 10^{11}$ for 180 days at $\overline{\text{P}}$ANDA and $1.11 \cdot 10^{11}$ for the beam time at COSY. The division of these numbers showed that the irradiation test was able to simulate $51.1\,\%$ of the full $\overline{\text{P}}$ANDA beam time which is 93.8 days. This is roughly $10\,\%$ less compared to the estimation without this latest correction. Applying the same correction to the second irradiation test reduced its estimate to 56 ± 9 days of $\overline{\text{P}}$ANDA.

5.3.2 Data analysis of the irradiation tests via pulse shape analysis

After the neutron load of both irradiation test beams was calculated and put in relation to $\overline{\text{P}}$ANDA, their effect on the detector signal had to be studied. This was done by a pulse shape analysis (PSA) of the digitized signal shapes. This technique has already been successfully used to study and reduce the effects of strong magnetic fields on EUROBALL HPGe crystals in [179]. These strong fields affect the movement of charge carriers. They begin to curl within the crystal which elongates their path length. This increases the rise time of the signal as well as the trapping chance. The resolution loss introduced by both effects could be partially annulled as shown in figure 5.22. In addition to that, this technique allows to disentangle pile up events of germanium signals as well as the application of filters that reduce the effect of neutron damage. This analysis is shown in the following section before the results of both beam tests will be presented.

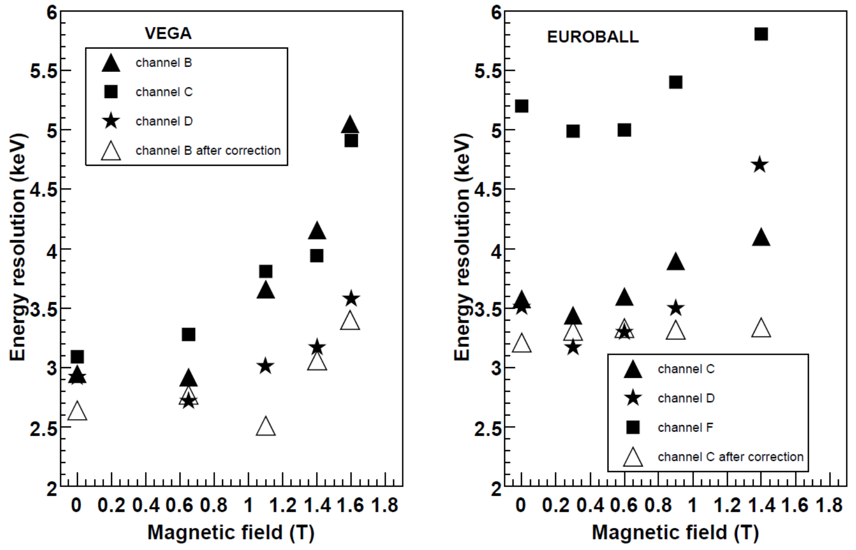

Figure 5.22: The performance of EUROBALL HPGe crystals in strong magnetic fields was studied in [179]. Pulse shape analysis was used to recover the loss of energy resolution caused by the magnetic field (figure from [179]).

Pulse shape analysis is the state of the art technique in the digital analysis of germanium detector signals. It is done via moving window deconvolution (MWD) which is explained in detail in [230]. This technique allows to recover the amplitude of the pulse while shortening the long detector signals which strongly increases the rate capabilities of the detector system. The MWD method can be separated in three major steps: deconvolution, differentiation and averaging. All these steps as well as the input signal are shown in figure 5.23 and are briefly explained in the following.

A typical signal of a germanium detector $f(t)$ consists of a quickly rising edge and a slow exponential decay afterwards. This slow decay is caused by the slow discharge of the charge collection capacitor of the preamplifier. The information of the deposited energy is solely contained in the amplitude of the signal A^f. The deconvolution of $f(t)$ is used to disentangle A from the exponential decay. The algorithm exploits the knowledge of the exponential shape of the decay and because of that any constant offset must be purged before its application. An isolated exponential decay that starts at $t_0 = 0$ can be described via

$$f(t) = \begin{cases} A \exp(-\frac{t}{\tau}) & t \geq 0 \\ 0 & t < 0. \end{cases} \tag{5.5}$$

With the signal $f(t_n)$ at the time t_n the signal amplitude $A(t)$ can be derived from

$$\begin{aligned} A(t) &= f(t_n) + A - f(t_n) \\ &= f(t_n) + A\left(1 - \exp\left(-\frac{t_n}{\tau}\right)\right) \\ &= f(t_n) + \frac{1}{\tau}\int_0^{t_n} f(t)dt \\ &= f(t_n) + \frac{1}{\tau}\int_{-\infty}^{t_n} f(t)dt\,. \end{aligned} \tag{5.6}$$

This gets rid of the exponential decay and yields a staircase signal with the step height equal to the height of the detector output. In the digital domain, where all computations of the detector signals will be performed, the discretized form $A[n]$ of $A(t)$ has to be considered:

$$\begin{aligned} A[n] &= x[n] + \frac{1}{\tau}\sum_{k=-\infty}^{n-1} x[k] \\ &= x[n] - \left(1 - \frac{1}{\tau}\right) x[n-1] + A[n-1]. \end{aligned} \tag{5.7}$$

This recursive form of $A[n]$ is implemented in the analysis algorithm. This deconvoluted signal $A[n]$ has an infinite length and can be identified as the output of a preamplifier with transistor reset.

The further processing of this signal requires to shorten the signal to prevent overflows in the software. This can be achieved by a numerical differentiation which yields

---

[f] Ignoring ballistic deficits at this point

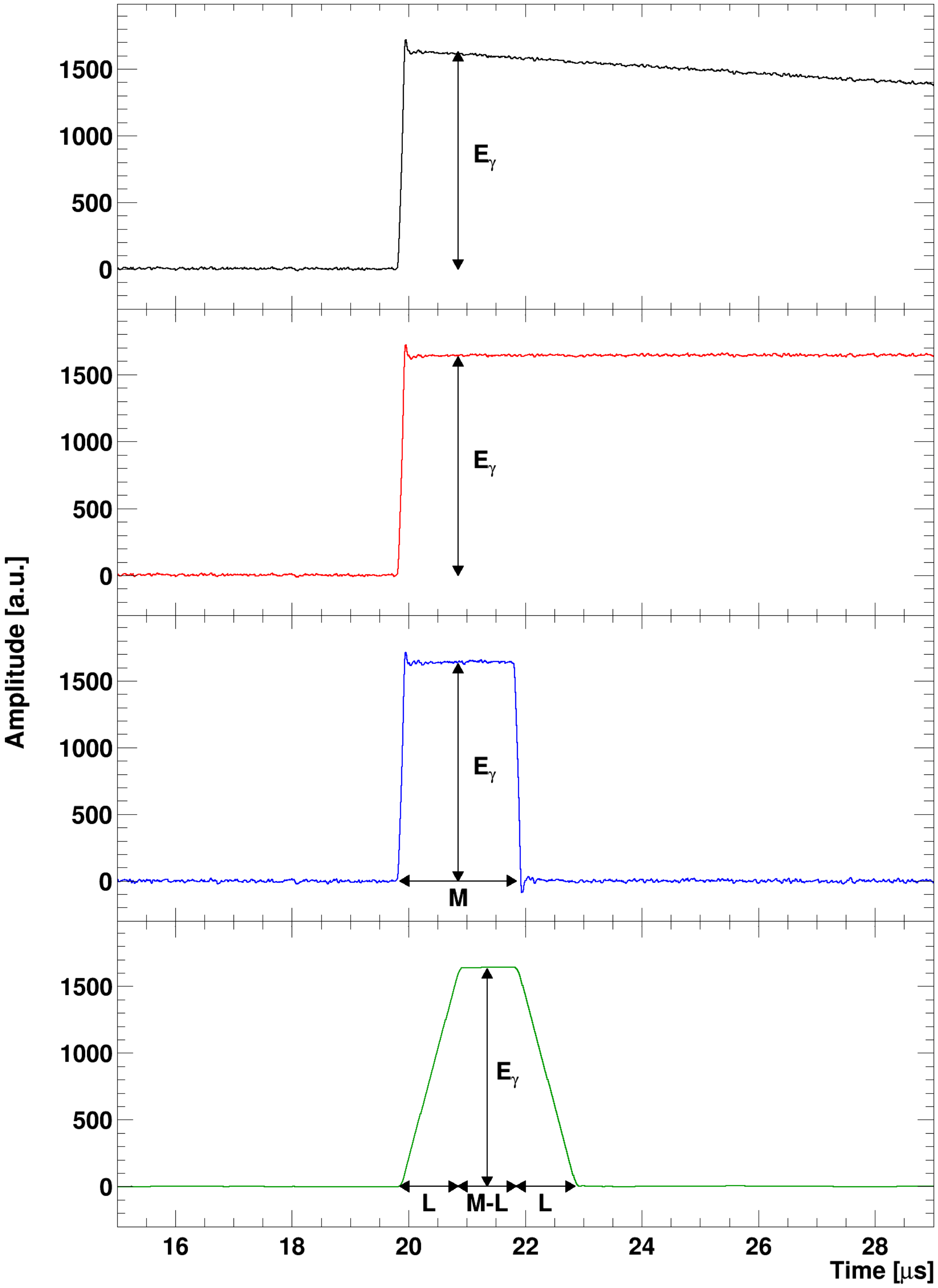

Figure 5.23: The moving window deconvolution algorithm requires three major steps. These are the deconvolution of the detector signal followed by a numerical differentiation and a final averaging which filters high frequent noise. The plot shows the input signal as well as the output of each step from top to bottom. Details are given in the text.

$$\begin{aligned} MWD_M[n] &= \nabla_M A[n] \\ &= A[n] - A[n-M] \\ &= x[n] - x[n-M] + \frac{1}{\tau} \sum_{k=n-M}^{n-1} x[k]. \end{aligned} \tag{5.8}$$

This produces a rectangular signal of the width M by subtracting the signal value delayed by M from the undelayed one.

The final step of the deconvolution algorithm is the application of a low pass filter $MA_L[n]$. This filtering is performed by a moving average filter as shown in equation 5.9.

$$\begin{aligned} MA_L[n] &= \frac{1}{L} \sum_{k=n-M}^{n-1} MWD_M[k] \\ &= MA_L[n-1] + \frac{1}{L}(MWD_M[n] - MWD_M[n-L]) \end{aligned} \tag{5.9}$$

This filter produces a trapezoidal ($L \neq M$) or triangular ($L = M$) signal. For $L < M$ the trapezoid has a flat top with the width $M - L$ with the same amplitude as the rectangular function $MWD_M[n]$. The high frequency delta noise however is reduced by the low pass properties of the filter which improves the signal-to-noise ratio of the detector and consequently its resolution. Multiple repetitions of this averaging can be applied in series to further reduce the noise if necessary. Testing of various combinations of the parameters M and L showed the best results for $M = 200$ and $L = 100$ for the used detectors [49].

In addition to the deconvolution a peak finding algorithm was required. The first derivative of the trapezoidal signal is a good candidate for this. This derivative is only positive in case of a rising edge of a triangle and because of that the signal of a detected particle can be identified by the first derivative surpassing a certain threshold. Furthermore, the second derivative was used to find the center of the trapezoid since this is positioned right in the middle of the first and last local maxima that occur due to the rising and falling edge of the trapezoid. Figure 5.24 shows an example of these derivatives and the corresponding trapezoid.

The signal amplitude is calculated from the average of the central half of the flat top. The averaging of these $\frac{M-L}{2} + 1$ values further decreases noise. In addition, this choice prevents any influence of varying rise times of the detector signal. The effect of these rise times on the algorithm is visible in the rounding of the edges of the flat top and can be ignored because of this choice. Additionally, the baseline of the signal must be subtracted from the flat top height to calculate the amplitude of the trapezoidal signal. 20 data points in front of the trapezoid are averaged for this. Their position is determined relative to the first maximum of the second derivative which marks the beginning of the rising edge of the trapezoid. Both regions of interest (ROI) used to calculate the amplitude - and hence the deposited energy - are marked in figure 5.24.

5.3.3 Results of the irradiation tests

Before going into more detail of the analysis, the influence of the irradiation on the full energy spectrum will be showcased. Figure 5.25 shows the measured energy spectrum before (left) and after the full irradiation of the first beam time (right). Both spectra are scaled to contain the same number of events in the $1332.5\,\text{keV}$ line of ^{60}Co. Before the irradiation, the only peaks in the

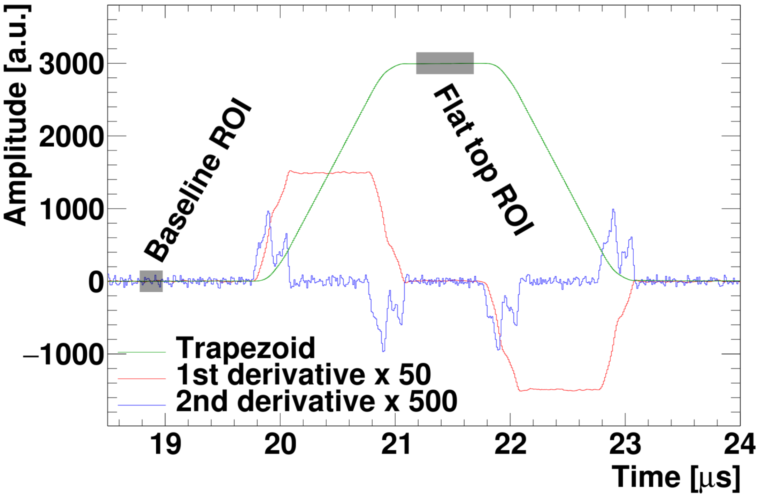

Figure 5.24: As described in the text, the first and second derivative of the trapezoid were used to identify a signal. Once the first derivative surpasses a specific threshold, the rising edge of a (shaped) detector signal was found. In addition to that, the maxima of the second derivative were used to find the center of the flat top, situated right in the middle of their positions. This information was used to calculate the height of the flat top as well as the baseline and hence the amplitude of the signal. The regions of interest (ROI) used to average these measures are marked in the plot.

spectrum were the two ^{60}Co transitions at $1173.2\,\mathrm{keV}$ and $1332.5\,\mathrm{keV}$. The irradiation increased the amount of detected lines. These were caused by short living isotopes created by neutron activation. The most prominent ones were the $139.7\,\mathrm{keV}$ line of ^{75m}Ge, the $1368.4\,\mathrm{keV}$ line of ^{77}Ge and the $1778.97\,\mathrm{keV}$ line of ^{28}Al. The half-life of these lines is short and ranges from $47.7\,\mathrm{s}$ for ^{75m}Ge to $11.3\,\mathrm{h}$ for ^{77}Ge [231] and hence their appearance is amplified compared to $\overline{\mathrm{P}}$ANDA due to the higher beam intensity at COSY to shorten the required beam time. Additionally, the electron-positron annihilation line at $511\,\mathrm{keV}$ can be prominently observed in the irradiated spectrum. Furthermore, the shape of the peaks changed, caused by the radiation damage of the germanium crystal. A low energy tail broadened the lines and decreased the energy resolution. The influence of this on the resolution with increasing amount of irradiation and ways to reduce this effect are the main topics of the following section.

As pointed out in [232] the sensitivity to radiation damage depends on the position of the interaction point of the photon within the germanium crystal. Figure 5.26 shows this for the central core as well as the segmented outer contacts of the AGATA detectors. Since the positive high voltage is applied to the central core, electrons are attracted by this central contact while holes travel to the outer segments. Because of that, the travel distance for both strongly varies with the interaction point of the photon, resulting in a high (low) sensitivity of hole (electron) trapping for central interactions and vice versa for interactions at large radii.

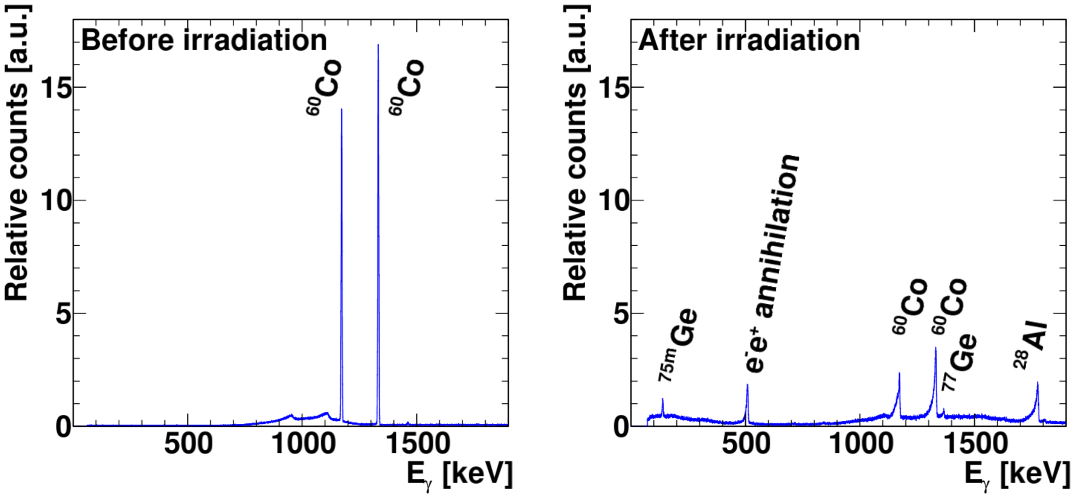

Figure 5.25: Comparison of the measured energy spectrum before and at the end of the irradiation. Both spectra are normalized to the content of the $1332.5\,\mathrm{keV}$ line of ^{60}Co. Multiple peaks arise due to the neutron activation of germanium an aluminum. In addition, the shape of the peak changes due the radiation damage of the germanium by developing a low energy tail.

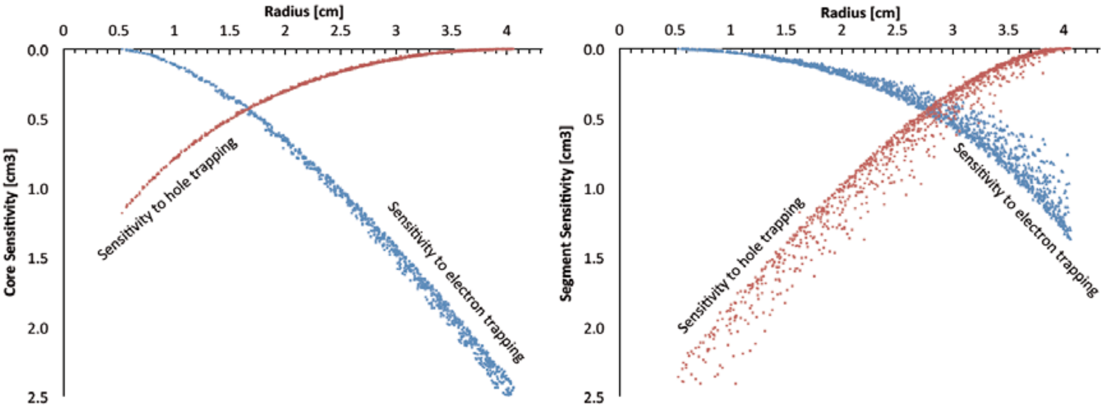

Figure 5.26: As calculated for AGATA, the trapping sensitivities for electrons and holes strongly depend on the radius of the interaction position and the corresponding travelling distance of the charge carriers. Due to the positive central core contact electrons are barely affected by trapping for small radii while holes are highly susceptible for it and vice versa for large radii. While the central core is more sensitive to electron trapping (left), the outer contacts are more affected by the energy loss due to hole trapping (figure from [232]).

With the knowledge of the interaction radius these trapping effects can be corrected. For AGATA this is shown in figure 5.27 where the blue data marks the radial dependence of the uncorrected centroids of the full-energy peaks. Fitting this data via

$$\eta^i_{\text{tot}}(r) \cong 1 - [N_e s^i_e(r) + N_h s^i_h(r)]$$

and performing an event-wise correction via this function yields the corrected data shown in red [232]. The fit function is the first order of the Taylor expansion of the collection efficiency $\eta^i_{\text{tot}}(r)$ which depends on the density of trapping sites for electrons and holes $N_{e/h}$ as well as their trapping probabilities $s^i_{e/h}(r)$. For the segments the uncorrected centroids show a severe drop at small radii. This shows the high sensitivity of the hole trapping since small radii are equivalent to long travel distances of holes. The effect of the hole trapping on the core is smaller as shown on the right. For large radii the trapping of electrons leads to measurable energy losses. Common to both distributions is that all data points are below the expected energy but this can be corrected by recalibration. When the corrections are applied both contacts show a much more even distribution along the full radial range.

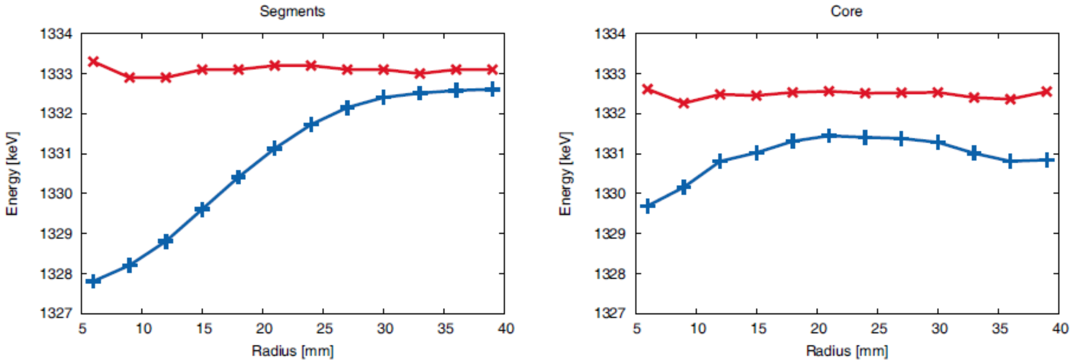

Figure 5.27: The trapping of charge carriers results in a radial dependence of the energy of the centroid of the ^{60}Co line (blue data points). As shown in this data from AGATA, this effect is strong for the outer contacts and small radii where the holes have to travel long distances. The central contact is less affected by this but a small drop in the energy is visible for large radii where the trapping of electrons is significant. Both data sets can be corrected (red data points) by fitting and correcting via the collection efficiency $\eta^i_{\text{tot}}(r)$ and recalibration afterwards. The corrected data is consistent in the position of the centroids for the full radial range (figure from [232]).

This improvement indicates that similar corrections should be performed on the obtained data of the irradiation test. In contrast to AGATA, the EUROBALL crystals are unsegmented and, because of that, the position of the interaction point must be extracted in another way. The rising edge of a pulse offers a way to estimate the interaction point and hence the travel times of both charge carriers. The rise time is the combination of the travel times of both charge carriers. It consists of the time between the first arrival of any charge carrier at one of the contacts and the full collection of all electrons and holes. A common measure for this is the time spent between the signal reaching $10\,\%$ and $90\,\%$ of its maximum t_{1090} . Unfortunately, the information carried by the rise time is not unique since the velocities of electrons and holes are too similar to distinguish events with small radii from large radii. In both types of events one type of charge carrier finishes its collection process significantly faster than the other one. Because of that, a closer look at the shape of the rising edge is required. This can be done by looking at the first derivative of the signal. Since the detector signal is proportional to the charge of the preamplifier capacitor, its first derivative can be identified as the detector current. This current is the sum of the current caused by the electrons and holes traveling through the crystal. The shape of this highly depends on the starting point of the electron-hole pairs and thus the interaction point of the detected photon. Figure 5.28, taken from [233], shows four examples of this signal. Holes travelling to the grounded outer contact are shown in pink, electrons traveling to the positive center in turquoise. As previously pointed out, the smallest and biggest radial position share the same long rise time. Intermediate starting points have a smaller rise time. In contrast to the rise time the peak of the current signal, dominated by the electrons, can be used to estimate the interaction radius uniquely. As the figure shows, this position depends on the travelling distance of the electrons which increases with the radius resulting in a delayed position of the maximum.

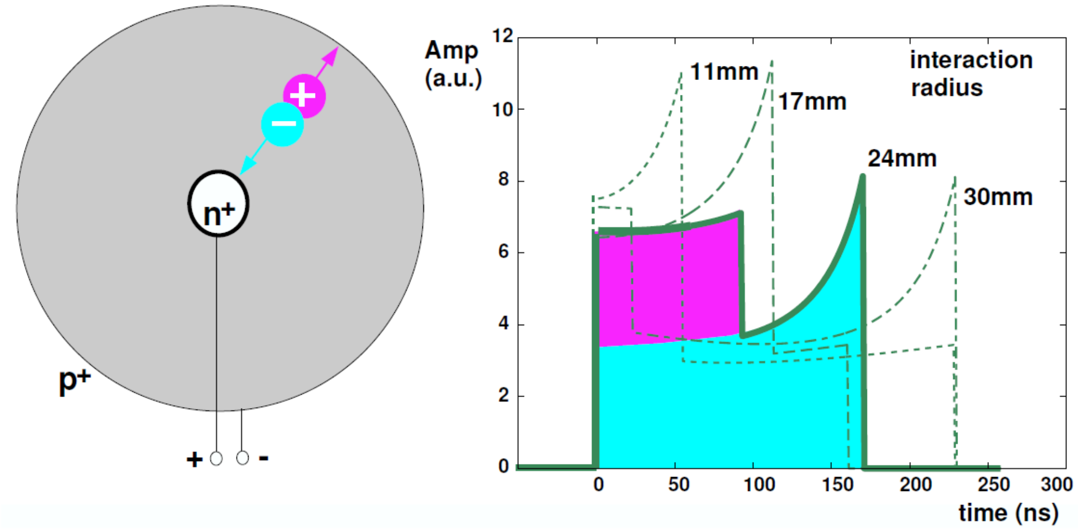

Figure 5.28: In contrast to the rise time, the position of the maximum of the detector current (right plot) is dominated by the electrons (turquoise). Because of that, it offers the possibility to estimate the interaction radius without ambiguities (figure from [233]).

Figure 5.29 shows two examples of rising edges of pulses and the corresponding current. Comparing these to figure 5.28 allows to estimate that the left one shows an event occurring close to the central contact. The interaction of the right one, however, must have occurred at a large radius. Both events can be clearly separated by using the time stamp of the maximum of the current signal t_{Imax}. Furthermore, the measures t_{10} and t_{90} are shown in both plots. They mark the time when the rising edge reaches $10\,\%$ and $90\,\%$ of the maximum of the pulse. The time between these measures is the rise time t_{1090}. Additionally, both measures can be combined with t_{Imax} to form relative measures which can be used to describe the shape of the pulse. These are $t_{10\text{Imax}}$ and $t_{\text{Imax}90}$ calculated by the differences of the corresponding values.

Further studies need to combine these three characteristics of the rising edge with the extracted signal height. Two-dimensional histograms have been formed for each of these three measures on the abscissa and the signal height on the ordinate. Examples for this are shown in figure 5.30. The histograms show the distribution of $t_{10\text{Imax}}$ in the range of both ^{60}Co lines. Again the histograms

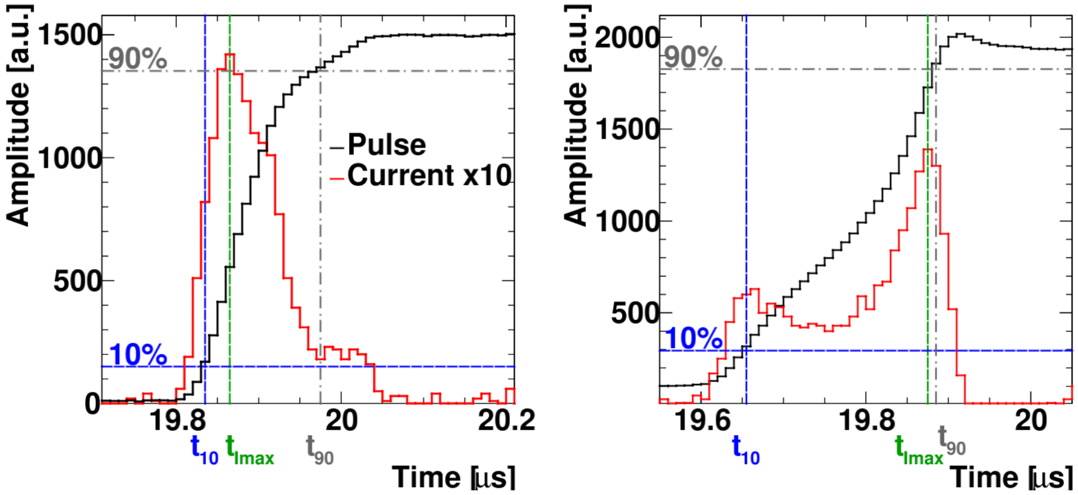

Figure 5.29: Two examples of the rising edge of a detector signal. The signal is proportional to the charge of the preamplifier capacitor. Its derivative consequently is the detector current. The left example shows an interaction at a small radius. The right one, however, is an example of an interaction point at a large radius. In both plots the thresholds to estimate t_{10} and t_{90} are marked as well as the resulting timestamps. In addition to that, the third time stamp to characterize a signal, the position of the maximum of the current t_{Imax}, is shown. Especially t_{Imax} varies strongly for both signals which allows to distinguish them.

before (left) and after (right) the irradiation of the first test are shown. In the unirradiated histogram the signal height does not depend on $t_{10\mathrm{Imax}}$ and hence the interaction point. In contrast to that, the signal height of the irradiated crystal strongly depends on $t_{10\mathrm{Imax}}$. Especially for small values of $t_{10\mathrm{Imax}}$ the decreased signal height is visible. These events correspond to small radii of the interaction point and consequently a long travel distance of the holes. Combined with their higher sensitivity to trapping explains the lost signal amplitudes in the distribution seen for both lines. This matches the expectations from the data of AGATA presented in figure 5.27.

To correct this signal height a similar procedure as for AGATA was performed. The irradiated data of the 1332 keV line was fitted and an event-based correction based on this was performed to align the centroids. This correction required the energy of the centroids of each vertical slice of the two-dimensional histogram and because of that each of these slices was fit independently. Since the shape of the distribution in these slices was influenced by the radiation damage, the best and most robust description was achieved by fitting the sum of two Gaussian functions and adding a constant background. For each slice, the maximum position of these fits was plotted versus the corresponding $t_{10\mathrm{Imax}}$. This data was fitted by a second-order polynomial which was used to correct the data. Figure 5.31 shows an example of such a correction procedure. The top left shows the uncorrected two-dimensional histogram. The centroids resulting from the slice fits are shown on the right. The standard deviation of the fit was used to weight the data points for the fitting. This reduced the influence of slices with only a few entries as well as broad distributions. The bottom left shows the corrected two-dimensional histogram. The centroids of the slices are

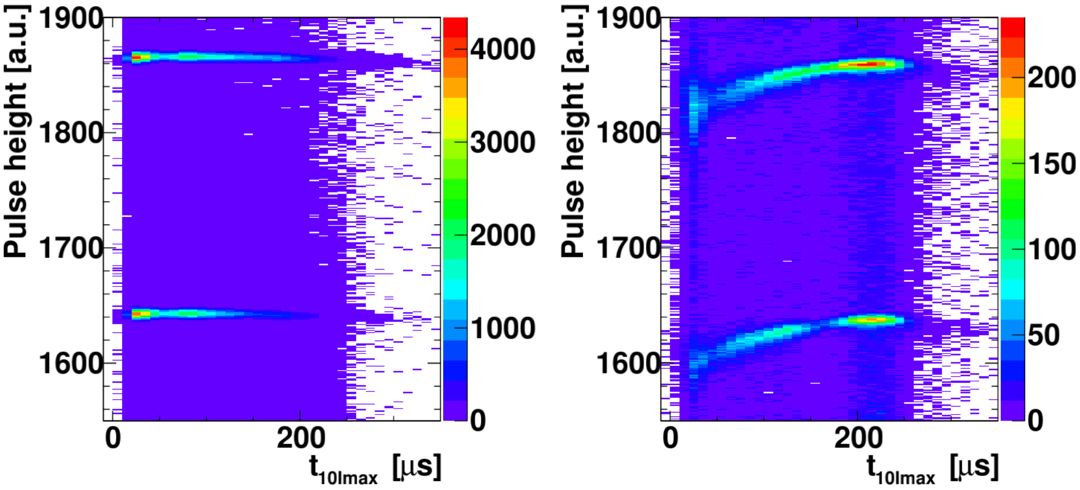

Figure 5.30: Histograms of $t_{10\text{Imax}}$ and the pulse height before and after the first irradiation test. The energy range containing both lines of ^{60}Co is shown. In the unirradiated histogram on the left, the pulse height is independent of $t_{10\text{Imax}}$. This changes after the irradiation as shown in the histogram on the right. The measured pulse height drops for decreasing $t_{10\text{Imax}}$. This behavior is expected because these events belong to smaller radii of the interaction point which is equivalent to long travel distances of the holes and consequently an increased influence of their trapping. The broadening of the distribution of these inner events originates from the same effect.

shifted to the same level. The influence of this on the shape of the pulse is shown in the bottom right. The correction eliminated the low energy tail and aligned these entries much better with the maximum of the distribution. All uncorrected distributions as well as their correction functions are shown in the appendix (figure A.6).

The evaluation of the influence of the irradiation and the corrections is based on comparing the FWHM, the FWTM and the ratio of both. Especially the FWTM is a measure for possible a tailing effect caused by the irradiation.

This correction was performed for all of the three previously presented measures and for 15 data points over the course of the first irradiation. The results are shown in figure 5.32. Besides the FWHM and the FWTM the fraction of both is shown. This fraction is a measure to compare the shape to a Gaussian peak shape where this fraction is 1.8226. The data shows a progressive decrease of the energy resolution with increasing irradiation. The data during the temperature issues of the detector and the varied high voltage due to it (compare section 5.3.1.1) is marked by the gray area. These were not taken into account for the data analysis and are only included for completeness to show the negative effect of incomplete biasing.

When looking into more detail at the FWHM at the beginning of the beam time, the starting resolution of more than $4\,\text{keV}$ was approximately twice as high as the specified resolution of the detector. This was the best performance that could be achieved during the irradiation test. This rather poor performance can be explained by the combination of two influences. Firstly, remaining electronic noise caused by other electronics in the periphery of the detector decreased the detector resolution. A lot of time and effort was invested to get rid of this noise but it

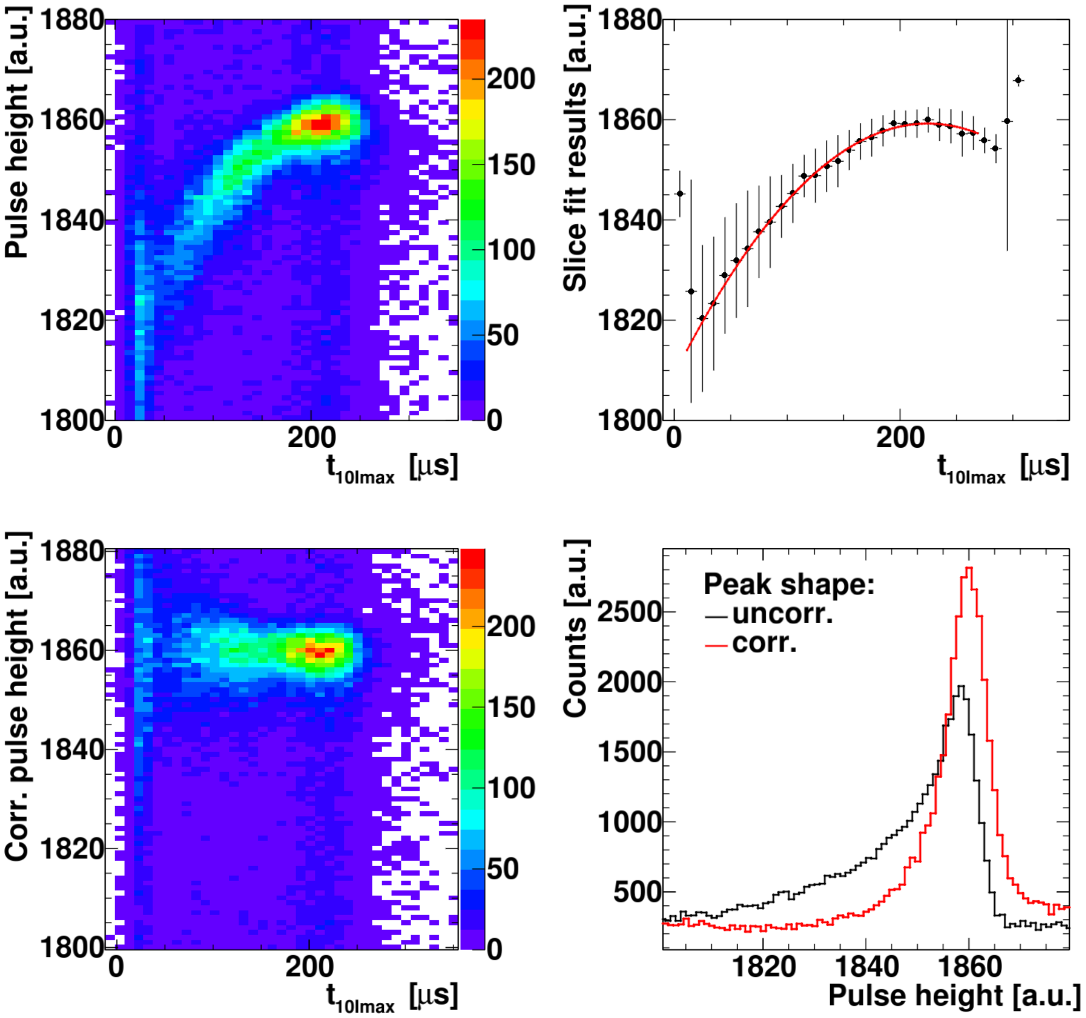

Figure 5.31: These figures show an example of the correction procedure. The two-dimensional histogram in the top left is uncorrected. Each vertical slice was individually fit and their centroid extracted. The distribution of these is shown in the top right. The width of the distributions in each slice was used to weight the fitting, done via a second-order polynomial. The bottom left shows the corrected two-dimensional histogram with the aligned centroids. Finally, the influence on the peak shape is shown in the bottom right plot. It shows the projection of the top left (black) and bottom left (red) two-dimensional histograms to their y-axis. The correction removes the biggest portion of the tailing of the peak.

can not be excluded that a remainder of it still influenced the resolution. Secondly and most probably the biggest limitation of the detector resolution was based on a lack of dynamic range of the combination of the detector and the data acquisition system. As shown in figure 5.30 the $1332.5\,\mathrm{keV}$ line was situated at approximately 1860 ADC channels which is only a small fraction of the possible 16384 channels of the 14 bit FlashADC. Unfortunately, it was not possible to increase the amplification of this preamplifier to improve the dynamic range in any way. In contrast to that, the high operational temperature should not have increased the leakage currents measurably at the beginning of the experiment (compare figure 5.3) but their effect should have been more prominent with progressing irradiation. Nevertheless, the data could still be used to study the effects of the irradiation and the performance of the applied corrections. The uncorrected resolution doubled from the beginning to the end of the irradiation. The resolution increased over time approximately linear with the amount of irradiation of the detector. At the same time, the FWTM roughly quadrupled from $7.66\,\mathrm{keV}$ to $30.86\,\mathrm{keV}$. Again the degradation seemed to be linear. This tailing seen in the FWTM was also visible in the FWTM/FWHM ratio which rises up to 3.6.

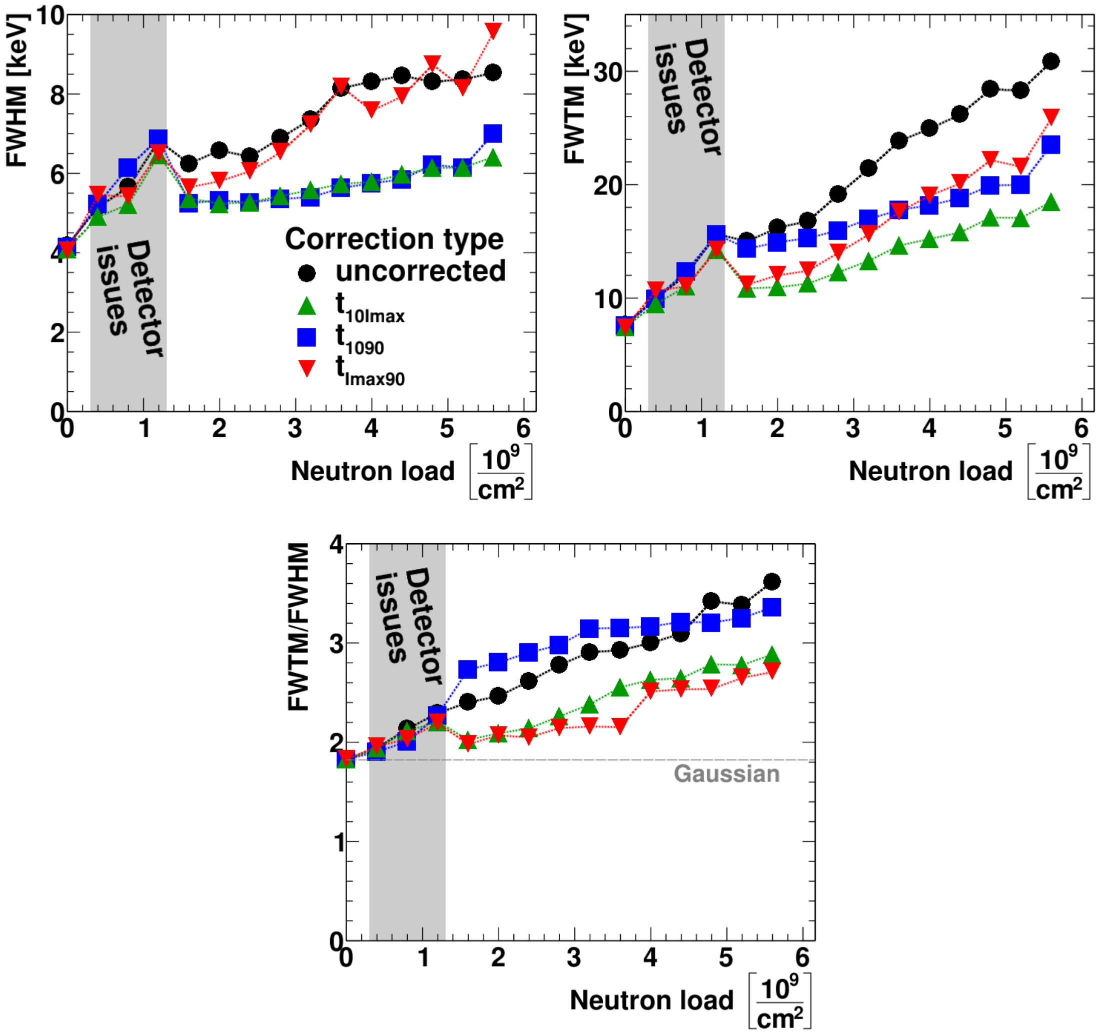

Figure 5.32: Progression of the detector resolution for the first irradiation beam time. The uncorrected data as well as the data for the three previously explained measures are shown for the FWHM, the FWTM and the ratio of both. The correction on $t_{10\mathrm{Imax}}$ performed best overall. The issues explained in section 5.3.1.1 are visible in the data. These data points were ignored in the analysis.

The application of the three corrections to this data highly differed in their performance. While the correction on t_{Imax90} barely improved or even worsened the FWHM, the effects of the other two corrections, based on t_{1090} and $t_{10\text{Imax}}$, were more pronounced. Both showed a comparable performance for the FWHM. Looking at the FWTM the situation differed. Here the correction based on $t_{10\text{Imax}}$ offered much better performance than t_{1090}. The correction based on t_{Imax90} started at similar values as $t_{10\text{Imax}}$ but performed worse for an increasing amount of neutrons. When looking at the ratio of both measures, none of the corrections allowed to recover a full Gaussian peak shape. At first glance, t_{Imax90} offered the best results for the ratio but this was biased by the large FWHM.

After testing these primary corrections, the application of a second order of corrections was tested. They use the corrected data of one measure and apply the correction based on one of the two remaining observables. This totaled in 6 second order corrections. Since these offered no significant improvement of the resolution compared to the correction using only $t_{10\text{Imax}}$ (compare figure A.7 in the appendix), they have not been studied further

To conclude the results of the measurements during the first beam time, table 5.3 includes the uncorrected resolutions for each data point as well as the results of the best performing correction, based on $t_{10\text{Imax}}$. When calculating the improvements of this correction, multiple options to specify them were available. The simplest one was to calculate the relative improvement of the full measured resolution I via

$$I = \frac{FWHM - FWHM_{\text{corr}}}{FWHM}. \tag{5.10}$$

This ignored that only a fraction of the resolution was influenced by the radiation damage. The electronic noise was unaffected and could be separated to study only the improvement of the fraction affected by the radiation damage in the crystal. Unfortunately, the limitation due to the data acquisition system prevented a proper separation. Because of that, the simplified method to quantify the improvement in equation 5.10 was used and it reached from $2.4\,\%$ at the beginning up to $30.4\,\%$. The average was $24.1 \pm 1.6\,\%$. The average was calculated using all data points after fixing the detector issues.

The same analysis procedure was applied to the data of the second beam time in July 2014. Figure 5.33 shows the progression of the detector resolution for the uncorrected as well as the three first-order corrections over the course of the irradiation. Looking at the beginning of the irradiation, the resolution of $3.4\,\text{keV}$ is better than in the first beam time. The reason for this was a higher amplification of the preamplifier of this detector. This can be seen in figure 5.34. The $1332\,\text{keV}$ line is shown at ADC channel 2510 which is significantly higher compared to the first beam time (compare figure 5.30, ADC channel 1860). Because of that, the signal was able to use more of the dynamic range of the data acquisition which lowered its limiting influence on the resolution. Nevertheless, the amplification was still too small to use the full dynamic range of the FlashADC and reach the resolution achieved in the analog data acquisition system at GSI ($1.96\,\text{keV}$). When looking at further data points of figure 5.33 the resolution first starts to deteriorate slowly but after the fifth data point a sudden degradation occurs. The moment of this degradation can be identified with the crash of the complete supply and data acquisition systems during the beam time. After restarting the system and resupplying the detector the system seemed fine and working properly again. Nevertheless, the noise of the system was still higher than before and regardless of the effort spent the resolution of the detector prior to the crash could not be recovered. Increasing the irradiation did not deteriorate the resolution further which shows the

Irradiation [n/cm^2]	**FWHM$_{\text{uncorr}}$ [keV]**	**FWHM$_{t_{\text{10Imax}}}$ [keV]**	**I [%]**
$0.0 \cdot 10^9$	4.19	4.09	2.4
$0.4 \cdot 10^9$	5.14	4.90	4.7
$0.8 \cdot 10^9$	5.65	5.21	7.7
$1.2 \cdot 10^9$	6.82	6.47	5.1
$1.6 \cdot 10^9$	6.24	5.37	14.0
$2.0 \cdot 10^9$	6.58	5.24	20.4
$2.4 \cdot 10^9$	6.42	5.27	17.9
$2.8 \cdot 10^9$	6.89	5.43	21.2
$3.2 \cdot 10^9$	7.36	5.58	24.2
$3.6 \cdot 10^9$	8.15	5.73	29.7
$4.0 \cdot 10^9$	8.31	5.79	30.4
$4.4 \cdot 10^9$	8.46	5.97	29.4
$4.8 \cdot 10^9$	8.31	6.14	26.1
$5.2 \cdot 10^9$	8.37	6.14	26.6
$5.6 \cdot 10^9$	8.53	6.41	24.8
		Average improvement:	$24.1 \pm 1.6\,\%$

Table 5.3: Tabulated resolutions of the data of the first beam time. Besides the uncorrected resolutions, the best correction based on t_{10Imax} is shown. The data taken during the detector issues is included in the table and marked by the horizontal lines. For the averaging only the data taken after these issues was considered.

limitation due to this introduced external noise. The resolution rather improved slightly over time. The effect of the corrections on the data was much less pronounced than for the data of the first beam time. Especially before the crash of the system the effect is negligible. Afterwards, it is small but again the correction using t_{10Imax} yields the best improvements. The FWTM in the right plot shows the same trend as the FWHM previously discussed. The influence of the corrections is rather small again. The fraction of both measures, shown in the bottom, highly differs from the first beam time. Independent of the application of any correction, the fraction remains constant over the full course of the beam time and seems to agree with the ratio expected for a Gaussian distribution. For a closer look ,the two-dimensional histograms of the ADC channel and t_{10Imax} for the first and last dataset are shown in figure 5.34. The histograms show the $1332\,\text{keV}$ line. The offset between the uncalibrated lines in both histograms can be explained by the required restart of the system which could have slightly changed the high voltage and consequently the position in the ADC. The dependence on t_{10Imax} that was seen in the irradiated data of the first beam time is much less pronounced. Because of that, no tailing of the peak occurs resulting in a negligible effect of the corrections. The width of the line increases in the right histogram which explains the increase in the FWHM and FWTM. Overall, the data of this beam time is dominated by the increased noise after the crash of the system which conceals the effects caused by the irradiation. This greatly reduces the significance of the data. Because of that, the data of the second beam time will not be considered in the final discussion.

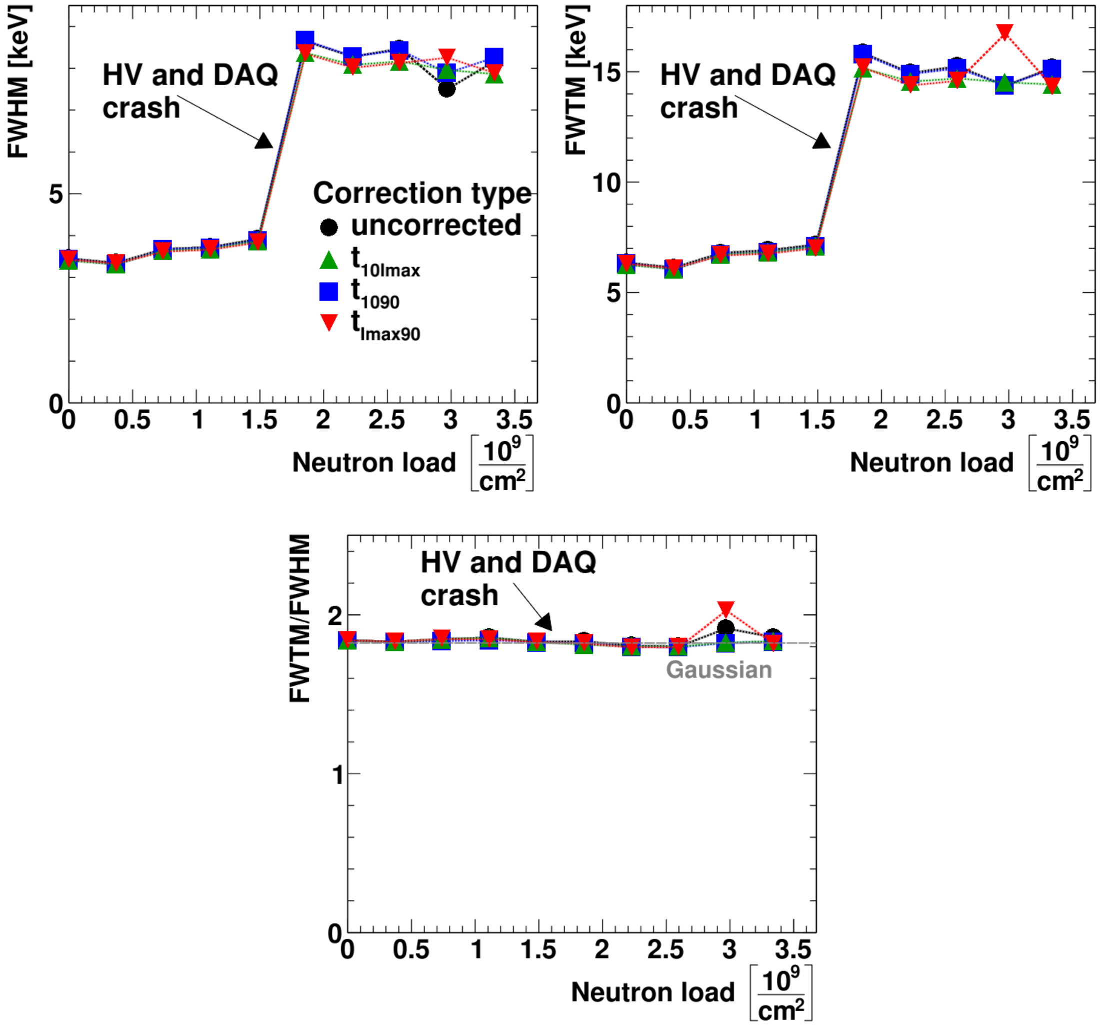

Figure 5.33: Progression of the detector resolution for the second irradiation test. Compared to the first beam time the initial resolution is better while still far from the specified 1.96 keV. This resolution slightly worsens with an increase of the irradiation until a sudden rise occurs after the fifth data point. This can be explained by a hardware crash that required a full restart of the system. Unfortunately, this crash had a negative influence on the noise of the system which could neither be completely eliminated nor specified more precisely. After this rise the resolution remains constant or even slightly improves over time which shows how the irradiation damage is masked by the increased noise. Because of that, the effects of the corrections are much smaller than for the data of the first beam time. The FWTM in the top right shows the same behavior as the FWHM previously explained. Since these increases of the FWHM and FWTM cancel out each other, the fraction of both remains in good agreement with a Gaussian peak shape. The fluctuations of the second last data point in each plot is a statistical artifact and can be ignored.

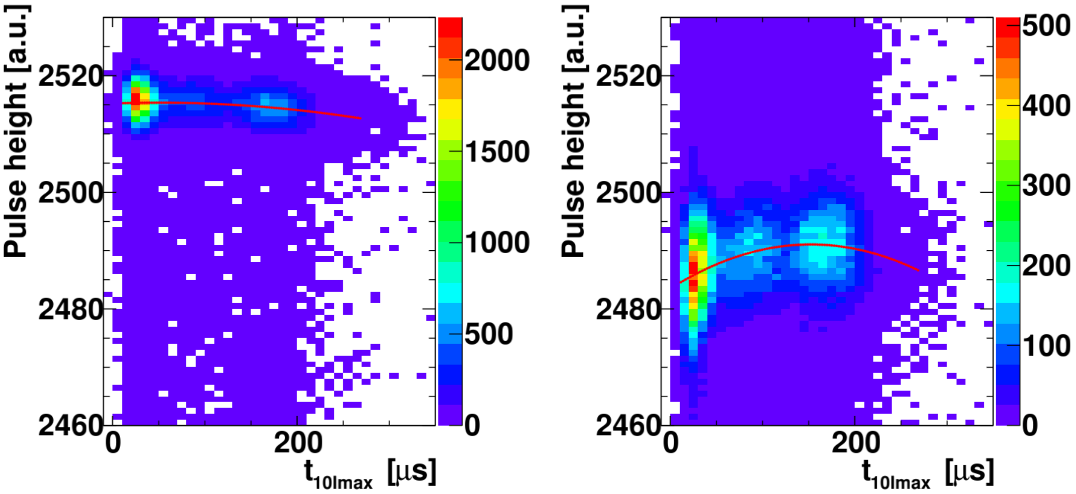

Figure 5.34: When looking at the two-dimensional histograms of the pulse height and $t_{10\rm Imax}$, the data of the second beam time does not show the strong dependence as the one of the first beam time. The data at the beginning (left) and the end (right) of the test is shown to confirm this. The offset between the 1332 keV line in both histograms can be explained by the required restart of the system and is of no consequence for the calibrated data. Besides this shift, the increased noise after the crash of the data acquisition increases the width of the line. This effect persists for the full range of $t_{10\rm Imax}$. A strong systematic drop for low values of $t_{10\rm Imax}$, however, can not be identified, in contrast to the data of the first beam time. This effect of the irradiation might be covered by the increased noise.

After each beam time the detector resolution was respecified in the laboratory at GSI. The same setup as before the irradiation was used for this. Since this setup has been running for multiple years the electronic noise is very low and stable. The setup consists of a timing filter amplifier as main amplifier followed by an analog ADC and MCA [g] combination to store the pulse height. The amplifier is shaping the detector pulses with a typical shaping time of 6 µs. Both detectors were biased with their specified high voltage as well as 500 V below that voltage. For the first detector, housing the crystal HEX 158, this resulted in a FWHM of 3.52 keV at 3000 V and 3.73 keV at 2500 V, respectively. The same measurements for the second detector (HEX 146) yielded a resolution of 3.44 keV at 4000 V and 3.73 keV at 3500 V. The analog setup offered no information on the pulse shape and an event-based application of the corrections found in the pulse shape analysis was not possible. Nevertheless, it is reasonable to apply the relative improvement gained in the digital analysis to the data. Since the data of the second beam time yielded no reliable results, this was only performed for HEX 158 irradiated in the first beam time. Applying the calculated average improvement of 24.1 % resulted in a corrected resolution of 2.67 keV at 3000 V.

---

[g] Multi Channel Analyzer

In addition to these measurements, the crystals were annealed and respecified afterwards. HEX 146 (second beam time) was annealed four months after the irradiation in November 2014. After this annealing, the performance of the crystal was fully restored. A resolution of $2.09\,\mathrm{keV}$ was measured for the reduced high voltage of $3500\,\mathrm{V}$. This small deviation can be caused by variations in the used cryostats and preamplifiers during this re-specification.

The annealing of HEX 158 (first beam time) was accidentally delayed and was performed in April 2018. This was more then 3.5 years after the irradiation. Due to this delay the lattice defects were able to crystallize within the crystal and thus the effect of this annealing was reduced. With a measured resolution of $2.60\,\mathrm{keV}$ at $3000\,\mathrm{V}$ the initial resolution could not be fully restored after the first annealing. Because of that, a second annealing was performed in July 2018. This improved the resolution to $2.42\,\mathrm{keV}$ at the same high voltage as previously applied. Additional annealing might further improve this resolution and restore the initial performance. All laboratory measurements are summarized in table 5.4.

Measurement	FWHM [keV]	FWTM/FWHM	HV
HEX 158			
Before irr. (June 2014)	2.25	1.924	3 kV
$5.6 \cdot 10^9\,\mathrm{n/cm^2}$ (August 2014)	3.52	2.209	3 kV
Before annealing (April 2018)	2.83	2.267	3 kV
After first annealing (June 2018)	2.60	not measured	3 kV
After second annealing (March 2019)	2.42	1.914	3 kV
HEX 146			
Before irr. (July 2014)	1.96	1.864	4 kV
$3.5 \cdot 10^9\,\mathrm{n/cm^2}$ (August 2014)	3.44	3.403	4 kV
After annealing (November 2014)	2.09	not measured	3.5 kV

Table 5.4: Summary of the laboratory measurements of the Germanium crystals before and after the irradiation. The long delay before the first annealing of HEX158 increased its annealing requirements. In contrast to that, HEX146 reached a very good performance after a prompt annealing. All measurements were performed with an analog data acquisition system with a shaping time of 6 µs.

5.4 Summary of the irradiation tests

This chapter showed the results of the irradiation tests of EUROBALL crystals at COSY. During the first beam time the EUROBALL crystal HEX 158 was irradiated by $5.6 \cdot 10^9\,\mathrm{neutrons/cm^2}$ which equals to 93 days of experimental time at $\overline{\text{P}}$ANDA under the conditions of the hyperatomic or hypernuclear experiment. The resolution worsened from $4.19\,\mathrm{keV}$ to $8.53\,\mathrm{keV}$ due to this irradiation. The bad starting resolution was caused by an insufficient amplification of the preamplifier which could only use a small fraction of the dynamic range of the data acquisition system. By analyzing the pulse shape an estimation of the radius of the interaction point was possible that allowed to partially correct the degradation due to the radiation damage. The best correction could be achieved when the difference of the timestamps of the rising edge reaching $10\,\%$ of its amplitude and the maximum of its derivative $t_{10\mathrm{Imax}}$ was used. This measure is dominated by the traveling of electrons in the crystal and less ambiguous than using the full rise time composed of electrons and holes. The average improvement achieved by this was $24.1\,\%$ which resulted in a resolution of $6.41\,\mathrm{keV}$ after the full irradiation. When this improvement is applied to the data measured in the laboratory after the irradiation the resolution improves from $3.52\,\mathrm{keV}$ to $2.67\,\mathrm{keV}$. Since the annealing of this crystal was accidentally delayed by 3.5 years the initial resolution of $2.25\,\mathrm{keV}$ could not be fully recovered yet. $2.42\,\mathrm{keV}$ could be achieved after two repetitions of the annealing process which still leaves room for improvement by additional annealing.

In the second beam time less irradiation of the crystal could be accumulated. With $3.5 \cdot 10^9\,\mathrm{neutrons/cm^2}$ this equaled to 56 days of $\overline{\text{P}}$ANDA. Unfortunately, the data of the second beam time was flawed by a crash of the experimental system in the middle of the beam time which suddenly increased the pick-up noise and deteriorated the resolution by a factor of two that could not be recovered. Nevertheless, the measurements of HEX 146 in the laboratory showed a significant decrease of the resolution from $1.96\,\mathrm{keV}$ to $3.44\,\mathrm{keV}$ which could be fully recovered by a prompt annealing. Figure 5.35 summarizes the results of irradiation experiments at COSY.

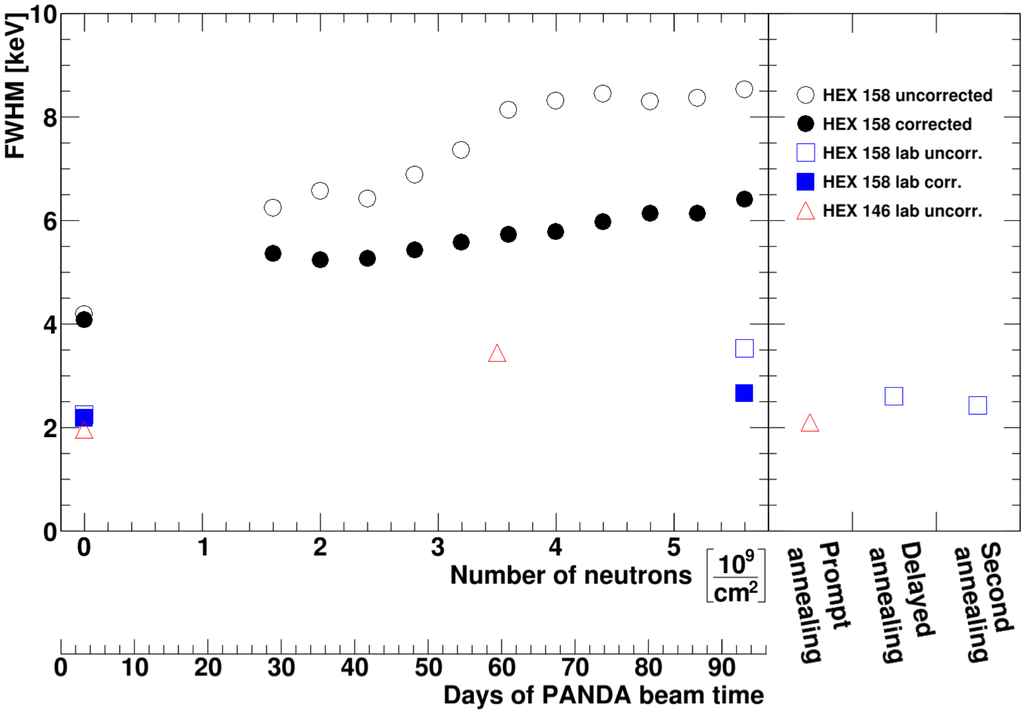

Figure 5.35: Summary plot of the irradiation test. During the first beam time HEX 158 was irradiated by an amount that equals to 93 days of $\overline{\text{P}}$ANDA. The resolution dropped during this but could by partially recovered by pulse shape analysis. Overall, the resolution was limited by the data acquisition system as the measurements in the laboratory at GSI showed. This analog system did not allow an event-based correction but it was reasonable to predict the same improvement as for the taken data with the digital system during the beam time. By accident, the annealing of the crystal was delayed by 3.5 years. The crystallization of lattice defects during this time prevented the full restoration of the original resolution after two repetitions of annealing. More repetitions are in planned. During the second beam time HEX 146 was irradiated with approximately 2/3 of the neutrons of the first beam time. A crash of the data acquisition resulted in a sudden degradation of the resolution. Because of that, no proper information could be extracted from it and only the resolutions before and after the experiment measured in the laboratory are shown. The prompt annealing 4 months after the irradiation allowed to recover the crystal to its full performance.

6 The hyperatom experiment of $\overline{\text{P}}$ANDA

As introduced in chapter 3, the study of heavy Ξ^- hyperatoms at $\overline{\text{P}}$ANDA is an important tool to investigate the Ξ^--nucleus interaction in the neutron-rich periphery. Due to the short life time of the Ξ^- the creation of these hyperatoms is not trivial. $\overline{\text{P}}$ANDA offers a unique way to create Ξ^- in large amount in antiproton annihilation reactions close to threshold. Relatively large fractions of low momentum Ξ^- can be produced in this primary reaction. Only these slow hyperons can be stopped before they decay in flight. The separated target design of $\overline{\text{P}}$ANDA allows to optimize the materials for the production of Ξ^- and their stopping individually. For the primary target, a carbon filament offers the best performance (see section 2.4.3.1 and for more details [66]). Possible materials for the absorber of the secondary target are discussed concerning their experimental properties at the beginning of this chapter.

After the choice of the target material, the optimization of its geometry is presented in section 6.2. The shape of this absorber was optimized in simulations concerning the best compromise of the Ξ^- stopping and the detection efficiency of the hyperatomic X-rays.

The last topic of this chapter (section 6.3) is the study of the feasibility of the hyperatomic experiment. Hyperatom events as well as background were studied in simulations and cuts to optimize the signal-to-background ratio were applied. The resulting event rates were scaled to the full beam time to predict the achievable precision in the measurement of the Ξ^--nucleus potential.

6.1 Choice of the absorber material

In [101], Batty et al. presented F, Cl, Sn, I or Pb as viable targets for the production of Ξ^--hyperatoms from a pure theoretical point of view. Additional factors have to be taken into account for experiments at $\overline{\text{P}}$ANDA. First of all practical properties in the handling of the material have to be considered. This includes that the absorber material should be solid at room temperature and chemically stable in air since an air-tight shielding would increase the material budget. The target material must be non-magnetic due to its operation within the strong magnetic field in the target spectrometer. Additionally, an ideal material is strong enough and vacuum tight to be integrated into the beam pipe and seal the vacuum chamber on its own as it is planned with the boron carbide layer of the hypernuclear experiment. This further reduces the passive material budget of the target system and hence increases its performance. Materials that do not fulfill this requirement will need a thin titanium foil as vacuum sealing which introduces dead material in-between the primary interaction point and the absorber and impairs the Ξ^- stopping efficiency in this dedicated absorber (compare figure 6.1).

The material also has to fulfill some experimental criteria. First of all the target has to stop the produced Ξ^- before their decay. Since their life time of $163.9 \pm 1.5\,\text{ps}$ ($c\tau = 4.9\,\text{cm}$) is small the system needs to be compact. The left part of figure 6.1 shows the range of the Ξ^- with a given momentum in some possible absorbers calculated via the Bethe formula. Boron is included as a comparison to the hypernuclear experiment. On the right the survival probability depending on the flight length is plotted for Ξ^- with a momentum of 100, 500 and $1000\,\mathrm{MeV}/c$. Energy loss is excluded in these calculations at this point for simplicity. Nevertheless, these calculations show that Ξ^- with small momenta below $100\,\mathrm{MeV/c}$ are stopped within the first $0.1\,\mathrm{mm}$ of each absorber material. Unfortunately, the minimum radius of the beam pipe is restricted by the HESR to $1\,\mathrm{cm}$ which has to be considered in the survival probability. This additional distance reduces the survival and consequently the stopping probability for the slowest Ξ^- to less than $10\,\%$. A $500\,\mathrm{MeV/c}$ Ξ^- requires 1 to $2\,\mathrm{cm}$ of material to be stopped which results in stopping probabilities of 20 to $30\,\%$. For higher momenta the material required for stopping increases exponentially which makes it practically impossible to stop these Ξ^- before their decay. Therefore, the typical momentum range of stoppable Ξ^- is 100 to $500\,\mathrm{MeV/c}$ and a compact target system in direct proximity to the interaction point is required. Detailed simulations later in this chapter (section 6.2.1) will confirm this.

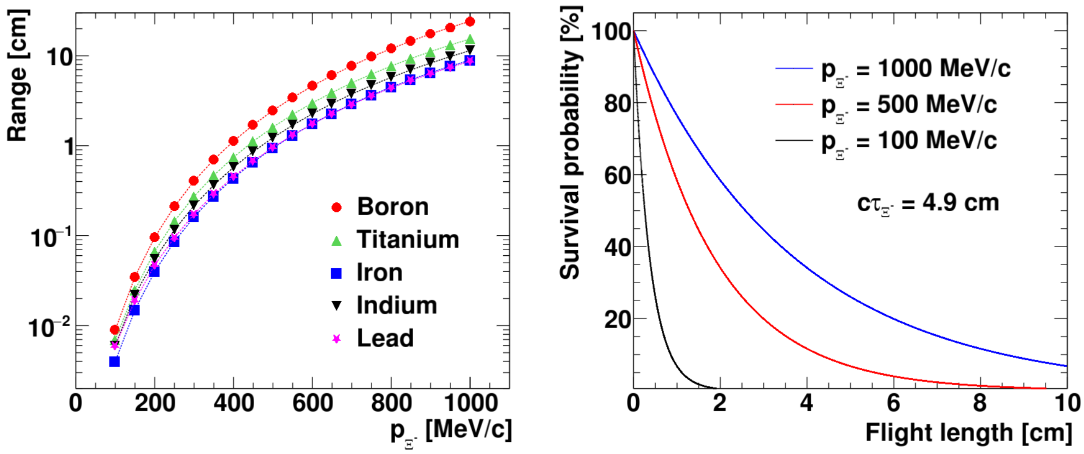

Figure 6.1: The plot on the left shows the range of Ξ^- with a specific momentum in various materials. The right one shows the survival probability of Ξ^- with a momentum of $100\,\mathrm{MeV/c}$, $500\,\mathrm{MeV/c}$ and $1000\,\mathrm{MeV/c}$. For simplicity the energy loss of the Ξ^- when passing the material is not included. The detailed simulations later in this chapter will include this. Combining both plots shows that Ξ^- below $100\,\mathrm{MeV/c}$ will barely reach the absorber that has a minimum distance from the interaction point of $1\,\mathrm{cm}$ due to the requirements of the HESR. Ξ^- above $500\,\mathrm{MeV/c}$, however, require too much material to be stopped before their decay and because of that the typical momentum range of stoppable Ξ^- in a heavy absorber spans from 100 to $500\,\mathrm{MeV/c}$. The upper limits slightly depend on the absorber material.

Additionally, the energies of the emitted X-rays have to be at least in the range of a few hundred keV to reach acceptable detection efficiencies in PANGEA (compare figure 4.29). Smaller energies suffer from to strong absorption within the absorber. The energy of an X-ray is determined in leading order by the atomic number Z of the emitting atom as shown in equation 3.3. This favors elements with high Z. At the same time, materials with high atomic numbers usually are very dense and because of that the absorption cross section for photons is high. Therefore, the shape of the absorber must be optimized as it will be shown in section 6.2.

Last but not least, the values of the observables of the hyperatom experiment (compare section 3.1) are crucial. Very small energy shifts or yields cannot be detected which rules out the corresponding absorber materials. A proper target has an energy shift in the keV range and a moderate yield to gather sufficient statistics. At the same time, the width of the X-ray transition should be small too simplify its discrimination from background events. Calculations for possible targets were performed (compare section 3.2). The strength of the observables depends on the proton and neutron composition of a nucleus. Because of that, each isotope of elements with multiple stable isotopes has to be calculated independently and will superimpose according to their relative fraction in the target. This favors targets made of elements that consist only of a single stable isotope or at least have a dominant one. Enriched targets are another possibility but can be expensive.

A detailed summary of viable materials is given in the following:

Aluminum

has only one stable isotope. It has a low atomic number and thus low energy X-ray transitions. The shift and width are small. Combining all this makes Al an unsuitable target for the experiment. Nevertheless aluminum will be used for the vacuum system and the support structures surrounding the hyperatomic target and is an unavoidable byproduct that could be detected in low rates.

Silicon

is similar to aluminum concerning its properties. The X-ray energies are low and shift and width are hardly higher than for aluminum. In the experimental setup silicon is as unavoidable as aluminum because of electronics close to the target region.

Calcium

is the first element of the list that would be a dedicated absorber material. With 20 protons and neutrons, it offers the possibility to study a double-magical nucleus. Physically, metallic calcium is soft and starts to form an oxide layer when in contact with air. Elemental calcium starts to burn when it reacts with water. Therefore, calcium should not be used as a reliable part of the vacuum system. It requires a thin foil of titanium to seal the beam line and the Ca target could then be placed around this foil. In addition to that, the calcium absorber should be encased for safety purposes. Furthermore, the shift and width of ^{40}Ca the hyperatom are small when the last observable transition is considered that has a reasonable yield (compare figure 3.4). Summing this all up, calcium does not seem like a very promising target material for first studies but on the other hand ^{40}Ca is an experimentally well known nucleus which could make up for the challenges in later experiments.

Titanium

will be present for most of the elements in the list. It can be used as a thin foil with a thickness of $250\,\mu\mathrm{m}$ to seal the vacuum if the absorber material can not fulfill this on its own. Therefore, the lowest momentum Ξ^- will be inevitably absorbed in titanium. Nevertheless, the rates of created hyperatoms in the absorber remain at viable levels (compare section 6.2). The X-ray energies as well as the strong interaction shift and width are in a reasonable range to be measured. ^{48}Ti is the dominant isotope in natural Ti with an isotopic abundance of $73\,\%$.

Vanadium

in its natural composition consists almost exclusively of the isotope ^{51}V. In contrast to titanium, elemental vanadium is not stable enough to seal the beam pipe. Alloys of vanadium could be used for this. Alternatively, the previously mentioned titanium foil is an option. Concerning its experimental measures, vanadium is comparable to titanium. The higher density of vanadium will result in a stronger absorption of X-rays compared to titanium. Summing it up, a titanium target should be favored compared to a vanadium one.

Iron

is used by the J-PARC E03 experiment. They propose it to be the best compromise for their needs of stopping and absorbing the Ξ^- in only a single target block as well as the X-ray detection efficiency [48]. The shift and width of iron are also in a feasible range. Unfortunately, the ferromagnetism of iron makes it impossible to use a pure iron target at $\overline{\text{P}}$ANDA due to the strong magnetic field. Non-magnetic steel alloys with a high fraction of iron could be a viable option. This steel target would be stable enough to be integrated into the beam pipe and seal it on its own.

Zirconium

The shape and size of the dominant isotope $^{90}_{40}$Zr is relatively well known. This decreases systematic uncertainties in the theoretical description. Physically, a target made of zirconium is not stable enough to withstand the pressure gradient and thus the titanium foil is required to seal the vacuum chamber. From the experimental point of view $^{90}_{40}$Zr offers a large energy shift while at the same time the width of the (7,6) $\rightarrow$ (6,5) line is large which leads to a bad signal-to-noise ratio. Additionally, the high absorptive width decreases the yield of the X-ray transitions which further decreases the signal-to-noise ratio. Similar to tin, presented later on, the multitude of stable Zr nuclei decreases the atomic abundance of $^{90}_{40}$Zr to approximately $51.5\,\%$.

Niob

consists of only one single stable isotope. The high density of niob is compensated by the high X-ray energies in this Z range. Just like the transition energies the strong interaction shift and width are very large. This width will strongly widen the detected signal which will make it hard to discriminate it from background. With the low counting rates expected this is unfavorable and thus niob should not be chosen for first experiments.

Indium

is a very soft metal at room temperatures. Therefore, it will require the titanium based beam pipe cover introduced before. This allows to use indium as target material which offers good properties from the experimental point of view. While the shift of $0.91\,\text{keV}$ can be precisely detected, the width of the transition is comparably small with only $0.50\,\text{keV}$. This translates to a high yield as well as a good signal-to-background ratio. Natural indium consists of nearly pure ^{115}In.

Tin

has a very broad range of stable isotopes. It ranges from ^{112}Sn with 62 neutrons to ^{124}Sn with 74. Measurements with pionic atoms [118] showed a strong isotopic dependence on the measured binding energy. The calculations for hyperatoms show the same trend (see table 6.1). The difference in their strong energy shift is up to $0.44\,\text{keV}$. Physically, the production of a tin target is simple but it also requires a titanium foil as vacuum sealing. The wide spread of isotopes, however, complicates the target. Natural tin is a mixture of all these 10 isotopes with ^{120}Sn being the most common. Enriched tin is commercially available, but compared to the experiments with pionic atoms huge amounts are required. Based on the information that was kindly given by Isoflex [a] a 50 g target of ^{112}Sn would costs more than 800 000 €[b] and should therefore not be considered for first experiments.

Tantalum

is a hard material which allows to use it without the addition of a foil of titanium. Its high density will allow to build a relatively small target for the Ξ^- stopping which reduces its strong X-ray absorption caused by its high atomic number. Natural tantalum is nearly entirely composed of ^{181}Ta. The high atomic number of the nucleus results in a high final state of (9,8) whose shift is small but measurable and rather narrow. This results in a high yield of the shifted X-ray.

Gold

has a lot of similarities to tantalum. It is very dense and naturally consists only of a single stable isotope. The shift and width as well as the transition energies are larger than for tantalum but still in a viable range for an experiment. The biggest difference compared to tantalum is that gold is much softer and a target made of gold would require a primary titanium foil.

Lead

has the highest atomic number of all studied possible target materials. Therefore, lead will have the highest absorption cross section for photons. The density, however, is smaller than the one of tantalum and gold and in contrast to these two elements natural lead consists of multiple stable isotopes with noteworthy fractions. The most prominent ones are $^{206}_{82}$Pb,$^{207}_{82}$Pb and $^{208}_{82}$Pb which sum up to more than 98 % of natural lead allowing to neglect other isotopes. Especially the last of these isotopes is very interesting for these studies due to its double-magical nucleus. The spherical symmetry of these nuclei makes them an excellent target to study the nuclear structure and thus $^{208}_{82}$Pb is one of the best-known nuclei which reduces systematic uncertainties in the estimation of the Ξ^--nuclear potential (compare figure 3.5 and section 6.3). Considering the three isotopes the difference in their transition energies is small. Besides a slight difference in the strong interaction shift, small variations due to the charge distribution of the isotopes has to be taken into account (see table A.12). Using an enriched target of up to 99 % of $^{208}_{82}$Pb, which is commercially available [c], removes these flaws. All in all, $^{208}_{82}$Pb is a very interesting target and offers a very prominent shift and an acceptable width and yield. Mechanically a lead target is not hard enough to be directly integrated into the beam pipe and requires a titanium sealing.

Table 6.1 summarizes these target materials. Their shifts and yields are visualized in figure 6.2. The parameters of the proton and neutron density distributions used within the calculations (compare equation 3.9) are summarized in table A.12 in the appendix.

---

[a] http://www.isoflex.com

[b] price of 1 mg ^{112}Sn is 20 \$ (email quotation by Isoflex (21.03.2018))

[c] price of 1 mg ^{208}Pb is 0.73 \$ (email quotation by Isoflex (28.08.2018))

Element	ρ [g/cm^2]	**Isotopic ab. [%]**	(n_0, l_0)	$\Delta E^{\text{nuc}}_{n_0}$ [keV]	$\Gamma^{\text{abs}}_{n_0}$ [keV]	E_{γ_1} [keV]	E_{γ_2} [keV]	Y_{γ_2} [%]
$^{27}_{13}$Al	2.70	100.0	(4,3)	0.09	0.04	69.43	128.09	89.3
$^{28}_{14}$Si	2.34	92.0	(4,3)	0.16	0.08	80.69	148.91	87.5
$^{40}_{20}$Ca	1.55	96.9	(5,4)	0.03	0.01	100.76	167.36	96.7
$^{48}_{22}$Ti	4.50	73.0	(5,4)	0.17	0.08	122.67	203.88	85.3
$^{51}_{23}$V	6.11	99.8	(5,4)	0.23	0.12	134.33	223.29	86.2
$^{56}_{26}$Fe	7.87	91.8	(5,4)	1.14	0.71	172.17	287.01	57.1
$^{90}_{40}$Zr	6.50	51.5	(6,5)	3.42	2.4	267.23	415.52	33.6
$^{93}_{41}$Nb	8.57	100.0	(6,5)	4.32	3.62	280.94	437.55	32.2
$^{115}_{49}$In	7.31	95.0	(7,6)	0.91	0.50	275.83	403.66	65.0
$^{112}_{50}$Sn	7.31	1.0	(7,6)	0.95	0.57	287.14	420.22	68.9
$^{120}_{50}$Sn	7.31	32.6	(7,6)	1.28	0.78	287.39	420.89	58.3
$^{124}_{50}$Sn	7.31	5.6	(7,6)	1.39	1.00	287.49	421.16	57.9
$^{181}_{73}$Ta	16.65	99.9	(9,8)	0.23	0.11	325.55	440.67	88.9
$^{197}_{79}$Au	19.32	100.0	(9,8)	0.68	0.43	381.71	517.12	78.4
$^{206}_{82}$Pb	11.34	24.1	(9,8)	1.76	1.21	411.52	558.47	57.0
$^{207}_{82}$Pb	11.34	22.1	(9,8)	1.82	1.26	411.53	558.54	56.0
$^{208}_{82}$Pb	11.34	52.4	(9,8)	1.83	1.33	411.54	558.57	56.5

Table 6.1: Overview of possible target materials for the hyperatom experiment. Besides their atomic and mass number, their density ρ is important for the stopping of Ξ^- and X-ray absorption. A high isotopic abundance of the main isotope of an element decreases the X-ray energy deviations due to multiple isotopes in the target. The electric dipole transition (Δn=Δl = 1) of the Ξ^--hyperatom leading to the atomic state with the quantum numbers (n_0, l_0) is shifted due to the strong interaction in the nuclear periphery by $\Delta E^{\text{nuc}}_{n_0}$ and has the strong absorptive width $\Gamma^{\text{abs}}_{n_0}$. The two energies E_{γ_1} and E_{γ_2} are the energies of the X-rays of the unshifted $(n_0 + 2, l_0 + 2) \to (n_0 + 1, l_0 + 1)$ and the shifted $(n_0 + 1, l_0 + 1) \to (n_0, l_0)$ transitions, respectively. In addition to a variation of $\Delta E^{\text{nuc}}_{n_0}$ the energies of different isotopes of the same element slightly differ due to QED effects. The last column shows the yield of the final X-ray γ_2 Y_{γ_2} that was calculated from the radiative and nuclear absorptive width of the $(n_0 + 1, l_0 + 1)$ state as shown in equation 3.5. The observables were calculated using the model described in section 3.1.

Summing up these studies, there are multiple options for the target selection. The calculations show a trend that light materials offer only a small effect due to the strong interaction and their low X-ray energies will suffer from strong absorption and high background (compare figure 6.16). At the same time the production probabilities will suffer from low Ξ^- stopping. In the intermediate region, elementary iron is magnetic and thus difficult to use within the magnetic field of $\overline{\text{P}}$ANDA. Niob seems like a bad option due to its high width and small production rates which both result in bad signal-to-noise ratios. The price of enriched tin targets makes it unsuitable for first experiments. All the other elements seem to be a possible choice as target while indium stands out as an appropriate choice in the intermediate atomic number range and lead shines for heavy elements due to the comparably well-known shape of the nucleus.

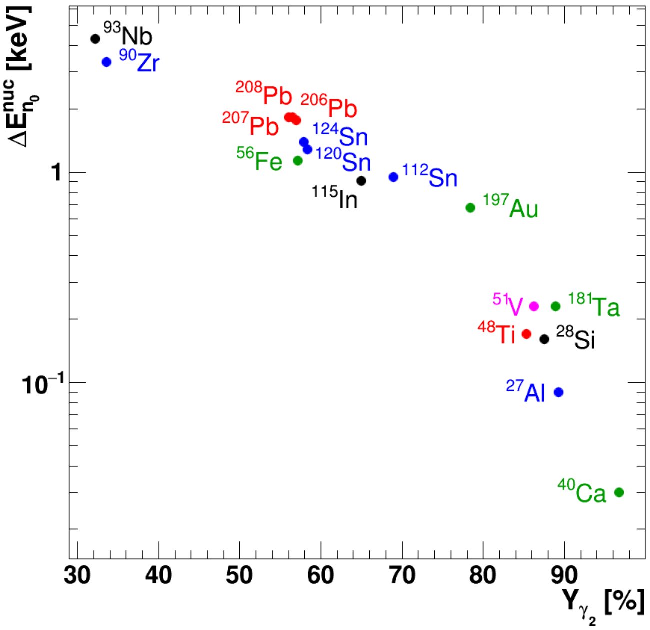

Figure 6.2: Visualization of the energy shift and the yield of the last X-ray transition. Elements with small energy shifts or low yields are difficult to study experimentally. The intermediate region where lead, iron and indium are situated seems experimentally most feasible for first studies. The requirement of an enriched target disqualifies tin for the first experiment due to the high price.

6.2 Optimization of the shape of the secondary target absorber

As explained previously, the main task of the secondary target is the absorption of Ξ^- that are produced in the primary antiproton-carbon reaction. Free Ξ^- have a life time of $163.9 \pm 1.5\,\mathrm{ps}$ and decay weakly into $\Lambda + \pi^-$ to almost $100\,\%$. Therefore, the secondary target has to be very compact and as close as possible to the primary interaction point. This distance is limited by the guidelines of the HESR which require a minimum beam pipe radius of $1\,\mathrm{cm}$ for beam preparation. Because of that, only slow Ξ^- can be stopped and subsequently form a hyperatom (compare figure 6.1). While the stopping of the Ξ^- can be improved by adding more absorber material, the X-ray absorption inside the target would increase at the same time and consequently the efficiency of their detection in PANGEA would suffer. Because of that, it was necessary to find an absorber geometry that achieved the best compromise of the Ξ^- stopping and the X-ray detection efficiency. A simple figure of merit f_{st} for this is the product of the Ξ^- stopping efficiency ϵ_{Ξ^-} and the detection efficiency ϵ_{coinc} of the coincident detection of γ_1 and γ_2

$$f_{\text{st}} = \epsilon_{\Xi^-} \cdot \epsilon_{\text{coinc}} \,. \tag{6.1}$$

Both components of this figure of merit were simulated individually for various configurations of the target absorber. The shape and the material of the absorber was varied in these studies. While indium and lead are viable targets for the experiment, iron is mostly added as a comparison to J-PARC E03.

6.2.1 Simulating the stopping of Ξ^-

Presently, the experimental knowledge of a detailed Ξ^- production cross section is missing. $\overline{\text{P}}$ANDA will measure this cross section in its starting phase. Because of that, the primary $\bar{\text{p}}$-carbon reaction had to be simulated and the resulting pseudodata could be used to optimize the geometry of the absorber. The Giessen Boltzmann-Uehling-Uhlenbeck transport framework (GiBUU) [82] was used for this purpose. In GiBUU 1000 events are calculated in parallel and the mean potential of these events is shared within these calculations. GiBUU only includes the strong interaction since the simulation time is limited to a few femtoseconds and hence strangeness is preserved in these reactions.

Since the computation time of these events was long [d] and the yield of Ξ^- low, the production cross section of hyperon-antihyperon pairs was internally increased by a factor of 10. With this boost the production of multiple pairs of hyperons and antihyperons in a parallel run was still very unlikely and thus the mean potential unaffected. The antiproton momentum for these calculations was chosen slightly above the $\Xi^-\bar{\Xi}^+$ production threshold of $2643.4\,\text{MeV/c}^2$ which corresponds to a beam momentum of $p_{\text{beam}} = 2622.6\,\text{MeV/c}$. The primary purpose of the generated pseudodata was to study the asymmetry of $\Xi^-\bar{\Xi}$-pairs produced in nuclei as introduced in section 2.4.1 [66], but these events could also be used for the optimization of the hyperatom target. Because of that, multiple configurations with a slight variation of the beam momentum and the antihyperon potential $\xi V_{\bar{\Xi}^-}$ were studied, which are summarized in table 6.2. Since neither the polar angle distribution nor the momentum distribution of the simulated Ξ^- largely differed within the stoppable momentum and angular range (compare figure 6.3) all runs could be combined to increase the statistics for the geometrical optimization.

A further increase could by achieved by reusing every event 1000 times with randomly varied azimuthal angle Φ of the Ξ^- particle, leading to 50,651,000 simulated events per absorber configuration. Figure 6.4 shows the two-dimensional histogram of the momentum and polar angle of the produced Ξ^-. Only a small fraction of the produced Ξ^- is inside the suitable momentum and angular range that can be stopped within the absorber.

---

[d] 1 week per run of 15.8 million events on the HPC cluster HIMster

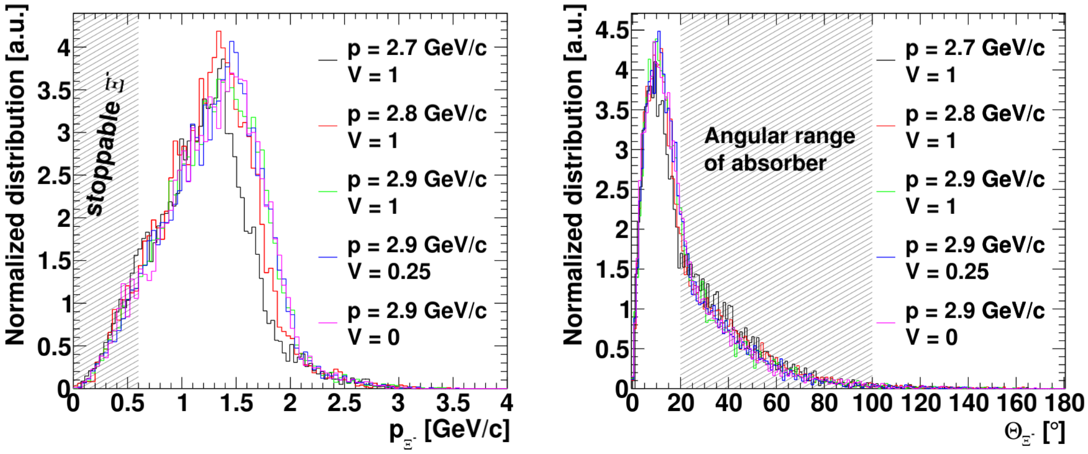

Figure 6.3: Comparison of the momentum (left) and polar angle distributions (right) of Ξ^- with various beam momentum configurations. The important momentum and angular regions are marked. The differences in these regions are negligible, which allowed to combine all configurations to increase the statistics. The distributions are normalized by the amount of Ξ^-.

Configuration	p_{beam} [GeV/c]	$\xi V_{\bar{\Xi}^-}$	Ξ^- events
1	2.7	1	8137
2	2.8	1	9722
3	2.9	1	10982
4	2.9	0.25	10745
5	2.9	0	11065

Table 6.2: Beam momentum p_{beam} and antihyperon potential scaling factor $\xi V_{\bar{\Xi}^-}$ configurations used as input for the GiBUU simulations. The variations were irrelevant for the studies in this thesis and were performed to study the sensitivity of the antihyperon potential experiment (compare section 2.4.1 and [66]). Each configuration comprises five GiBUU simulation runs with a total of 79 million $\bar{p}$-^{12}C reactions.

During the experiments the primary target will be placed in the beam halo. This offset from the center of the beam is required to achieve the specified average interaction rate of 2 MHz (compare section 2.4.3.1 and [66] for more details), This displacement was mimicked in the simulations by shifting the primary vertex by $-3\,\text{mm}$ in x direction. The small adjustments of the target position during the experimental cycle are irrelevant for these optimization studies and hence not included in the simulation.

The optimization process of a target geometry itself was independent of its material. Therefore, only details of the procedure for lead are shown in the following. Results will be presented for iron and indium too. Additionally, the results of the various iron and indium absorber geometries can be found in appendix A.7.

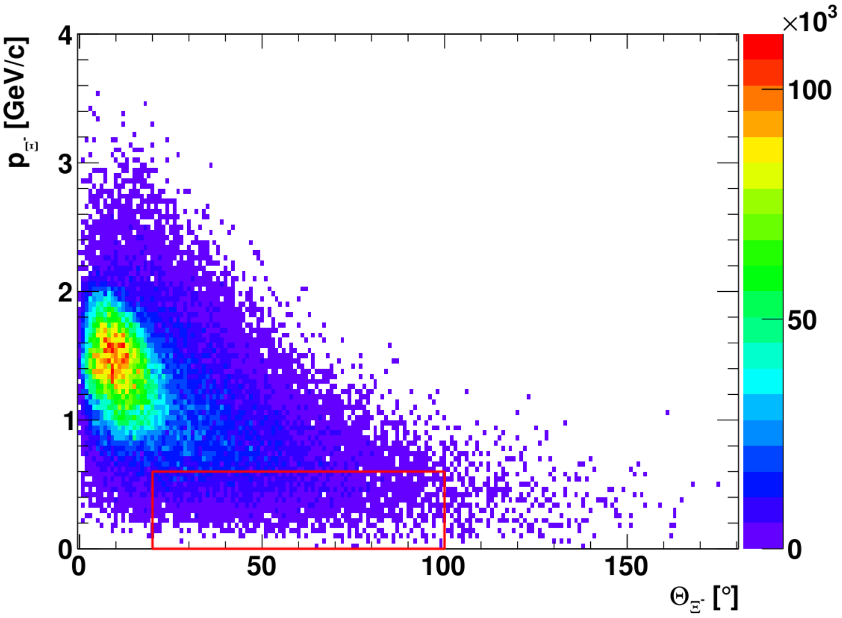

Figure 6.4: Two-dimensional distribution of the generated Ξ^-. The momentum is plotted versus its polar angle. The distribution peaks at forward angles of approximately $10°$ and a momentum of $1.5\,\mathrm{GeV/c}$. Only a small fraction of these Ξ^- are in the stoppable angular and momentum range which is marked by the red box.

In the first step of the optimization of the absorber a massive block of material was used. This block was much bigger than the designated absorber geometries, but it allowed to identify important regions for the stopping. Figure 6.5 shows the simplified geometry built for PandaRoot simulations. All geometries in this chapter were created with the geometry framework of ROOT just as PANGEA (compare section 4.3.1.3). The right side of this figure shows the implemented simplified version of the primary target system (section 2.4.3.1) which included simplified models of the piezo actuators, the moving carriage, the carbon target filament and a preliminary version of its holding frame. The titanium foil with a thickness of $250\,\mu\mathrm{m}$ that ensures the vacuum-tightness was also included in this geometry. It is drawn in red and spans the full target area around the interaction point from $z = -60$ to $-50\,\mathrm{cm}$.

Results of this first study are shown in figure 6.6. The left side of this figure shows the stopping points in the lead absorber projected to the yz plane. They pile up close to the interaction point which is marked by the red cross. Based on this data, a trapezoidal shape for the absorber was chosen. The z coordinate of its four basic points in this projection as well as its thickness were subject of the following study. The plot on the right in figure 6.6shows the projection perpendicular to the beam axis. The primary interaction, and starting point of the Ξ^-, is marked again by the red cross. Due to its offset the distribution of stopping points is not symmetrical, but - like the target - shifted to the left. To match this, the outer shape of the absorber was varied elliptically. The length of both semi axes a_x and a_y were subject of the optimization of the target geometry. Inside the vacuum chamber additional absorbers with a round cutout for the beam pipe and a slit for the primary target were added to further increase the solid angle coverage.

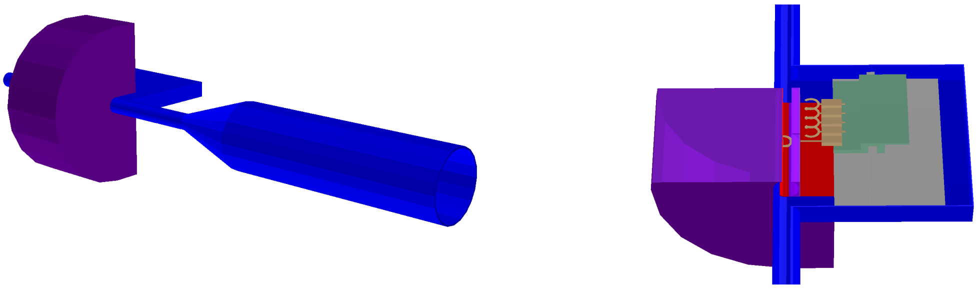

Figure 6.5: The left picture shows the thick target block (purple) that was used for the first studies of the stopping. The geometry included a simplified version of the primary target stage that is shown in the sectional view on the right. The titanium foil was also included in this geometry and is drawn in red.

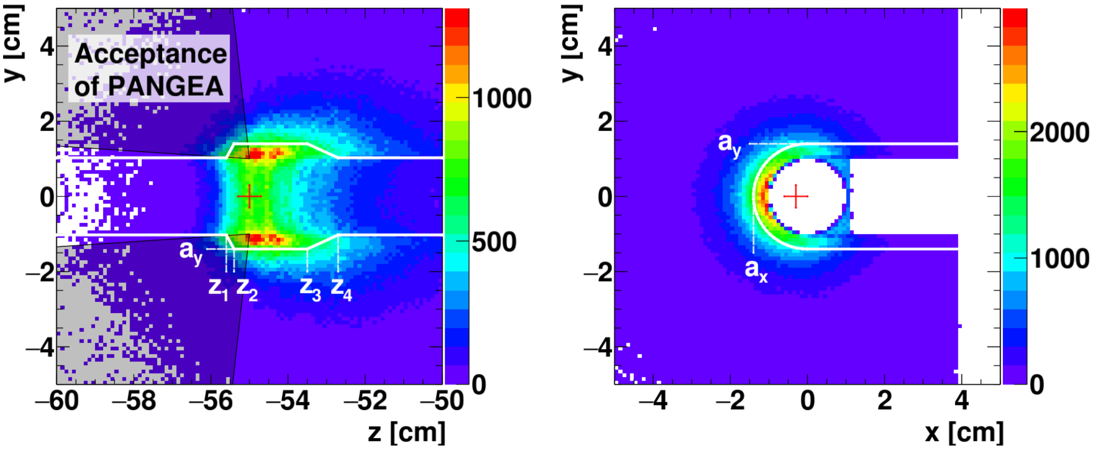

Figure 6.6: Stopping points of the studies with the massive lead block absorber. This absorber was used as a start for the optimization of the absorber shape. The yz projection is shown in the left plot. The angular range of the germanium detectors is visualized. It shows that a specifically shaped absorber is required for the experiment which reduces the absorption of X-rays produced at the stopping points of the Ξ^-. The white line corresponds to the trapezoidal shape of the absorber that was used for further optimization with four parameters along the beam axis, z_1 to z_4. The stopping points in the xy plane are shown on the right. The maximum of stopped Ξ^- is close to the primary interaction point due to their short life time. The shift of the primary vertex by $-3\,\mathrm{mm}$ in x direction accounts for the asymmetry of the interaction point in this direction. Therefore, an elliptically shaped absorber seemed reasonable to mimic this shift. The length of both semi axes a_x and a_y needed to be optimized in the simulation.

At first ,the trapezoidal shape along the beam axis was optimized. Five configurations were tested in simulations. The z coordinates of each of the four corner points z_1 to z_4 of these geometries can be found in Table 6.3. The length of the semi axes of the absorber was kept constant in this study (a_x = $1.6\,\mathrm{cm}$, a_y = $1.4\,\mathrm{cm}$). Since these lengths were be optimized afterwards, the information of the configuration of each axis was coded into a three figure code: The first figure is the absorber shape along the beam axis (z axis), the second and third hold the information of the maximum thickness of the absorber in x and y direction. Each of them is the length of the corresponding half axis minus the inner radius of the beam pipe of $1\,\mathrm{cm}$. Following this code the geometries in this study were 164, 264, 364, 464 and 564.

Geometry	z_1 **[cm]**	z_2 **[cm]**	z_3 **[cm]**	z_4 **[cm]**
164	-55.60	-55.40	-53.50	-52.70
264	-55.70	-55.50	-53.40	-52.60
364	-55.80	-55.60	-53.30	-52.50
464	-55.90	-55.70	-53.20	-52.40
564	-56.00	-55.80	-53.10	-52.30

Table 6.3: Geometrical configurations of the absorbers along the beam axis (yz plane) used in the optimization studies. The primary interaction point was situated at $z = -55\,\mathrm{cm}$.

The stopping points of the Ξ^- from these studies were used as starting points for X-rays in the study of their detection efficiency. $1 \cdot 10^7$ events of two coincident photons with $559\,\mathrm{keV}$ and $412\,\mathrm{keV}$[e] (compare table 6.1) were generated in PandaRoot. As in section 4.3.2 the polar angle of these X-rays was limited to backward angles (90° to 180°). This virtually increased the produced statistics of the coincidence by a factor of four compared to a distribution in the full solid angle. The event-wise analysis of the simulation used the cluster add-back algorithm introduced in section 4.3.2. The energy of all individual clusters was stored and all possible pairs of these energies are plotted in a two-dimensional histogram. The larger energy or each pair was plotted on the x axis. Figure 6.7 shows exemplary results for geometry 144. A two-dimensional Gaussian function[f] was fitted to the distribution. Its amplitude A translates to the detection efficiency ϵ_{coinc} via

$$\epsilon_{\text{coinc}} = \frac{A \cdot 2\pi \cdot 100}{4 \cdot 10^7} \,. \tag{6.2}$$

In this equation the factor 2π normalizes the Gaussian distribution. The factor 100 corresponds to the binning of $0.1\,\mathrm{keV}$ in either dimension. With these scaling factors, the nominator holds the number of detected coincidences and is divided by the total number of simulated events with regard to the full solid angle.

The efficiencies of the Ξ^- stopping ϵ_{Ξ^-} as well as the X-ray detection ϵ_{coinc} and their product f_{st} are shown in table 6.4. They are visualized in figure 6.8. The left plot shows the results of the studies of both individual criteria of each geometry. The stopping efficiency increases with rising geometry number which corresponds to more absorber material. At the same time the γ-detection efficiency decreases due to more absorption in the target material. The plot on the right visualizes the figure of merit f_{st} which is maximal for the smallest geometry 164. Increasing the size of the absorber decreases the figure of merit. The biggest geometry 564 shows a loss of $7.5\,\%$ compared to geometry 164. Even smaller geometries were not studied at this point because

---

[e] Both energies were changed for the studies of iron and indium to their respective transition energies.

[f] The predefined "xygaus" function of ROOT was used.

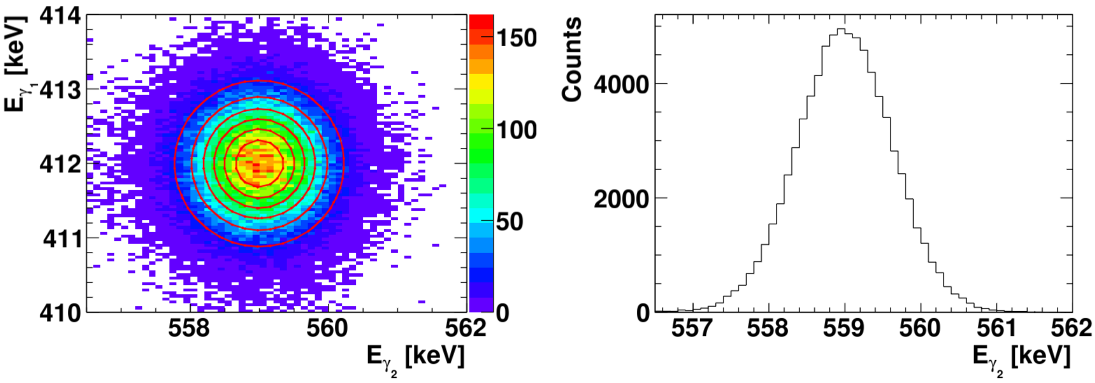

Figure 6.7: Two-dimensional plot of the coincident detection of the $559\,\mathrm{keV}$ and $412\,\mathrm{keV}$ photon of simulated lead hyperatoms. All possible combinations of two measured energies were plotted. The higher energy of a pair was plotted on the x-axis and the lower one on the y-axis. A two-dimensional Gaussian function was fitted to the pseudodata and its amplitude A was used to calculate the coincidence efficiency via equation 6.2. In this example of the Pb geometry 144 the amplitude was $A = 137.8 \pm 0.7$. The resolution of the higher energy photon $\sigma_{\gamma_2} = 0.614 \pm 0.002\,\mathrm{keV}$ and the lower energy one $\sigma_{\gamma_1} = 0.563 \pm 0.002\,\mathrm{keV}$ were of similar size. The energy spectrum on the right is a projection of the two-dimensional histogram to the x-axis and shows the Gaussian shape of the pr.

the possible further increase of f_{st} was expected to be statistically insignificant, especially when keeping in mind that the final optimization of the absorber will be based on reliable Ξ^- production cross section data measured in the early days of $\overline{\mathrm{P}}$ANDA which might differ from the pseudodata generated via GiBUU.

For the further optimization perpendicular to the beam the first z configuration 164 was used. Now the semi axes a_x and a_y were varied consecutively. At first a_x was varied in the range of 1.4 to $1.8\,\mathrm{cm}$ and secondly a_y from 1.2 to $1.6\,\mathrm{cm}$ based on the stopping points shown in figure 6.6. The results of these studies are shown in figure 6.9 and are structured in the same way as figure 6.8. The stopping as well as the detection efficiency show the same trends as in the previous study: The stopping increases with more material while the γ detection decreases. Since geometry 144 with a_x = $1.4\,\mathrm{cm}$ showed the best combined results of the five configurations it served as basis for the

Geometry	ϵ_{Ξ^-} [%]	$\epsilon_{\mathrm{coinc}}$ [%]	f_{st} [10^{-4}]
164	0.612 ± 0.001	0.162 ± 0.001	0.0989 ± 0.0004
264	0.640 ± 0.001	0.150 ± 0.001	0.0967 ± 0.0004
364	0.676 ± 0.001	0.143 ± 0.001	0.0969 ± 0.0004
464	0.699 ± 0.001	0.134 ± 0.001	0.0939 ± 0.0004
564	0.719 ± 0.001	0.127 ± 0.001	0.0915 ± 0.0004

Table 6.4: Results of the geometrical optimization of the absorber along the beam axis (yz plane). The best figure of merit f_{st} can be achieved by the smallest geometry 164. Increasing the absorber size decreases f_{st} due to too disproportionate X-ray absorption.

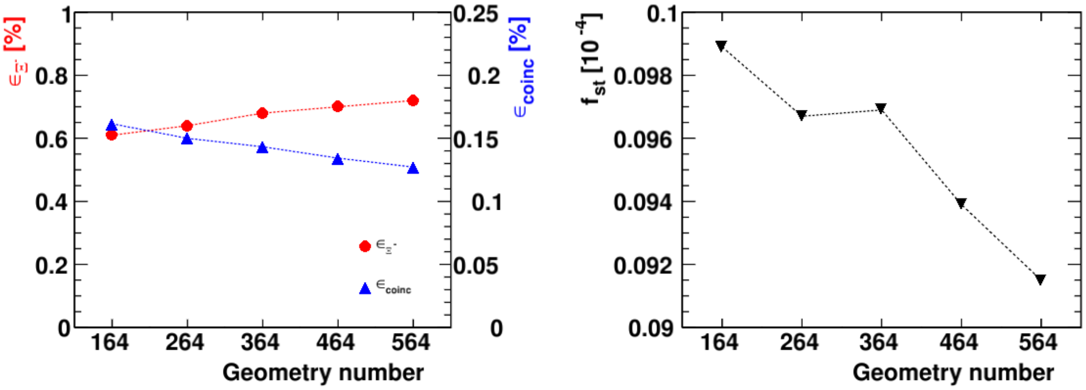

Figure 6.8: Visualization of the optimization of the absorber geometry along the beam axis. The left plot shows both individual parameters for each geometry. When the target volume was increased the stopping of the Ξ^- increased while the photon detection efficiency decreased at the same time. The right plot is the figure of merit which is the product of both observables on the left. This distribution maximizes for the smallest of the five geometries, geometry 164. When the target size was increased, the total efficiency decreased with a maximum loss of $7.5\,\%$ for the biggest geometry. The error bars in both plots are smaller than the marker size and thus not visible.

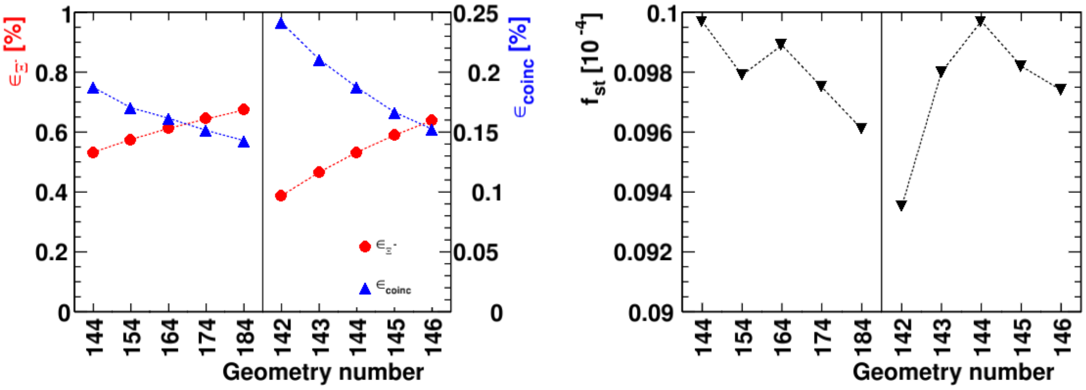

Figure 6.9: Visualization of the optimization of the absorber geometry perpendicular to the beam axis. The optimization of these half axes was performed consecutively starting with the x-direction. In the plots both directions are combined and a vertical line is drawn to separate the optimization of a_x (left) from the optimization in y direction (right). The figure has the same structure as figure 6.8 showing the individual simulation results in the left plot and the combined figure of merit in the right one. After all optimization steps the symmetrical geometry with $a_x = a_y = 1.4\,\mathrm{mm}$ (geometry 144) performed best. The elliptical geometries 143 and 145 followed closely within less than $2\,\%$. The other geometries showed a larger performance loss.

optimization in y direction. The variation of a_y showed that the maximum of the figure of merit is achieved for $a_y = 1.4\,\mathrm{cm}$ (geometry 144). The results of these studies are also summarized in table A.13.

The design of this optimized geometry is shown in figure 6.10. The upper left picture is directly taken from the ROOT geometry that was used for simulations. The lead absorber is colored in purple, surrounded by the silicon detectors (green and brown) and the vacuum chamber of the

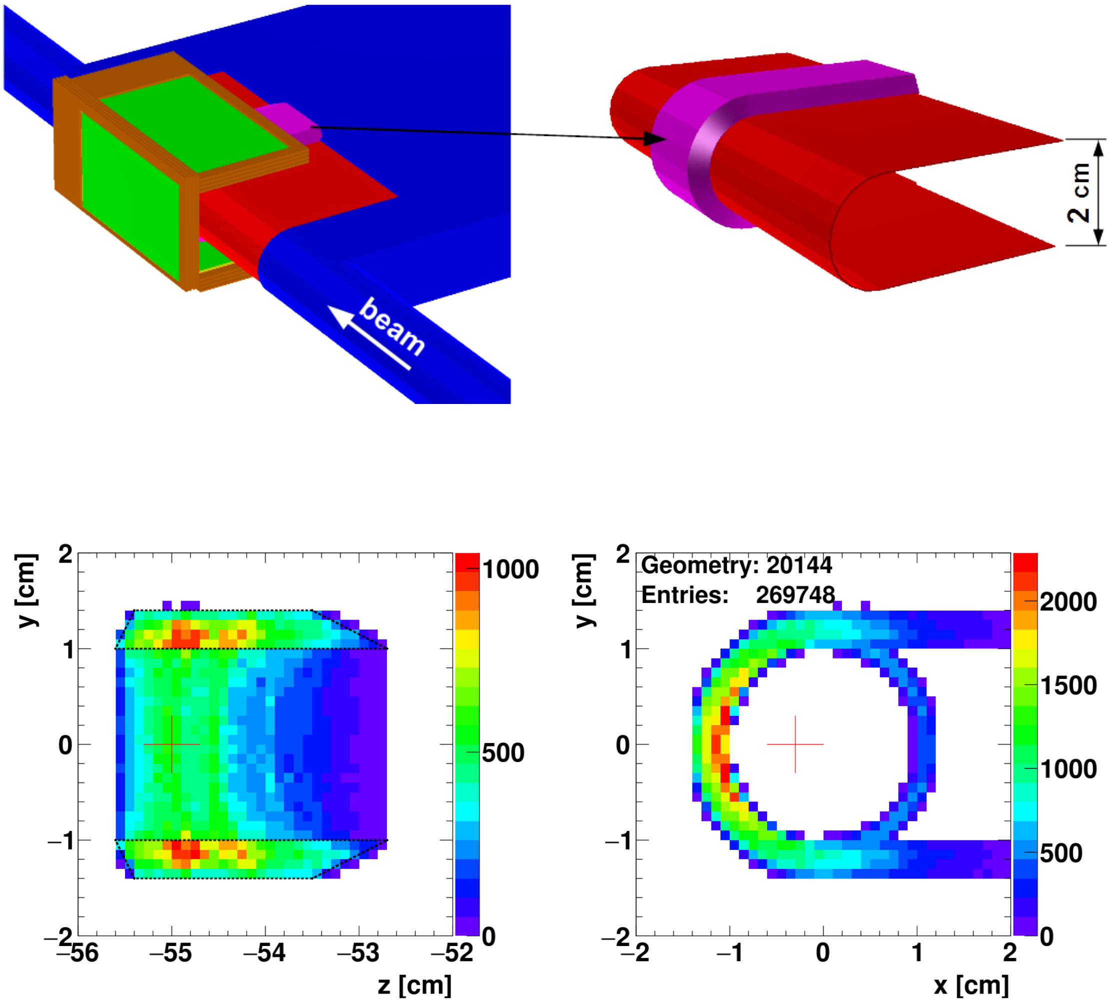

Figure 6.10: Visualization of the best absorber geometry 144. Since most of the absorber in the top left picture is hidden by the silicon detectors in green and brown, the absorber (purple) and the titanium foil (red) are separately shown on the right. The histograms below show the stopping points of this geometry in a projection to the yz plane (left) as well as in the xy plane (right). The red cross marks the position of the primary interaction point.

primary target in blue [g]. The thin titanium foil is shown in red. Since most of the absorber is hidden in this picture, it is shown separately on the right. The two plots at the bottom of the figure show the Ξ^- stopping points of this geometry along the beam axis and perpendicular to it. The maximum of both distributions is close to the primary interaction point.

Further details of the stopping are presented in figure 6.11. The upper half shows the one-dimensional momentum distribution of stopped Ξ^- compared to the distribution of generated ones. As expected only Ξ^- hyperons with a momentum below approximately $500\,\mathrm{MeV/c}$ could be stopped. This is stressed by the stopping probability, plotted on the right. It peaked at $18.3\,\%$ for a momentum of $250\,\mathrm{MeV/c}$ and vanished above $500\,\mathrm{MeV/c}$. The two-dimensional diagrams at the bottom add the polar angular distribution to form two-dimensional distributions. These show that the hard momentum cut-off of stopped Ξ^- does not depend on the polar angle. The main stopping angle ranges from 25° to 95°. Again, the stopping probability is shown on the right, which puts the plot on the left in context to the generated Ξ^- shown in figure 6.4. The stopping probabilities of up to $30\,\%$ are high compared to the total stopping chance of $0.53\,\%$. This shows that the main limitation of the stopping efficiency is the kinematics of produced Ξ^- defined by the fixed-target setup.

The same optimization procedure was performed for iron and indium. Table 6.5 summarizes the results of these optimizations. Iron has the highest efficiencies for stopping as well as the X-Ray detection and consequently for the figure of merit. Due to the comparably low atomic number of iron [h] the X-rays are less affected than by indium or lead and thus it allows to build a bigger absorber which increases the stopping probability of the Ξ^-. Following this logic it is understandable that indium [i] occupies the intermediate position. Details of the optimization for iron and indium can be found in appendix A.7. Nevertheless, lead will be chosen for the hyperatom experiment since its experimental advantages concerning the smaller uncertainties of the nuclear potential and the expected lower background due to the higher transition energies (compare figure 6.12) outweigh the estimated higher signal rate for iron and indium.

Material	**Geometry**	ϵ_{Ξ^-} **[%]**	ϵ_{coinc} **[%]**	f_{st} $[10^{-4}]$
iron	355	0.817 ± 0.001	0.568 ± 0.001	0.4640 ± 0.0012
indium	564	0.568 ± 0.001	0.370 ± 0.001	0.2090 ± 0.0007
lead	144	0.533 ± 0.001	0.187 ± 0.001	0.0996 ± 0.0006

Table 6.5: Summary of the optimized geometries for iron, indium and lead. The iron geometry 355 showed the best results with more than 4.5 times the efficiency of lead. Indium still reaches more than double the efficiency of lead with geometry 564. Nevertheless, further studies will be based on a lead absorber since its experimental advantages outweigh the estimated reduced statistics.

---

[g] At this point, this silicon detectors were still included in the simulation to allow for possible cuts in the data analysis. As it will be shown in section 6.3.3 they will not be required for the hyperatom experiment.

[h] best iron geometry 355 ($z_1 = -56.35$, $z_2 = -55.60$, $z_3 = -53.70$, $z_4 = -52.00$, $a_x = 1.5$, $a_y = 1.5$)

[i] best indium geometry 564 ($z_1 = -56.20$, $z_2 = -55.60$, $z_3 = -53.40$, $z_4 = -52.80$, $a_x = 1.6$, $a_y = 1.4$)

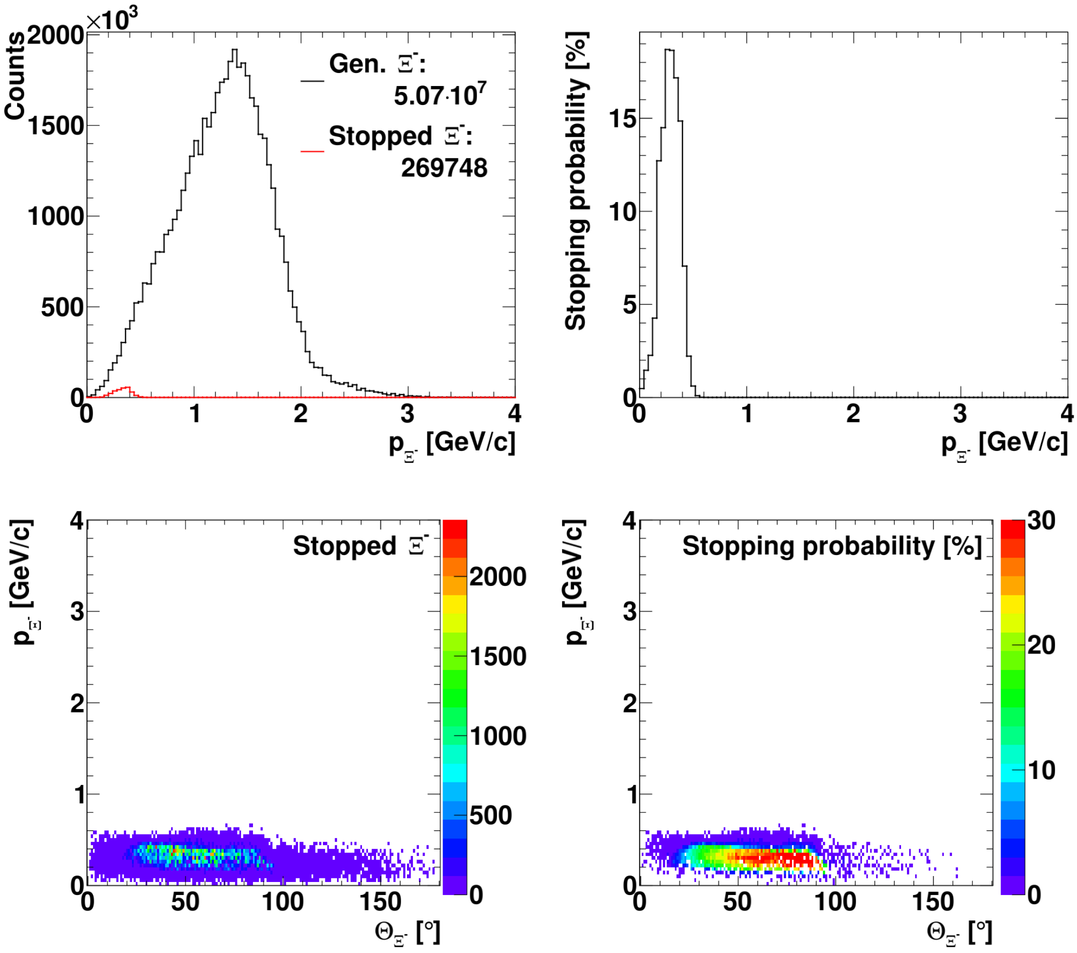

Figure 6.11: Comparison of the stopped and generated Ξ^-. The upper left plot shows the momentum distribution for both. The right diagram shows the stopping probability. It peaks at a momentum of $250\,\mathrm{MeV/c}$ and drops to zero above approximately $500\,\mathrm{MeV/c}$. The lower plots show the two-dimensional distributions after adding the polar angle. Most Ξ^- are stopped in the angular range for Θ between $25°$ and $95°$. The stopping probability is strongly decreased by the kinematics of the primary reaction. It can locally reach up to $30\,\%$.

6.3 Experimental considerations for the hyperatom experiment

After the optimal configuration of the absorber geometry was found in the last section, this geometry could be used for predictions of the experimental counting rates. Due to the high event rates, a simple and fast online trigger had to be found that fulfills the requirements of the $\overline{\text{P}}$ANDA DAQ system (see subsection 6.3.1). Afterwards, the number of detectable hyperatomic transitions and the remaining background was examined. This required to scale the results of the Ξ^- stopping and X-ray efficiency studies to a full experimental period of $\overline{\text{P}}$ANDA. This had to include a compensation for the increased hyperon-antihyperon production probability within the GiBUU simulations (see subsection 6.3.2). Since the background exceeds the signal events by multiple orders of magnitude, filtering algorithms based on cuts on the measured energy deposit and the event topology were developed and implemented. These aimed at a reduction of the background rate while retaining the highest possible number of signal events. These filters are discussed in subsection 6.3.3. At the end of this section, the final counting rate estimations were used to predict the resulting experimental resolutions of the various experimental observables. All calculations in the following subsections were performed for the lead absorber geometry 144 creating Ξ^--^{208}Pb hyperatoms.

6.3.1 Reduction of the online trigger rate

The data storage of $\overline{\text{P}}$ANDA is specified to handle an event rate in the range of up to $100\,\text{kHz}$. Because of that, a simple first-level online triggering must be established that reduces the reaction rate of $2\,\text{MHz}$ to acceptable levels for the DAQ. For the hyperatom experiment this can be based on the energy measurement within PANGEA. The FlashADCs will be able to perform a fast online energy measurement of an incoming pulse. Because of that, a simple triggering filter based on the coincident measurement of the X-ray energies was studied. Individual trigger windows were spanned for $\gamma_1 \wedge \gamma_2$ and $\gamma_0 \wedge \gamma_1$[j] (compare figure 3.3). γ_0 is the $(12, 11) \rightarrow (11, 10)$ hyperatomic transition which is required to study the relative yield of γ_2 (see section 6.3.7). Figure 6.12 shows possible trigger windows for each coincidence. They are marked by the red boxes and span an energy range of $\pm 50\,\text{keV}$ around each calculated X-ray energy in either dimensions. Even this very loose energy cut is able to reduce the trigger rate to a combined rate of $36.3\,\text{kHz}$ which is compatible with the requirements of $\overline{\text{P}}$ANDA. This rate already includes the calculated dead times of the germanium detectors (compare 6.3.4). The trigger window of $\gamma_1 \wedge \gamma_2$ includes the positron annihilation peak at $511\,\text{keV}$. This line dominates the triggered events and can be used for online monitoring and calibration of the system. Further reductions of the trigger rate could easily be achieved by shrinking the energy window of the X-ray coincidence or trigger on the detection of event-associated strangeness in $\overline{\text{P}}$ANDA already at this point. Due to the small number of channels of PANGEA, this simple triggering algorithm that only requires information of PANGEA can be directly implemented within the FPGA that is integrated in the 64 channel FlashADC used for the readout (compare section 4.4.2.1).

---

[j] $E_{\gamma_0} = 312.68\,\text{keV}$

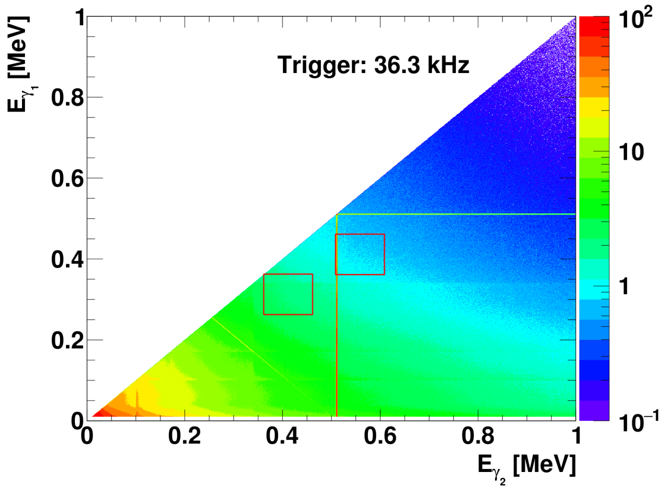

Figure 6.12: The trigger rate of the experiment can be reduced by using the coincident detection of the cascading X-rays. The plot of the pseudodata shows all coincidences below $1\,\mathrm{MeV}\cdot 1\,\mathrm{MeV}$ scaled to one second of beam time. The higher energy of each detected pair is plotted on the x-axis. This energy was gained using the cluster add-back method that sums up the energy of all three crystals of a cluster detector. Trigger windows for both coincidences - $\gamma_1 \wedge \gamma_2$ and $\gamma_0 \wedge \gamma_1$ - are marked by red boxes. Even a very loose energy window of $\pm 50\,\mathrm{keV}$ in either direction allows to decrease the trigger rate to $36.3\,\mathrm{kHz}$ which fits the requirements of the $\overline{\mathrm{P}}$ANDA DAQ. Positron annihilation photons dominate this rate. This allows to use them for online monitoring and calibration. Life time corrections of PANGEA have been applied (see section 6.3.4).

6.3.2 Estimations of the amount of hyperatom transitions in $\overline{\mathrm{P}}$ANDA

First of all, the rate of Ξ^- at $\overline{\mathrm{P}}$ANDA had to be estimated. Here the generated GiBUU events could be used. A single run consisted of 15.8 million primary antiproton-carbon reactions. A large fraction of these antiprotons was Coulomb scattered and in approximately 1/3 of the total events their scattering angle was below $2.857\,\mathrm{mrad}$ so that the antiproton remained inside the HESR acceptance [66]. These events were rejected and not considered for the calculations. In addition to that, the production of hyperon-antihyperon pairs was enhanced by a factor 10 in the production runs. The influence of this on the total number of stoppable Ξ^- was studied by comparing a run of GiBUU events with and without this enhancement. Figure 6.13 shows 63 Ξ^- below $500\,\mathrm{MeV}/c$ for the unmodified run compared to 105 when the amplification was included. The quotient of these numbers results in a correction factor $c_{\Xi^-,\mathrm{GiBUU}} = 0.6 \pm 0.1$ which had to be considered in further calculations.

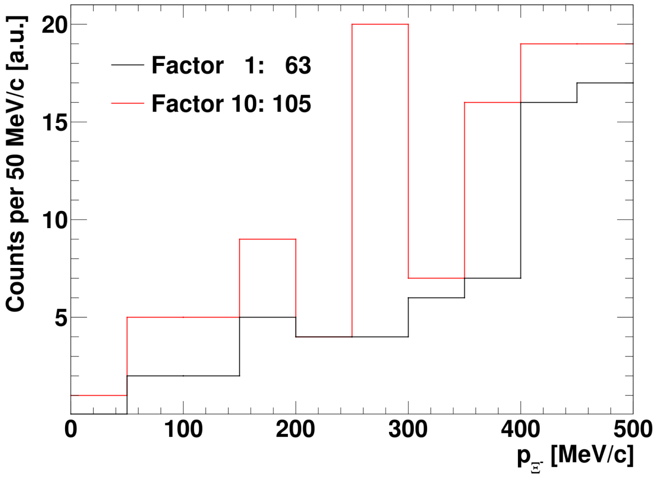

Figure 6.13: Comparison of stoppable Ξ^- in GiBUU runs with and without an enhanced production cross section of hyperon-antihyperon pair production. The quotient of these numbers resulted in a correction factor $c_{\Xi^-,\text{GiBUU}} = 0.6 \pm 0.1$ that had to be considered when calculating the expected number of detected hyperatom transitions.

With this correction, the average amount of Ξ^- per GiBUU run was 1217 ± 203 (compare table 6.2). This yielded 231 ± 39 Ξ^- per second at the planned average interaction rate of 2 MHz. Multiplying this Ξ^- rate with f_{st}, the yield of the shifted X-ray line Y_{γ_2} as well as the isotopic abundance resulted in the rate of detected coincidences in the case of a negligible duration of the atomic cascade. The factors of this multiplication can be found in table 6.5 and table 6.1. For lead the three major isotopes are barely distinguishable (compare table 6.1) and therefore their isotopic abundances were added up which is similar to an enriched target of ^{208}Pb.

The stopping probabilities of the Ξ^- included their survival probability before their atomic capture. A possible decay during the atomic cascade, however, was still missing and could be included by calculating the duration of this cascade t_c. This could be calculated in the software provided by E. F.[k]. The results showed a strong variation of this duration for the kind of studied hyperatom. For Ξ^--^{208}Pb this time was $t_{c,Pb} = 1.88 \cdot 10^{-13}$ s which was negligible compared to the Ξ^- life time. This duration increased for Ξ^--^{115}In to $t_{c,In} = 1.92 \cdot 10^{-12}$ s. This yielded a small loss of $1.17\,\%$ in the detected transitions. Following this trend, the largest effect occurred for Ξ^--^{56}Fe. The cascading duration of $t_{c,Fe} = 1.94 \cdot 10^{-11}$ s decreased the expectation of the observed transitions r_{coinc} by $11.84\,\%$. The results of these studies are summarized in table 6.6. In addition, the expected amount of detected coincidences for a typical $\overline{\text{P}}$ANDA measurement period of 180 days was added to this table.

---

[k] Fortran program cascade0213.f (code on attached CD), Input files in appendix A.7 in listings A.1, A.2 and A.3

Material	r_{coinc} [mHz]	$N_{\text{coinc,180d}}$
Fe	4.95	$76\,884$
In	1.28	$46\,120$
Pb	1.23	$19\,793$

Table 6.6: Predictions for the amount of detected hyperatomic transitions. The coincidence rates r_{coinc} were calculated by multiplying the rate of produced Ξ^-, the yield of γ_2 (Y_{γ_2}), the isotopic abundance and the calculated figure of merit of the target geometry f_{st}. In addition to that, the survival probability of the Ξ^- during its atomic cascade was considered in these calculations. For lead the three major isotopes are barely distinguishable and therefore their isotopic abundances were added up which resembles the usage of an enriched target of ^{208}Pb. The total amount of detected events $N_{\text{coinc,180d}}$ was gained by multiplying r_{coinc} with the beam time designated to the hyperatom experiment. Analogous to f_{st}, the highest amount of detected events is expected for iron, descending with the atomic number of the elements.

6.3.3 Estimations of background events and event filtering

While the results in table 6.6 include the stopping and detection efficiencies of the hyperatomic setup, further actions were required when background events were added. Considering a beam time of 180 days and an average interaction rate of $2\,\text{MHz}$ the total number of primary events sums up to $3.1 \cdot 10^{13}$. Because of this large amount of background, event filtering will be mandatory to increase the signal-to-noise ratio. This filtering was studied in dedicated simulations of complete background events. These were only performed for the lead secondary target but similar results are expected for any other target material. The $\overline{\text{P}}$ANDA barrel DIRC, the STT as well as the magnet system were included as additional material surrounding the dedicated experimental setup. The pseudodata of 10 full runs of GiBUU calculations was used as input for the background events. This corresponded to approximately 100 million events which equaled to $50\,\text{s}$ of $\overline{\text{P}}$ANDA beam time. For the hyperatom events the generated Ξ^- of 30 runs were used to further increase the statistics. This corresponded to 50341 Ξ^- [l] of which only a small fraction could be stopped in the absorber (compare figure 6.11). Even without considering this stopping probability, these quantities illustrated that a lot of background reduction was necessary while the loss of signal events had to be kept minimal. Multiple consecutive cuts had to be combined for this purpose. Before the effects of any of these cuts can be discussed, the topology of a full hyperatom event and its modeling in the simulation had to be studied. This knowledge shows possibilities to implement cuts on various measures.

---

[l] The total number of Ξ^- events in the simulation was 62926. In approximately $20\,\%$ of these, the total strangeness of a full event was unequal to 0. This seemed to be based on a small issue in GiBUU release 1.5 and because of that these events were ignored [66]. An addition of these events would further improve the achieved signal-to-noise ratio.

1. The production of a Ξ^- in the primary interaction requires the coincident production of two units of antistrangeness resulting in associated antihyperons or antistrange mesons. While these mesons are able to escape the primary nucleus, a large fraction of the produced antihyperons annihilate inside. This reaction conserves strangeness which can be carried away by kaons. In addition to these particles the primary interaction produces additional associated particles which must be handled as event-correlated background.
2. In the second step the deexcitation and decay of the hyperatoms was simulated. Since the decay of stopped Ξ^- was deactivated in the specific configuration of GEANT4 used in these simulations, both X-rays were simulated independently starting at the stopping point of the Ξ^-. In contrast to the previously performed efficiency studies, the X-rays were distributed in the full solid angle. In addition to that, the non-mesonic weak decay of the Ξ^- inside the heavy nucleus was modeled by adding two protons with a kinetic energy up to the Fermi energy of $80\,\mathrm{MeV}$ [234]. These slow protons are distributed isotropically in this momentum range and the solid angle. They were added to the X-ray simulations but due to their low momentum, they could barely leave the lead absorber and hardly affected the X-ray detection.

Figure 6.14 sketches the composition of a hyperatom event. All cuts will be individually presented in the following.

6.3.3.1 Strangeness cut

The first cut to filter out hyperatom events aims at getting rid of all events without strangeness. Therefore, it is based on the detection of a single K^+ within $\overline{\text{P}}$ANDA to tag the strangeness event. $\overline{\text{P}}$ANDA has a high detection probability for charged kaons. Looking at the simulated events, background as well as signals, the distribution of K^+ is boosted forward as shown on the left side of figure 6.15. The momentum of the K^+ peaks in the range of $500\,\mathrm{MeV/c}$. In this energy range the separation of pions and kaons, using a combination of tracking, energy loss, time of flight and Cherenkov radiation measurements of the various $\overline{\text{P}}$ANDA components [70, 235, 236], is close to $100\,\%$ so that wrongly identified pions can be ignored. To estimate the detection efficiency of K^+ the results of [179] were used. $28.3\,\%$ of $\Xi^-\bar{\Xi}^+$ pairs could be identified in this work by the detection of the K^+ by only using the time of flight detectors of $\overline{\text{P}}$ANDA. Only a fraction of these $\Xi^-\bar{\Xi}^+$ events contained K^+ and because of that this fraction could be used at this point to estimate the K^+ detection efficiency. In the simulations of the present work the total number of stopped Ξ^- was 226 with 126 of these events containing K^+. Scaling the K^+ efficiency with these factors resulted in a K^+ detection efficiency of $\epsilon_{K^+} = 50.7\,\%$. Applying this cut on K^+ only removed $44\,\%$ of the events with stopped Ξ^-. At the same time, more than $95\,\%$ of the total 10^8 events were filtered out, based on the $4.67 \cdot 10^6$ K^+ included in these events.

Since the production of strangeness and consequently of K^+ was influenced by the increased hyperon-antihyperon pair production in GiBUU this had to be corrected in the calculations. Therefore, the number of events including any kind of strangeness were compared in the GiBUU runs with and without the enhanced hyperon-antihyperon production. Their quotient c_{boost} was used to compensate the enhancement. This correction only had to be performed on the background events since the boost in the Ξ^- production had already been included before. These counts are shown in the right plot of figure 6.15 and the quotient of both results in $c_{\text{boost,bg}} = 1.209$. A detailed look at the right plot shows that the number of events which only contained kaons does not differ in the unmodified and boosted run. This is expected as these were untouched by the

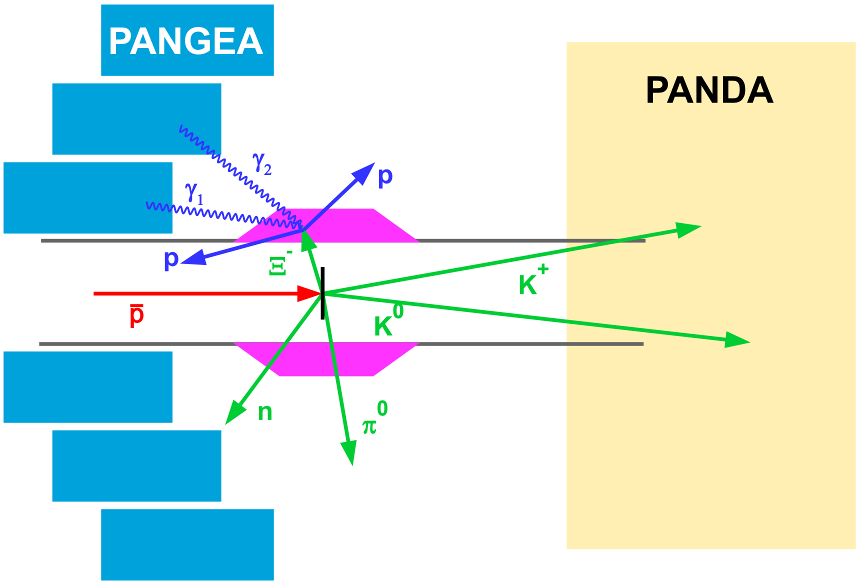

Figure 6.14: In the simulation, a hyperatom event was composed of two steps. The reaction of the antiproton and the primary target was simulated using the GiBUU transport framework (red). The outgoing particles of these reactions were simulated in the PandaRoot framework using GEANT4 as transport code. These particles are shown in green. A K^+ was used as tag for the strangeness production. These need to be detected by P̄ANDA (yellow). When a Ξ^- was stopped inside the secondary target (magenta) its decay was deactivated in GEANT4. Instead of this, a new simulation was performed which simulates the produced hyperatom. Besides both X-rays that have to be detected in PANGEA (cyan), this included two associated protons below their Fermi energy of $80\,\mathrm{MeV}$ which correspond to the hadronic decay of the Ξ^- inside the lead nucleus. The start vertex of these four particles, sketched in blue, originated from the stopping point of the Ξ^-. In addition to the protons from the hyperatomic decay, the primary reaction can also include associated particles (e.g. n and π^0) that need to be considered as event-correlated background.

enhancement of the antihyperon-hyperon pair production. The factor of 10 is visible in events that only contain hyperon-antihyperon pairs. In mixed events of (anti)hyperons and (anti)kaons the same total increase as for the hyperon-antihyperon events is observable. This can be interpreted in a way that half of the produced antihyperons were able to leave the nuclei and the other half annihilated within and produced kaons. The surviving ones will decay weakly and produce an antinucleon in their final state. In the case of an antiproton, it might offer an additional event tag which can be used in future studies but is not considered in this work.

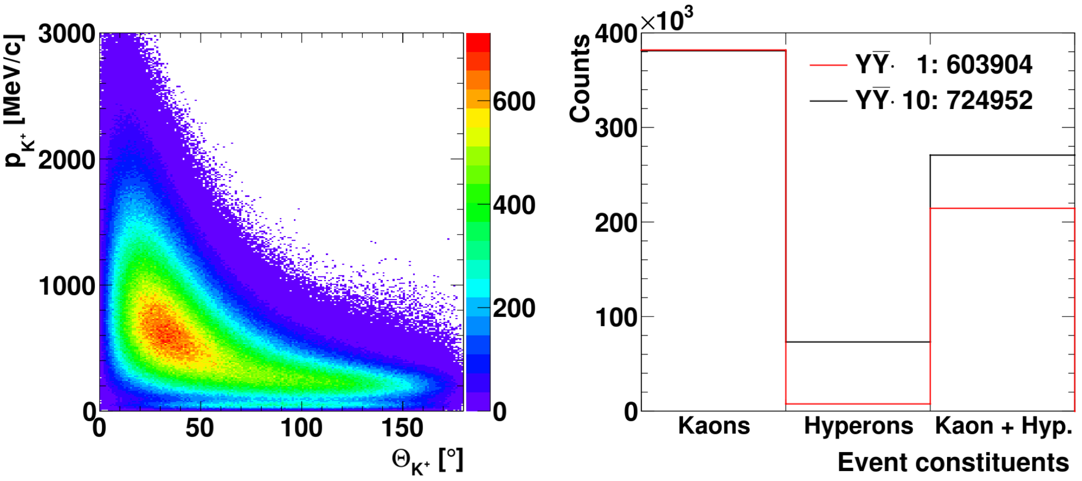

Figure 6.15: K^+ are a viable tag for an event inheriting strangeness. The distribution of them (left) peaks at around $500\,\mathrm{MeV/c}$ and in forward angles where they can be detected by P̄ANDA. On the right side, the number of events containing strangeness is shown and broken down into events with (anti)kaons, (anti)hyperons or mixed events of both. Only particles produced in the primary reaction generated via GiBUU were considered. The diagram compares the results of an unmodified run with a run where the hyperon-antihyperon pair production is enhanced by a factor of ten. This enhancement is directly visible in the events with (anti)hyperons but without (anti)kaons. An increase of the same absolute size in the mixed events hints that half of the antihyperons annihilated inside the primary nucleus. Based on the fraction of the amounts of strange events for both runs, a correction factor $c_{\text{boost,bg}} = 1.209$ was calculated that was required to scale the background events.

6.3.3.2 Coincident X-ray detection in PANGEA

Unfortunately, the K^+ filtering was not sufficient and further cuts were required. The second filter was based on the coincident detection of both X-rays. Unfortunately, PANGEA can only measure the energy deposit and not identify the particle type of a hit. Consequently, this information could not be used for discrimination in the simulation. However, for proper detection of a hyperatom event at least two different clusters have to be hit in coincidence and the energy deposit of each hit can be limited to the range of the expected X-ray energy. The left plot of figure 6.16 shows the spectrum after this filter has been applied in addition to the K^+ filter. Both X-ray energies of the ^{208}Pb hyperatom are marked and are far from any other significant photon line.

As shown in figure 6.7 the energy resolution of the photon used for event tagging (γ_1) is in the order of $\sigma_{\gamma_1} = 0.5\,\mathrm{keV}$ and therefore a cut on a $\pm 2\sigma$ interval around the central energy of $411.5\,\mathrm{keV}$ will contain $\epsilon_{\text{trigger}} = 98\,\%$ of the Gaussian distributed signal events. For γ_2 the width of the (n=9,l=8) state is not negligible due to its strong interaction with the nucleus. This width can be modeled by a Breit-Wigner distribution with $\Gamma_{\gamma_2} = 1.33\,\mathrm{keV}$, based on the absorptive width for ^{208}Pb (compare table 6.1). This distribution needed to be convoluted with the detector resolution of $\sigma_{\gamma_2} = 0.6\,\mathrm{keV}$ for a proper estimation which resulted in a Voigt distributed signal (see equation 6.8). Since this distribution is broader than the distribution of γ_1 a wider energy window had to be considered. A range of $\pm 5\,\mathrm{keV}$ was reasonable for further calculations. After the application of multiple cuts on the background events, the statistics in this small 2 keV × 5 keV window was very small due to the limited input. A solution for this was to extend the energy range for the counting of background events for both X-rays to ±30 keV around the X-ray energy and re-scale it to the small window afterwards. The introduced error was negligible because the background in this extended range was nearly constant and the average of both ranges differed only insignificantly. This is shown in the right plot of figure 6.16 where both energy ranges were fitted by a constant function. This plot was also used to count the amount of background events after only adding the requirement of at least two cluster hits in an event. It totals to 25 010 for 50 s of beam time inside the range of ±5 keV around γ_2.

A further decrease of this background was possible by using the coincident occurrence of both X-ray. This was done by collecting all energy deposits in the clusters and combine all possible pairs. The higher energy deposit was plotted on the abscissa. Figure 6.17 shows this in an extended energy range of ±30 keV around both X-rays energies. Using this event-wise coincidence decreased the number of background to 19 846 in the extended range or 110 when rescaled to the 2 keV × 10 keV window which was still too much. At this point it must be mentioned, that the coincidence time window is important. Long time windows will linearly increase the background while barely gaining any signal events. For germanium detectors with a time resolution of $t_{\text{FWHM}} = 10\,\text{ns}$ a typical time window of 25 ns is usually chosen [188] and this window includes $\epsilon_{\text{time}} = 99.6\,\%$ of all real coincidences when considering a Gaussian time distribution.

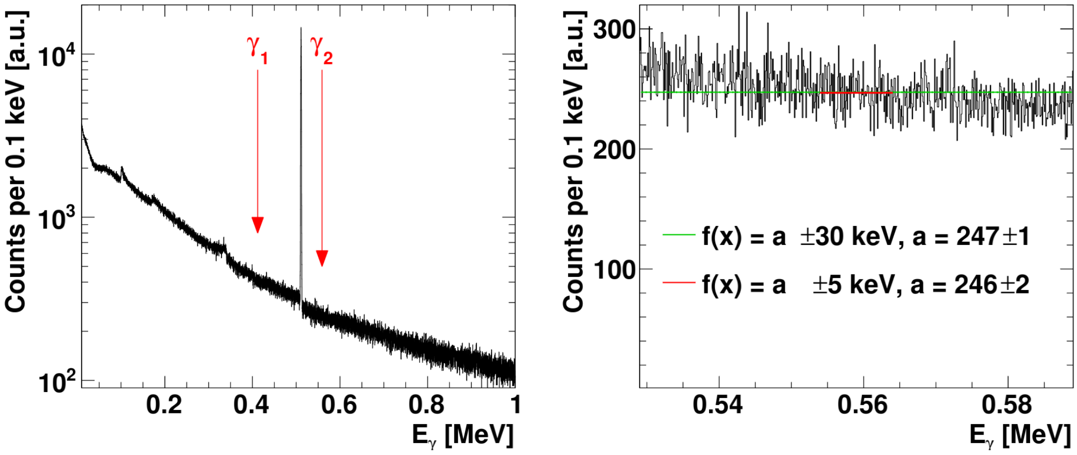

Figure 6.16: The plot on the left shows the simulated energy spectrum below 1 MeV that would be measured by PANGEA within 50 s of $\overline{\text{P}}$ANDA beam time. Cluster add-back was used for it and only events with K^+ and at least two cluster hits are included. Both transition X-Rays γ_1 and γ_2 are far from any other line. The right side is a zoom into the energy range of γ_2. The background in this range is rather constant and fits in the ±5 keV range around γ_2 as well as the wider ±30 keV range did not differ systematically. Because of that, the wider energy range with higher statistics will be used in further studies and then scaled down to estimate the background.

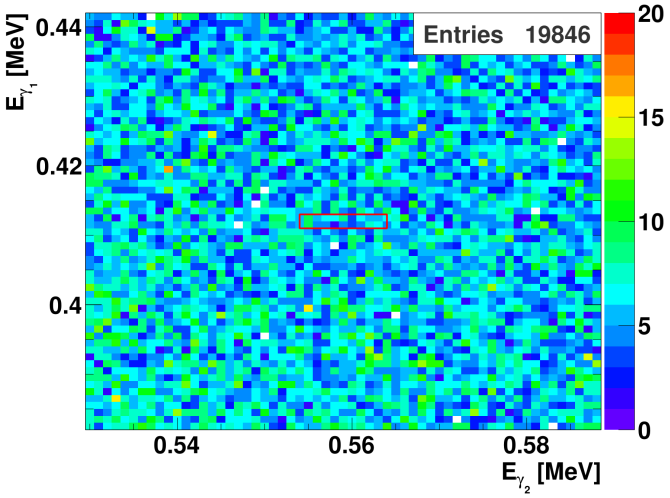

Figure 6.17: Distribution of accidental coincidences γ_1 and γ_2 in the background events. The plot shows the extended energy range around E_{γ_1} and E_{γ_2} of events that passed the K^+ filter. All possible pairs of energy deposits in two different cluster detectors are included. The larger deposit of each pair is plotted on the abscissa. The smaller energy range considered as event background is marked by the red box.

6.3.3.3 Cut on the event topology

The topology of the events could be used to improve the signal-to-noise ratio further. This required to study the signal and background events independently and to find criteria to distinguish both of them.

At first, the main source of background had to be found. This is shown in figure 6.18. The left plot shows the type of particles that interacted with the germanium detectors. It is dominated by neutral particles, photons and neutrons. On the right, the origin of these particles is shown. Since the measured energy was the sum of all particle hits within the crystal, particles that were created in reactions inside a crystal but did not leave it are hidden in this plot. These hits were already registered by their mother particle. Nevertheless, the energy loss of these particles was included in the energy measurements. The simulation showed that most of the detector hits originate from secondary particles produced in direct proximity.

Comparing this to the hyperatom events, the full energy of an X-ray had to be deposited within a cluster and no neighboring clusters would be affected by this detection. This could be used to reduce the background. An algorithm (NN1) was implemented that removed cluster hits when any neighboring cluster measured more than $10\,\mathrm{keV}$ in the same event. This highly decreased the background level to 396 events in the extended energy range or 2.2 when scaled down. At the same time this filter decreased the event rate, because an event where both X-rays were detected in neighboring clusters was filtered out. This resulted in a decrease of the signal efficiency by $59.3\,\%$.

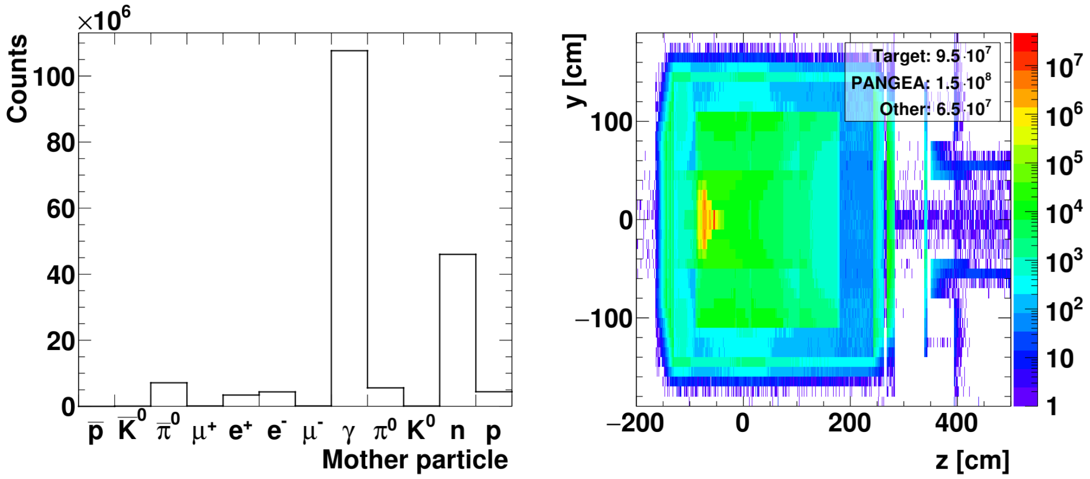

Figure 6.18: Most particles hitting the germanium crystals in the simulations were photons and neutrons as shown in the left plot. The origins of these particles are shown on the right in a projection to the yz plane. Most of the background particles were produced within PANGEA and thus a suppression algorithm for these was developed.

In a second revision the algorithm was altered to prevent this drop of signal efficiency. This new algorithm (NN2) ignored neighboring cluster hits close to the energy of the X-rays. The previously explained $2\,\mathrm{keV} \times 10\,\mathrm{keV}$ window around E_{γ_1} and E_{γ_2} was chosen for this. Using this algorithm was less efficient in the background suppression. 4.7 events remained in the small energy window. On the other hand the number of signal events was unaffected by the cut.

Nevertheless, the background events still dominated the signals with either configuration. The veto detector of PANGEA could be used to finally improve this situation. Three PWO crystals are integrated in every cluster for this purpose (compare section 4.2.2.3). Figure 6.19 shows their placement behind the germanium crystals.

Because of that, particles that hit the veto detector had to pass the germanium crystals in front of it which implied that the particle could not deposit its complete energy inside the crystal. This is the case for either high energetic charged particles or Compton scattered photons and thus any event with one or more hits in the veto detector was discarded. Using this information of the veto detector decreased the number of background events in the small energy window to 0.29 for the first next-neighbor filter or 0.36 for the second one. The veto filter cleaned the background by a large portion of events that were still unaffected by the second next-neighbour filter (NN2) so that their suppression power becomes similar. At the same time, the hyperatomic X-ray coincidence signals were barely affected. These dropped only by $2.7\,\%$ (NN1) or $3.0\,\%$ (NN2), respectively, because for this one of the low energy protons had to hit the veto crystals. In addition to that, the effect of the veto filter on the associated particles of the hyperatom event had to be studied. These particles in events with stopped Ξ^- hit the veto detector in more than half of the events so that only 55 of the 126 events that passed the K^+ filter remained. Nevertheless, the background suppression of this cut outweighed its influence on the hyperatomic events.

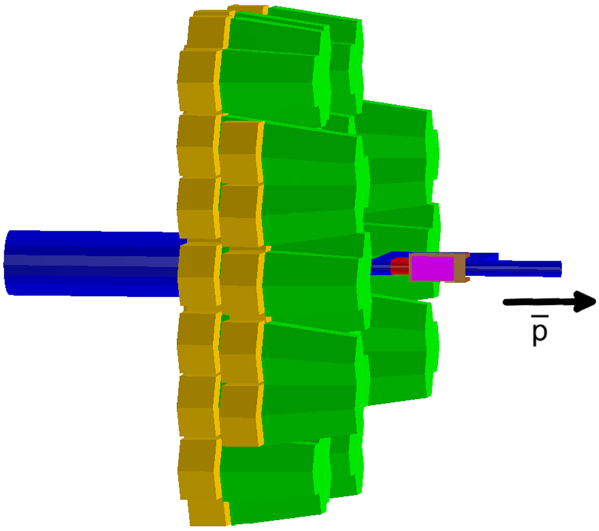

Figure 6.19: Picture of the simulated geometry with added veto detectors. The veto detector (compare section 4.2.2.3), situated behind the germanium crystals, are painted in orange.

To compare these cuts the signal efficiency ϵ_{signal} as well as the background suppression factor s_{BG} needed to be calculated. For both of them, the remaining events had to be scaled with the total number of events which was 19 796 for the signal studies and $1 \cdot 10^8$ for the corresponding background events. Based on these a simple figure of merit f_{filter} to compare the performance of the filter version could be calculated. The product of the signal efficiency and the background suppression factor is proportional to the signal-to-background ratio and thus a good benchmark. f_{filter} is shown in table 6.7. For the cuts that include the veto detector the fraction of discarded events with stopped Ξ^-, α_{Ξ^-},

$$\alpha_{\Xi^-} = \begin{cases} 1 & \text{no veto} \\ \frac{55}{126} & \text{with veto} \end{cases}$$

also had to be considered in f_{filter}:

$$f_{\text{filter}} = \epsilon_{\text{signal}} \cdot s_{\text{BG}} \cdot \alpha_{\Xi^-} \tag{6.3}$$

The best overall performance showed the NN2 filter in combination with the veto detector. This filter was used for all further studies.

Filter	ϵ_{signal} [%]	s_{BG}	f_{filter}
NN1	59.3	$4.6 \cdot 10^7$	$2.7 \cdot 10^7$
NN2	100	$2.1 \cdot 10^7$	$2.1 \cdot 10^7$
NN1 $\wedge$ veto	57.7	$3.5 \cdot 10^8$	$8.7 \cdot 10^7$
NN2 $\wedge$ veto	97.0	$2.8 \cdot 10^8$	$1.2 \cdot 10^8$

Table 6.7: Comparison of the various event filtering methods. While NN1 filtered out all cluster hits with neighboring ones, the NN2 filter was less strict by letting hits in the energy range of the hyperatomic X-rays pass. When the veto detector was used for filtering the reduced number of events with stopped Ξ^- had to be considered in the figure of merit f_{filter}. f_{filter} is proportional to the signal-to-background ratio and hence had to be maximized. The less severe NN2 filter showed the best performance when it was combined with the veto detector.

6.3.4 Estimation of the life time of PANGEA in $\overline{\text{P}}$ANDA conditions

At this point the life time of PANGEA under $\overline{\text{P}}$ANDA conditions still had to be estimated. Traditionally germanium detectors are limited in their rate capabilities due to their long preamplifier signals with exponential decay times in the order of 50 µs. PANGEA, however, has to handle too high rates for such slow signals and the implementation of a fast reset is mandatory. This fast reset clears the charge collection capacitor within less than 1 µs when an adjustable threshold is exceeded (compare section 4.2.2.2). Additionally, the digital pulse shape analysis allows to disentangle the possible pile up of consecutive events (compare chapter 5). The present implementation of this analysis requires a minimum of 4 µs of a signal pulse for a proper analysis, which limits the interval between two subsequent fast resets. This is represented by summing both times to a total reset time of 5 µs. Such a reset can be forced in two ways that were distinguished in the simulation. On the one hand, a single hit could deposit more energy than the threshold energy. On the other hand, multiple hits could add-up and exceed the threshold. To distinguish these the first ones will be called hard resets and the accumulated ones soft resets. Both types of resets are sketched in figure 6.20. The upper part of the figure shows a detector without fast resetting preamplifier. The first signal already exceeds the energy threshold which results in a blind detector and due to the high interaction rate and slow discharge of the capacitor the detector never recovers to an active state within the visible period of time. The plot at the bottom shows the same detector hits with the fast resetting preamplifier. After the first hit, the energy threshold is exceeded and this results in a hard reset of the detector. 5 µs later the detector is discharged and ready to measure again [m]. While the second hit can be processed the energy threshold is surpassed when the third hit occurs and adds up to the previous charge. This triggers a soft reset. After two more hits another large energy deposit occurs leading to another hard reset.

The time occupied by both kinds of reset determines the dead time of the detector. To quantify it, the rate of hits below and above the energy threshold had to be determined. For this purpose, the measured energy spectrum for a single crystal before any cuts was taken into account. Figure 6.21 shows this spectrum rescaled to a beam time of 1 s. The spectrum was generated from the

---

[m] This includes the required signal length for proper analysis as previously explained

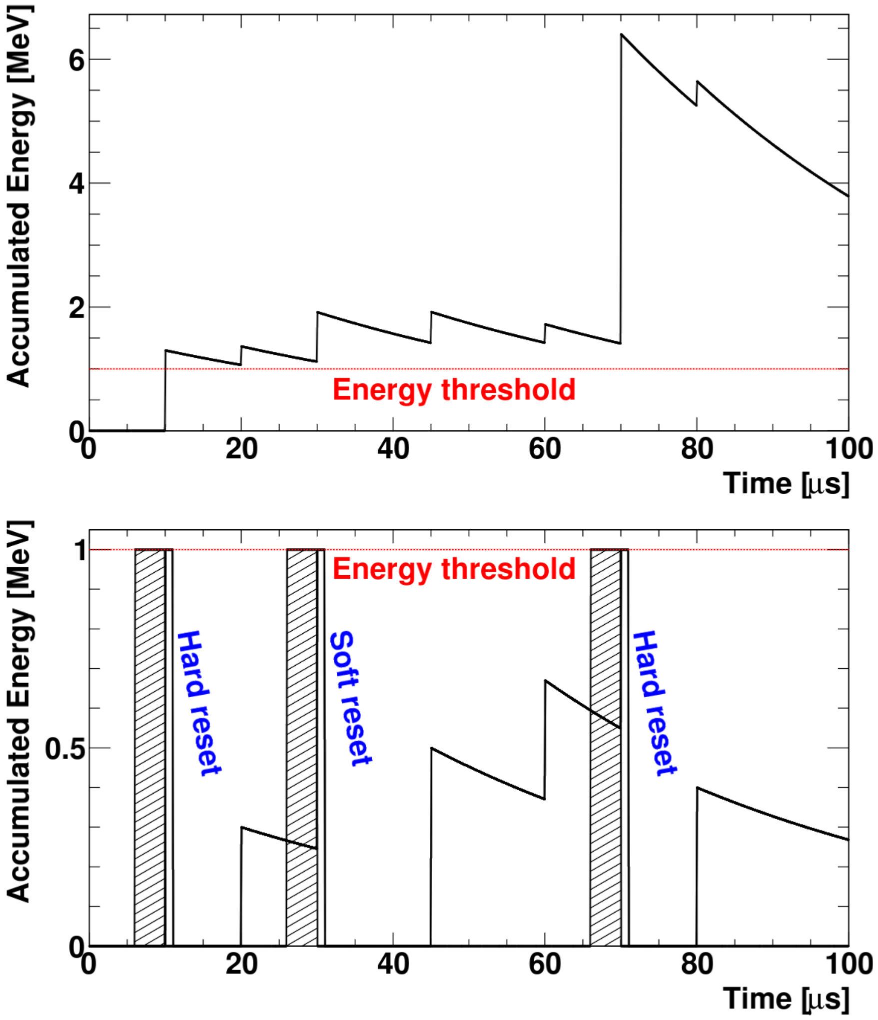

Figure 6.20: Visualization of the fast reset of the preamplifier. The upper plot shows the case of an ordinary germanium detector without fast reset. The first hit exceeds the energy threshold resulting in a blind detector. The high interaction rate never allows the detector to recover from this state due to its slow decaying signals. In contrast to that, the fast reset of the PANGEA preamplifier recovers the detector quickly. This drastically increases the rate capabilities of the detector. In the simulations to estimate the life time of PANGEA direct resets, originating from particle hits above the energy threshold, and accumulating ones can be distinguished. First ones are called hard resets and the second ones soft resets. The shaded area before every sketched reset marks the period where a proper analysis of an incoming signal will not be possible.

average of all crystals to increase the statistics. At this point, one had to consider that the average interaction rate at $\overline{\text{P}}$ANDA of $2\,\text{MHz}$ includes a duty factor of approximately $50\,\%$ (compare figure 2.13). Consequently, the doubled interaction rate of $4\,\text{MHz}$ is present during the data taking phase and had to be considered to calculate the dead time of the detector.

To start this, the number of hard resets was extracted from the energy spectrum. This was done by counting the number of hits above the energy threshold n_{hard}. For the shown threshold of $1\,\text{MeV}$ $n_{\text{hard}} = 4.6 \cdot 10^4$ hard hits were counted. The same had to be done for the hits below the threshold n_{soft}. Energies above $10\,\text{keV}$ were considered for this which yields $n_{\text{soft}} = 8.8 \cdot 10^4$.

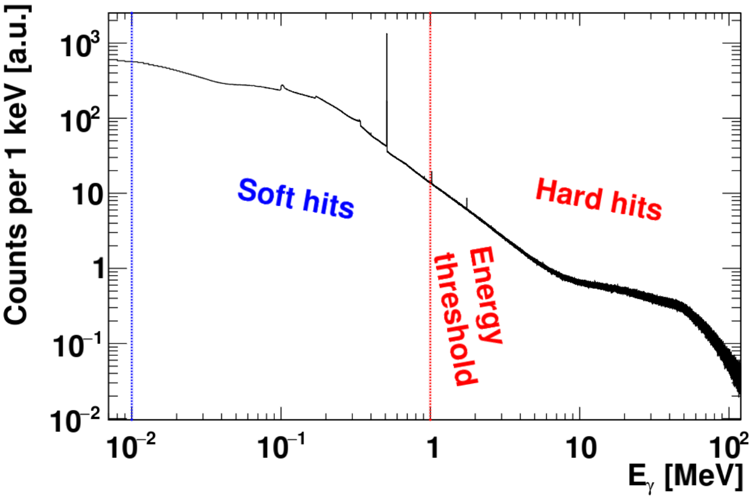

Figure 6.21: The energy spectrum of a single crystal was gained by scaling the total energy spectrum of all crystals without add-back down to a single crystal and a duration of one second. The energy threshold of the fast reset divided the spectrum into soft and hard hits that were treated individually in the life time estimations.

These numbers served as input to a simplified time-based simulation. At first, random timestamps for both kinds of hits were generated in the $1\,\text{s}$ time window and sorted chronologically. The time difference between two consecutive hard hits was calculated and the time required for a reset of the preamplifier of $1\,\mu\text{s}$ substracted. Figure 6.22 shows the distribution of these differences. Negative times represented an overlap of two consecutive hard hits. Times below $4\,\mu\text{s}$ were too short for the pulse shape analysis and therefore all time differences above $4\,\mu\text{s}$ were added up to estimate the life time of the detector when only hard resets were considered.

At this point, the effect of the soft hits was still missing. To take these into account, they were split into subsets between two consecutive hard resets. The energy of each soft hit was randomly generated according to the distribution of figure 6.21 in a range of $10\,\text{keV}$ to $1\,\text{MeV}$. Starting at each hard reset, the total energy was reset to 0 and a detector hit with the corresponding energy deposit and time stamp was generated. The detector signal was mimicked by adding a slow exponential decay with a decay constant of $50\,\mu\text{s}$. Considering the high rate of soft hits, they are expected to pile up which might surpass the energy threshold and trigger a reset. These occurrences were added up and for each of them $5\,\mu\text{s}$ were substracted from the life time calculated previously. In this way, a total life time t_{life} of $76.15 \pm 0.04\,\%$ remained for an energy threshold of $1\,\text{MeV}$.

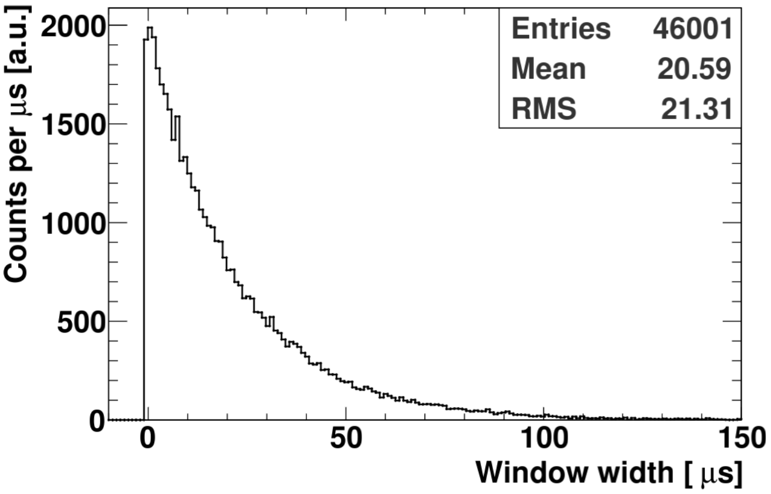

Figure 6.22: Distribution of the time windows between two hard resets. Due to the limits of the pulse shape analysis, each reset was characterized by a dead time of 5 µs. Negative time windows were formed by consecutive resets overlapping each other. Time windows below 4 µs were too short to analyze an intermediate signal. Because of that, all data points above 4 µs were summed for the estimation of the life time.

This life time was the estimation for a single crystal. However, when add-back of multiple crystals is factored in, the life time of the full system of crystals involved has to be considered. For this, the average number of crystals hit in the full detection of a X-rays with an energy of $411.5\,\text{keV}$ and $558.5\,\text{keV}$, respectively, was essential (see figure 6.23). For both energies most events were detected within a single crystal. If multiple crystals were required for the measurement, all of them had to be ready to measure at the specific time. The probability for this is given by

$$t_{\text{life,multi}}(N) = {t_{\text{life,single}}}^{N}$$

with the number of crystals involved N. To calculate the expected life time of the system of crystals $t_{\text{life,multi}}$, N was randomly generated 1000 times according to the respective distribution in figure 6.23 and the result was averaged. With $72.45 \pm 0.08\,\%$ ($411.5\,\text{keV}$) and $71.51 \pm 0.09\,\%$ ($558.5\,\text{keV}$) the estimates of the life time of the involved crystals were slightly lower than for a single crystal.

Before varying the threshold value, its influence on the expected energy resolution had to be taken into account. Since this threshold value also defined the upper limit of the measuring range of the preamplifier it also influenced the dynamic range of the data acquisition system and hence the energy resolution. This resolution δE_{FWHM} is a combination of a constant δE_{const} and an energy dependant term δE_{E}:

$$\delta E_{\text{FWHM}}(E) = 2\sqrt{2\ln 2} \cdot \sqrt{{\delta E_{\text{const}}}^{2} + \delta E_{\text{E}}^{2} \cdot E} \tag{6.4}$$

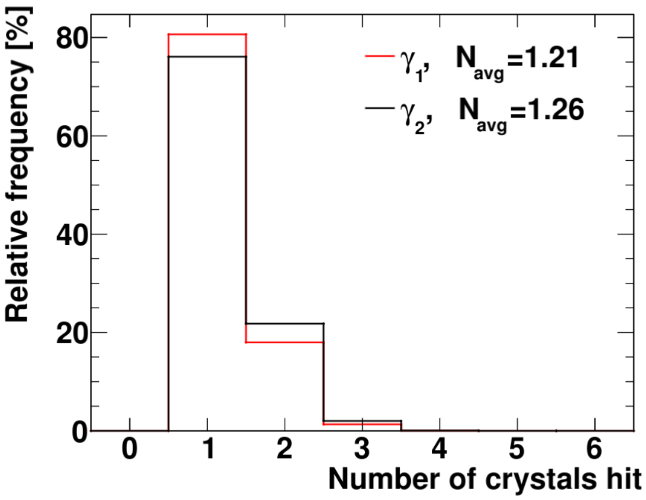

Figure 6.23: The number of crystals involved in the detection of a X-ray is small. For the energies of $E_{\gamma_1} = 411.5\,\text{keV}$ and $E_{\gamma_2} = 558.5\,\text{keV}$ most events only required a single crystal. When multiple crystals were involved the life time of all of them had to be considered.

While δE_E depends on effects of the crystal and is affected e.g. by radiation damage (compare chapter 5), the constant term δE_const is dominated by noise introduced by the readout electronics and thus varies with the measurement range. Considering a linear dependence of δE_const on the measurement range is a reasonable estimate. The values of $\delta E_\text{E} = 6.45 \cdot 10^{-4}\,\sqrt{\text{MeV}}$ and $\delta E_\text{const} = 3.75 \cdot 10^{-4}\,\text{MeV}$ have been determined experimentally (compare equation 4.5) using a measurement range of up to $1.5\,\text{MeV}$. This had to be considered for a proper scaling of δE_const:

$$\delta E_\text{const}(E_t) = \delta E_\text{const} \cdot \frac{E_t}{1.5\,\text{MeV}}.$$

For $E_{\gamma_2} = 558.5\,\text{keV}$ the scaled resolution for the threshold energy of $1\,\text{MeV}$ is $\delta E_\text{FWHM}(558.5\,\text{keV}) = 1.3\,\text{keV}$. Varying this threshold energy yields the results summarized in table 6.8. While the life time could be increased by up to $17\,\%$ when the threshold would be increased, the resolution would worsen drastically. A figure of merit f_lt to decide on the optimal threshold energy could be based on the estimated resolution of the energy measurement. This is determined by the detector resolution ($FWHM$) divided by the square root of the number of counts N_c inside the peak. N_c is proportional to the life time of the full detection system which can be estimated by the product of the life time of both measured X-rays

$$N_c \propto t_\text{life,multi}(\gamma_1) \cdot t_\text{life,multi}(\gamma_2).$$

This yields

$$f_\text{lt} = \frac{FWHM}{\sqrt{N_c}} \propto \frac{FWHM}{\sqrt{t_\text{life,multi}(\gamma_1) \cdot t_\text{life,multi}(\gamma_2)}} \tag{6.5}$$

and had to be minimized. Based on the results summarized at the end of table 6.8 the $1\,\mathrm{MeV}$ threshold performed slightly better that $2\,\mathrm{MeV}$. Higher thresholds were ruled out. Because of that, a threshold energy of $1\,\mathrm{MeV}$ was used in all further studies.

It is important to note that these simulations ignored the clustering of hits in nearby crystals produced by high energy particle interactions. This effect could not be modeled by the averaging that was used to generate the input signals. The clustering could shift the hard resets towards events that would be sorted out by the analysis cuts anyways and thus the dead time for signal event could be lower than the estimated value. Since this could not be quantified here, the estimated life times were used for signal as well as background events. For a more detailed analysis of this effect full time-based simulations will be required in the future.

Threshold E_t **[MeV]**	**Hard hits [Hz]**	**Soft Hits [Hz]**	$t_{\text{life,single}}$ **[%]**	$t_{\text{life,multi}}$ γ_1 **[%]**	$t_{\text{life,multi}}$ γ_2 **[%]**	δE_{FWHM} $(558.5\,\mathrm{keV})$ **[keV]**	f_{lt}
1	$4.6 \cdot 10^4$	$8.8 \cdot 10^4$	76.15 ± 0.04	72.45 ± 0.08	71.51 ± 0.09	1.3	1.8
2	$3.7 \cdot 10^4$	$9.6 \cdot 10^4$	82.68 ± 0.02	79.75 ± 0.06	79.00 ± 0.07	1.6	2.0
5	$3.0 \cdot 10^4$	$10.4 \cdot 10^4$	86.07 ± 0.02	83.61 ± 0.05	82.98 ± 0.06	3.2	3.8
10	$2.5 \cdot 10^4$	$10.8 \cdot 10^4$	88.25 ± 0.01	86.12 ± 0.04	85.57 ± 0.05	6.0	6.9

Table 6.8: Results of the life time calculations and the corresponding estimation of the detector resolution. Increasing the energy threshold increased the life time by up to $17\,\%$ but at the same time the resolution decreased by more that a factor of 4. This was combined in the figure of merit f_{lt}. Small values of f_{lt} are favored. This ruled out the $5\,\mathrm{MeV}$ and $10\,\mathrm{MeV}$ thresholds. The $1\,\mathrm{MeV}$ threshold performed slightly better that $2\,\mathrm{MeV}$.

6.3.5 Summary of the detectable number of events

After all the efficiencies were calculated, they were summarized in this section. Furthermore, the expected counts of detected hyperatom X-ray coincidences and background events were calculated. To estimate the number of detected signal events $n_{\text{d,sig}}$ the total number of events $n_{\text{T,sig}}$ had to be multiplied with their detection efficiency ϵ_{signal} for the X-rays, the correction factor for K^+ in stopped Ξ^- events c_{Ξ^-} [n] and the probability to detect a K^+ in $\overline{\text{P}}$ANDA ϵ_{K^+}. In addition, the corrections for the life time t_{life}, the time coincidence cut ϵ_{time} and the efficiency of the coincidence trigger $\epsilon_{\text{trigger}}$ had to be multiplied which resulted in

$$n_{\text{d,sig}} = n_{\text{T,sig}} \cdot \epsilon_{\text{signal}} \cdot c_{\Xi^-} \cdot \epsilon_{K^+} \cdot t_{\text{life}} \cdot \epsilon_{\text{time}} \cdot \epsilon_{\text{trigger}} \tag{6.6}$$

and $n_{\text{d,sig}} = 1237$ signal events.

The calculations for the background events are similar. The event detection efficiency was replaced by the reciprocal of the background suppression factor $\frac{1}{s_{\text{BG}}}$ and the effect of the increased hyperon-antihyperon pair production c_{boost} had to be considered. This resulted in

$$n_{\text{d,BG}} = \frac{n_{\text{T,BG}}}{s_{\text{BG}}} \cdot \frac{\epsilon_{K^+} \cdot t_{\text{life}} \cdot \epsilon_{\text{time}} \cdot \epsilon_{\text{trigger}}}{c_{\text{boost}}} \tag{6.7}$$

and $n_{\text{d,BG}} = 23\,805$ background events in the ± 5 keV region around E_{γ_2}. All these input parameters are summarized in table 6.9. The effect of the multiple stages of event filtering are shown in figure 6.24. The logarithmic plot on the left shows how the significance of the signal events increases by the consecutive application of each cut. Only the usage of all described cuts allows to see a proper peak on top of the remaining background. The same effect is visible in the total-to-background ratio shown on the right side.

	Signal events	**Background** [± 5 keV]
Total events n_T	19 796	$3.11 \cdot 10^{13}$
Signal detection efficiency ϵ_{signal}	97.0 %	
Correction for K$^+$ in stopped Ξ^- events c_{Ξ^-}	24.4 %	
Background suppression factor s_{BG}		$2.8 \cdot 10^8$
GiBUU strangeness correction c_{boost}		1.209
K^+ efficiency ϵ_{K^+}	50.7 %	50.7 %
Time coincidence cut ϵ_{time}	99.6 %	99.6 %
Trigger window cut $\epsilon_{\text{trigger}}$	98.0 %	98.0 %
Life time correction t_{life}	51.8 %	51.8 %
Events detected n_{det}	**1237**	**23 805**

Table 6.9: Summary of the counting rates of the signal and background events. Applying all cuts and efficiencies reduced the background events to feasible numbers while affecting the signal to a lesser extent. While the hyperatom transitions are peaking at E_{γ_2}, the background events are distributed uniformly in a ± 5 keV interval around this energy.

---

[n] c_{Ξ^-} is given by the fraction of the total amount of Ξ^- stopped (= 226) and the number of stopped Ξ^- events with K^+ that pass the veto filter (= 55).

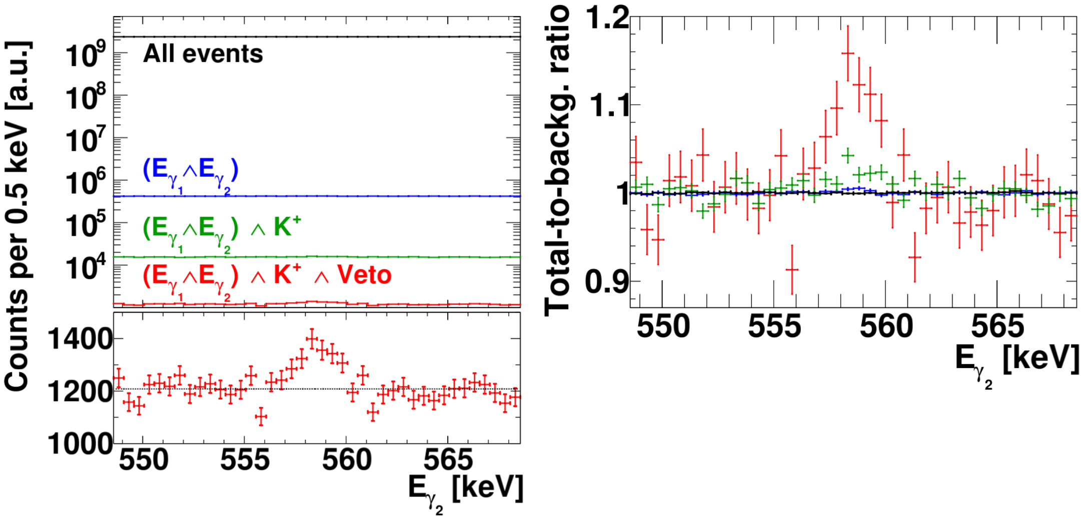

Figure 6.24: The figure shows the effect of the event filtering. The logarithmic plot on the left shows a simulation of the remaining signal and background events after the consecutive application of each cut. Only the combination of all cuts allowed to detect a significant signal on top of the background events as emphasized by the linear plot on the bottom left. The plot on the right shows this increase in significance in the total-to-background ratio.

These calculated event rates were compared to the experiments at J-PARC in figure 6.25. Based on the simulations, $\overline{\text{P}}$ANDA will be able to measure the highest amount of transitions by the detection of two coincident X-ray transitions. Experiments with lead and other absorbers with high atomic numbers are only possible due to the separated target design of $\overline{\text{P}}$ANDA. The estimated results of E07 in an intermediate Z range are two orders of magnitude lower than the predictions for $\overline{\text{P}}$ANDA. At the same time, the background estimations for both experiments at J-PARC are lower due to the kaon beam which partially compensates the lower predicted number of hyperatom transitions. All these three experiment complement each other in covering a wider range of the periodic table and measuring the Ξ^- potential.

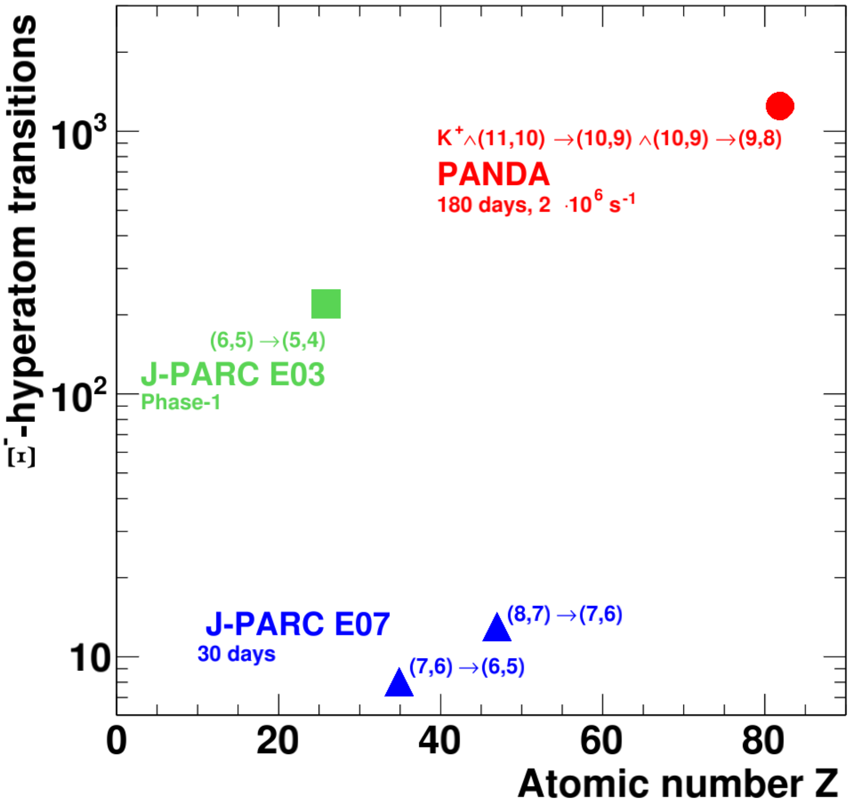

Figure 6.25: Comparison of the expected events of the $\overline{\text{P}}$ANDA hyperatom experiment and J-PARC E03 and E07. The heavy Ξ^--^{208}Pb hyperatoms studied at $\overline{\text{P}}$ANDA are complementary to the experiments at J-PARC. $\overline{\text{P}}$ANDA will be able to study more hyperatomic transitions than both experiments at J-PARC and is unique in its ability to study coincidences in large amounts and heavy targets. The estimates for E03 and E07 are based on [163, 165].

6.3.6 Estimations of the experimental precision of $\Delta E^{\text{nuc}}_{n_0}$ to study Re($V_0^{\Xi^-}$)

The experimental precision in the estimation of Re($V_0^{\Xi^-}$) could be predicted from the measurements of the strong energy shift. Since its resolution is affected by the quality of the fit, the calculated amount of hyperatom transitions and background had to be mixed to get a realistic estimate. A proper description of the signal line shape had to consider the line width as well as the detector resolution. This convolution of a Breit-Wigner distribution and a Gaussian distribution resulted in the Voigt distribution $V(x)$. Its main parameters are the widths of both constituents of the convolution, γ_{decay} and σ_{detector}. When using the scaled complex error function (Faddeeva function)

$$w(z) = \exp^{-z^2} erfc(-iz)$$

with $z = \frac{x+i\gamma_{\text{decay}}}{\sigma_{\text{detector}}\sqrt{2}}$ the Voigt distribution could be expressed as

$$V(x) = \frac{Re[w(z)]}{\sigma_{\text{detector}}\sqrt{2}}. \tag{6.8}$$

The background events on the other hand were distributed uniformly inside the small energy window around $E_{\gamma_2} = 558.57\,\text{keV}$ (compare figure 6.16). The statistics of both kinds of events were calculated in the previous section (6.3.5). For the parameters of the Voigt distribution $\gamma_{\text{decay}} = 1.33\,\text{keV}$ was utilized as calculated for ^{208}Pb (see table 6.1). For σ some considerations were required that did not only include the dynamic range of the data acquisition system, but also the irradiation of the detector. On the one hand, as shown in table 6.8, a dynamic range of $1\,\text{MeV}$ will be sufficient for the experiment but the scaling in the simulation was based on a wider measurement range up to $1.5\,\text{MeV}$. On the other hand, the irradiation will decrease the resolution of the detector over time as shown in chapter 5. Since the influence of the dynamic range is energy independent, in contrast to the radiation damage, both effects could be disentangled for an estimation.

At first, the irradiation was considered and the results of chapter 5 could be used. Since the irradiation at COSY was roughly equivalent to half of the full experimental time of the hyperatomic experiment, it was a reasonable estimation to use the detector resolution after this irradiation as an average of the full beam time. Since the data taken at COSY was affected by the issue of the DAQ system, the measurements at GSI after the irradiation were used. Assuming that this data could be further improved in the same way as the data taken at COSY, the estimated resolution was $2.67\,\text{keV}$ for the $1332\,\text{keV}$ line of ^{60}Co.

Based on this resolution the parameters of equation 6.4 had to be recalculated. At first, the energy independent term, and thus the measurement range, was kept constant. The predicted irradiation resolution could be attained with $\delta E_{\text{E}} = \delta E_{\text{E}_{\text{rad}}} = 9.27 \cdot 10^{-4}\,\sqrt{\text{MeV}}$. After that, the measurement range was adjusted. The typical range for a measurement of ^{60}Co is 0 to $1.5\,\text{MeV}$. The scaling procedure was shown in subsection 6.3.4. Repeating this procedure resulted in $\delta E_{\text{const}} = \delta E_{\text{const,1MeV}} = 2.50 \cdot 10^{-4}\,\text{MeV}$ for an upper measurement range of up to $1\,\text{MeV}$. Using these parameters in equation 6.4 yielded a resolution (FWHM) of $\delta E = 1.73\,\text{keV}$ for E_{γ_2} which resulted in $\sigma = 0.74\,\text{keV}$ as input to equation 6.8.

These parameters were used in a toy Monte Carlo study performed in RooFit [237]. Signal and background events were generated in an extended unbinned maximum-likelihood study, using a Poisson distributed variation of the simulated number of events. One of these studies is shown in the left diagram of figure 6.26. The signal peak sticks out of the uniform background and can be properly fit by the Voigt distribution and an added constant background. This generation was repeated 1000 times to predict the uncertainties of the energy measurement. The result of these repetitions is shown in the right histogram of figure 6.26. This histograms shows the fit results of the measured energy peaks for all repetitions. These were fit by a Gaussian distribution. The expectation value of this fit is $\mu = 558.58\,\mathrm{keV}$ which reflected the input value. The uncertainty of the energy measurement equals to the standard deviation of this fit, $\sigma = 0.14\,\mathrm{keV}$.
This uncertainty could be translated to an estimation of the uncertainty in the measurement of the Ξ^- nuclear potential $V_0^{\Xi^-}$. This was done by repeating the calculations presented in section 3.2 with a variation of the real part of the scattering length b_0 until the limits of the range spanned by the statistical deviations were hit. This resulted in $\mathrm{Re}(b_0) = 0.25 \pm 0.01\,\mathrm{fm}$ which corresponded to $\mathrm{Re}(V_0^{\Xi^-}) = 20.5 \pm 0.8\,\mathrm{MeV}$ using the relation shown in equation 3.10.

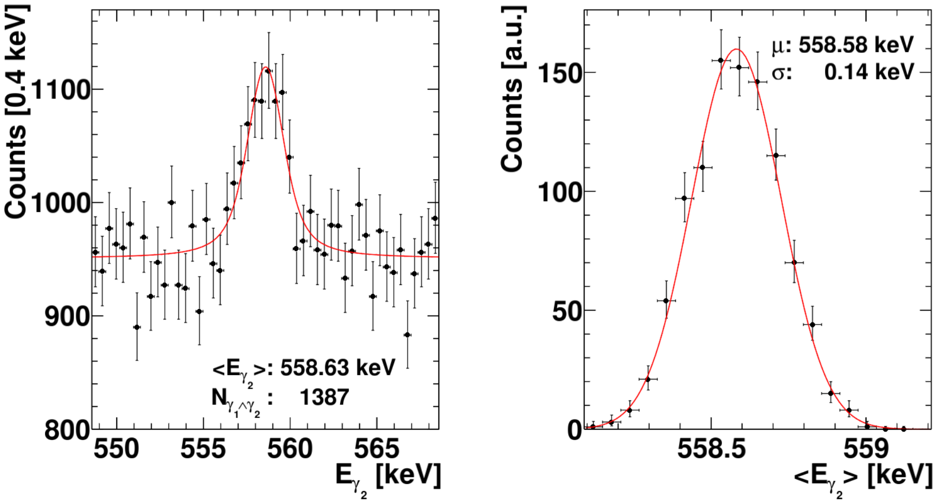

Figure 6.26: To estimate the precision and accuracy of the measurement, signal and background events were generated according to their estimations. While the background was distributed uniformly, the signal followed a Voigt distribution. The peak of the signal sticks out of the background as shown on the left and could be fitted to obtain the peak position. Repeating this simulation 1000 times and filling the peak positions into a histogram yielded the plot on the right. The mean value of the Gaussian fit shows no systematic shift compared to the input energy. The standard deviation of $\sigma = 0.14\,\mathrm{keV}$ equals to the expected statistical uncertainty of the experiment.

After having estimated the statistical uncertainties, it was important to have a look at the systematics of the experiment. The main factor here is the description of the nuclear potential (compare equation 3.11). The description of this potential, even in the simplest $t\rho$ form, has two main uncertainties, its depth, defined by the parameter b_0 (compare equation 3.10), and shape of the nucleon distributions. The uncertainty of the proton and neutron distribution can be condensed to the uncertainty of the thickness of the neutron skin of the nucleus Δr_{np} (see equation 3.12). Since the strength of the potential will be the subject of the studies, the thickness of the neutron skin had to be determined from the data of other experiments. Here $^{208}_{82}$Pb shines because its neutron skin is experimentally well-established. Multiple experiments measured $\Delta r_{\text{np},^{208}Pb}$ with comparatively high precision. These range from the elastic proton scattering [238, 239], the spectroscopy of the pygmy and giant dipole resonance [240, 241, 242] and antiprotonic atoms [135]. In addition to that, the PREX experiment used parity violation to measure the neutron radius of ^{208}Pb [243]. Finally, this radius could be extracted from measurements of the tidal polarizability of binary neutron star systems in gravitational wave signals [244]. Especially the latter two limited the possible range of Δr_{np}: the estimations of PREX are model-independent and thus do not inhibit systematic uncertainties of any underlying model and the neutron star measurement yields an upper limit for the neutron skin thickness. All these measurements are condensed in figure 6.27. The blue and red data points for the strong interaction width $\Gamma^{\text{abs}}_{n_0}$ and the energy shift $\Delta E^{\text{nuc}}_{n_0}$ were calculated while varying Δr_{np} in a range according to the results of the former experiments. A linear dependence is visible for both observables. When using the limits given by PREX and the neutron stars a simple projection of the corresponding data points is possible. This resulted in a systematic uncertainty of $\delta(\Delta E^{\text{nuc}}_{(10,9)\rightarrow(9,8)}) = \pm 0.1\,\text{keV}$ which is slightly smaller than the estimated statistical uncertainty.

In addition to that, a precise energy calibration will be mandatory to achieve the required precision. Calibration sources with energies close to both X-ray lines will be needed. Especially ^{152}Eu shines for the calibration of both X-rays of the hyperatomic cascade with transition energies at $411.1163\,\text{keV}$ and $556.9907\,\text{keV}$ ^{o} as well as other closely situated γ lines in its rich spectrum (compare figure 6.28). The precise knowledge of the energies of this standard calibration source will allow a precise calibration. Frequent calibration measurements will assure this. Further, an online monitoring of possible energy shifts is possible by using the positron annihilation line at $510.999\,\text{keV}$ which will be very prominent and close enough to the expected energies to monitor and correct possible energy deviations online as well as in the offline analysis. Because of that, the expected systematic error introduced by the calibration will be much smaller than the one caused by the theoretical description. In addition to that, the annihilation line will allow to monitor the influence of the irradiation damage in real time and adapt the PSA corrections accordingly (compare section 5.3.3).

6.3.7 Measurement of Y_{γ_2} to study Im$(V_0^{\Xi^-})$

The energy measurement of the shifted X-ray will allow to access mainly the real part of the potential $V_0^{\Xi^-}$. The imaginary part, in contrast, can be studied by measuring the width of γ_2 or its relative yield Y_{γ_2}. The first of these observables could be extracted from the measured peak shape of γ_2. Unfortunately, the limited detector resolution, the background and the progressing radiation damage of the crystals will deteriorate the accuracy of this observable. Because of that, it will be easier to use Y_{γ_2} to investigate Im$(V_0^{\Xi^-})$. This relative yield Y_{γ_2} requires the knowledge of two observables. The first is the amount of detected γ_2 transitions Y_{n_0}. As explained in section 3.1, this amount is proportional to the radiative width $\Gamma^{rad}_{n_0+1}$ of the (n_0+1, l_0+1) level. The absorbed fraction of Ξ^- can not be measured directly. Because of that, the total population Y_{n_0+1} of the (n_0+1, l_0+1) level has to be observed too. This population corresponds to the sum of $\Gamma^{rad}_{n_0+1}$ and the strong absorption width $\Gamma^{\text{abs}}_{n_0+1}$.

---

[o] Information from `http://nucleardata.nuclear.lu.se/toi/nuclide.asp?iZA=630152`

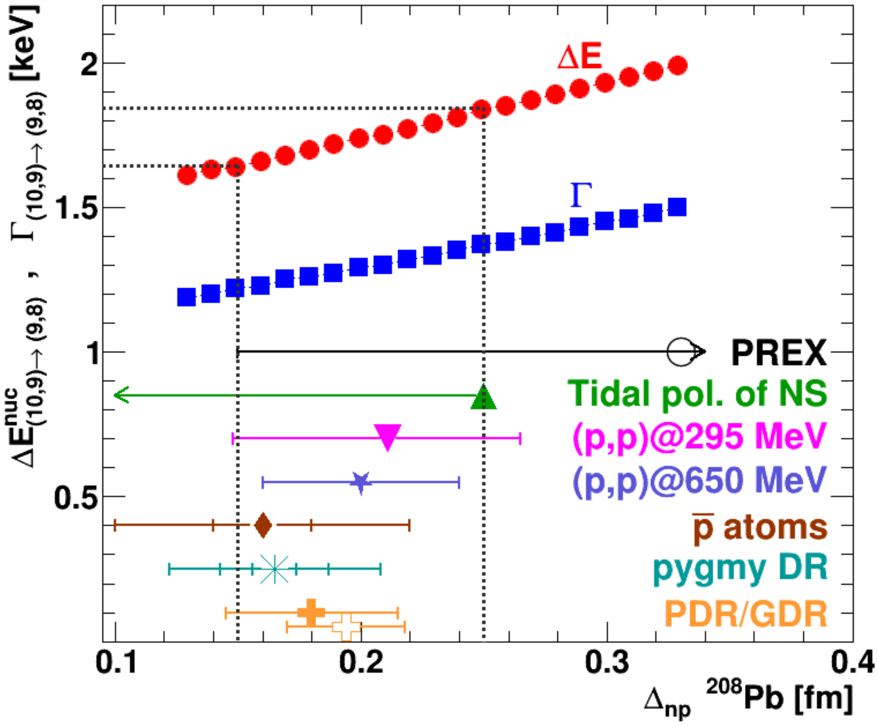

Figure 6.27: The thickness of the neutron skin of ^{208}Pb nuclei Δr_{np} has been studied in multiple experiments over the last decades [135, 238, 239, 240, 241, 242, 243, 244]. PREX, using model-independent parity violating, and the measurement of the tidal polarizability of a neutron star, that gave an upper limit for Δr_{np}, limited the possible range of the neutron skin thickness. The strong energy shift (red points) and the strong absorptive width (blue squares) show a linear dependence on a variation of Δr_{np}. The systematic uncertainty could be deduced from projecting limits of Δr_{np} to the variation of the energy shift within these limits and resulted in $\delta(\Delta E^{\text{nuc}}_{(10,9)\to(9,8)}) = \pm 0.1\,\text{keV}$.

Since $\Gamma^{rad}_{n_0+1}$ can be calculated precisely within QED, $\Gamma^{\text{abs}}_{n_0+1}$ can be deduced by

$$Y_{\gamma_2} = \frac{Y_{n_0}}{Y_{n_0+1}} = \frac{\Gamma^{rad}_{n_0+1}}{\Gamma^{rad}_{n_0+1} + \Gamma^{\text{abs}}_{n_0+1}}. \tag{6.9}$$

As previously explained, Y_{n_0} can be observed by measuring the amount of coincidences of γ_1 and γ_2 $N_{\gamma_1\wedge\gamma_2}$. With the same approach Y_{n_1} can be deduced from $N_{\gamma_0\wedge\gamma_1}$ with γ_0 defining the transition $(n_0+2, l_0+2) \to (n_0+1, l_0+1)$. This cascade is sketched in the left half of figure 6.29. The coincidence defining the population is marked in red, Y_{n_0} in green. Measuring both coincidences reduces the systematics of the experiment and when the detection efficiencies $\epsilon_{\text{coinc},N_{\gamma_1\wedge\gamma_2}}$ and $\epsilon_{\text{coinc},N_{\gamma_0\wedge\gamma_1}}$ are taken into account, Y_{γ_2} is given by

$$Y_{\gamma_2} = \frac{N_{\gamma_1\wedge\gamma_2}}{\epsilon_{\text{coinc},N_{\gamma_1\wedge\gamma_2}}} \cdot \frac{\epsilon_{\text{coinc},N_{\gamma_0\wedge\gamma_1}}}{N_{\gamma_0\wedge\gamma_1}}. \tag{6.10}$$

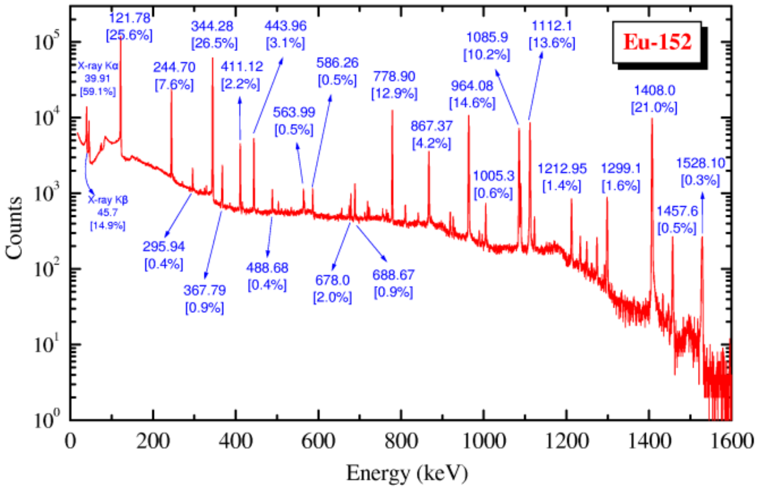

Figure 6.28: ^{152}Eu offers a multitude of γ transitions in the required energy range to calibrate the hyperatom measurement. Especially the $411.1163\,\mathrm{keV}$ and $556.9907\,\mathrm{keV}$ lines are very close to the expected energies of the ^{208}Pb hyperatom (figure from [245]).

For ^{208}Pb the energy of γ_0 is $E_{\gamma_0} = 312.68\,\mathrm{keV}$ and thus in a good energy range for the detection with PANGEA. The estimates of $N_{\gamma_0 \wedge \gamma_1}$ could be obtained in the same way as previously shown for $N_{\gamma_1 \wedge \gamma_2}$ (compare section 6.2.1). This resulted in a total amount of 25 609 events before all cuts were applied. The lack of strong explained the larger yield ($Y_{\gamma_1} = 1$). When all the cuts from section 6.3.5 were applied $N_{\gamma_1 \wedge \gamma_0}$ was reduced to 1600 signal events. For the background 71 416 events passed all the cuts. Since the (n_0+1, l_0+1) barely overlaps the nuclear potential, $\Gamma^{\mathrm{abs}}_{n_0+1=10} = 0.017\,\mathrm{keV}$ (compare figure 3.4) is too small to significantly influence the peak shape of γ_1. Because of that, only the Gaussian detector resolution had to be considered which improved the signal-to-background ratio and allowed to handle the increased background as shown in the right of figure 6.29.

The main influence on the precision of the estimation of Y_{γ_2} came from the estimations of the counting rates $N_{\gamma_1 \wedge \gamma_2}$ and $N_{\gamma_0 \wedge \gamma_1}$. These could be gained from the same toy Monte Carlo studies that were performed to estimate the precision of the energy measurements. The background affected the fitting which resulted in larger uncertainties. This yielded $N_{\gamma_1 \wedge \gamma_2} = 1216 \pm 151$ and $N_{\gamma_0 \wedge \gamma_1} = 1571 \pm 137$ (compare figure 6.30).

With these results and the previously estimated X-ray detection efficiencies ($\epsilon_{\mathrm{coinc},N_{\gamma_1 \wedge \gamma_2}} = 0.1872 \pm 0.0007\,\%$ (section 6.2.1), $\epsilon_{\mathrm{coinc},N_{\gamma_0 \wedge \gamma_1}} = 0.1368 \pm 0.0001\,\%$ (calculated analog to section 6.2.1)) the estimation for Y_{γ_2} was $57 \pm 9\,\%$. With this result the imaginary part of the potential could be estimated to $\mathrm{Im}(b_0) = 0.04^{+0.017}_{-0.012}\,\mathrm{fm}$[p] which translated to a potential depth of $\mathrm{Im}(V_0^{\Xi^-}) = 3.3^{+1.4}_{-1.0}\,\mathrm{MeV}$.

The uncertainties of this simulation were dominated by the estimations of the counting rates. Because of that, improvements can be expected once the time structure of events will be used to further increase the signal-to-background ratio in time-based simulations. Additionally, more advanced analysis techniques like neural networks or artificial intelligence might help to improve the cuts even more.

---

[p] $Y_{\gamma_2}(\mathrm{Im}(b_0) = 0.028) = 64.8\,\%$, $Y_{\gamma_2}(\mathrm{Im}(b_0) = 0.057) = 47.9\,\%$

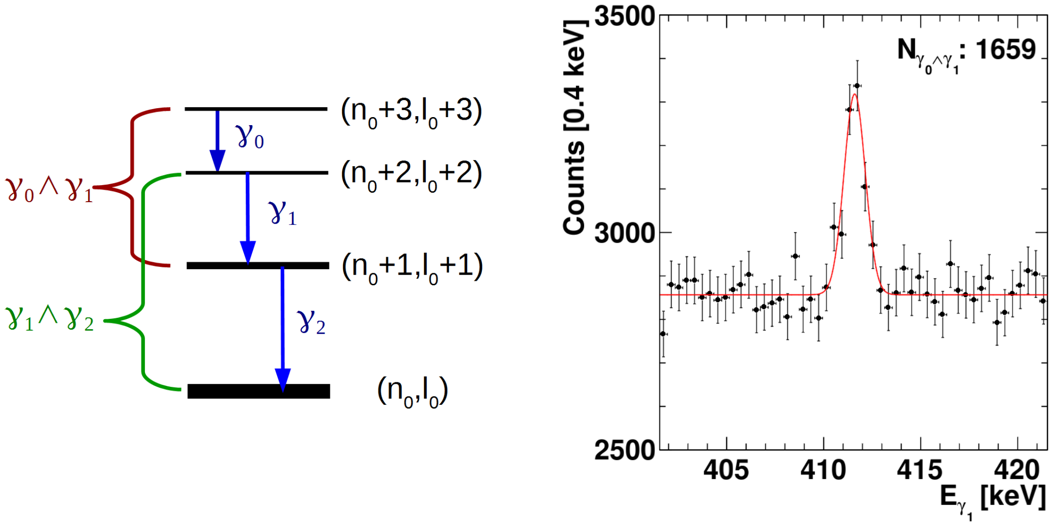

Figure 6.29: To calculate the relative yield of γ_2, Y_{γ_2}, the ratio of both coincidences shown in the left sketch can be studied. The red one describes the population of the (n_0+1, l_0+1) level. The green one, however, is a measure of the radiative width of the amount of γ_2 transitions. The fraction of both observables is Y_{γ_2} when detection efficiencies are considered. The right plot shows the estimations of the coincidence $\gamma_1 \wedge \gamma_0$. While the background is higher due to the lower transition energies (compare figure 6.12), the signal-to-background ratio is still acceptable due to the small $\Gamma^{\text{abs}}_{n_0+1=10}$ which results in no further broadening of the line shape.

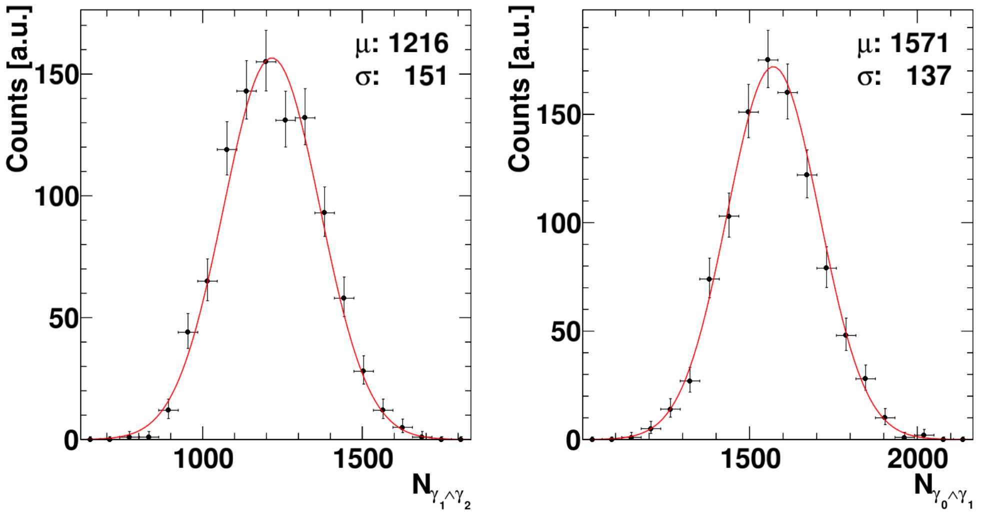

Figure 6.30: Estimations of the amount of detected coincidences $N_{\gamma_1 \wedge \gamma_2}$ (left) and $N_{\gamma_0 \wedge \gamma_1}$ (right). Both were simulated in a toy Monte Carlo study which was repeated 1000 times. The large background increased the uncertainty of the counting rate estimations. In addition to that, the width of γ_2 further worsens the signal-to-background ratio resulting in a reduced precision of $N_{\gamma_1 \wedge \gamma_2}$ compared to $N_{\gamma_0 \wedge \gamma_1}$.

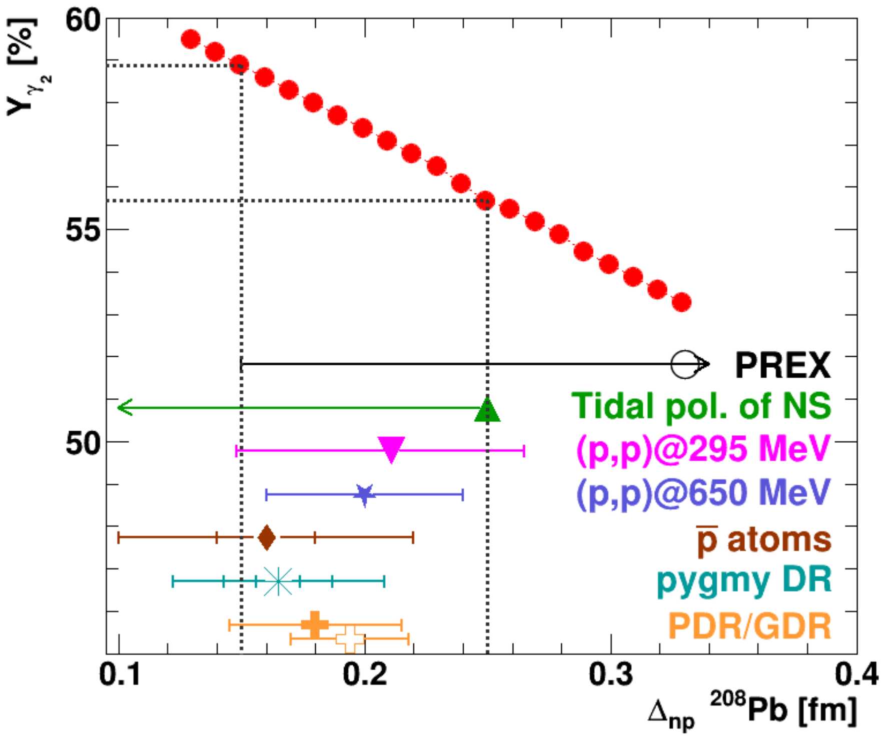

Figure 6.31: The systematic uncertainty of the relative yield Y_{γ_2} could be estimated in analogy to ΔE_{nuc} (compare figure 6.27). The same experimental data was used [135, 238, 239, 240, 241, 242, 243, 244] and yielded $\sigma(Y_{\gamma 2,sys}) = \pm 1.6\,\%$.

The systematic error of this measurement could be estimated in the same way as for the energy shift measurement (compare figure 6.27). Figure 6.31 shows this and results in $\sigma(Y_{\gamma 2,sys}) = \pm 1.6\,\%$ which is more than a factor five smaller than the present estimations of the statistical uncertainties.

6.4 Summary of the Ξ^--hyperatom experiment

In this chapter the feasibility of the X-ray spectroscopy of Ξ^--hyperatoms at $\overline{\mathrm{P}}$ANDA was studied. Multiple possible isotopes across the periodic table were investigated in their feasibility to stop Ξ^- and their influence on the X-ray detection efficiency. Lead showed the most promising results and especially the well established knowledge of the neutron skin of the double-magic ^{208}Pb nucleus will reduce the systematic uncertainties in the estimation of the potential of the Ξ^--nucleus interaction. The study of these heavy isotopes is unique at $\overline{\mathrm{P}}$ANDA and its two-stage target system will allow to observe cascades of their X-ray transitions in coincidence.

Using these coincidences and further topology of the hyperatom events allowed to reduce the background levels in the full simulations while keeping sufficient signal events. Approximately 1200 nuclearly affected Ξ^--^{208}Pb X-ray transitions $((10,9) \to (9,8))$ were estimated to survive all cuts which resulted in an uncertainty of the energy measurement of $\pm 140\,\mathrm{eV}$. The estimation of the relative yield $\mathrm{Y}_{\gamma 2}$ was more affected by the remaining background resulting in a larger relative uncertainty.

Figure 6.32 summarizes the results of these feasibility studies. Based on the model presented in section 3.2 it converts the described uncertainties in the observation of the strong energy shift $\Delta E^{\mathrm{nuc}}_{(10,9)\to(9,8)}$ and $\mathrm{Y}_{\gamma 2}$ into estimations for the real and imaginary part of the Ξ^- potential $V_0^{\Xi^-}$. The predicted low statistic uncertainty of $E^{\mathrm{nuc}}_{(10,9)\to(9,8)}$ will allow a precise estimation of $\mathrm{Re}(V_0^{\Xi^-})$ at $\overline{\mathrm{P}}$ANDA. The systematic uncertainty for this observable will be of similar size. The uncertainties

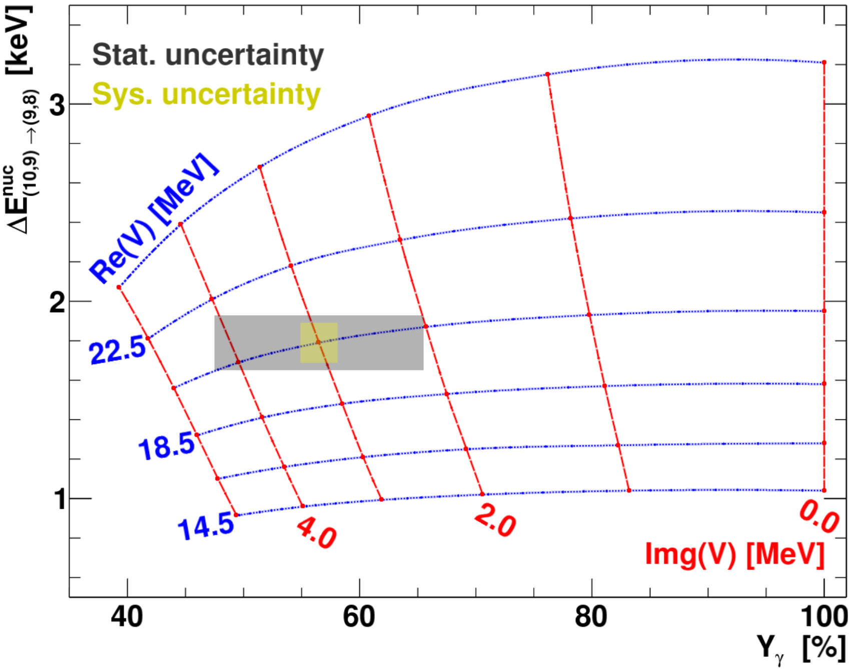

Figure 6.32: The variation of the real and imaginary part of the Ξ^--^{208}Pb nuclear potential allowed to quantify the calculated uncertainties of the experiment. Since the uncertainty of the energy shift $E^{\mathrm{nuc}}_{(10,9)\to(9,8)}$ was small, a statistical uncertainty below $10\,\%$ can be expected for the determination of the real part of the potential $\mathrm{Re}(V_0^{\Xi^-})$ at $\overline{\mathrm{P}}$ANDA with a similar sized systematic uncertainty. In contrast to that, the uncertainties of the yield $\mathrm{Y}_{\gamma 2}$ in the simulations were dominated by statistics which translate to higher relative uncertainties in the estimation of $\mathrm{Im}(V_0^{\Xi^-})$. This uncertainty was caused by the low number of events and a large amount of background. This might improve with more sophisticated cuts and analysis techniques that can improve the signal-to-background ratio. Nevertheless, already the predicted uncertainties will allow to determine $\mathrm{Re}(V_0^{\Xi^-})$ as well as $\mathrm{Im}(V_0^{\Xi^-})$ at $\overline{\mathrm{P}}$ANDA with a statistical uncertainty of approximately $\pm 1\,\mathrm{MeV}$.

of the imaginary part, however, will be dominated by statistics. This statistic uncertainty will be dominated by the uncertainties in the estimation of the counting rates of detected hyperatom transitions caused by the low statistics and high background. More sophisticated cuts and analysis techniques might reduce these uncertainties in the future.

Nevertheless, already the predicted uncertainties will allow to determine $\mathrm{Re}(V_0^{\Xi^-})$ as well as $\mathrm{Im}(V_0^{\Xi^-})$ at $\overline{\text{P}}$ANDA with a statistical uncertainty of approximately $\pm 1\,\mathrm{MeV}$.

7 Summary and outlook

The composition of neutron star matter is still an open question in today's physics. It is possible that hyperons are formed in the high density core region, but this hypothesis requires more experimental input. $\overline{\text{P}}$ANDA will help to solve this so called "hyperon puzzle" by measuring the optical potential of hyperons and antihyperons within nuclear matter. Due to the short life time of hyperons, atomic or nuclear bound systems are the most feasible way to study these potentials. Therefore, the main topic of this thesis was the interaction of double strange Ξ^- hyperons in an atomic bound system. The high mass of the Ξ^- shrinks the radial probability density function of these exotic atoms. For states with small principal quantum numbers, the strong interaction in these hyperatoms influences the X-ray spectrum by shifting the energy as well as broadening the line width of the emitted X-rays. These measurements have been performed for various kinds of exotic atoms in the past and present.

Since the effects of the strong interaction on the X-ray spectrum are small, a high resolution γ detector is required that can be positioned close to the primary interaction point. PANGEA is specifically designed to fulfill this purpose. High purity Germanium crystals are used for this high-resolution spectroscopy. They need to be cooled down which is usually done via liquid nitrogen. In $\overline{\text{P}}$ANDA such a cooling is not possible due to spatial limitations inside the target spectrometer. Because of that, electro-mechanically cooled detectors with improved thermal capabilities are developed in cooperation with the DEGAS collaboration. These detectors house three crystals each and contain most of the readout and supply electronics which reduces the amount of connections to the outside improving its robustness against external noise. In addition to that, the strong magnetic field of $\overline{\text{P}}$ANDA and its large flux of background particles must be considered in the development of the electronics. Especially the preamplifiers require a fast reset to handle the high interaction rates and need to be adaptable to the required energy range of the experiments. Further, the detector control system of PANGEA has to use EPICS to be compatible to $\overline{\text{P}}$ANDA. Each detector houses its own radiation tolerant control board to monitor and operate the detector. These individual units are connected to a sub-network that is connected to the $\overline{\text{P}}$ANDA DCS via a channel access gateway.

Various arrangements of detectors were compared to optimize the full-energy-peak efficiency of the system. Detectors oriented in parallel to the beam axis allowed to integrate more detectors into the available space than detectors pointing towards the interaction point. This resulted in a higher solid angle coverage and consequently a better full-energy-peak efficiency of $4.8\,\%@1.332\,\mathrm{MeV}$ in the simulations. This efficiency was achieved using an add-back algorithm that adds up the measured energy of all three crystals of the same detector. A total of 20 triple detectors could be integrated into the $\overline{\text{P}}$ANDA target spectrometer. In z (beam axis) direction, this compact package of detectors is arranged in a column-based structure which offered slightly better efficiencies than arrangements with more complex positioning of the detectors. This simplicity also allowed to design a rather simple support structure which consists of a skeleton of plates and bars to hold the detectors. In this structure, the detectors are grouped in modules of three, four or six that can be easily attached or detached from the remaining holding frame for maintenance. A full maintenance will only be possible when $\overline{\rm P}$ANDA is in its parking position. This position is generally required to change components of $\overline{\rm P}$ANDA which includes switching to the hyperatomic or hypernuclear setup. The necessary steps of this conversion procedure were studied and the time estimate of 12 weeks fits nicely into the specified time slots.

In addition to that, the influence of the strong hadronic background on the High Purity Germanium crystals during experiments at $\overline{\rm P}$ANDA was investigated experimentally. Especially fast neutrons will damage the lattice structure of the crystal and influence their high energy resolution. The amount of neutrons and their origin could be estimated in simulations using events generated in GiBUU and a further processing in GEANT4 integrated into the PandaRoot framework. With an average load of $1.00 \cdot 10^{10}\,\mathrm{n/cm^2}$ per crystal over a full $\overline{\rm P}$ANDA beam time of 180 days, a high amount of fast neutrons must be taken into account. Because of that, two irradiation tests at the COSY proton accelerator in Jülich, Germany, were performed in June and July 2014. Two different EUROBALL crystals, HEX 158 and HEX 146, were irradiated with $5.6 \cdot 10^9\,\mathrm{neutrons/cm^2}$ and $3.5 \cdot 10^9\,\mathrm{neutrons/cm^2}$, respectively. This equals to 93 and 56 days of experiment at $\overline{\rm P}$ANDA. In both cases the detector resolution was limited by a lack of dynamic range of the digital data acquisition system and mechanical issues of the cryostat which increased the operational temperature of the electro-mechanically cooled detectors. Despite these technical difficulties, a systematic decrease of the resolution due to the irradiation was observed. Especially the data of the first beam time could be used for pulse shape analysis. Studying the rising edge of a pulse and its first derivative allowed to locate the radial position of the interaction point within the crystal. Since the effect of the radiation damage depends on the path lengths of charge carriers inside the crystal, this geometrical knowledge could be used to improve the measured energy resolution by $24\,\%$ in average.
A prompt annealing of the crystal allowed to remove the radiation damage of the crystal and restored its initial conditions. Delaying this annealing causes the individually distributed lattice defects to gather and crystallize. Because of that, HEX 158 required multiple repetitions to return to an acceptable performance level after it was stored accidentally for 3.5 years at room temperature before the first annealing took place.

Finally, the feasibility of the hyperatom experiment was studied. Lead is selected from several possible absorber materials after the consideration of various experimental and physical properties. This production of heavy Ξ^--^{208}Pb hyperatoms is unique for $\overline{\rm P}$ANDA and complementary to the experiments at J-PARC E03 and E07. These Ξ^--^{208}Pb hyperatoms offer a large energy shift of $\Delta E^{\mathrm{nuc}}_{(10,9)\rightarrow(9,8)} = 1.83\,\mathrm{keV}$ for the X-ray transition $(n = 10, l = 9) \rightarrow (9, 8)$. The relative yield of this transition is $56.5\,\%$. Both observables were calculated using a simplified model based on a $t\rho$ potential that is sufficient to study the experimental sensitivities. The geometrical shape of this lead absorber was optimized for the best balance of the Ξ^- absorption and the X-ray detection efficiency in PANGEA. The optimum could be achieved by a $4\,\mathrm{mm}$ thick absorber integrated into the beam pipe.
Based on the results of the simulation studies approximately 20 000 of these (10,9)→(9,8) X-ray transitions could be detected in PANGEA using this absorber geometry within half a year in $\overline{\rm P}$ANDA. This number is reduced when the high background is considered and the required event filtering is added. The main cuts filter on the coincident detection of two cascading X-rays in PANGEA and the strangeness tag via K$^+$ detection in $\overline{\rm P}$ANDA. A further background suppression

could be achieved by a detailed study of the event topology and the usage of the veto detectors included in PANGEA. After adding the consideration of the life time for the coincident detection of both X-rays, the estimation of observed signal events drops to approximately 1200, which exceeds the predictions for Fe-hyperatoms at J-PARC E03. At the same time approximately $24\,000$ background events pass all cuts evenly distributed in a $10\,\mathrm{keV}$ interval. A Monte-Carlo simulation was performed with these counting rates to estimate the achievable precision in the observables. These estimations for the experimental measures were converted to the underlying optical potential $(V_0^{\Xi^-})$. Based on the studies in this work, $\overline{\mathrm{P}}$ANDA will be able to measure the real and imaginary part of $(V_0^{\Xi^-})$ with a statistical uncertainty of approximately $\pm 1\,\mathrm{MeV}$.

In 2020 the finished full-size prototype of the first triple detector will allow to study its full capabilities concerning the thermal design and the electronics. This detector will be used for a follow-up irradiation test. This test is planned at the TRIGA reactor at the Institute for Nuclear Chemistry in Mainz and will allow to irradiate multiple crystals with high neutron doses at the same time. Preparations for this test are ongoing.

The efficiency of the hyperatom experiment might be further improved by a modified design of the target system. Since the silicon trackers will not be required for this experiment, they can be left out in the setup. This reduces the material budget and allows more freedom in the design of the vacuum chamber. One example could be a bigger chamber that contains the absorber on its inside which opens up new possibilities for its design. Especially enriched isotopes might benefit from this freedom because it could reduce the amount of required absorber material and consequently reduce its price. Future simulations have to show if this design idea improves the efficiency of the hyperatom spectroscopy. In addition to that, the final design of the absorber needs to be adapted to measurements of the Ξ^- distributions that will be performed in the beginning of $\overline{\mathrm{P}}$ANDA. These might differ from the distributions implemented in GiBUU.

Finally, time-based simulation have to be implemented in the future. They will allow to study the internal time structure of events and the event-mixing. This timing information might introduce additional ways to cut on the data and further improve the signal-to-background ratio. This ratio may be improved even more by the usage of more refined cuts. More sophisticated analysis techniques like machine learning and neural networks will help to find and improve these.

A Appendix

A.1 Description of the implementation of the germanium detectors in PandaRoot

The implementation of the germanium detector in the simulation will be described briefly. The version of PandaRoot used for the simulation and including theses geometries can be found on the CD attached to this thesis. Since the detector array is composed of multiple copies of the same cluster detector, it is convenient to construct these first and add an interface to compose them by giving their position and tilting angle. This is implemented in an object-oriented way. The class files for this are placed in the “hypGe/geometry” subdirectory in PandaRoot. These consist of base classes that inherits general properties and functions to all child classes used for the various geometrical objects. In this thesis, this has been used to implement the triple detectors designated for $\overline{\text{P}}$ANDA as well as for the single crystal detector used to simulate the irradiation tests performed at COSY. The base class includes multiple implementations of the interface function“PlaceCluster” that is used to place the cluster in a global geometry or array arrangement. These differ in the geometrical parameters available to control the position of the cluster. The version mostly used in this thesis requires the coordinates of the central position of the front face of the detector as well as the Euler angles relative to the beam (z) axis to define the tilting of the detector.

```
virtual void PlaceCluster(TGeoVolume *top,
        Double_t x, Double_t y, Double_t z, Double_t GlobalZOffset,
        Double_t phi, Double_t theta, Double_t psi,
        int_t *CrystalNumber)
```

The definition of the Euler angles matches the one of classical mechanics which means that the first rotation Φ is around the z axis, the second one, Θ, rotates around the new y' axis and the last one with the angle Ψ is rotated around the new z' axis. The final parameter “CrystalNumber” should increase with every detector placed and is responsible for the proper numbering of all objects of the detector. These objects are created in individual sub-classes and functions and are combined in the corresponding cluster class. The main objects of every cluster are the encapsulated crystal(s), the cryostat and the backcatcher (veto) detectors:

The encapsulated crystal(s)

is (are) a composition of the germanium crystal and its surrounding aluminum capsule. The geometry of both is created in the class “PndGeoHypGeCrystal”. The crystal as well as the capsule have a tapered shape which starts with a hexagonal front and transfers to a round back. This can be achieved in ROOT by using composite shapes, which can consist of sums, divisions, unions or intersections of multiple simple shapes. For the tapered shape a cylindrical base (TGeoTube) is chosen which is cut by a hexagonal cone (TGeoPgon) on its outer side. Additionally the inner hole as well as the guard ring on the back of the crystal are added by using another cylinder respectively torus (TGeoTorus) which allow to mimic the rounded edges of the crystal. For the capsule on the other hand it is required to hollow it which is achieved by substracting a shrunken version of the tapered shape on the inside. On its back, a cylindrical cover is added to close the capsule. For a triple detectors three of these simplified encapsulated crystals are placed in triangular, tilted way so that the side by side faces of two crystals are parallel to each other.

The cryostat

depends on the type of detector used. In the simple case of only a single crystal detector the cryostat is a composition of multiple cylinders. Things gets much more complex when the cryostat has to house multiple crystals. The cryostat of these detectors has to mimic the outer shape of the crystals to maximize the solid angle coverage. Because of that, such a cryostat is a complex object. For the example of the triple crystal detector the triangular placement of the crystals create a geometry with 12 edges on its frontal side. Because of that the cryostat is implemented as a composition of many TGeoArb8 elements. This class forms trapezoidal shapes with two parallel planes and 4 vertices on each. TGeoArb8 are the most flexible shapes included in ROOT. The cryostat of the triple detector is composed of a total of 46 of these trapezoids. An interface to load the coordinates of the corner points of these TGeoArb8 from parameter files based on the measurements of the CAD drawings has been implemented and simplifies modifications of the cryostat.

The backcatchers

are located on the outside of the cryostat and one of them is placed behind each germanium crystal in the triple detector. The backcatchers implemented in the geometry are more simplified than the other components and each consists only of a hexagonal BGO crystals.

Figure A.1 shows pictures of these components. In the top, a crystal, its capsule and the triangular arrangement is shown. The bottom shows the cryostat of the PANGEA triple detector in green and the three backcatchers in orange.

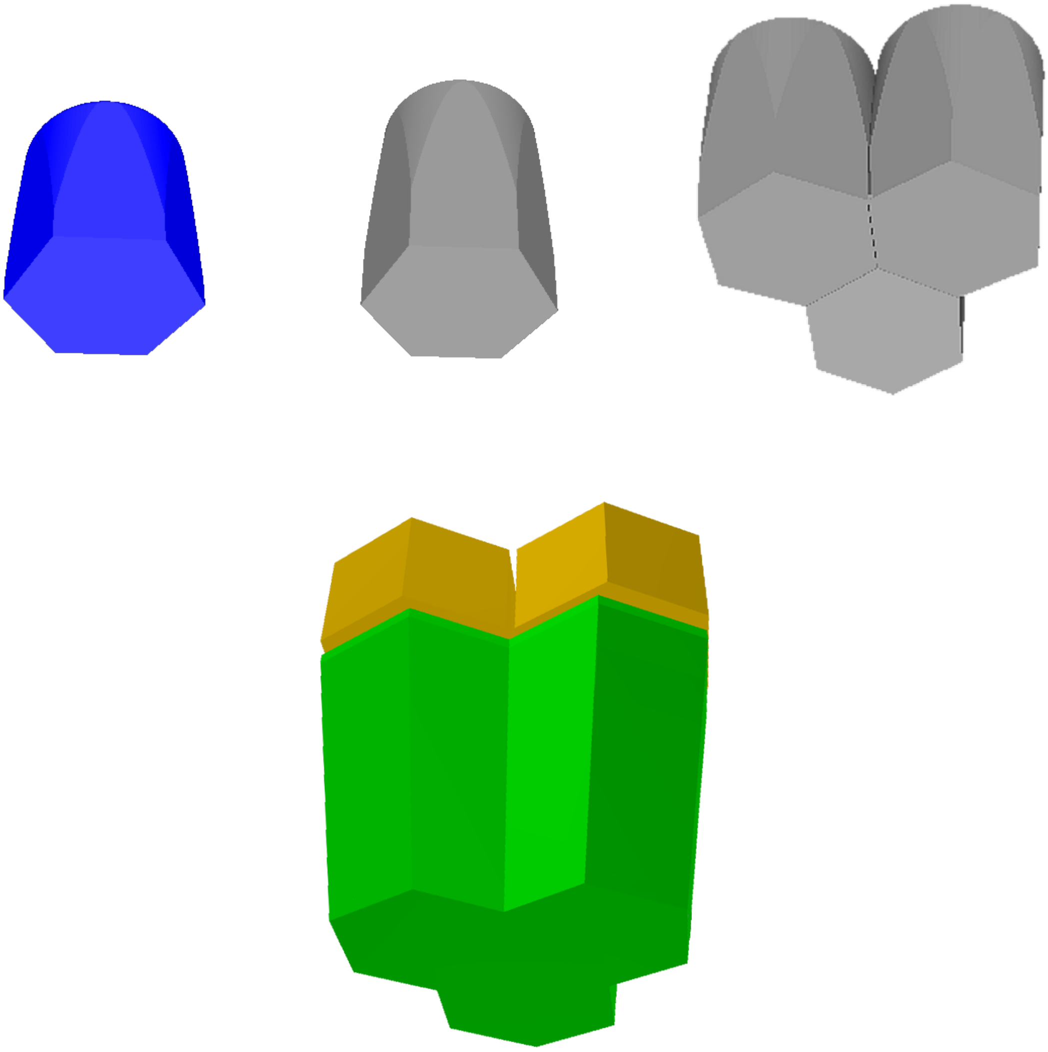

Figure A.1: Overview of the components of a triple detector implemented as ROOT geometry. The top pictures show the implementation of an individual EUROBALL HPGe crystal (left), its aluminum encapsulation (middle) and the triangular placement of the encapsulated crystals (right). These crystals are surrounded by the cryostat, shown at the bottom picture. Besides the cryostat (green) the BGO backcatchers are also included behind the crystals (orange).

A.2 PANGEA slow control signals

Signal	Function	Variable Type	Direction
HV			
HV-SET ON A	Set HV module A ON	TTL/CMOS	OUT
HV-SET ON B	Set HV module B ON	TTL/CMOS	OUT
HV-SET ON C	Set HV module C ON	TTL/CMOS	OUT
HV-STATUS A	Check ON/OFF status HV module A	TTL/CMOS	IN
HV-STATUS B	Check ON/OFF status HV module B	TTL/CMOS	IN
HV-STATUS C	Check ON/OFF status HV module B	TTL/CMOS	IN
HV SET A	Set HV module A to a given value	REAL (I2C)	OUT
HV SET B	Set HV module B to a given value	REAL (I2C)	OUT
HV SET B	Set HV module C to a given value	REAL (I2C)	OUT
HV-V-A	Check HV set to the module A	REAL (ADC)	IN
HV-V-B	Check HV set to the module B	REAL (ADC)	IN
HV-V-C	Check HV set to the module C	REAL (ADC)	IN
HV-I-A	Check current of HV module A	REAL (ADC)	IN
HV-I-B	Check current of HV module B	REAL (ADC)	IN
HV-I-C	Check current of HV module C	REAL (ADC)	IN
HV-SET-BSD-A	Set BSD of HV module A ON	TTL/CMOS	OUT
HV-SET-BSD-B	Set BSD of HV module B ON	TTL/CMOS	OUT
HV-SET-BSD-C	Set BSD of HV module C ON	TTL/CMOS	OUT
HV-BSD-A	Check status of BSD of HV module A	TTL/CMOS	IN
HV-BSD-B	Check status of BSD of HV module B	TTL/CMOS	IN
HV-BSD-C	Check status of BSD of HV module C	TTL/CMOS	IN
Temperatures			
T-COLDFRAME	Temperature at the cold frame	REAL (ADC)	IN
T-COOLER	Temperature at the cooler	REAL (ADC)	IN
T-BC A	Temperature at the backcatcher A	REAL (ADC)	IN
T-BC B	Temperature at the backcatcher B	REAL (ADC)	IN
T-BC C	Temperature at the backcatcher C	REAL (ADC)	IN
T-PA	Temperature in the PA compartment	REAL (ADC)	IN
T-POWER	Temperature in the power converter compartment	REAL (ADC)	IN
T-CT COOLING	Temperature of the water coolant of the CT-Cooler	REAL (ADC)	IN
Power Management			
P-POS24V SET	Set +24V converter ON	TTL/CMOS	OUT
P-NEG24V SET	Set -24 V converter ON	TTL/CMOS	OUT
P-POS6V SET	Set +6 V converter ON	TTL/CMOS	OUT
P-NEG6V SET	Set -6 V converter ON	TTL/CMOS	OUT
P-POS12V SET	Set +12 V converter ON	TTL/CMOS	OUT
P-POS3.3V SET	Set +3.3 V converter ON	TTL/CMOS	OUT
P-POS24V STATUS	Check ON/OFF status of +24V converter	TTL/CMOS	IN
P-NEG24V STATUS	Check ON/OFF status of -24V converter	TTL/CMOS	IN
P-POS6V STATUS	Check ON/OFF status of +6V converter	TTL/CMOS	IN
P-NEG6V STATUS	Check ON/OFF status of -6V converter	TTL/CMOS	IN
P-POS12V STATUS	Check ON/OFF status of +12V converter	TTL/CMOS	IN
P-POS3.3V STATUS	Check ON/OFF status of +3.3V converter	TTL/CMOS	IN
P-POS24V	Check the output voltage of +24V converter	REAL (ADC)	IN
P-NEG24V	Check the output voltage of -24V converter	REAL (ADC)	IN
P-POS6V	Check the output voltage of +6V converter	REAL (ADC)	IN
P-NEG6V	Check the output voltage of -6V converter	REAL (ADC)	IN
P-POS12V	Check the output voltage of +12V converter	REAL (ADC)	IN
P-POS3.3V	Check the output voltage of +3.3V converter	REAL (ADC)	IN

Signal	Function	Variable Type	Direction
HV-ENABLE A	Enable HV module A	TTL/CMOS	OUT
HV-ENABLE B	Enable HV module B	TTL/CMOS	OUT
HV-ENABLE C	Enable HV module C	TTL/CMOS	OUT
PA-ENABLE A	Enable PA A	TTL/CMOS	OUT
PA-ENABLE B	Enable PA B	TTL/CMOS	OUT
PA-ENABLE C	Enable PA C	TTL/CMOS	OUT
BC-ENABLE A	Enable backcatcher A	TTL/CMOS	OUT
BC-ENABLE B	Enable backcatcher B	TTL/CMOS	OUT
BC-ENABLE C	Enable backcatcher C	TTL/CMOS	OUT
	Varia		
CT-OPERATIONAL STATUS	Check the operational status of the CT-Cooler	TTL/CMOS	IN
CT-COOLING STATUS	Check the water cooling status of the CT-Cooler	TTL/CMOS	IN
XC-OPERATIONAL STATUS	Check the operational status of the X-Cooler	TTL/CMOS	IN
PA-AMP-A	Adjust the amplification of the last preamplifier stage	REAL (I2C)	OUT
PA-AMP-B	Adjust the amplification of the last preamplifier stage	REAL (I2C)	OUT
PA-AMP-C	Adjust the amplification of the last preamplifier stage	REAL (I2C)	OUT

Table A.1: The slow control signals of each cluster detector. All these signals has to be set or read out by the small slow control computer included into the cluster detector.

A.3 PANGEA layout coordinates

Cluster	x [cm]	y [cm]	z [cm]	Θ [°]	ϕ [°]	α [°]	ψ [°]
1	12.65	0.00	-17.95	144.83	-90.00	18.43	-90.00
2	6.32	10.95	-17.95	144.83	-30.00	18.43	-90.00
3	-6.32	10.95	-17.95	144.83	30.00	18.43	-90.00
4	-12.65	0.00	-17.95	144.83	90.00	18.43	-90.00
5	-6.32	-10.95	-17.95	144.83	150.00	18.43	-90.00
6	6.32	-10.95	-17.95	144.83	210.00	18.43	-90.00
7	24.26	0.00	-11.80	115.94	-90.00	37.34	-90.00
8	12.13	21.01	-11.80	115.94	-30.00	37.34	-90.00
9	-12.13	21.01	-11.80	115.94	30.00	37.34	-90.00
10	-24.26	0.00	-11.80	115.94	90.00	37.34	-90.00
11	-12.13	-21.01	-11.80	115.94	150.00	37.34	-90.00
12	12.13	-21.01	-11.80	115.94	210.00	37.34	-90.00
13	19.45	11.23	-13.10	120.26	-60.00	34.15	-30.00
14	0.00	22.46	-13.10	120.26	0.00	34.15	-30.00
15	-19.45	11.23	-13.10	120.26	60.00	34.15	-30.00
16	-19.45	-11.23	-13.10	120.26	120.00	34.15	-30.00
17	0.00	-22.46	-13.10	120.26	180.00	34.15	-30.00
18	19.45	-11.23	-13.10	120.26	240.00	34.15	-30.00

Table A.2: Coordinates of spherical PANGEA geometry. Θ is the polar angle used for positioning. The other three angles are the Euler angles describing the tilting of the detector. 18 of the tilted detector can be put inside the available space.

Cluster	x [cm]	y [cm]	z [cm]	Θ [°]	ϕ [°]	α [°]	ψ [°]
1	28.55	13.50	-2.69	94.68	0.00	0.00	-120.00
2	31.54	0.00	-6.41	102.04	0.00	0.00	-60.00
3	28.55	-13.50	-2.69	94.68	0.00	0.00	-120.00
4	16.52	26.51	-5.91	100.98	0.00	0.00	-60.00
5	13.52	13.50	-14.53	125.72	0.00	0.00	-120.00
6	16.52	0.00	-17.07	138.65	0.00	0.00	-60.00
7	13.52	-13.50	-14.53	125.72	0.00	0.00	-120.00
8	16.52	-26.51	-5.91	100.98	0.00	0.00	-60.00
9	1.50	26.51	-9.95	110.58	0.00	0.00	-60.00
10	-1.50	13.50	-17.65	142.59	0.00	0.00	-120.00
11	-1.50	-13.50	-17.65	142.59	0.00	0.00	-120.00
12	1.50	-26.51	-9.95	110.58	0.00	0.00	-60.00
13	-13.52	26.51	-5.91	100.98	0.00	0.00	-60.00
14	-16.52	13.50	-14.53	125.72	0.00	0.00	-120.00
15	-13.52	0.00	-17.07	138.65	0.00	0.00	-60.00
16	-16.52	-13.50	-14.53	125.72	0.00	0.00	-120.00
17	-13.52	-26.51	-5.91	100.98	0.00	0.00	-60.00
18	-31.54	13.50	-2.69	94.68	0.00	0.00	-120.00
19	-28.55	0.00	-6.41	102.04	0.00	0.00	-60.00
20	-31.54	-13.50	-2.69	94.68	0.00	0.00	-120.00

Table A.3: Coordinates of sphere-like PANGEA geometry. Θ is the polar angle. Since the detectors are not tilted, ϕ and α are always set to 0. Only ψ is used to describe the rotation around the beam axis. The z position is based on the radial distance of the center of the front face of the detector. The missing tilting of the individual detectors increases the total amount of cluster detectors to 20.

Cluster	x [cm]	y [cm]	z [cm]	Θ [°]	ϕ [°]	α [°]	ψ [°]
1	28.55	13.50	-5.81	100.00	0.00	0.00	-120.00
2	31.54	0.00	-5.81	100.94	0.00	0.00	-60.00
3	28.55	-13.50	-5.81	100.00	0.00	0.00	-120.00
4	16.52	26.51	-5.81	100.79	0.00	0.00	-60.00
5	13.52	13.50	-16.10	128.56	0.00	0.00	-120.00
6	16.52	0.00	-16.10	136.98	0.00	0.00	-60.00
7	13.52	-13.50	-16.10	128.56	0.00	0.00	-120.00
8	16.52	-26.51	-5.81	100.79	0.00	0.00	-60.00
9	1.50	26.51	-5.81	102.35	0.00	0.00	-60.00
10	-1.50	13.50	-16.10	140.02	0.00	0.00	-120.00
11	-1.50	-13.50	-16.10	140.02	0.00	0.00	-120.00
12	1.50	-26.51	-5.81	102.35	0.00	0.00	-60.00
13	-13.52	26.51	-5.81	100.79	0.00	0.00	-60.00
14	-16.52	13.50	-16.10	128.56	0.00	0.00	-120.00
15	-13.52	0.00	-16.10	136.98	0.00	0.00	-60.00
16	-16.52	-13.50	-16.10	128.56	0.00	0.00	-120.00
17	-13.52	-26.51	-5.81	100.79	0.00	0.00	-60.00
18	-31.54	13.50	-5.81	100.00	0.00	0.00	-120.00
19	-28.55	0.00	-5.81	100.94	0.00	0.00	-60.00
20	-31.54	-13.50	-5.81	100.00	0.00	0.00	-120.00

Table A.4: Coordinates of PANGEA ring geometry. The z position is based on the average radial distance of the center of the front face of the detector of all detectors in a ring. This reduces the number of different z coordinates to only 2.

Cluster	x [cm]	y [cm]	z [cm]	Θ [°]	ϕ [°]	α [°]	ψ [°]
1	28.55	13.50	-4.03	96.98	0.00	0.00	-120.00
2	31.54	0.00	-4.03	97.65	0.00	0.00	-60.00
3	28.55	-13.50	-4.03	96.98	0.00	0.00	-120.00
4	16.52	26.51	-12.53	112.36	0.00	0.00	-60.00
5	13.52	13.50	-12.53	121.82	0.00	0.00	-120.00
6	16.52	0.00	-12.53	129.84	0.00	0.00	-60.00
7	13.52	-13.50	-12.53	121.82	0.00	0.00	-120.00
8	16.52	-26.51	-12.53	112.36	0.00	0.00	-60.00
9	1.50	26.51	-14.64	118.91	0.00	0.00	-60.00
10	-1.50	13.50	-14.64	137.32	0.00	0.00	-120.00
11	-1.50	-13.50	-14.64	137.32	0.00	0.00	-120.00
12	1.50	-26.51	-14.64	118.91	0.00	0.00	-60.00
13	-13.52	26.51	-12.53	112.36	0.00	0.00	-60.00
14	-16.52	13.50	-12.53	121.82	0.00	0.00	-120.00
15	-13.52	0.00	-12.53	129.84	0.00	0.00	-60.00
16	-16.52	-13.50	-12.53	121.82	0.00	0.00	-120.00
17	-13.52	-26.51	-12.53	112.36	0.00	0.00	-60.00
18	-31.54	13.50	-4.03	96.98	0.00	0.00	-120.00
19	-28.55	0.00	-4.03	97.65	0.00	0.00	-60.00
20	-31.54	-13.50	-4.03	96.98	0.00	0.00	-120.00

Table A.5: Coordinates of PANGEA column geometry. The z position is based on the average radial distance of the center of the front face of the detector of all detectors in a column. This requires 3 different z coordinates for the complete setup.

A.4 Efficiency studies

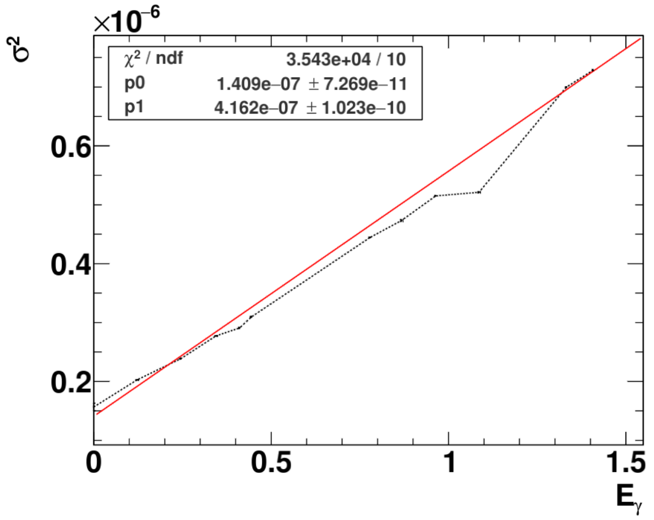

Figure A.2: Measured resolutions of ^{152}Eu used as input for the energy dependent resolution in the simulations of PANGEA.

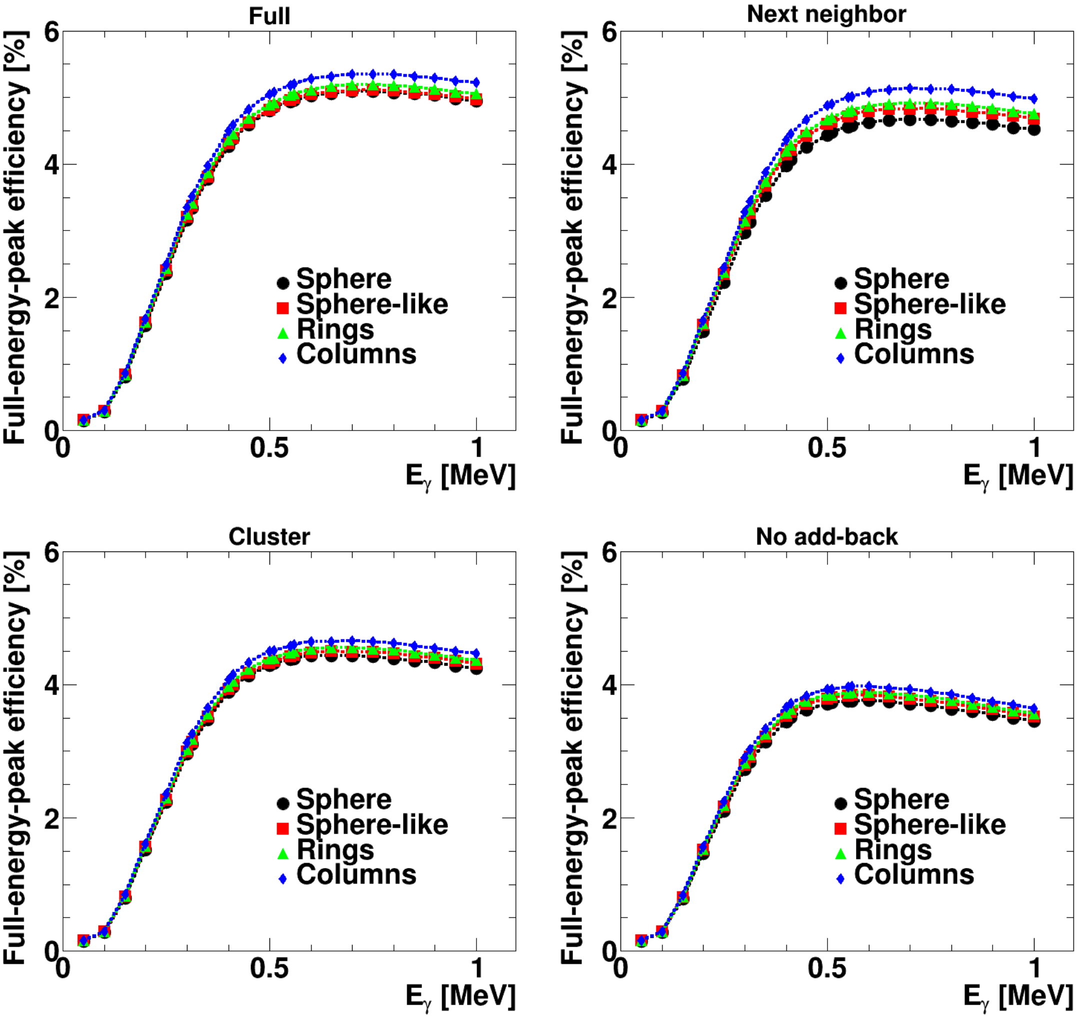

Figure A.3: Comprehensive picture of the X-ray detection efficiency for all possible combinations of PANGEA geometries and add-back method for the hyper atomic target and energy range up to 1 MeV.

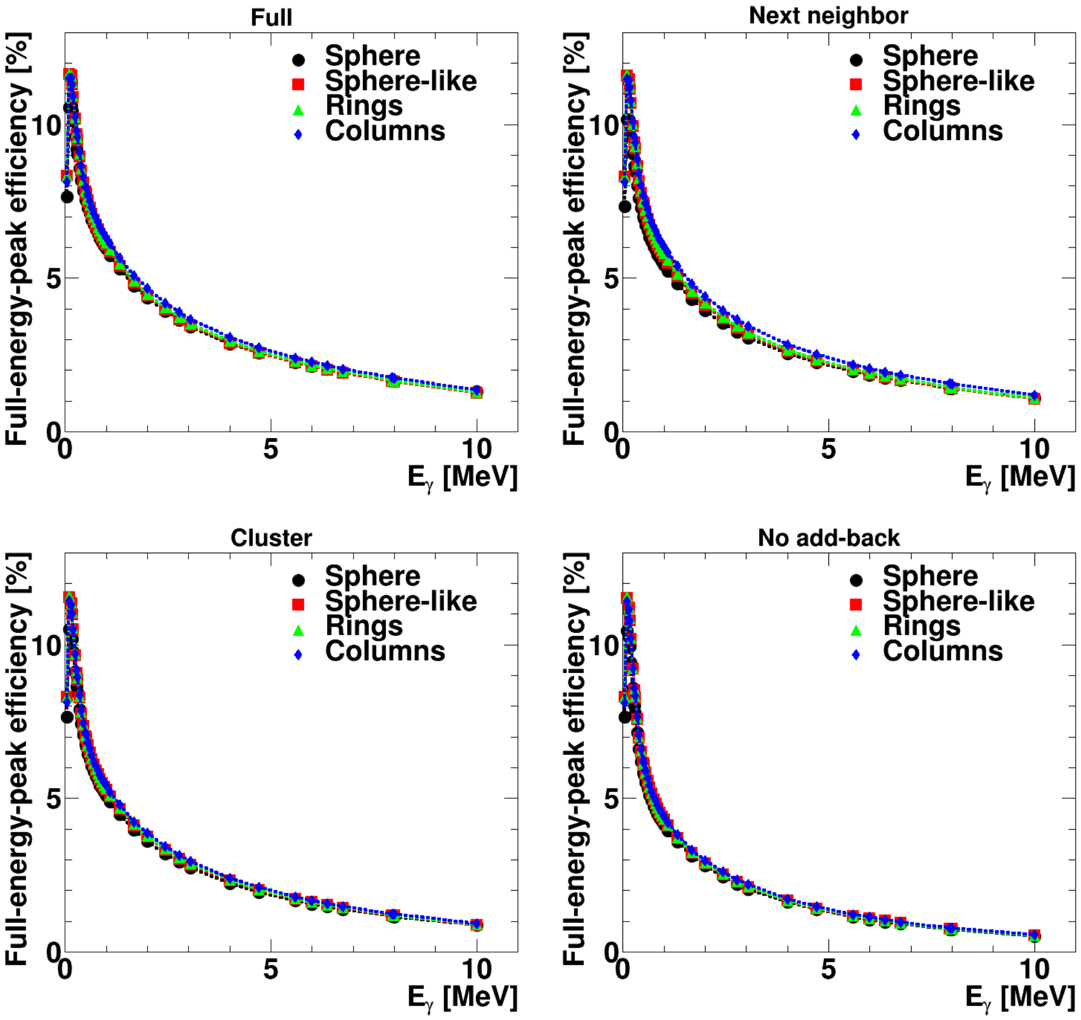

Figure A.4: Comprehensive picture of the γ detection efficiency for all possible combinations of PANGEA geometries and add-back method for the hyper nuclear target and energy range up to $10\,\mathrm{MeV}$.

A.5 Irradiation tests

A.5.1 First test in June 2014

Date	Begin	End	Files	Comments
10. Jun	17:37	18:45	run1/data	first measurement with beam, $3 \cdot 10^9$ protons per spill, 17 s spill time, 6 s extraction, micro-pulsing, Beam shutdown due to neutron monitors, Beam monitoring via active neutron detector started (n_Doselog.log)
	18:50	19:55	run2/data	Beam shutdown due to neutron monitors, beam must be reduced
	19:00			Beam reduced to $2.2 \cdot 10^9$ per spill, same times
	19:55	20:22	run3/data	Detector temperature higher as expected, HV reduced to 2000 V
	20:30			beam reduces to $0.3 \cdot 10^9/\mathrm{s}$ (during extraction)
	22:30			beam reduced to $0.25 \cdot 10^9/\mathrm{s}$ (during extraction)
	23:02	05:24	run4/data	after dinner measurement
11. Jun	05:34	12:03	run1/data	data0001.lmd was broken, start with data0002.lmd
	10:30			Beam increased to $0.3/\mathrm{s}$ again, "optimization " of the radiation protection to increase tolerable rates (room above beam area added to controlled area)
	12:20	16:50	run2/data	
	12:35			Beam increased to $0.35/\mathrm{s}$
	15:10	15:30		short break
	17:55	20:40	run3/data	HV to 2500 V, leakage current to high (spikes up to 0.2 µA, correlated to beam cycle!), HV back to 2000 V before starting the run, interrupted by broken pipe!
	18:30			Beam increased to $0.4/\mathrm{s}$
	19:35			Beam increased to $0.45/\mathrm{s}$
	20:41			Broken pipe to DAQ PC, crash of DAQ PC inside the area, reboot fixed everything
	21:12			new file for beam monitoring (n_Doselog2.log)
	21:10	01:50	run4/data	new measurement after broken pipe!
12. Jun	02:27	06:44	run1/data	
	06:49	08:10	run2/data	measurement stopped, after measurement: HV raised to 2500 V, high currents caused by high energy particles
	09:27	10:00	run3/data	measurement with HV = 2500 V
	11:02	14:47		maintenance break of COSY, setup seems fine, Ivan arrived and checked, HV raised to 3000 V
	15:00			Beam reduced to $0.35/\mathrm{s}$
	15:30			Beam increased to $0.4/\mathrm{s}$
	15:38	22:01	run4/data	
	16:00	17:10		Break for visitors group, setup runs good
	22:11	04:18	run5/data	
13. Jun	04:20	10:22	run1/data	
	09:30	10:00		Break
	10:54	11:04		Beam shutdown due to neutron monitors
	11:04	17:05	run2/data	
	17:20	23:18	run3/data	
	23:20	05:23	run4/data	
14. Jun	06:13	12:05	run1/data	
	09:19	09:27		Beam shutdown due to neutron monitors
	11:20	11:40		Short maintenance
	12:06	18:10	run2/data	
	18:12	00:15	run3/data	
15. Jun	00:18	06:30	run1/data	
	06:31	12:51	run2/data	

Date	Begin	End	Files	Comments
	07:41	10:50		Maintenance break of COSY, failure in magnet
	12:58	18:14	run3/data	Measurement stopped for dinner, 87 files
	18:14	21:45	run4/data	
	23:00	02:30	run5/data	60 files starting at 150
16. Jun	05:34	05:41		Beam shutdown due to neutron monitors
	06:56	07:02		Beam shutdown due to neutron monitors
	07:09	07:25	run1/data	short measurement, beam off at 7:25

Table A.6: Log file of the first irradiation test in June 2014

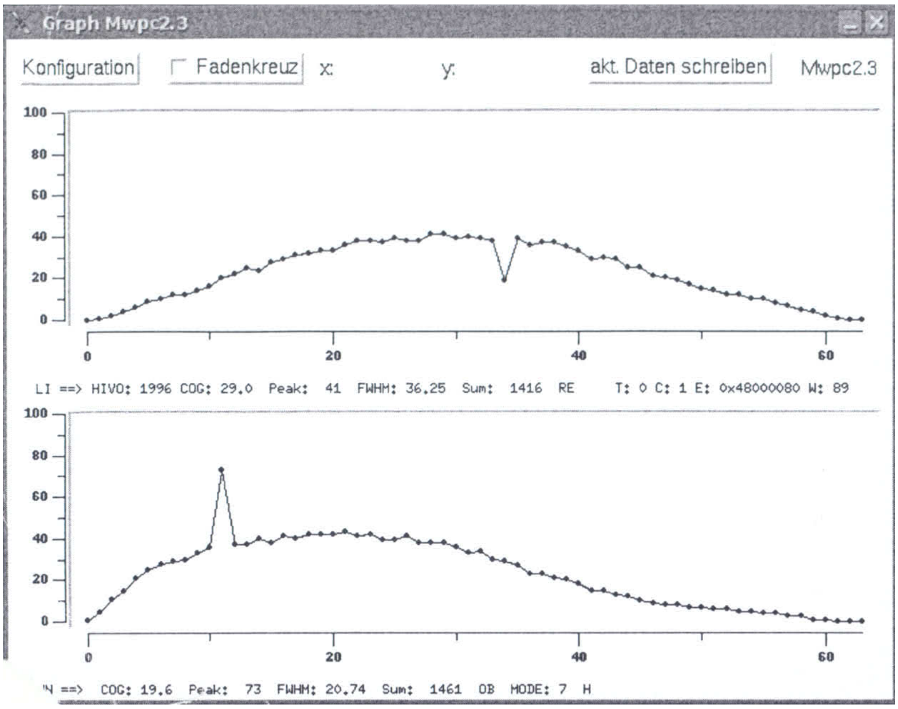

```
LI ==> HIVO: 1996 COG: 29.0   Peak:  41  FWHM: 36.25  Sum:  1416  RE     T: 0 C: 1 E: 0x48000080 W: 89
```

```
'N ==>  COG: 19.6  Peak:  73  FWHM: 20.74  Sum:  1461  OB  MODE: 7  H
```

Figure A.5: The multi-wire chamber at the beam outlet of the JESSICA allowed to estimate the size of the COSY proton beam. For both dimensions (top: horizontal, bottom: vertical) a FWHM in the order of $32\,\mathrm{mm}$ can be extracted from the measurement. Considering the Gaussian shape of the signal, the standard deviation of the beam is $\sigma = 13.6\,\mathrm{mm}$ for both dimensions.

Remark	Start	End	Duration	Start n_{det}	End n_{det}	Duration [s]	Extraction [s]	Protons
	10.06, 18:12:44	10.6.14 18:51	00:38:50	110	343	2330	822	4.11E+11
	10.06, 19:33:24	10.6.14 20:26	00:53:30	484	805	3210	1133	4.53E+11
	10.06, 20:38:24	10.6.14 21:36	00:57:50	874	1221	3470	1225	3.67E+11
	10.06, 21:45:34	10.6.14 22:40	00:54:50	1277	1606	3290	1161	3.48E+11
🟥 -	10.06, 22:30:00		00:10:24			624	220	-1.10E+10
	10.06, 22:58:34	11.6.14 09:12	10:13:40	1715	5397	36820	12995	3.25E+12
	11.06, 09:28:44	11.6.14 09:37	00:08:50	5496	5549	530	187	4.68E+10
	11.06, 10:06:14	11.6.14 15:26	05:19:50	5721	7640	19190	6773	1.69E+12
🟨 +	11.06, 10:30:00		04:56:04			17764	6270	3.13E+11
🟪 +	11.06, 13:55:00		01:31:04			5464	1928	9.64E+10
	11.06, 15:47:14	11.6.14 16:16	00:29:20	7767	7943	1760	621	2.17E+11
	11.06, 16:22:04	11.6.14 20:50	04:28:50	7976	9589	16130	5693	1.99E+12
🟩 +	11.06, 18:30:00		02:20:54			8454	2984	1.49E+11
🟦 +	11.06, 19:35:00		01:15:54			4554	1607	1.61E+11
DAQ Crash	11.06, 20:50:54	11.06, 21:12:34	00:21:40			1300	459	2.06E+11
	11.06, 21:12:34	12.06, 11:01:14	13:48:40	0	4972	49720	17548	7.90E+12
	12.06, 14:43:44	12.06, 15:52:24	01:08:40	6307	6719	4120	1454	6.54E+11
⬛ -	12.06, 15:00:00		00:52:24			3144	1110	-1.11E+11
	12.06, 17:04:14	13.06, 09:29:14	16:25:00	7150	13060	59100	20859	8.34E+12
	13.06, 09:58:04	13.06, 10:54:34	00:56:30	13233	13572	3390	1196	4.79E+11
	13.06, 11:05:24	14.06, 09:18:34	22:13:10	13637	21636	79990	28232	1.13E+13
	14.06, 09:25:54	14.06, 11:23:04	01:57:10	21680	22383	7030	2481	9.92E+11
	14.06, 11:39:44	15.06, 07:39:14	19:59:30	22483	29680	71970	25401	1.02E+13
	15.06, 10:48:54	16.06, 05:34:04	18:45:10	30818	37569	67510	23827	9.53E+12
	16.06, 05:41:14	16.06, 06:56:04	01:14:50	37612	38061	4490	1585	6.34E+11
	16.06, 07:02:04	16.06, 07:23:34	00:21:30	38097	38226	1290	455	1.82E+11
						Total duration [h]	**Total extraction [h]**	**Total protons**
						121	**43**	**5.97E+13**

	Beam intensity
10.06, 17:15:00	5.00E+08
10.06, 19:00:00	4.00E+08
10.06, 20:30:00	3.00E+08
10.06, 22:30:00	2.50E+08
11.06, 10:30:00	3.00E+08
11.06, 13:55:00	3.50E+08
11.06, 18:30:00	4.00E+08
11.06, 19:35:00	4.50E+08
DAQ crash	
12.06, 15:00:00	3.50E+08
12.06, 15:30:00	4.00E+08

Measurement interval [s]	00:00:10
Extraction time [s]	6
Storage time [s]	11
Cycle time [s]	17
Start log1	10.06, 17:54:24
Start log 2	11.06, 21:12:34

Table A.7: Calculation of the total number of protons in the first beam time in June 2014. Summing up the protons in all individual intervals results in $6 \cdot 10^{13}$ protons. The beam intensity as well as the starting time of this configuration are shown in the bottom of the table. The colored remarks mark correction requires due to a change in the beam intensity while the measurement continued.

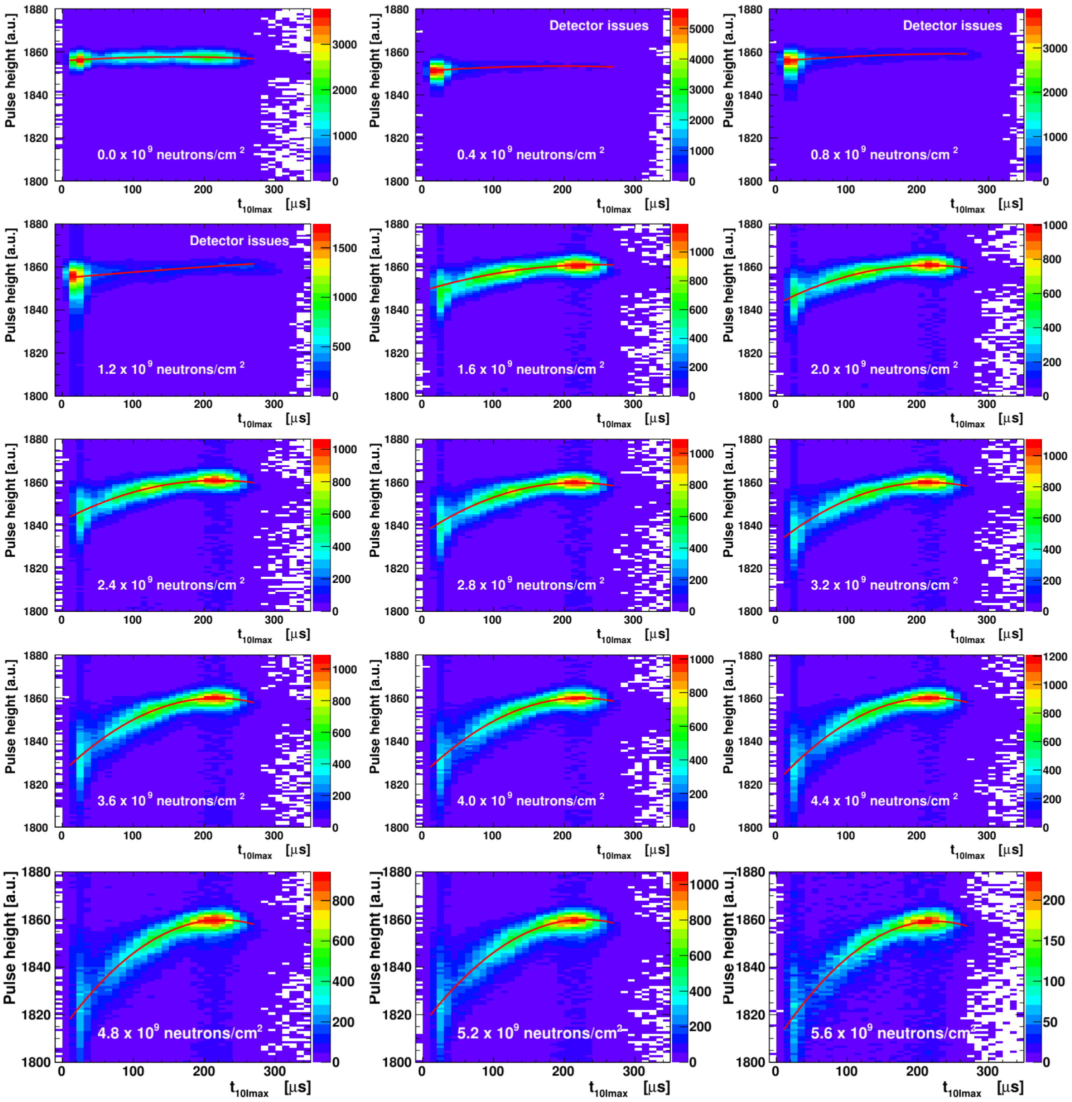

Figure A.6: The progression of the irradiation damage in the June 2014 beam time can be studied in this distributions of $t_{10\mathrm{Imax}}$ and the extracted pulse height. The histograms show a zoom on the 1332 keV line. While the distribution is constant at the beginning, the deviation, especially for small $t_{10\mathrm{Imax}}$, grows for an increasing amount of radiation damage. In addition to that, the statistical spread within a vertical slice increases. The red function shows the correction function extracted from the slice fits. The data of the second to fourth plot is influenced by detector issues during the irradiation. Because of that, the high voltage was reduced which causes the visible deviations from the other plots. After fixing the issues the high voltage was restored to of 3000 V which restored the $t_{10\mathrm{Imax}}$ distribution.

	Date	Time	TLD No.	Measure I	Measure II	Measure III	Measure IV	Unit
Background	06.06.2014	135102	10701	19.29	24.45	29.24	16.57	µSv
Irradiation	20.06.2014	163854	10701	397201.66	13946.22	12686.36	379028.44	µSv
Difference				39718.37	13921.77	12657.12	379011.87	µSv
Total				187403.84	µSv			
				187.40	mSv			

Table A.8: Measurements of the passive neutron detector in the June 2014 beam time performed by the radiating protection department of GSI. For the estimation of the total irradiation during the beam time the results before the experiment has to be substracted. Concerning the four measures, the first and last has to be summed up. The second and third however need to be substracted to gain the total neutron load. This averages to a total neutron dose of $187.40\,\mathrm{mSv}$ on the thermoluminescent dosimeters (TLD) during the experiment [246].

A.5.2 Second test in July 2014

Date	Begin	End	Files	Comments
26. Jul	12:00			Beam switched on $6 \cdot 10^9$ per spill, $80\,\%$ extraction, cycle time $20\,\mathrm{s}$, extraction $10\,\mathrm{s}$
	12:42	13:00		Shutdown by neutron monitors
	16:35	02:17	run1/data	Measurements started, MBS crash at night, no signal from detector, but detector is fine
	16:40			Beam reduced to $1.8 \cdot 10^9$ per spill extracted
	17:15			Beam reduced to $1 \cdot 10^9$ per spill extracted
26. Jul	11:00			DAQ problem: after beam injection, DAQ doesn't work (gives no or strange signals),
	12:00			Beam cycle changed to$10\,\mathrm{s}$ extraction, $40\,\mathrm{s}$ dead time, $10\,\mathrm{s}$ acceleration/cooling ($60\,\mathrm{s}$ total), protons increased to $2.9 \cdot 10^9$ per spill to have a similar number of protons
	13:10	05:28	run1/data	Measurements continued after problems with DAQ solved
27. Jul	05:46	22:40	run1/data	
	22:41	15:26	run2/data	
28. Jul	04:30			Somehow less beam $4 \cdot 10^8$ per spill
	09:30			Cyclotron requires optimization to recover proton rates, break of beam for optimization, Lumi setup (MuPix) position slightly changed
	10:45			Beam switched on again, rates recovered, back to $2.9 \cdot 10^9$ per spill
	15:51	21:00	run1/data	Measurement ended by DAQ crash, Ethernet switch replaced, HV down, reramped to $4000\,\mathrm{V}$
29. Jul	00:25	15:38	run1/data	Setup recovered, beam switched on again
	17:00	08:03	run2/data	
	18:00			Heavy rain, water in the anteroom of the beam area, experiment not affected
30. Jul	08:17	19:58	run1/data	Co60 measurements, beam
	09:40			Beam break for modification of lumi setup (MuPix closer to beam)
	10:50			Beam on
	14:00			Beam break for modification of lumi setup (thinner MuPix6)
	14:35			Beam on
	14:50			Short break, Ethernet cable of lumi setup reattached
	14:55			Beam on

	17:50			Beam break for modification of lumi setup (back to original position
	17:55			Beam on
	22:05	14:05	run2/data	
31. Jul	14:40	05:34	run1/data	
	15:10			Short COSY maintenance
	15:25			Beam on
01. Aug	06:55	08:23	run1/data	Co60 measurements, beam
	08:05			End of beam time

Table A.9: Log file of the second irradiation test in July 2014

Remark	t_{start} [min]	t_{end} [min]	Duration [min]	Flux [1/s]	Protons
Beam1	0	42	42	2.4E+08	6.05E+11
n dose shutdown	42	60	18	0	0
	60	102	42	2.4E+08	6.05E+11
n dose shutdown	102	120	18	0	0
	120	162	42	2.4E+08	6.05E+11
n dose shutdown	162	180	18	0	0
	180	222	42	2.4E+08	6.05E+11
n dose shutdown	222	240	18	0	0
	240	282	42	2.4E+08	6.05E+11
n dose shutdown	282	300	18	0	0
Beam2	300	315	15	9.0E+07	8.10E+10
Beam3	315	1440	1125	5.0E+07	3.38E+12
Beam4	1440	3870	2430	4.8E+07	7.05E+12
Beam5	3870	4170	300	6.7E+06	1.20E+11
beam optimization	4170	4245	75	0	0
Beam6	4245	4860	615	4.8E+07	1.78E+12
DAQ Crash, resetting setup, rerunning HV	4860	4920	60	0	0
	4920	6120	1200	4.8E+07	3.48E+12
weather break	6120	6135	15	0	0
	6135	7060	925	4.8E+07	2.68E+12
Modification MuPix6 setup	7060	7130	70	0	0
	7130	7320	190	4.8E+07	5.51E+11
Modification MuPix6 setup	7320	7355	35	0	0
	7355	7550	195	4.8E+07	5.66E+11
Modification MuPix6 setup	7550	7555	5	0	0
	7555	8830	1275	4.8E+07	3.70E+12
COSY maintenance	8830	8845	15	0	0
	8845	9845	1000	4.8E+07	2.90E+12
					Total protons
					2.93E+13
Beam1	25. Jul	12:00:00	2.40E+08		
Beam2	25. Jul	16:40:00	9.00E+07		
Beam3	25. Jul	17:15:00	5.00E+07		
Beam4	26. Jul	12:00:00	4.83E+07		
Beam5	28. Jul	04:30:00	6.67E+06		
Beam6	28. Jul	10:45:00	4.83E+07		

Table A.10: Calculation of the total number of protons in the second beam time in July. In contrast to the first beam time, the active neutron detector was not available and because of that less precision in the length of the irradiation periods is expected. Nevertheless it is possible to estimate the total number of protons to $2.93 \cdot 10^{13}$ which is half of the first beam time.

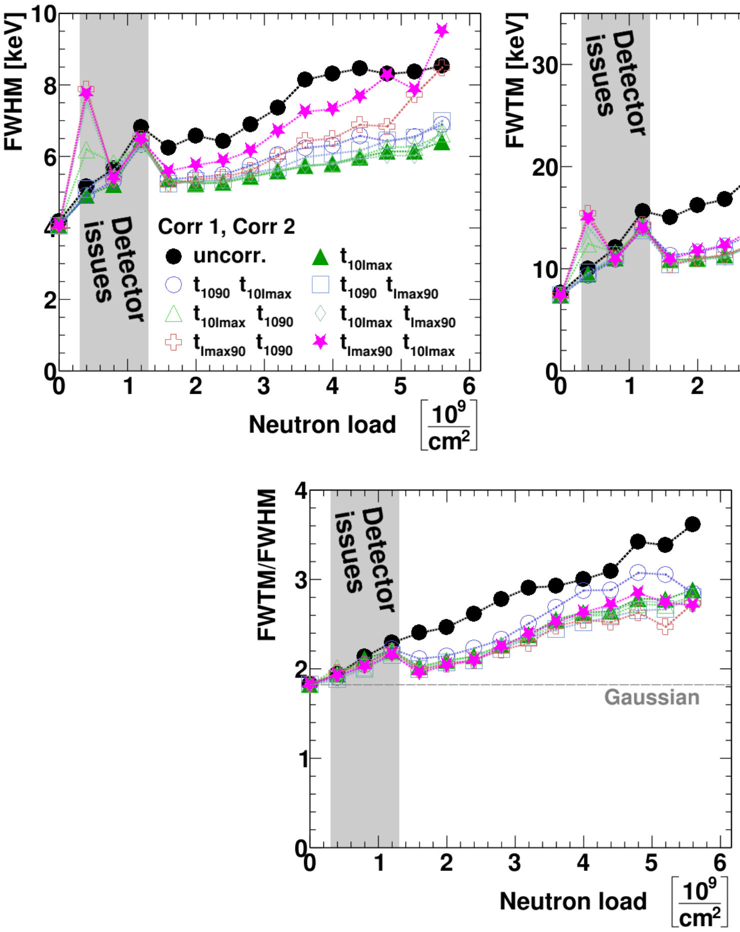

Figure A.7: Overview of the secondary corrections of the data of the June 2014 beam time. None of them offers a significantly increased performance than the correction solely based on $t_{10\mathrm{Imax}}$.

	Date	Time	TLD No.	Measure I	Measure II	Measure III	Measure IV	Unit
Background	06.06.2014	135102	10701	71.43	26.36	32.48	72.64	µSv
Irradiation	20.06.2014	163854	10701	2993305.47	9347.55	8397.91	261119.02	µSv
Difference				293234.04	9321.19	8365.52	261046.37	µSv
Total				134148.42	µSv			
				134.15	mSv			

Table A.11: Measurements of the passive neutron detector in the July beam time performed by the radiating protection department of GSI. For the estimation of the total irradiation during the beam time the results before the experiment has to be substracted. Concerning the four measures, the first and last has to be summed up. The second and third however need to be substracted to gain the total neutron load. This averages to a total neutron dose of 134.15 mSv on the thermoluminescent dosimeters (TLD) during the experiment [246].

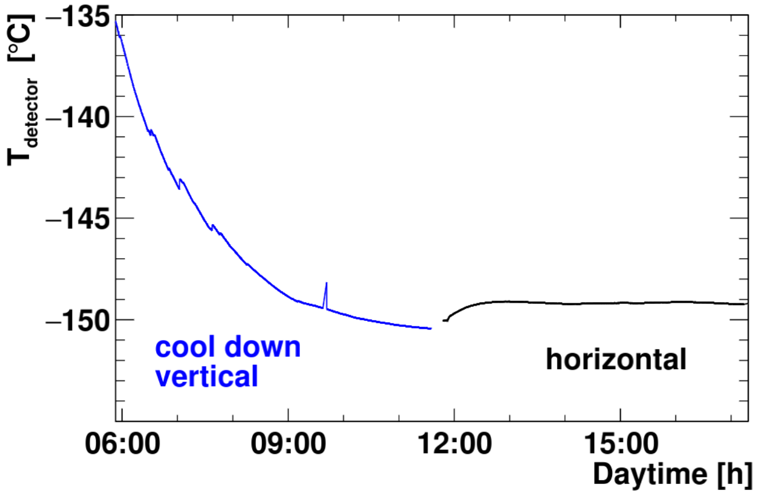

Figure A.8: For the second irradiation test at COSY the precursor of the first detector had to be used. This detector is less optimized in its thermal capabilities and because of that only a running temperature in the range of $-149\,^{\circ}\mathrm{C}$ ($124\,\mathrm{K}$) could be achieved in the horizontal orientation.

A.6 Parameters for X-ray energy calculations of hyperatoms

Element	c_p	a_p	w_p	c_n	a_n	w_n	c_q	a_q	w_q
$^{27}_{13}$Al	3.013	0.491	0	3.031	0.491	0	3.070	0.519	0
$^{28}_{14}$Si	3.361	0.485	-0.245	3.306	0.485	-0.245	3.340	0.580	-0.233
$^{40}_{20}$Ca	3.787	0.485	-0.139	3.733	0.485	-0.139	3.766	0.586	-0.161
$^{48}_{22}$Ti	3.897	0.503	0	4.001	0.503	0	3.843	0.588	0
$^{51}_{23}$V	4.002	0.396	0	4.126	0.396	0	3.940	0.505	0
$^{56}_{26}$Fe	4.169	0.460	0	4.248	0.460	0	4.111	0.558	0
$^{93}_{41}$Nb	4.921	0.479	0	5.081	0.479	0	4.870	0.573	0
$^{115}_{49}$In	5.193	0.560	0	5.410	0.560	0	5.357	0.563	0
$^{112}_{50}$Sn	5.422	0.464	0	5.560	0.464	0	5.375	0.560	0
$^{120}_{50}$Sn	5.295	0.535	0	5.543	0.535	0	5.315	0.576	0
$^{124}_{50}$Sn	5.535	0.445	0	5.820	0.445	0	5.490	0.534	0
$^{181}_{73}$Ta	6.148	0.562	0	6.438	0.562	0	6.380	0.640	0
$^{197}_{73}$Au	6.419	0.449	0	6.708	0.449	0	6.380	0.535	0
$^{206}_{82}$Pb	6.571	0.505	0	6.873	0.505	0	6.610	0.545	0
$^{207}_{82}$Pb	6.583	0.506	0	6.891	0.506	0	6.620	0.546	0
$^{208}_{82}$Pb	6.654	0.475	0	6.966	0.475	0	6.610	0.545	0

Table A.12: Input for the calculation of the X-ray energies. The data for the proton distribution are taken from [108] and the one of the charge distributions from [247]. The parameters of the neutron distributions have been calculated from the proton distributions via equation 3.12 and 3.13.

A.7 Optimization of the secondary target for the hyper atomic experiment

Geometry	a_x [cm]	a_y [cm]	ϵ_{Ξ^-} [%]	ϵcoinc [%]	f_{st} $[10^{-4}]$
144	1.4	1.4	0.533 ± 0.001	0.187 ± 0.001	0.0997 ± 0.0004
154	1.5	1.4	0.575 ± 0.001	0.170 ± 0.001	0.0979 ± 0.0004
164	1.6	1.4	0.612 ± 0.001	0.162 ± 0.001	0.0989 ± 0.0004
174	1.7	1.4	0.644 ± 0.001	0.151 ± 0.001	0.0975 ± 0.0004
184	1.8	1.4	0.673 ± 0.001	0.143 ± 0.001	0.0961 ± 0.0004
142	1.4	1.2	0.387 ± 0.001	0.243 ± 0.001	0.0935 ± 0.0004
143	1.4	1.3	0.465 ± 0.001	0.211 ± 0.001	0.0980 ± 0.0004
144	1.4	1.4	0.533 ± 0.001	0.187 ± 0.001	$0.0997 \pm 0.0004)$
145	1.4	1.5	0.589 ± 0.001	0.167 ± 0.001	0.0982 ± 0.0004
146	1.4	1.6	0.638 ± 0.001	0.153 ± 0.001	0.0974 ± 0.0004

Table A.13: Results of the optimization of the lead hyperatom target in x and y direction.

Geometry	z_1 [cm]	z_2 [cm]	z_3 [cm]	z_4 [cm]	ϵ_{Ξ^-} [%]	$\epsilon_{\mathrm{coinc}}$ [%]	f_{st} $[10^{-4}]$
175	-56.15	-55.40	-53.50	-52.20	0.898 ± 0.001	0.513 ± 0.001	0.4614 ± 0.0014
275	-56.25	-55.50	-53.60	-52.10	0.923 ± 0.001	0.484 ± 0.001	0.4469 ± 0.0013
375	-56.35	-55.60	-53.70	-52.00	0.945 ± 0.001	0.462 ± 0.001	0.4365 ± 0.0013
475	-56.45	-55.70	-53.80	-51.90	0.967 ± 0.001	0.433 ± 0.001	0.4184 ± 0.0013
575	-56.55	-55.80	-53.90	-51.80	0.982 ± 0.001	0.422 ± 0.001	0.4142 ± 0.0012

Table A.14: Results of the optimization of the iron hyperatom target in z direction.

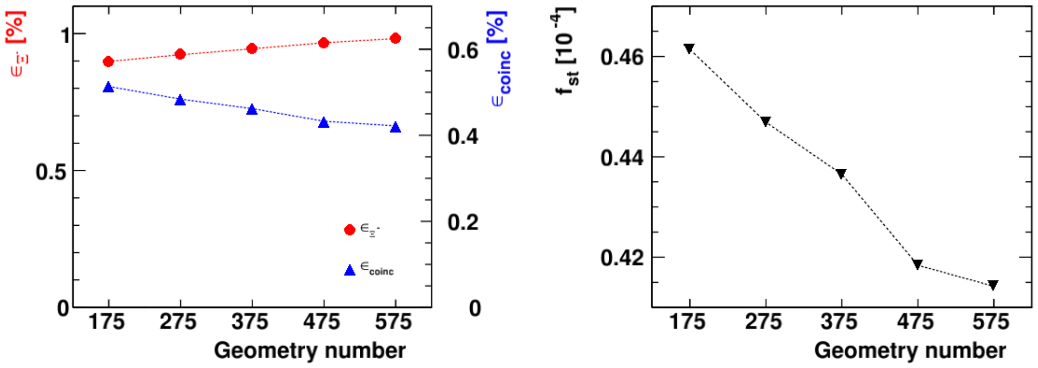

Figure A.9: Optimization of the absorber geometry along the beam axis (z) for iron

Geometry	a_x [cm]	a_y [cm]	ϵ_{Ξ^-} [%]	ϵcoinc [%]	f_{st} [10^{-4}]
355	1.5	1.5	0.817 ± 0.001	0.569 ± 0.001	0.4614 ± 0.0014
365	1.6	1.5	0.862 ± 0.001	0.538 ± 0.001	0.4469 ± 0.0013
375	1.7	1.5	0.898 ± 0.001	0.513 ± 0.001	0.4365 ± 0.0013
385	1.8	1.5	0.933 ± 0.001	0.490 ± 0.001	0.4184 ± 0.0013
395	1.9	1.5	0.961 ± 0.001	0.168 ± 0.001	0.4142 ± 0.0012
353	1.5	1.3	0.670 ± 0.001	0.673 ± 0.001	0.4508 ± 0.0012
354	1.5	1.4	0.748 ± 0.001	0.613 ± 0.001	0.4586 ± 0.0012
355	1.5	1.5	0.817 ± 0.001	0.568 ± 0.001	0.4640 ± 0.0012
356	1.5	1.6	0.876 ± 0.001	0.529 ± 0.001	0.4630 ± 0.0012
357	1.5	1.7	0.927 ± 0.001	0.496 ± 0.001	0.4596 ± 0.0012

Table A.15: Results of the optimization of the iron hyperatom target in x and y direction.

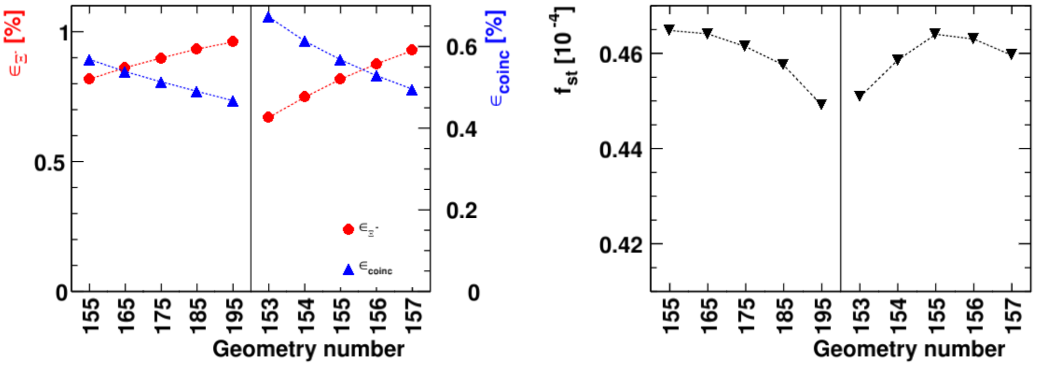

Figure A.10: Optimization of the absorber perpendicular to the beam axis (x and y)for iron

Geometry	z_1 [cm]	z_2 [cm]	z_3 [cm]	z_4 [cm]	ϵ_{Ξ^-} [%]	ϵcoinc [%]	f_{st} [10^{-4}]
164	-55.80	-55.20	-53.80	-53.20	0.426 ± 0.001	0.466 ± 0.001	0.1988 ± 0.0006
264	-55.90	-55.30	-53.70	-53.10	0.453 ± 0.001	0.446 ± 0.001	0.2022 ± 0.0006
364	-56.00	-55.40	-53.60	-53.00	0.477 ± 0.001	0.431 ± 0.001	0.2058 ± 0.0006
464	-56.10	-55.50	-53.50	-52.90	0.500 ± 0.001	0.414 ± 0.001	0.2068 ± 0.0006
564	-56.20	-55.60	-53.40	-52.80	0.518 ± 0.001	0.400 ± 0.001	0.2074 ± 0.0007

Table A.16: Results of the optimization of the indium hyperatom target in z direction.

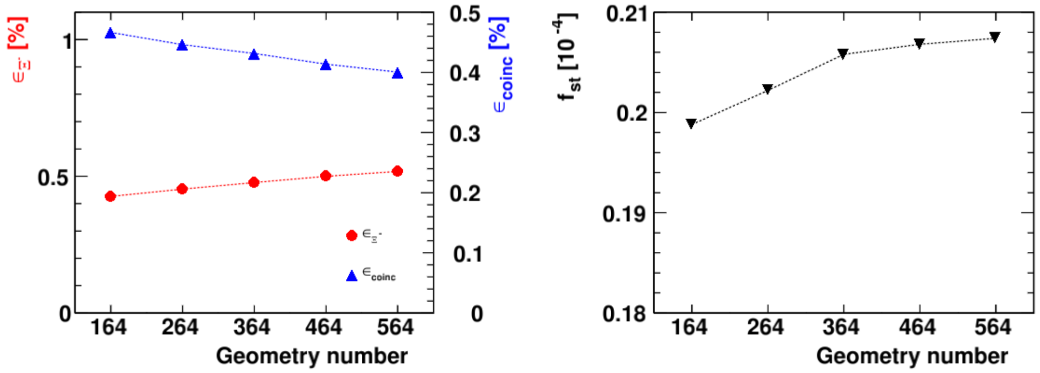

Figure A.11: Optimization of the absorber geometry along the beam axis (z) for indium

Geometry	a_x [cm]	a_y [cm]	ϵ_{Ξ^-} [%]	ϵcoinc [%]	$f_{\rm st}$ [10^{-4}]
544	1.4	1.4	0.449 ± 0.001	0.450 ± 0.001	0.2020 ± 0.0006
554	1.5	1.4	0.517 ± 0.001	0.400 ± 0.001	0.2065 ± 0.0007
564	1.6	1.4	0.518 ± 0.001	0.400 ± 0.001	0.2074 ± 0.0007
574	1.7	1.4	0.544 ± 0.001	0.378 ± 0.001	0.2056 ± 0.0007
584	1.8	1.4	0.566 ± 0.001	0.360 ± 0.001	0.2041 ± 0.0007
562	1.6	1.2	0.395 ± 0.001	0.479 ± 0.001	0.1891 ± 0.0006
563	1.6	1.3	0.460 ± 0.001	0.438 ± 0.001	0.2012 ± 0.0006
564	1.6	1.4	0.518 ± 0.001	0.400 ± 0.001	0.2074 ± 0.0007
565	1.6	1.5	0.565 ± 0.001	0.370 ± 0.001	0.2090 ± 0.0007
566	1.6	1.6	0.609 ± 0.001	0.342 ± 0.001	0.2084 ± 0.0007

Table A.17: Results of the optimization of the indium hyperatom target in x and y direction.

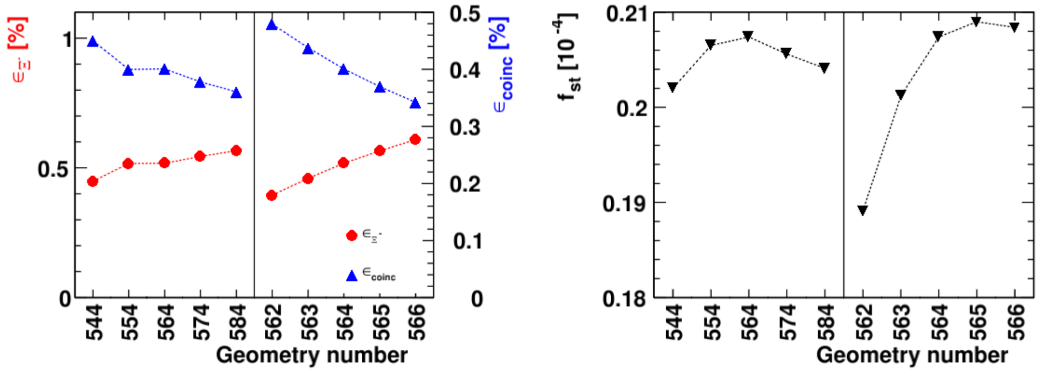

Figure A.12: Optimization of the absorber geometry perpendicular to the beam axis ()x and y) for indium

```
0.6094d10
2587.74
1.8d5  0.7d3  2.4  1.d-3  1.d-6  1.d-7  1.d-7  1.d-7
CASCADE for Xi 56 Fe atoms, b0=0.25+i*0.04 fm
26.0      56.      17000.     6.539 0.769     1.d7     5.d7  1.d6
50 00 02 08 00        0.0         0.0        0.0
30.0      00.0
```

Listing A.1: Input parameters for the calculation of the atomic cascade of Ξ^--^{56}Fe

```
0.6094d10
2587.74
1.d7  0.7d7  2.4d4  0.909d3  0.013d3  0 0 0
CASCADE for Xi 115 In atoms, b0=0.25+i*0.04 fm
49.0      115.      62633.8     26.711 4.018     10.8d7     1.8d7  1.8d7
50 00 02 08 00        0.0         0.0        0.0
30.0      00.0
```

Listing A.2: Input parameters for the calculation of the atomic cascade of Ξ^--^{115}In

```
0.6094d10
2587.74
1.8d7  0.7d7  2.4d6  1.d5  1.d4  1.83d3  3.8d1  1.d0
CASCADE for Xi 208 Pb atoms, b0=0.25+i*0.04 fm
82.0      208.      176457.     65.540 15.367     10.8d7     1.8d7
1.8d7
50 00 02 11 00        0.0         0.0        0.0
30.0      00.0
```

Listing A.3: Input parameters for the calculation of the atomic cascade of Ξ^--^{208}Pb

B List of Figures

C List of Tables

D Bibliography

[1] G. Bertone *et al.* “History of dark matter”. In: *Rev. Mod. Phys.* 90.4 (2018), p. 045002. arXiv: `1605.04909 [astro-ph.CO]`.

[2] N. Yunes *et al.* “Gravitational-Wave Tests of General Relativity with Ground-Based Detectors and Pulsar-Timing Arrays”. In: *Living Rev. Relativ.* 16.1 (2013), p. 9.

[3] K. Yagi *et al.* “Challenging the presence of scalar charge and dipolar radiation in binary pulsars”. In: *Phys. Rev. D* 93 (2016), p. 024010.

[4] R. Konoplya *et al.* “Detection of gravitational waves from black holes: Is there a window for alternative theories?” In: *Phys. Lett. B* 756 (2016), pp. 350–353.

[5] J. Antoniadis *et al.* “A Massive Pulsar in a Compact Relativistic Binary”. In: *Sci.* 340.6131 (2013). eprint: `http://science.sciencemag.org/content/340/6131/1233232.full.pdf`.

[6] P. Demorest *et al.* “A two-solar-mass neutron star measured using Shapiro delay”. In: *Nature* 467 (2010), pp. 1081–1083.

[7] H. T. Cromartie *et al.* “Relativistic Shapiro delay measurements of an extremely massive millisecond pulsar”. In: *Nat. Astron.* (2019).

[8] E. Berti *et al.* “Testing general relativity with present and future astrophysical observations”. In: *Class. Quantum Gravity* 32.24 (2015), p. 243001.

[9] Douchin, F. *et al.* “A unified equation of state of dense matter and neutron star structure”. In: *Astron. Astrophys* 380.1 (2001), pp. 151–167.

[10] M. Burgay *et al.* “An increased estimate of the merger rate of double neutron stars from observations of a highly relativistic system”. In: *Nature* 426 (2003), pp. 531–533.

[11] A. Bauswein *et al.* “Revealing the high-density equation of state through binary neutron star mergers”. In: *Phys. Rev. D* 90 (2014), p. 023002.

[12] S. Bernuzzi *et al.* “How loud are neutron star mergers?” In: *Phys. Rev. D* 94 (2016), p. 024023.

[13] D. Radice *et al.* “GW170817: Joint Constraint on the Neutron Star Equation of State from Multimessenger Observations”. In: *ApJL* 852.2 (2018), p. L29.

[14] L. Rezzolla *et al.* “Gravitational-wave signal from binary neutron stars: A systematic analysis of the spectral properties”. In: *Phys. Rev. D* 93 (2016), p. 124051.

[15] K. Takami *et al.* “Constraining the Equation of State of Neutron Stars from Binary Mergers”. In: *Phys. Rev. Lett.* 113 (2014), p. 091104.

[16] B. Abbott *et al.* “GW170817: Observation of Gravitational Waves from a Binary Neutron Star Inspiral”. In: *Phys. Rev. Lett.* 119 (2017), p. 161101.

[17] B. Abbott *et al.* “Gravitational Waves and Gamma-Rays from a Binary Neutron Star Merger: GW170817 and GRB 170817A”. In: *ApJL* 848.2 (2017), p. L13.

[18] T. Baker *et al.* “Strong Constraints on Cosmological Gravity from GW170817 and GRB 170817A”. In: *Phys. Rev. Lett.* 119 (2017), p. 251301.

[19] P. Creminelli *et al.* “Dark Energy after GW170817 and GRB170817A”. In: *Phys. Rev. Lett.* 119 (2017), p. 251302.

[20] J. M. Ezquiaga *et al.* “Dark Energy After GW170817: Dead Ends and the Road Ahead”. In: *Phys. Rev. Lett.* 119 (2017), p. 251304.

[21] D. Pooley *et al.* “GW170817 Most Likely Made a Black Hole”. In: *Astrophys. J.* 859.2 (2018), p. L23.

[22] M. Shibata *et al.* “Modeling GW170817 based on numerical relativity and its implications”. In: *Phys. Rev. D* 96 (2017), p. 123012.

[23] B. Margalit *et al.* “Constraining the Maximum Mass of Neutron Stars from Multi-messenger Observations of GW170817”. In: *ApJL* 850.2 (2017), p. L19.

[24] L. Rezzolla *et al.* “Using Gravitational-wave Observations and Quasi-universal Relations to Constrain the Maximum Mass of Neutron Stars”. In: *ApJL* 852.2 (2018), p. L25.

[25] M. Ruiz *et al.* “GW170817, general relativistic magnetohydrodynamic simulations, and the neutron star maximum mass”. In: *Phys. Rev. D* 97 (2018), p. 021501.

[26] D. Blaschke *et al.* “Topical issue on exotic matter in neutron stars”. In: *Eur. Phys. J. A* 52.3 (2016), p. 71.

[27] F. Weber. “Strange quark matter and compact stars”. In: *Prog. Part. Nuc. Phys.* 54.1 (2005), pp. 193–288.

[28] J. R. Stone. “Neutron stars interiors: Theory and reality”. In: *Eur. Phys. J. A* 52.3 (2016), p. 66.

[29] A. G. Cameron. “Neutron Star Models.” In: *Astrophys. J.* 130 (1959). *Provided by the SAO/NASA Astrophysics Data System*, p. 884.

[30] A. Hewish *et al.* “Observation of a Rapidly Pulsating Radio Source”. In: *Nature* 217 (1968), p. 709.

[31] V. Ambartsumyan *et al.* “The Degenerate Superdense Gas of Elementary Particles”. In: *Sov. Astron.* 4 (1960), p. 187.

[32] I. Bombaci. “The Hyperon Puzzle in Neutron Stars”. In: *JPS Conf. Proc.* 17 (2017), p. 101002. arXiv: `1601.05339 [nucl-th]`.

[33] B. Singh *et al.* "Technical Design Report for the Hyperatom and Hypernuclear Studies at PANDA". *in preparation*.

[34] L. Tolos *et al.* “The Equation of State for the Nucleonic and Hyperonic Core of Neutron Stars”. In: *Publ. Astron. Soc. Austr.* 34 (2017), e065.

[35] J. Adams *et al.* “Proton-Λ correlations in central Au+Au collisions at $\sqrt{s_{NN}} = 200$ GeV”. In: *Phys. Rev. C* 74 (2006), p. 064906.

[36] L. Adamczyk *et al.* “$\Lambda\Lambda$ Correlation Function in Au+Au Collisions at $\sqrt{s_{NN}} = 200$ GeV”. In: *Phys. Rev. Lett.* 114 (2015), p. 022301.

[37] J. Adam *et al.* “The proton-Ω correlation function in Au+Au collisions at $\sqrt{s_{NN}} = 200$ GeV”. In: *Phys. Lett. B* 790 (2019), pp. 490–497.

[38] K. Morita *et al.* “$\Lambda\Lambda$ interaction from relativistic heavy-ion collisions”. In: *Phys. Rev. C* 91 (2015), p. 024916.

[39] S. Acharya *et al.* “p$-$p, p$-\Lambda$, and $\Lambda-\Lambda$ correlations studied via femtoscopy in pp reactions at $\sqrt{s} = 7\,\mathrm{TeV}$”. In: *Phys. Rev. C* 99 (2019), p. 024001.

[40] S. Acharya *et al.* “Study of the Λ-Λ interaction with femtoscopy correlations in pp and p-Pb collisions at the LHC”. In: *Phys. Lett. B* 797 (2019), p. 134822.

[41] S. Acharya *et al.* “First Observation of an Attractive Interaction between a Proton and a Cascade Baryon”. In: *Phys. Rev. Lett.* 123 (2019), p. 112002.

[42] K. Nakazawa *et al.* “The first evidence of a deeply bound state of Ξ^--^{14}N system”. In: *Prog. Theor. Exp. Phys.* 2015.3 (2015). *033D02*. eprint: `http://oup.prod.sis.lan/ptep/article-pdf/2015/3/033D02/9720010/ptv008.pdf`.

[43] K. Imai *et al.* Proposal for K1.8 beam line at J-PARC. URL: `http://j-parc.jp/NuclPart/pac_0606/pdf/p07-Nakazawa.pdf` (visited on 09/23/2019).

[44] T. Fukuda *et al.* “Cascade hypernuclei in the (K^-, K^+) reaction on ^{12}C”. In: *Phys. Rev. C* 58 (1998), pp. 1306–1309.

[45] P. Khaustov *et al.* “Evidence of Ξ hypernuclear production in the ^{12}C (K$^-$,K$^+$) $^{12}_{\Xi}$Be reaction”. In: *Phys. Rev. C* 61 (2000), p. 054603.

[46] K. Aoki. PSpectroscopic Study of Ξ^--Hypernucleus, $^{12}_{\Xi^-}$Be, via the ^{12}C(K$^-$;K$^+$) Reaction. URL: `https://j-parc.jp/researcher/Hadron/en/pac_0606/pdf/p05-Nagae.pdf` (visited on 10/29/2019).

[47] T. Nagae. Proposal for the next E05 run with the S - 2S spectrometer. URL: `https://is.j-parc.jp/researcher/Hadron/en/pac_1801/pdf/P70_2018-10.pdf` (visited on 10/29/2019).

[48] S. Dairaku *et al.* A J-PARC E03 Proposal: Measurement of X Rays from Ξ^- Atom. URL: `http://www.j-parc.jp/researcher/Hadron/en/pac_0606/pdf/p03-Tanida.pdf`.

[49] T. Rathmann. “"Einfluss von Strahlenschäden auf die Auflösung eines Germanium-Detektors für das PANDA Experiment"”. Bachelor’s thesis. JGU Mainz, 2014.

[50] C. Batty. “Strange exotic atoms”. In: *Nucl. Phys. A* 585.1 (1995). *Hypernuclear and Strange Particle Physics*, pp. 229–237.

[51] J. Pochodzalla *et al.* “Many Facets of Strangeness Nuclear Physics with Stored Antiprotons”. In: *JPS Conf. Proc.* 17 (2017), p. 091002. arXiv: `1609.01916 [nucl-ex]`.

[52] B. Singh *et al.* “Study of doubly strange systems using stored antiprotons”. In: *Nucl. Phys. A* 954 (2016). *Recent Progress in Strangeness and Charm Hadronic and Nuclear Physics*, pp. 323–340.

[53] P. Achenbach *et al.* "Write-ups for workshop on the project for the hadron experimental facility of J-PARC, Partial collection of LOIs at the extended hadron hall and the related topics". 2019. arXiv: `1906.02357 [nucl-ex]`.

[54] J. Pochodzalla *et al.* “Strangeness nuclear physics at PANDA in a nutshell”. In: *Write-ups for workshop on the project for the extended hadron experimental facility of J-PARC*. 2019, p. 7.

[55] M. Steinen. “Heavy Ξ^--atoms at PANDA”. *STRANEX: Recent progress and perspectives in STRANge EXotic atoms studies and related topics; ECT*, Trento, Italy*. 2019. URL: `http://indico.ectstar.eu/event/61/`.

[56] M. Steinen. “Heavy Ξ^--atoms at PANDA”. *Theia-Strong2020 Workshop 2019; Speyer, Germany*. 2019. URL: `hhttps://indico.gsi.de/event/8950/`.

[57] O. Boine-Frankenheim *et al.* “"FAIR forges its future"”. In: *CERN Courier* 57.6 (2017), pp. 41–44. (Visited on 08/29/2019).

[58] FAIR GmbH and GSI. [MSV] Green Paper, The Modularized Start Version : FAIR - Facility for Antiproton and Ion Research. Damstadt: FAIR, 2009, 19p. URL: `http://repository.gsi.de/record/54094`.

[59] J. Gerl *et al.* "NUSTAR Progress Report". 2012. URL: `http://www.fair-center.eu/fileadmin/fair/experiments/NUSTAR/Pdf/NUSTAR_ProgressReport_SC_Nov2012_final.pdf` (visited on 12/01/2019).

[60] T. Stöhlker *et al.* “APPA at FAIR: From fundamental to applied research”. In: *Nucl. Instrum. B* 365, Part B (2015). *Swift Heavy Ions in Matter, 18 - 21 May, 2015, Darmstadt, Germany*, pp. 680–685.

[61] V. Friese *et al.*, eds. "CBM Progress Report 2015". Darmstadt: GSI, 2016, 155 S. : Ill., graf. Darst. URL: `https://repository.gsi.de/record/186952` (visited on 12/01/2019).

[62] M. F. M. Lutz *et al.* "Physics Performance Report for PANDA: Strong Interaction" Studies with Antiprotons. 2009. arXiv: `0903.3905 [hep-ex]`.

[63] PANDA collaboration. Phase One paper. *in preparation*. 2019. URL: `https://panda.gsi.de/publication/in-prp-2019-002` (visited on 11/11/2019).

[64] U. Kurilla. General PANDA material for slides, logos, detector drawings, etc. 2017. URL: `https://panda.gsi.de/publication/rn-det-2017-001` (visited on 09/23/2019).

[65] S. Pacetti *et al.* “Proton electromagnetic form factors: Basic notions, present achievements and future perspectives”. In: *Phys Rep.* 550-551 (2015). *Proton electromagnetic form factors: Basic notions, present achievements and future perspectives*, pp. 1–103.

[66] S. Bleser. “The target system of the hypernuclear experiment at PANDA”. PhD thesis. JGU Mainz, in preparation.

[67] W. e. a. Erni. "Technical Design Report for the PANDA Internal Targets". 2012. URL: `https://panda.gsi.de/system/files/user_uploads/u.kurilla/RE-TDR-2012-002.pdf` (visited on 09/23/2019).

[68] W. Erni *et al.* Technical Design Report for the PANDA Luminosity Detector. 2017.

[69] W. Erni *et al.* “Technical Design Report for the: PANDA Micro Vertex Detector”. In: *ArXiv* (2012). arXiv: `1207.6581 [physics.ins-det]`.

[70] W. Erni *et al.* “Technical design report for the PANDA (AntiProton Annihilations at Darmstadt) Straw Tube Tracker”. In: *Eur. Phys. J.* A49 (2013), p. 25. arXiv: `1205.5441 [physics.ins-det]`.

[71] W. Erni *et al.* “Technical Design Report for the PANDA Solenoid and Dipole Spectrometer Magnets”. In: *ArXiv* (2009). arXiv: `0907.0169 [physics.ins-det]`.

[72] W. Erni *et al.* “Technical Design Report for PANDA Electromagnetic Calorimeter (EMC)”. In: *ArXiv* (2008). arXiv: `0810.1216 [physics.ins-det]`.

[73] B. Singh *et al.* "Technical Design Report for the PANDA Forward Spectrometer Calorimeter". 2016. URL: `https://panda.gsi.de/system/files/user_uploads/admin/RE-TDR-2015-002.pdf` (visited on 09/23/2019).

[74] W. Erni *et al.* "Technical Design Report on the PANDA Muon System". 2012. URL: `https://panda.gsi.de/system/files/user_uploads/u.kurilla/RE-TDR-2012-003.pdf` (visited on 09/23/2019).

[75] S. Teis *et al.* “Analysis of subthreshold antiproton production in p-nucleus and nucleus-nucleus collisions in the relativistic Boltzmann-Uehling-Uhlenbeck approach”. In: *Phys. Rev. C* 50 (1994), pp. 388–405.

[76] T. D. Lee *et al.* “Charge conjugation, a new quantum number G, and selection rules concerning a nucleon-antinucleon system”. In: *Il Nuovo Cimento* 3.4 (1956), pp. 749–753.

[77] T. Gaitanos *et al.* “How deep is the antinucleon optical potential at FAIR energies”. In: *Phys. Lett. B* 703.2 (2011), pp. 193–198.

[78] T. Gaitanos *et al.* “Non-linear derivative interactions in relativistic hadrodynamics”. In: *Nucl. Phys. A* 828.1 (2009), pp. 9–28.

[79] T. Gaitanos *et al.* “Momentum dependent mean-field dynamics of compressed nuclear matter and neutron stars”. In: *Nucl. Phys. A* 899 (2013), pp. 133–169.

[80] R. d. O. Gomes *et al.* “Many-body forces in the equation of state of hyperonic matter”. In: *Astrophys. J.* 808.1 (2015), p. 8.

[81] J. Pochodzalla. “Exploring the potential of antihyperons in nuclei with antiprotons”. In: *Phys. Lett. B* B669 (2008), pp. 306–310. arXiv: `0807.3302 [nucl-ex]`.

[82] O. Buss *et al.* “Transport-theoretical Description of Nuclear Reactions”. In: *Phys. Rept.* 512 (2012), pp. 1–124. arXiv: `1106.1344 [hep-ph]`.

[83] A. Sanchez Lorente *et al.* “Antihyperon potentials in nuclei via exclusive antiproton-nucleus reactions”. In: *Phys. Lett. B* 749 (2015), pp. 421–424.

[84] J. Pochodzalla *et al.* “Two-particle correlations at small relative momenta for ^{40}Ar induced reactions on ^{197}Au at E/A=60 MeV”. In: *Phys. Rev. C* 35 (1987), pp. 1695–1719.

[85] E. Hiyama *et al.* “Four-body cluster structure of A=10 double-Λ hypernuclei”. In: *Phys. Rev. C* 66 (2002), p. 024007.

[86] K. Tanida *et al.* “Measurement of the B(E2) of $^{7}_{\Lambda}Li$ and Shrinkage of the Hypernuclear Size”. In: *Phys. Rev. Lett.* 86 (2001), pp. 1982–1985.

[87] Y. Yoshida. "Status report of J-PARC E07". *Presentation at the 27th J-PARC PAC Meeting*. 2019. URL: `https://kds.kek.jp/indico/event/29923/contribution/28/material/slides/0.pdf` (visited on 09/23/2019).

[88] Y. Tanimura. “"Clusterization and deformation of multi-Λ hypernuclei within relativistic mean-field model"”. In: *Phys. Rev. C* C99.3 (2019), p. 034324. arXiv: `1812.07713 [nucl-th]`.

[89] E. Garrido *et al.* “Rotational bands in the continuum illustrated by ^{8}Be results”. In: *Phys. Rev. C* 88 (2013), p. 024001.

[90] B. Sauer. “Carbon fiber as primary target at the hypernuclear experiment of PANDA”. Bachelor’s thesis. JGU Mainz, 2018.

[91] F. Schupp. Private communication. *Helmholtz-Institut Mainz.*

[92] F. Schupp. “Entwicklung einer Methode zur strahlenharten Positionierung für das primäre Hyperkerntarget an PANDA”. Diploma thesis. JGU Mainz, 2017.

[93] Michael Bölting. “Design, Realisierung und Test der Steuersoftware für das primäre Target des PANDA-Hyperkernexperiments”. Diploma thesis. JGU Mainz, 2017.

[94] A. S. Lorente *et al.* “Production of excited double hypernuclei via Fermi breakup of excited strange systems”. In: *Phys. Lett. B* 697.3 (2011), pp. 222–228.

[95] R. Schnell *et al.* “The readout chain for the PANDA MVD strip detector”. In: *J. Instrum.* 10.02 (2015), pp. C02003–C02003.

[96] V. Akylas *et al.* “Muonic atom cascade program”. In: *Comput. Phys. Commun.* 15.3 (1978), pp. 291–302.

[97] H. Backe *et al.* “Study of X-rays and nuclear γ-rays in muonic thallium”. In: *Nucl. Phys. A* 189.3 (1972), pp. 472–512.

[98] Hüfner, Jörg. “A cascade calculation for muonic lead”. In: *Z. Phys* 195.4 (1966), pp. 365–369.

[99] Y. Eisenberg *et al.* “On the μ-mesonic atoms”. In: *Il Nuovo Cimento* 19.6 (1961), pp. 1195–1210.

[100] T. Aramaki *et al.* “A measurement of atomic X-ray yields in exotic atoms and implications for an antideuteron-based dark matter search”. In: *Astropart. Phys.* 49 (2013), pp. 52–62.

[101] C. J. Batty *et al.* “Experiments with Ξ^- atoms”. In: *Phys. Rev. C* 59 (1999), pp. 295–304.

[102] G. Backenstoss *et al.* “Strong interaction effects in antiprotonic atoms”. In: *Phys. Lett. B* 41.4 (1972), pp. 552–556.

[103] G. Backenstoss *et al.* “Intensity measurements on Σ-hyperonic and kaonic atoms”. In: *Z. Phys A* 273.2 (1975), pp. 137–156.

[104] G. Dugan *et al.* “Mass and magnetic moment of Σ^- by the exotic atom method”. In: *Nucl. Phys. A* 254.2 (1975), pp. 396–402.

[105] E. Friedman *et al.* “In-medium nuclear interactions of low-energy hadrons”. In: *Phys Rep.* 452.4 (2007), pp. 89–153.

[106] T. E. O. Ericson *et al.* Pions and nuclei. Vol. 74. Internat. Ser. Mono. Phys. Oxford: Clarendon Press, 1988. URL: `https://cds.cern.ch/record/112241` (visited on 12/01/2019).

[107] E. Friedman. Private communication. *Racah Institue of Physics, Hebrew University of Jerusalem.*

[108] J. Patterson *et al.* “Empirical distributions of protons within nuclei”. In: *Nucl. Phys. A* 717.3 (2003), pp. 235–246.

[109] R. Pohl *et al.* “The size of the proton”. In: *Nature* 466 (2010), pp. 213–216.

[110] R. Pohl *et al.* “Laser spectroscopy of muonic deuterium”. In: *Sci.* 353.6300 (2016), pp. 669–673. eprint: `https://science.sciencemag.org/content/353/6300/669.full.pdf`.

[111] J. C. Bernauer *et al.* “High-Precision Determination of the Electric and Magnetic Form Factors of the Proton”. In: *Phys. Rev. Lett.* 105 (2010), p. 242001.

[112] J. J. Krauth *et al.* The proton radius puzzle. 2017. arXiv: `1706.00696 [physics.atom-ph]`.

[113] N. Bezginov *et al.* “A measurement of the atomic hydrogen Lamb shift and the proton charge radius”. In: *Sci.* 365.6457 (2019), pp. 1007–1012. eprint: `https://science.sciencemag.org/content/365/6457/1007.full.pdf`.

[114] W. Xiong *et al.* “A small proton charge radius from an electron-proton scattering experiment”. In: *Nature* 575.7781 (2019), pp. 147–150.

[115] H. Hill. Proton radius puzzle may be solved. URL: `https://physicstoday.scitation.org/do/10.1063/PT.6.1.20191106a/full/` (visited on 11/14/2019).

[116] P. H. Collaboration. *et al.* “Pionic hydrogen”. In: *Int. J. Mod. Phys. A* 20.08n09 (2005), pp. 1644–1649.

[117] T. Yamazaki *et al.* “Discovery of deeply bound π^- states in the 208-Pb(d,3He) reaction”. In: *Z. Phys A* 355.1 (1996), pp. 219–221.

[118] K. Suzuki *et al.* “Precision Spectroscopy of Pionic 1s States of Sn Nuclei and Evidence for Partial Restoration of Chiral Symmetry in the Nuclear Medium”. In: *Phys. Rev. Lett.* 92 (2004), p. 072302.

[119] M. Iwasaki *et al.* “Observation of Kaonic Hydrogen K_α XRays”. In: *Phys. Rev. Lett.* 78 (1997), pp. 3067–3069.

[120] G. Beer *et al.* “Measurement of the Kaonic Hydrogen X-Ray Spectrum”. In: *Phys. Rev. Lett.* 94 (2005), p. 212302.

[121] C. Milardi *et al.* “Present status of the DAΦNE upgrade and perspectives”. In: *Int. J. Mod. Phys.* A24 (2009), pp. 360–368.

[122] J. Zmeskal *et al.* “Probing Strong Interaction with Kaonic Atoms – from DAΦNE to J-PARC”. In: *Proceedings of the 12th International Conference on Hypernuclear and Strange Particle Physics (HYP2015).* 2017, p. 10. URL: `https://journals.jps.jp/doi/abs/10.7566/JPSCP.17.071001` (visited on 09/23/2019).

[123] M. Bazzi *et al.* “Kaonic helium-4 X-ray measurement in SIDDHARTA”. In: *Phys. Lett. B* 681.4 (2009), pp. 310–314.

[124] M. Bazzi *et al.* “Measurements of the strong-interaction widths of the kaonic ^{3}He and ^{4}He 2p levels”. In: *Phys. Lett. B* 714.1 (2012), pp. 40–43.

[125] M. Bazzi *et al.* “First measurement of kaonic helium-3 X-rays”. In: *Phys. Lett. B* B697 (2011), pp. 199–202. arXiv: `1010.4631 [nucl-ex]`.

[126] H. Tatsuno *et al.* “Future projects of light kaonic atom X-ray spectroscopy”. In: *EPJ Web Conf.* 130 (2016), p. 01018.

[127] P. D. Barnes *et al.* “Strong-Interaction Effects in Antiprotonic Atoms”. In: *Phys. Rev. Lett.* 29 (1972), pp. 1132–1134.

[128] A. Deloff *et al.* “Strong-interaction effects in antiprotonic atoms”. In: *Phys. Rev. C* 10 (1974), pp. 2657–2658.

[129] A. Deloff *et al.* “Erratum: Strong-interaction effects in antiprotonic atoms”. In: *Phys. Rev. C* 11 (1975), pp. 1067–1067.

[130] R. Bryan *et al.* “Nucleon-antinucleon potential from single-meson exchanges”. In: *Nucl. Phys. B* 5.2 (1968), pp. 201–219.

[131] G. Backenstoss. “Antiprotonic atoms”. In: *Contemp. Phys.* 30.6 (1989), pp. 433–448. eprint: `https://doi.org/10.1080/00107518908221991`.

[132] A. Trzcińska *et al.* “Information on antiprotonic atoms and the nuclear periphery from the PS209 experiment”. In: *Nucl. Phys. A* 692.1 (2001). *Sixth Biennial Conference on Low-Energy Antiproton Physics*, pp. 176–181.

[133] A. Trzcińska *et al.* "Antiprotonic atoms X rays". Ed. by A. Hirtl *et al.* Wien: Verlag der Österreichischen Akademie der Wissenschaften, 2006, pp. 303–310. URL: `http://austriaca.at/?arp=0x000fd4f1`.

[134] A. Trzcińska *et al.* “Neutron Density Distributions Deduced from Antiprotonic Atoms”. In: *Phys. Rev. Lett.* 87 (2001), p. 082501.

[135] B. Klos *et al.* “Neutron density distributions from antiprotonic ^{208}Pb and ^{209}Bi atoms”. In: *Phys. Rev. C* 76 (2007), p. 014311.

[136] A. Trzcińska. “Antiprotonic Atoms as a Tool to Study the Nuclear Periphery”. In: *Acta Phys. Polon.* B41 (2010), pp. 311–316.

[137] J. Jastrzębski *et al.* “Signature of a neutron halo in ^{232}Th from antiproton absorption”. In: *Nucl. Phys. A* 558 (1993), pp. 405–414.

[138] P. LubiÅ„ski *et al.* “Neutron Halo in Heavy Nuclei from Antiproton Absorption”. In: *Phys. Rev. Lett.* 73 (1994), pp. 3199–3202.

[139] S. Wycech *et al.* “Nuclear surface studies with antiprotonic atom X-rays”. In: *Phys. Rev. C* 76 (2007), p. 034316.

[140] E. Widmann. “Precision Physics with Low-energy Antiprotons - from AD to FLAIR”. In: *Acta Phys. Polon.* B41 (2010), pp. 249–260. arXiv: `1003.1444 [hep-ex]`.

[141] E. Widmann. “Plans for a Next-Generation Low-Energy Antiproton Facility”. In: *Phys. Scr.* 72.6 (2005), p. C51.

[142] G. Backenstoss *et al.* “Observations of Σ hyperonic atoms”. In: *Phys. Lett. B* 33.3 (1970), pp. 230–232.

[143] C. Batty *et al.* “Measurement of strong interaction effects in Σ atoms”. In: *Phys. Lett. B* 74.1 (1978), pp. 27–30.

[144] R. J. Powers *et al.* “Strong-interaction effect measurements in sigma hyperonic atoms of W and Pb”. In: *Phys. Rev. C* 47 (1993), pp. 1263–1273.

[145] C. J. Batty *et al.* “Density Dependence in Σ^- Atoms and Implications for Σ^-Hypernuclei”. In: *Prog. Theor. Phys. Supp.* 117 (1994), pp. 227–240. eprint: `http://oup.prod.sis.lan/ptps/article-pdf/doi/10.1143/ptp.117.227/5421615/117-227.pdf`.

[146] C. Batty *et al.* “Strong interaction physics from hadronic atoms”. In: *Phys Rep.* 287.5 (1997), pp. 385–445.

[147] T. Harada *et al.* “Σ^- production spectrum in the inclusive (π^-, K^+) reaction on ^{209}Bi and the Σ-nucleus potential”. In: *Nucl. Phys. A* 767 (2006), pp. 206–217.

[148] C. Batty. “Nuclear bound states of negatively charged hadrons?” In: *Phys. Lett. B* 87.4 (1979), pp. 324–326.

[149] C. Batty *et al.* “Density dependence of the Σ^- nucleus optical potential derived from Σ^- atom data”. In: *Phys. Lett. B* 335.3 (1994), pp. 273–278.

[150] H. Noumi *et al.* “Sigma-Nucleus Potential in $A = 28$”. In: *Phys. Rev. Lett.* 89 (2002), p. 072301.

[151] H. Noumi *et al.* “Erratum: Sigma-Nucleus Potential in $A = 28$ [Phys. Rev. Lett. 89, 072301 (2002)]”. In: *Phys. Rev. Lett.* 90 (2003), p. 049902.

[152] P. K. Saha *et al.* “Σ^--nucleus potential studied with the (π^-, K^+) reaction on medium-to-heavy nuclear targets”. In: *Phys. Rev. C* 70 (2004), p. 044613.

[153] J. Mareš *et al.* “Constraints on Σ-nucleus dynamics from dirac phenomenology of Σ^- atoms”. In: *Nucl. Phys. A* 594.3 (1995), pp. 311–324.

[154] K. Tsubakihara *et al.* “Hypernuclei and nuclear matter in a chiral SU(3) RMF model”. In: *Eur. Phys. J. A* 33.3 (2007), pp. 295–298.

[155] R. S. Hayano *et al.* “Evidence for a bound state of the $^4_\Sigma$He hypernucleus”. In: *Phys. Lett. B* 231.4 (1989), pp. 355–358.

[156] T. Nagae *et al.* “Observation of a $^4_\Sigma$He Bound State in the ^{4}He(K^-, π^-) Reaction at $600 MeV/c$”. In: *Phys. Rev. Lett.* 80 (1998), pp. 1605–1609.

[157] T. Harada *et al.* “Structure of the $^4_\Sigma$He hypernuclear bound state”. In: *Nucl. Phys. A* 507.3 (1990), pp. 715–730.

[158] T. Harada *et al.* “Coulomb-assisted Σ^--nucleus bound states in the (K^-, π^+) reaction”. In: *Nucl. Phys. A* 829.1 (2009), pp. 100–125.

[159] T. Hatsuda *et al.* “pΣ^- Correlation in Relativistic Heavy Ion Collisions with Nucleon-Hyperon Interaction from Lattice QCD”. In: *Nucl. Phys. A* 967 (2017). *The 26th International Conference on Ultra-relativistic Nucleus-Nucleus Collisions: Quark Matter 2017*, pp. 856–859.

[160] K. Sasaki *et al.* “Baryon interactions from lattice QCD with physical masses – S=-2 sector –”. In: *Proc. Sci.* LATTICE2016 (2017), p. 116. arXiv: `1702.06241 [hep-lat]`.

[161] K. Tanida. “Status of J-PARC K1.8 Beam Line”. In: *EPJ Web Conf.* 20 (2012), p. 05003.

[162] T. Koike *et al.* “Development of a low-temperature germanium detector via mechanical cooling with a compact pulse-tube refrigerator”. In: *Nucl. Instrum. A* 770 (2015), pp. 1–7.

[163] M. Fujita. The Ξ^--atom X-ray spectroscopy at J-PARC (Poster). *8th International Conference on Quarks and Nuclear Physics (QNP2018), Tsukuba, Japan*. URL: `https://conference-indico.kek.jp/indico/event/33/session/52/contribution/182` (visited on 09/23/2019).

[164] J. Yoshida. “"Status of J-PARC E07: Systematic study of double strangeness nuclei with hybrid emulsion method"”. In: *Proc. of the 13th International Conference on Hypernuclear and Strange Particle Physics*. 2018, p. 8. URL: `https://www.jlab.org/conferences/hyp2018/talks/wed/am/05_yoshida.pdf`.

[165] K. Tanida *et al.* "Status report and beam request: E03: Measurement of X rays from Ξ^- atom". `https://kds.kek.jp/indico/event/29923/contribution/27/material/slides/0.pdf`. Presentation at the 27th J-PARC PAC Meeting. 2019. (Visited on 09/23/2019).

[166] T. Moon. "Development of Matrix Trigger Module for J-PARC E03". In: *Proceedings of the 12th International Conference on Hypernuclear and Strange Particle Physics (HYP2015)*. 2017, p. 2.

[167] A. Messiah. "Quantum Mechanics". Quantum Mechanics Bd. 2. Elsevier Science, 1981. URL: `https://books.google.ch/books?id=VR93vUk8d%5C_8C`.

[168] G. Ramalho *et al.* "Extracting the Ω^- electric quadrupole moment from lattice QCD data". In: *Phys. Rev. D* 83 (2011), p. 054011.

[169] R. M. Sternheimer *et al.* "Possibility of Ω^--Hyperonic Atoms and the Electric Quadrupole Moment of the Ω^- Particle". In: *Phys. Rev. A* 8 (1973), pp. 2207–2213.

[170] M. Giannini *et al.* "The Ω^- exotic atom". In: *Phys. Lett. B* 291.3 (1992), pp. 329–335.

[171] G. Karl *et al.* "Quadrupolar contact terms and hyperfine structure". In: *Phys. Rev. C* 74 (2006), p. 024001.

[172] M. Krivoruchenko *et al.* "Decays, contact P-wave interactions and hyperfine structure in Ω^- exotic atoms". In: *Nucl. Phys. A* 803.3 (2008), pp. 173–209.

[173] L. W. Alvarez. "Certification of Three Old Cosmic-Ray Emulsion Events as Ω^- Decays and Interactions". In: *Phys. Rev. D* 8 (1973), pp. 702–711.

[174] Y. Eisenberg. "Possible Existence of a New Hyperon". In: *Phys. Rev.* 96 (1954), pp. 541–543.

[175] W. F. Fry *et al.* "K-Mesonic Decay of a Slow Secondary Particle". In: *Phys. Rev.* 97 (1955), pp. 1189–1190.

[176] V. E. Barnes *et al.* "Observation of a Hyperon with Strangeness Minus Three". In: *Phys. Rev. Lett.* 12 (1964), pp. 204–206.

[177] A. B. Kaidalov *et al.* "Binary reactions in $\overline{p}p$ collisions at intermediate energies". In: *Z. Phys C* 63.3 (1994), pp. 517–524.

[178] R. Palit *et al.* "Technical Report for the Design, Construction and Commissioning of the DESPEC Germanium Array Spectrometer DEGAS". 2014. URL: `https://edms.cern.ch/file/1813618/2/TDR_HISPEC_DESPEC_DEGAS_public.pdf` (visited on 09/23/2019).

[179] A. Sanchez Lorente. "Feasibility study of performing high precision gamma spectroscopy of $\Lambda\Lambda$ hypernuclei in the PANDA experiment". PhD thesis. JGU Mainz, 2010.

[180] J. Simpson. "The Euroball Spectrometer". In: *Z. Phys A* 358.2 (1997), pp. 139–143.

[181] P. H. Regan *et al.* "Decay Studies of Exotic Nuclei using RISING and the GSI Fragment Separator". In: *GSI Propos.* (2005).

[182] J. Eberth *et al.* "Development of a composite Ge detector for EUROBALL". In: *Prog. Part. Nuc. Phys.* 28 (1992), pp. 495–504.

[183] I. Kojouharov *et al.* “Optimization of Electrically Cooled Complex HPGe Detector”. In: *2012 Sixth UKSim/AMSS European Symposium onComputer Modeling and Simulation (EMS)*. 2012, pp. 461–465.

[184] P. Lebrun. "Introduction to cryogenics". *CAS and ALCA school on vacuum in accelarators, 2006*. URL: `https://cas.web.cern.ch/sites/cas.web.cern.ch/files/lectures/platjadaro-2006/lebrun.pdf` (visited on 09/23/2019).

[185] T. Engert *et al.* Waermeübergangsleiter. Tech. rep. *P270*. GSI, 2009. URL: `http://repository.gsi.de/record/66842`.

[186] Advanced Measurement Technology. "X-Cooler III, Mechanical Cooler for HPGe Detectors, Manual Revision F". 2014. URL: `https://www.ortec-online.com/-/media/ametekortec/manuals/x-cooler-iii-mnl.pdf` (visited on 09/23/2019).

[187] N. W. Lane. “Commercialization status of free-piston Stirling machines”. In: *12th International Stirling Engine Conference, Durham, UK September*. 2005.

[188] I. Kojouharov. Private communication. *GSI, Darmstadt*.

[189] AMETEK.Inc. Sunpower CryoTel Website. URL: `https://www.sunpowerinc.com/products/cryocoolers/cryotel-cryocoolers?sc_lang=de-DE` (visited on 12/06/2019).

[190] F. Farinon *et al.* “Development and test of Isomer TAGging detector”. In: *GSI Sci. Rep.* (2009), p. 303.

[191] iseg Spezialelektronik GmbH. "High Voltage Power Supply BPS-series (4W), RoHS compliant". URL: `https://iseg-hv.com/en/products/detail/BPS` (visited on 12/01/2019).

[192] R. Cantemir. “Konzeption eines Slow Control Systems für Germanium-Detektoren”. MA thesis. THM Friedberg, 2017.

[193] I. Kojouharov *et al.* DEGAS Triple Prototype. in preparation.

[194] P. Marciniewski. "A Compact Size, 64-Channel, 80 MSPS, 14-Bit Dynamic Range ADC Module for the PANDA Electromagnetic Calorimeter". 2017. URL: `https://indico.cern.ch/event/608587/contributions/2614165/attachments/1521599/2377353/TWEPP_2017.pdf` (visited on 09/23/2019).

[195] I. Konorov *et al.* “SODA: Time distribution system for the PANDA experiment”. In: *2009 IEEE Nuclear Science Symposium Conference Record (NSS/MIC)*. IEEE. 2009, pp. 1863–1865.

[196] "Datasheet: nanoDPP". labZY. URL: `http://www.labzy.com/wp-content/uploads/nanoDPP_Data_Sheet_Rev_02a.pdf` (visited on 09/23/2019).

[197] L. R. Dalesio *et al.* “EPICS architecture”. In: *ICALEPCS*. Vol. 91. 1991, pp. 92–15.

[198] Website: BeagleBone Black. BeagleBoard.org Foundation. URL: `https://beagleboard.org/black` (visited on 11/18/2019).

[199] J. A. Lucio Martinez. “Development of a radiation hard DCS board”. PhD thesis. GU Frankfurt, in preparation.

[200] J. A. Lucio Martinez. Private communication. *Infrastructure and Computer Systems in Data Processing, Goethe Universität, Frankfurt am Main*.

[201] S. Spataro *et al.* "The PandaRoot framework for simulation, reconstruction and analysis". In: *J. Phys. Conf Ser.* 331.3 (2011), p. 032031.

[202] R. Brun *et al.* "ROOT - An object oriented data analysis framework". In: *Nucl. Instrum. A* 389.1 (1997), pp. 81–86.

[203] I. Hřivnáčová *et al.* The Virtual Monte Carlo. 2003. arXiv: `cs/0306005 [cs.SE]`. URL: `http://arxiv.org/abs/cs.SE/0306005`.

[204] S. Agostinelli *et al.* "GEANT4 - a simulation toolkit". In: *Nucl. Instrum. A* 506.3 (2003), pp. 250–303.

[205] R. Brun *et al.* "The ROOT geometry package". In: *Nucl. Instrum. A* 502.2-3 (2003). *Proceedings of the {VIII} International Workshop on Advanced Computing and Analysis Techniques in Physics Research*, pp. 676–680.

[206] M. Steinen. "Untersuchung von Germanium-Detektoren für das PANDA-Experiment". Diploma thesis. JGU Mainz, 2011.

[207] T. Stockmanns. "STEP-to-ROOT - from CAD to Monte Carlo Simulation". In: *J. Phys. Conf Ser.* 396.2 (2012), p. 022050.

[208] J. Lühning. Private communication. *GSI, Darmstadt*.

[209] D. Rodriguez Pineiro. Private communication. *Helmholtz-Institute Mainz, Mainz*.

[210] P. Wintz. Private communication. *Institute for nuclear physics, FZ Jülich*.

[211] M. Bragadireanu. PANDA Detector Control System. 2014. URL: `https://panda-wiki.gsi.de/foswiki/bin/view/DCS/WebHome` (visited on 09/19/2018).

[212] J. Cleland *et al.* "Radiation Damage in Semiconductors". In: *Acad. Press, N.Y.* (1964), p. 401.

[213] W. Hoffelner. "Irradiation Damage in Nuclear Power Plants". In: *Handbook of Damage Mechanics: Nano to Macro Scale for Materials and Structures*. Ed. by G. Z. Voyiadjis. New York, NY: Springer New York, 2015, pp. 1427–1461. URL: `https://doi.org/10.1007/978-1-4614-5589-9_36`.

[214] L. Darken. "Role of disordered regions in fast-neutron damage of HPGe detectors". In: *Nucl. Instrum. B* 74.4 (1993), pp. 523–526.

[215] R. H. Pehl *et al.* "Gamma-Ray Escape-peak Response from a Radiation-Damaged Reverse-Electrode Coaxial Germanium Detector". In: *IUCF Ann. Sci. Tech. Rep.* (1995), pp. 124–130.

[216] R. H. Pehl *et al.* "Radiation Damage Resistance of Reverse Electrode GE Coaxial Detectors". In: *IEEE Trans. Nuc. Sci.* 26.1 (1979), pp. 321–323.

[217] E. Hull *et al.* "Radiation Damage Effects on High-Purity Germanium Detectors". In: *IUCF Ann. Sci. Tech. Rep.* (1993), pp. 143–148.

[218] H. Thomas *et al.* "Neutron induced radiation damage of a n-type Ge detector influence of the operating temperature". In: *Nucl. Instrum. A* 332.1 (1993), pp. 215–219.

[219] N. Fourches *et al.* "Neutron-induced defects in high-purity germanium". In: *J. Appl. Phys.* 69.4 (1991), pp. 2033–2043. eprint: `https://doi.org/10.1063/1.348728`.

[220] M. Tanabashi *et al.* “Review of Particle Physics”. In: *Phys. Rev. D* 98 (2018), p. 030001.

[221] R. Maier. “Cooler synchrotron COSY â€” Performance and perspectives”. In: *Nucl. Instrum. A* 390.1 (1997), pp. 1–8.

[222] H. Stelzer *et al.* “JESSICA, the test facility for an advanced cold moderator system for ESS”. In: *11th International Conference on Nuclear Engineering (ICONE-11) Tokyo, Japan*. 2003. URL: `http://www.fz-juelich.de/cae/servlet/contentblob/930158/publicationFile/12557/JESSICA.pdf`.

[223] U. Bechstedt *et al.* “Status of the Cooler Synchrotron COSY Juelich”. In: *Conf. Proc.* C0106181 (2001). *[,3350(2001)]*, pp. 3350–3352.

[224] H. G. Essel *et al.* “The general purpose data acquisition system MBS”. In: *IEEE Trans. Nuc. Sci.* 47.2 (2000), pp. 337–339.

[225] J. Adamczewski *et al.* “Go4 on-line monitoring”. In: *IEEE Trans. Nuc. Sci.* 51.3 (2004), pp. 565–570.

[226] H. Patterson *et al.* "Accelerator Health Physics". Academic Press rapid manuscript reproductions. Academic Press, 1973. URL: `https://books.google.de/books?id=TF5RAAAAMAAJ`.

[227] M. Pelliccioni. “Overview of Fluence-to-Effective Dose and Fluence-to-Ambient Dose Equivalent Conversion Coefficients for High Energy Radiation Calculated Using the FLUKA Code”. In: *Radiat. Prot. Dosim.* 88.4 (2000), pp. 279–297. eprint: `/oup/backfile/content_public/journal/rpd/88/4/10.1093_oxfordjournals.rpd.a033046/1/279.pdf`.

[228] I. Jun *et al.* “Proton nonionizing energy loss (NIEL) for device applications”. In: *IEEE Trans. Nuc. Sci.* 50.6 (2003), pp. 1924–1928.

[229] A. Vasilescu *et al.* Displacement damage in silicon, on-line compilation. 2000. URL: `https://rd50.web.cern.ch/rd50/NIEL/default.html` (visited on 10/18/2018).

[230] M. Lauer. “Digital signal processing for segmented HPGe detectors: Preprocessing algorithms and pulse shape analysis”. PhD thesis. Heidelberg University, 2004. URL: `http://weblib.cern.ch/abstract?CERN-THESIS-2004-047`.

[231] S. Chu *et al.* "The Lund/LBNL Nuclear Data Search web page". 1999. URL: `http://nucleardata.nuclear.lu.se/toi/` (visited on 12/01/2019).

[232] B. Bruyneel *et al.* “Correction for hole trapping in AGATA detectors using pulse shape analysis”. In: *Eur. Phys. J. A* 49.5 (2013), p. 61.

[233] M. Nespolo. “Pulse Shape Analysis with germanium detectors: from MARS to AGATA”. PhD thesis. Universita’ degli studi die Padova, 2004. URL: `http://npgroup.pd.infn.it/Tesi/PhD-thesisNespolo.pdf`.

[234] M. Agnello *et al.* “Proton spectra from Non-Mesonic Weak Decay of p-shell Lambda-Hypernuclei and evidence for the two-nucleon induced process”. In: *Phys. Lett. B* B685 (2010), pp. 247–252. arXiv: `0910.4939 [nucl-ex]`.

[235] L. Gruber *et al.* “Barrel time-of-flight detector for the PANDA experiment at FAIR”. In: *Nucl. Instrum. Meth.* A824 (2016), pp. 104–105. arXiv: `1507.05845 [physics.ins-det]`.

[236] J. Schwiening *et al.* “The PANDA Barrel DIRC”. In: *J. Instrum.* 13.03 (2018), p. C03004. arXiv: `1803.10642 [physics.ins-det]`.

[237] W. Verkerke *et al.* “The RooFit toolkit for data modeling”. In: *ArXiv* (2003). eprint: `physics/0306116`.

[238] H. Sakaguchi *et al.* “Proton elastic scattering from stable and unstable nuclei - Extraction of nuclear densities”. In: *Prog. Part. Nuc. Phys.* 97 (2017), pp. 1–52.

[239] V. E. Starodubsky *et al.* “Extraction of neutron densities from elastic proton scattering by ^{206,207,208}Pb at 650 MeV”. In: *Phys. Rev. C* 49 (1994), pp. 2118–2135.

[240] A. Klimkiewicz *et al.* “Nuclear symmetry energy and neutron skins derived from pygmy dipole resonances”. In: *Phys. Rev. C* 76 (2007), p. 051603.

[241] A. Tamii *et al.* “Electric dipole response of 208-Pb from proton inelastic scattering: Constraints on neutron skin thickness and symmetry energy”. In: *Eur. Phys. J. A* 50.2 (2014), p. 28.

[242] A. Bracco. “The Gamma Decay of the Pygmy Resonance and the Neutron Skin of Nuclei”. In: *J. Phys. Conf Ser.* 312.9 (2011), p. 092005.

[243] S. Abrahamyan *et al.* “Measurement of the Neutron Radius of ^{208}Pb through Parity Violation in Electron Scattering”. In: *Phys. Rev. Lett.* 108 (2012), p. 112502. arXiv: `1201.2568 [nucl-ex]`.

[244] F. J. Fattoyev *et al.* “Neutron Skins and Neutron Stars in the Multimessenger Era”. In: *Phys. Rev. Lett.* 120.17 (2018), p. 172702. arXiv: `1711.06615 [nucl-th]`.

[245] Nuclear Physics Laboratory, University of Cyprus. "Experimental technique, gamma-ray detection system". 2018. URL: `http://www-np.ucy.ac.cy/radio_isotopes/wwwen/gamma/gamma_setup.html` (visited on 04/30/2018).

[246] K. Beverung. Private communication. *Radiation protection department GSI, Darmstadt*. 2014.

[247] H. D. Vries *et al.* “Nuclear charge-density-distribution parameters from elastic electron scattering”. In: *At. Data. Nucl. Data Tables* 36.3 (1987), pp. 495–536.

Acknowledgments